Universidad Autónoma de Madrid

Degree of Doctor of Philosophy in

Condensed Matter Physics and Nanoscience

Symmetry breaking effects in spin(orbit)tronic systems: *from universality of anisotropic magnetoresistance in in-plane anisotropy systems to chiral Dzyaloshinskii-Moriya interaction effects in epitaxial metallic and graphene-based perpendicular anisotropy systems*

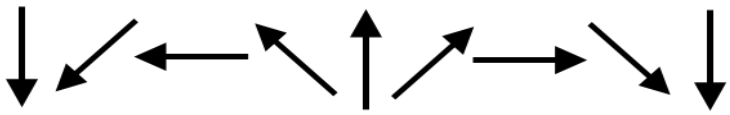

Candidate:

Fernando Ajejas Bazán

Supervisors:

Julio Camarero de Diego and Paolo Perna

Symmetry breaking effects in spin(orbit)tronic systems:

from universality of anisotropic magnetoresistance in in-plane anisotropy systems to chiral Dzyaloshinskii-Moriya interaction effects in epitaxial metallic and graphene-based perpendicular anisotropy systems

Thesis submitted to

Universidad Autónoma de Madrid

for the degree of:

Doctor of Philosophy in

Condensed Matter Physics and Nanoscience

Departamento de Fisica de la Materia Condensada

Facultad de Ciencias

Candidate:

Fernando Ajejas Bazán

Supervisors:

Julio Camarero de Diego and Paolo Perna

UAM UNIVERSIDAD AUTONOMA DE MADRID

instituto imdea nanociencia

A mi madre,

Contents

Resumen

La tecnología, actual y futura, basada en espintrónica se fundamenta en la capacidad para crear nanoestructuras magnéticas en las que tanto el estado de magnetización como la respuesta de transporte puedan ajustarse según los requisitos de la aplicación. Los efectos de magnetoresistencia (MR), estan relacionados al cambio de la resistividad de un material cuando se encuentra bajo estímulos externos, en la actualidad se explotan en dispositivos de espintronica para aplicaciones avanzadas de detección magnética, grabación y memoria no volátil. Sin embargo, la comprensión microscópica de la MR durante la inversión de la magnetización no ha sido totalmente estudiada experimentalmente en muchos materiales tradicionales y especialmente en nuevos sistemas. En el campo emergente de la espinorbitrónica, que añade el grado de libertad de controlar los efectos de intercara de acoplamiento spin-órbita (SOC), los nuevos dispositivos basados en nanoestructuras magnéticas quirales prometen mayor densidad de almacenamiento y procesos más rápidos con un consumo de energía mucho menor. En este caso, se requieren más investigaciones básicas para poder adaptar los dispositivos espinorbitrónicos del futuro.

Esta tésis proporciona un estudio sistemático de nanoestructuras con simetría magnética bien definida (diseñada), que incluye tanto sistemas espintrónicos como espinorbitrónicos, e introduce avances tecnológicos y científicos. Respecto al desarrollo técnico, se ha implementado una instalación experimental única, denominada M (R) OKE, que permite determinar simultáneamente el transporte y las propiedades magnéticas (resueltas vectorialmente) en las nanoestructuras magnéticas. Por otra parte, el manuscrito describe la metodología experimental para a realización de medidas (en plano y perpendicular) de anisotropías magnéticas, y como preparar nanoestructuras magnéticas con efectos quirales en la inversión de la imanación. Desde el punto de vista científico, la tesis se ha dividido en dos partes principales. La primera tiene como objetivo lograr una mejor comprensión y control de los procesos de inversión de magnetización y respuestas magnetorresistivas en sistemas espintrónicos con anisotropía en plano, incluyendo nanoestructuras de una y múltiples capas, desentrañando las diferentes contribuciones y los efectos de la simetría magnética efectiva.

El segundo se ocupa de los sistemas espinorbitrónicos, incluyendo las nanoestructuras magnéticas poli-cristalinas y epitaxiales y las estructuras magnéticas basadas en grafeno, con anisotropía magnética perpendicular (PMA), incluyendo un detallado estudio de preparación y caracterización que proporciona los primeros pasos para hacer ingeniería con acoplo espín-órbita y obtener efectos quirales, ajustando PMA y la interacción Dzyaloshinskii-Moriya (DMI). Dos conclusiones generales, en primer lugar, la comprensión fundamental de las nanoestructuras magnéticas requiere medidas angulares en configuración vectorial. En segundo lugar, la clave que controla las propiedades de las nanoestructuras magnéticas es la simetría magnética efectiva (diseñada).

A lo largo del manuscrito se presentan varios aspectos científicos importantes. En la primera parte, i) determinación de la relación directa entre el transporte y las propiedades magnéticas de los sistemas nanoestructurados. ii) Demostración experimental de la universalidad del fenómeno de la magneto-resistencia anisotrópica, en sistemas con procesos magneto-resistivos de diferente origen (AMR y GMR) y en sistemas ferromagnéticos de diferente naturaleza (metálicos y óxidos). iii) Observación y determinación de los efectos quirales de la MR y su dependencia directa de la anisotropía unidireccional. En la segunda parte, iv) identificación de los parámetros clave que controlan PMA y DMI tanto en sistemas policristalinos como epitaxiales. v) Observación y determinación de efectos quirales sobre sistemas asimétricos con PMA, compuestos de una película FM con intercaras asimétricas, por la presencia de DMI efectivo. vi) Descubrimiento de PMA fuerte en tricapas epitaxiales basadas en grafeno (Pt/Co/gr), con espesores de Co hasta 15 monocapas. Por lo tanto, los resultados proporcionan nuevos conocimientos fundamentales dentro del nanomagnetismo abriendo nuevas vías para mejorar los dispositivos espintrónicos y desarrollar futuros dispositivos espinorbitrónicos avanzados, ambos basados en nanoestructuras magnéticas con simetría efectiva (quiral) diseñada.

Abstract

The current and future spintronic-based technology relies on our ability to create magnetic nanostructures in which both magnetization state and transport response can be set on demand in accordance with application requirements. Magnetoresistance (MR) effects, referred to the change of a material's resistivity upon external stimuli, are exploited in today's spintronic devices for advanced magnetic sensing, recording, and non-volatile memory applications. However, the microscopic understanding of MR during magnetization reversal has not been fully addressed experimentally in many traditional materials and especially in new systems. In the emerging field of spinorbitronics, which adds the degree of freedom of controlling interfacial spin-orbit coupling (SOC) effects, new devices based on chiral magnetic nanostructures promise larger storage density and faster processes with much lower energy consumption. In this case, further basic investigations are required in order to tailor the spinorbitronic-based devices of the future.

This thesis provides a systematic study on magnetic nanostructures with defined (tailored) magnetic symmetry of interest in spintronics and spinorbitronics, and introduces both technological and scientific advances. With respect to the technical development, it has been implemented a unique experimental setup, named M(R)OKE, that allows to determine simultaneously transport and (vectorial-resolved) magnetic properties in magnetic nanostructures. Moreover, the manuscript describes the experimental methodology to tailor (in-plane and perpendicular) magnetic anisotropy, and to prepare magnetic nanostructures with chiral effects. From the scientific point of view, the thesis has been divided in two main parts. The first one aims at achieving a better understanding and control on magnetization reversal processes and magnetoresistive responses in spintronic systems with tailored in-plane anisotropy, including both single and multilayered nanostructures, via the disentangling of the different contributions and the effects to the effective magnetic symmetry. The second one deals with spinorbitronic systems, including polycrystalline and epitaxial metallic and graphene-based (multilayered) magnetic nanostructures with perpendicular magnetic anisotropy (PMA). It includes a

detailed preparation and characterization study of samples, which provides the first steps to engineer interfacial spin-orbit coupling chiral effects, by tuning PMA and the Dzyaloshinskii-Moriya interaction (DMI). Two general conclusions are addressed. First, the fundamental understanding of magnetic nanostructures requires angular-dependent investigations with vectorial-resolved capabilities. Second, the key that controls the properties of magnetic nanostructures is the (tailored) effective magnetic symmetry.

Several important scientific highlights are introduced along the manuscript. In the first part, it is reported: *i)* the determination of the direct relationship between transport and magnetic properties of magnetic nanostructures, *ii)* the experimental proof of the universality of the phenomenon of anisotropic magneto-resistance, demonstrated in systems with magneto-resistive processes of different origin (AMR and GMR) and in ferromagnetic systems of different nature (metallic and oxides), *iii)* the observation and determination of chiral effects of MR and its direct dependence on unidirectional anisotropy. In the second part, *iv)* the identification of the key parameters controlling PMA and DMI in both polycrystalline and epitaxial systems, *v)* the observation and determination of chiral effects on asymmetric PMA systems, composed of a FM film with asymmetric interfaces, by the presence of effective DMI, *vi)* the discovery of strong PMA in epitaxial graphene-based trilayers, i.e., Pt/Co/gr, with Co thicknesses up to 15 monolayers. Therefore, the results provide new fundamental insights within nanomagnetism opening additional avenues to improve spintronic devices and to develop future advanced spinorbitronic devices, both based on magnetic nanostructures with tailored (chiral) effective symmetry.

Introduction

The use of magnetic materials in the form of thin films and multilayered structures at nanometer scale is allowing the development of new devices with innovative concepts useful in many technological areas (sensors, storage, communication, energy) of great impact in society. These magnetic nanostructures are the object of study of a scientific discipline known as spintronics, which combines Solid State Physics, Magnetism and Nanoscience whose goal is to develop tailored (magnetic symmetry) systems that make use of both spin and charge electron in a controlled way to exploit magnetoresistance (MR) effects in magnetic-based devices. Both magnetic anisotropy and magnetoresistive effects originate from spin-orbit coupling (SOC). In the last years a variant known as spin-orbitronics has emerged targeting, in addition, the investigation of the role and the control of interfacial SOC. Novel magnetic nanoarchitectures promise to be used as efficient source of large chiral exchange interaction, commonly known as Dzyaloshinskii–Moriya interaction (DMI), leading the stabilization and manipulation of pure spin currents and/or chiral magnetic structures.

Although spintronics is already used in a multitude of magnetic-based devices, we still do not have a full understanding. In a worse situation is what refers to spin-orbitronics, not only for its novelty but also for the lack of full control of the systems, where a more accurate control is required on smaller thicknesses and better defined interfaces. In both disciplines the physical (magnetic and transport) properties converge in such a way that the control and understanding of the former will allow the design of the devices of the future.

This thesis addresses fundamental questions in the area of nanomagnetism, introducing relevant technological and scientific advances in the field of spintronics and spinorbitronics. The common nexus of the work stays in the SOC effects, whether the research focuses on the influence of magnetic symmetry on physical (magnetic and transport) properties or on the existence of chiral phenomena. In addition, this work explores the possibility to prepare novel full epitaxial graphene-based spin-orbitronic systems in order to can exploit the extraordinary electronic, mechanical and optical

properties of graphene (gr), and in particular its long spin diffusion length and low resistivity. This knowledge will certainly open additional avenues to develop future advanced spintronic and spin-orbitronic devices.

Outline of the thesis

The experimental techniques used in this thesis are discussed in **Chapter 1**, emphasizing several technological advances developed along the thesis work. In particular, the improvements of the multipurpose ultra-high-vacuum chamber, the growth and analysis methodology, and the M(R)OKE instrument are described in detail.

The basic concepts in magnetism required to understand the experimental results of the thesis are introduced in **Chapter 2**, which focuses on the different energies existing in magnetic nanostructures, the basics of the magnetotransport phenomena, and the characteristics of the dynamic of domain wall motion under external magnetic fields.

Chapter 3 points the attention on the correlation between the magnetoresistance responses and the magnetization reversal behaviours in different spintronics systems, such as single FM layer, exchange biased systems and half-metals. In fact, despite the enormous market moving around the spintronic technologies, the microscopic understanding of magnetoresistive effects in low dimensional structures has not been fully addressed experimentally so far. It will be experimentally demonstrated that both magnetoresistance outputs and magnetization reversals strongly depend on the magnetic anisotropy of the system. A special emphasis is devoted to the chiral asymmetric magnetotransport behaviours upon the effect of a unidirectional magnetic anisotropy.

The last two chapters are dedicated to the study of novel spin-orbitronics architectures proposed as potential candidates for next generation magnetic-based information technology applications. These structures exploits the creation and displacement of chiral domain walls (DWs) induced by spin-orbit coupling (SOC) effects, promising smaller sizes, higher speeds, and lower power consumption.

In particular, **Chapter 4** presents the first steps to engineer interfacial SOC chiral effects in multilayered perpendicular magnetic anisotropy (PMA) metallic systems by using asymmetric interfaces and by tuning PMA and an

effective interfacial (chiral) Dzyaloshinskii-Moriya interaction (DMI). These spin-orbitronic systems combine ferromagnetic (FM) films and heavy metals (HM) with large SOC. A detailed study of the influence of the buffer layer, number of repetitions, FM thickness, and HM type has been carried out in multilayer stacks, mainly focusing on asymmetric HM1/FM/HM2 trilayers. Averaged and imaging information derived from different magnetometry techniques have been used to identify the parameters controlling both PMA and DMI.

Finally, **Chapter 5** is devoted to the description of the growth and characterization of high quality epitaxial multilayers based on graphene, consisting in epitaxial HM/Co/gr trilayers deposited on (111)-oriented oxide substrates. Such novel nanostructures benefit from the outstanding properties of gr, as high electronic mobility, large spin lifetimes and long spin diffusion length, and artificially tuneable (large) PMA and effective DMI. Remarkably, both chiral effects and very large PMA (up to 15 MLs thick Co films) are found in these structures. The results open the way for the development of the next generation of (low-power, faster and smaller) gr-based spin-orbitronic devices in 21st century.

I. Experimental techniques

Several technological advances have been developed along this thesis, aiming to prepare high quality (tailored) magnetic nanostructures as well as to get a deeper understanding of their underlying physical properties. In particular, the improvements done in the multipurpose ultra-high-vacuum chamber, the growth and analysis methodology, and the M(R)OKE instrument are described in detail. The basics, methodologies, and procedures of the other experimental techniques used are briefly discussed.

The understanding of the fundamental properties together with the aim to improve the device performance and reliability, the realization of high purity samples, defect-free, and with an atomic control of the surface and interfaces is of extremely importance in nowadays technology. To do that, we need to monitor and control at atomic (nano) scale the growth mode of materials (both inorganic and organic) on solid surfaces. A series of in-situ and ex-situ sample's analyses are strongly required in order to optimize the quality of the surfaces and interfaces, particularly in the case of the thin films. With this concern, the technological advances achieved in the growth and characterization techniques allow us to fabricate nanostructures with high crystal perfection and free of contaminants.

Within the scope of the thesis, I have employed different strategies with the aim to prepare nanostructures with tailored properties. To do that, I had to choose conveniently the deposition method, the substrate employed for the epitaxial thin film growth, the growth parameters (such as deposition temperature, rate and geometry), .. as well as the suitable analysis tools. I have resorted to a complex UHV systems available at the Nanomagnetism laboratories in IMDEA Nanociencia, which allows for sputtering and molecular beam epitaxy (MBE) growth, together with X-ray - UV photemission spectroscopy (XPS-UPS) and low electron energy diffraction (LEED) surface characterization technique of thin films. The system permits hence to deposit (polycrystalline and epitaxial) films and analyse their surface/interface properties in-situ, i.e. avoiding any contamination. Further

structural and magneto-transport characterizations were then performed ex-situ exploiting X-ray diffraction (XRD), vectorial-Kerr magnetometry and microscopy and synchrotron based X-ray absortption spectroscopy and magnetic circular dichroism (XAS-XMCD) measurements.

In this chapter, I report on the above-mentioned film deposition and characterizations techniques, with particular emphasis on the multipurpose growth and analysis UHV chamber and the dual Kerr-MR magnetometry set-up that I have contributed to develop.

1.1 Epitaxial Growth and Surface analysis chambers

Together with Dr. Miguel Angel Niño, Dr. Cristina Navío and Dr. Paolo Perna, I developed an innovative UHV system for growth and analysis of organic and inorganic thin films (the first installed in Spain) in the Multi-purpose UHV growth/spectroscopy Laboratory at IMDEA Nanociencia.

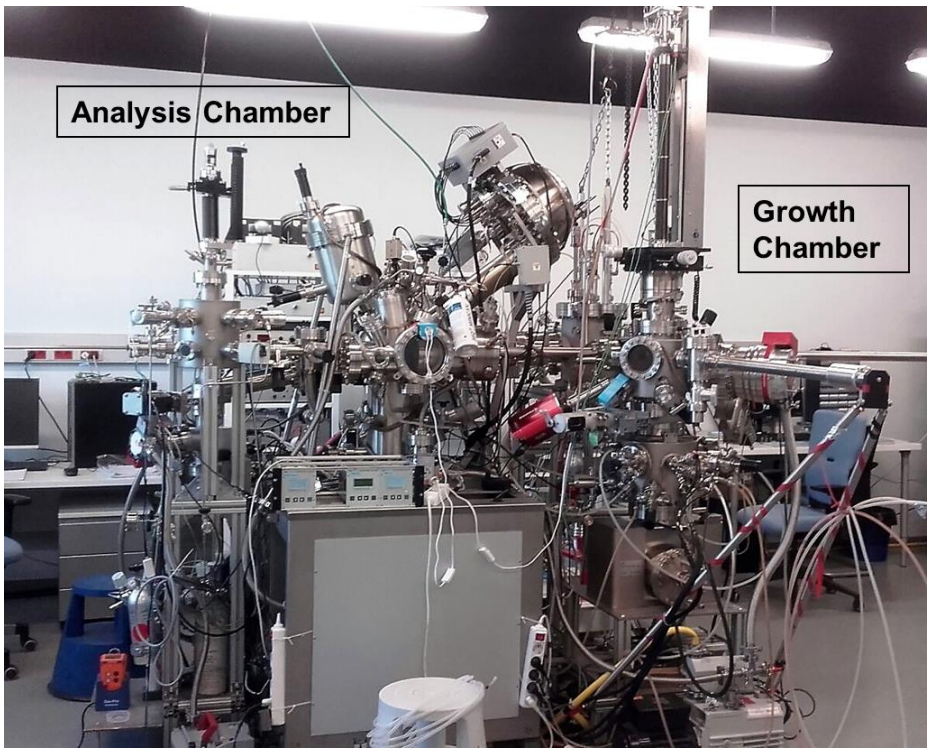

Figure (1.1) Photograph of the growth and analysis UHV system. It consists in two main UHV chambers, one dedicated to the growth and the other to the analysis of thin films. On the right side there are the growth chambers that are composed by two chambers dedicated to molecules and metal MBE growth, and another specific for the sputtering deposition of metals and oxides. On the left side, there is the complex surface analysis chamber, equipped with XPS, UPS, LEED and a mass-spectrometer for chemical reactions studies.

In particular, I contributed to the installation of a DC-RF Sputtering vacuum chamber connected in-situ to the whole system. This complex UHV system (shown in Figure (1.1)) is composed by two UHV chambers dedicated to the growth of inorganic and organic thin films (by e-beam and thermal evaporation) and one chamber equipped with 5 DC and 1 RF sputtering magnetrons for the deposition of metals and oxides. These fabrication chambers are in-situ connected with a UHV chamber devoted to the chemical and electronic structure analyses by means of X-ray photoemission Spectroscopy (XPS), with a monochromatic X-ray source (Al Kα line) and UV lamp for Ultraviolet Photoemission Spectroscopy (UPS), and Low Energy Electron Diffraction (LEED).

1.1.1 The growth chambers

The vacuum chambers dedicated to the deposition of thin films are two: MBE on the left (with base pressure of 10^{-10}mbar) and sputtering on the right (with base pressure of 10^{-8}mbar) in Figure (1.2). These two chambers are separated by a small chamber that allows for parking and distribution of the samples. Each chamber is equipped with a fast entry for sample introduction.

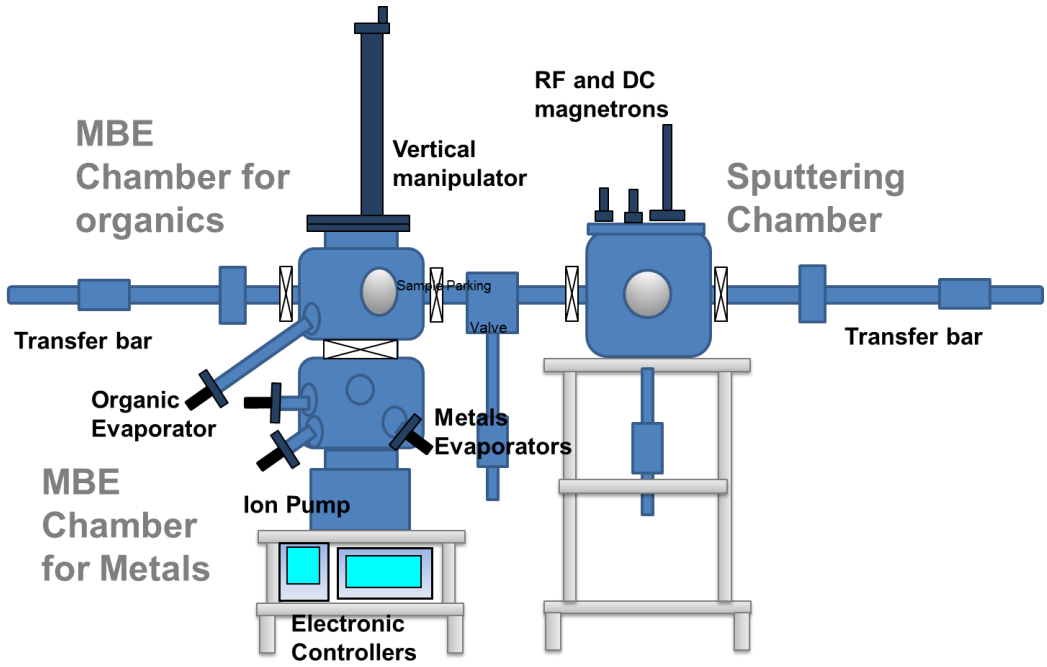

Figure (1.2) Schematic configuration of the growth system. On the left, the MBE chamber. On the right, the sputtering chamber.

Molecular Beam Epitaxy chamber

This chamber was designed for the growth of organic molecules and metals films in ultra high vacuum conditions. The MBE chamber is equipped with six different water cooled evaporators: four homemade electron-beam evaporator, one commercial (Omicron) triple evaporator, for metals, and a latter commercial (Kentax) evaporator for organics. The evaporators are located in the lower part of the UHV chamber with different orientations with respect to the sample surface.

The samples are mounted to a vertical manipulator, located on top of the chamber, with four degrees of freedom, three translational (x; y; z) and one rotational around the z axis. The sample holder can be resistively heated up 700 K, its temperature can be monitored by means of a K-type thermocouple.

In addition, during the evaporation or the sample preparation, it is possible to introduce into the chamber a partial pressure gas, such as O_2. Actually, a leak valve allows us to control the rate of the flowing gas in order to achieve the best condition of the sample growth.

Sputtering Chamber

Sputter deposition has a high degree of signficance in thin film science as well as in industry. The main advantage of sputtering stays in the possibility to deposit the materials over a quite large area. Due to its high deposition rate the thickness of films fabricated with such a technique can range from less than 1nm to several microns. One advantage of this deposition technique is its concept easiness and low cost, making it very scalable in industrial regime. The principle of the sputtering process can be seen in Figure (1.3). The target is placed at the cathode. An inert gas such as Ar, is inserted between the electrodes. When an electric eld in DC or at radiofrequency (RF) (typically 13.56MHz) is applied across the electrodes, electrons are emitted from the cathode. The electrons, being accelerated by the field, collide with the gas atoms, generating ions and yet more electrons (secondary electrons). The Ar^+ ions are accelerated towards the cathode and sputter the material that constitutes the target. The trajectories of the electrons are bent by a magnetic field in the so-called magnetron sputtering, leading to a certain degree of connement of electrons around the cathode (target) surface.

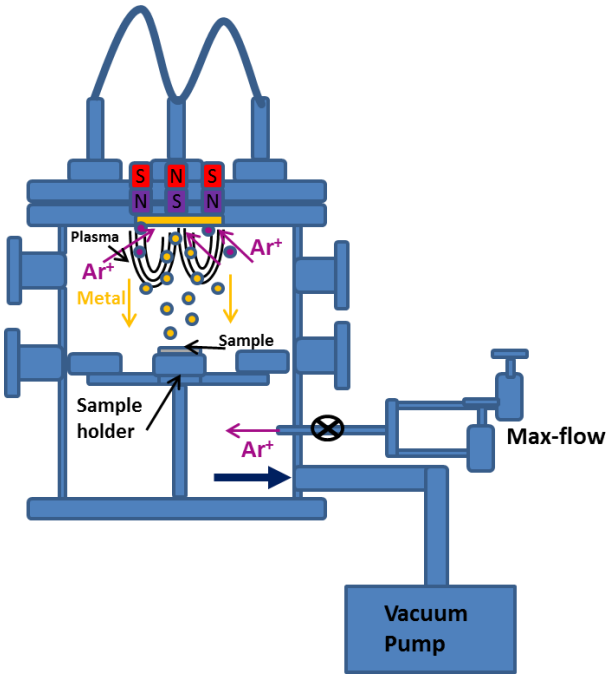

Figure (1.3) Sketch of magnetron sputtering deposition.

The sputtering chamber is equipped with 5 DC magnetrons and one RF magnetron. It allow us to growth multylayered samples with a variety of materials. In Figure (1.4) is shown a picture of the inside of the sputtering chamber during a deposition, with two magnetrons switched on.

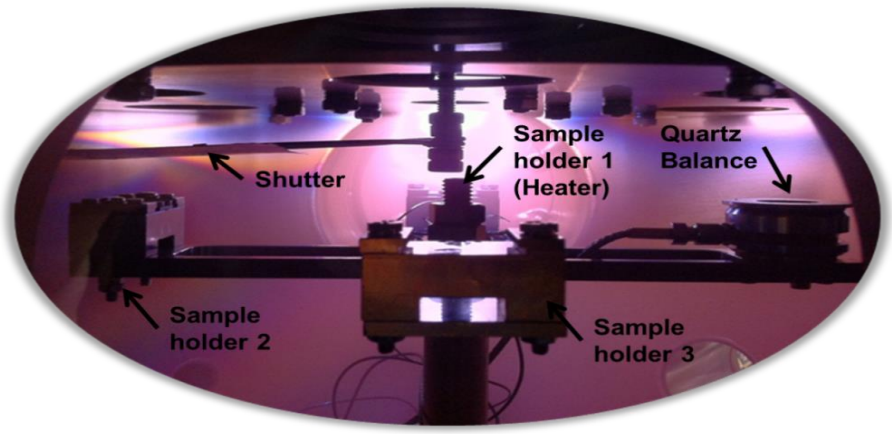

Figure (1.4) Inside of sputtering chamber. Rotating stage for sample holders (three) and quarzt balance. One of the sample holders is equipped with a heater capable for reaching 500°C. A shutter is located near of the magnetron collimatros in order to stop the deposition.

The sputtering chamber is equipped with a rotating stage with three sample holders and one quartz balance to promediate the rate of the deposition. One of the sample holders are provide of a heater, capable to reach 500°C.

1.1.2 Photoelectron spectroscopy

Relevant information about the elemental and chemical nature of the surface of samples is achieved by Photoelectron spectroscopy (PES). It is an experimental technique widely employed in surface science.

The photoelectrons can be produced by the exposition of the sample to beams having different wavelength. The two mostly diffused techniques that exploit X-ray and ultra-violet (UV) light to produce photoelectrons are "XPS" and "UPS" respectively, in this thesis will be discussed about X-ray Photoelectron Spectroscopy (XPS). Figure (1.5) shows a schematic diagram of the photoemission process. An electron is removed from the illuminated surface with a kinetic energy E_{Ks} when the energy of the photon ($h\nu$) fulfils:

$$h\nu = E_b + E_{Ks} + \boldsymbol{\Phi}_S \tag{1.1}$$

where E_b and Φs indicate the electron binding energy and the work function in the sample respectively. Therefore, the electron kinetic energy is

$$E_{Ks} = h\nu - E_b - \boldsymbol{\Phi}_S \tag{1.2}$$

Since $\Phi s \neq \Phi d$ the electron energy is altered during the absorption process in the analyzer. However, it is still possible to determine the initial binding energy of the electron that is distinctive of the chemical state of the belonging atom. In fact, since the sample and the detector are electrically connected (grounded), the respective Fermi energy levels equalize to a same value $E_F s = E_F d = E_F$. Assuming this, the energy conservation leads

$$E_{Ks} + \boldsymbol{\Phi}_S = E_{Kd} + \boldsymbol{\Phi}_d \tag{1.3}$$

That finally gives:

$$E_b = h\nu - E_K + \boldsymbol{\Phi}_d \tag{1.4}$$

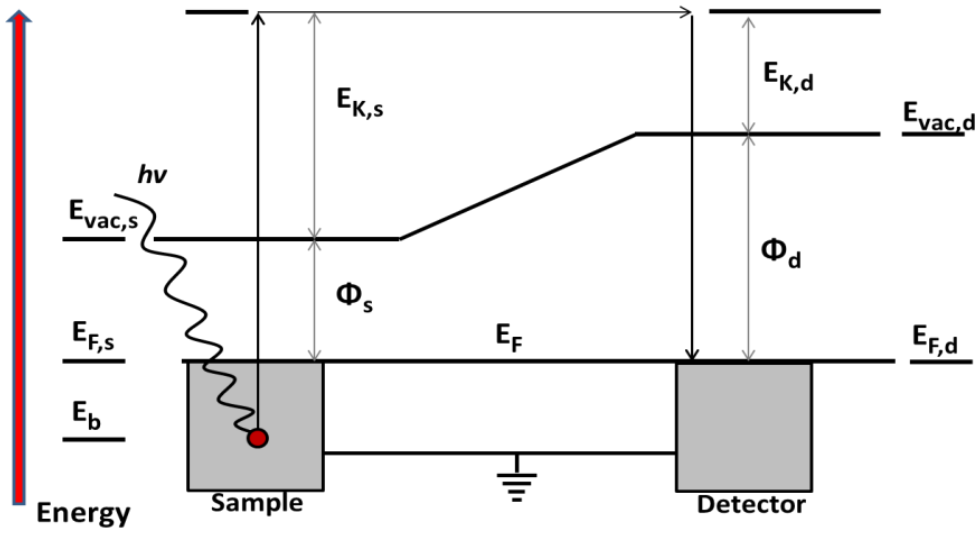

Figure (1.5) Energy diagram of the processes that photoelectrons undergo: electrons from states with a binding energy Eb are removed from the sample, upon the radiation illumination, and reach the detector. The sample and the detector are electrically in contact and grounded so that the respective Fermi levels assume the same value. In this way it is possible to determine the electron binding energy of origin by equation (1.4)

allowing the determination of the binding energy of the photoemitted electrons. A typical photoelectron spectrum is given as a plot of number of detected electron per energy interval (intensity) versus their measured kinetic energy or their calculated binding energy. The position and intensity of the peaks in the energy spectrum provide the desired chemical state and quantitative information.

X-ray Photoelectron Spectroscopy (XPS)

The photoemission process is led by X-ray irradiation of the sample surface. Typically in XPS, monoenergetic X-ray are generetad by Mg Kα (1253.6 eV), Al Kα (1486.6 eV) or synchrotron radiation. At such high energy X-rays are able to excite up to core electrons. Although the X-ray photons have a penetrating depth in a solid on the order of 1 ÷ 10 micrometers, the detected electrons generally originate from a depth of 5 ÷ 6 nm of the surface, because of the inelastic mean free path of electrons (IMFP) in solids is very small [3]. In Figure (1.6) it can be seen that XPS can result very surface sensitive at electron energies in the range of 20 ÷ 100 eV, where the IMFP curve shows a minimum. Moreover, an enhancement of the surface sensitivity it is also possible by moving from the normal emission (detection of the photoelectrons escaping normal to the sample surface) to a higher

electron emission angle (which means that the analyser detects photoelectrons emitted at a more grazing angle with respect to the sample surface).

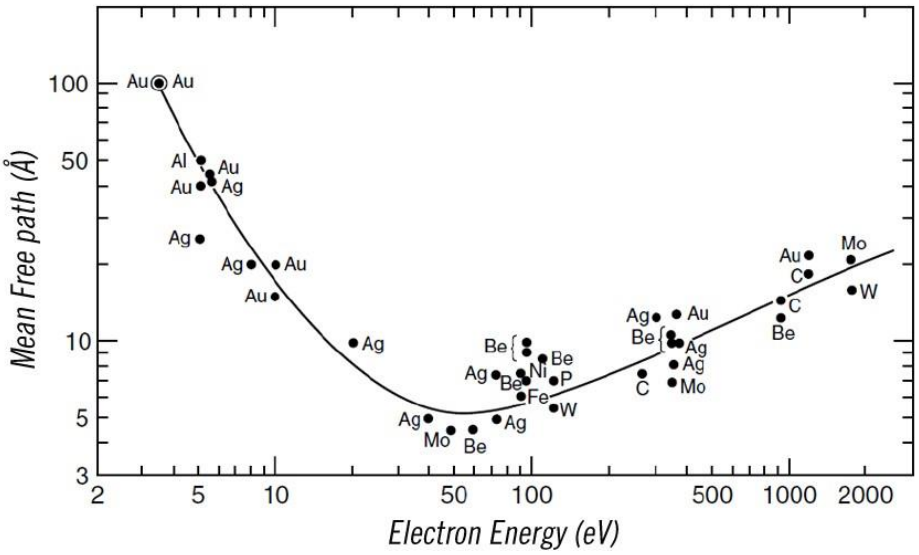

Figure (1.6) Universal curve of inelastic mean free path of electrons (IMFP) in solids as a function of their energy. Picture adapted from [2]

It is worth to note in eq. (1.2) and eq (1.4) that, although the kinetic energy of the emitted electrons can vary with the energy of the incoming photons, the binding energy stays unchanged for electrons from a certain element. In fact, the binding energy of an electron is peculiar for each element and its chemical state. An elemental analysis of the examined surface can be made, by means of the XPS spectra, comparing the binding energy of experimentally observed peaks with the tabulated values. In fact, XPS can provide qualitative and quantitative data regarding the elemental identities and composition of components on a surface, as well as the chemical nature of these elements.

In Figure (1.7) Example of a survey XPS scan of a Pt/Co/graphene stack. From this spectrum, it is possible to study the chemical composition of the surface by comparing the binding energy position of the peaks with respect the tabulated values. To note that we can recognize the photelectron peaks originated in the orbitals of carbon, belonging to the graphene layer, cobalt and platinum atoms.it is shown an XPS spectrum obtained from the intercalation of cobalt below graphene grown on Pt(111). The survey scan is made at low resolution for covering the entire range of binding energies

accessible with X-ray source employed. In this case, as well as the other entire XPS spectrum shown in this thesis, the excitation of the photoemission is achieved by ***Al Kα X-***rays exposition.

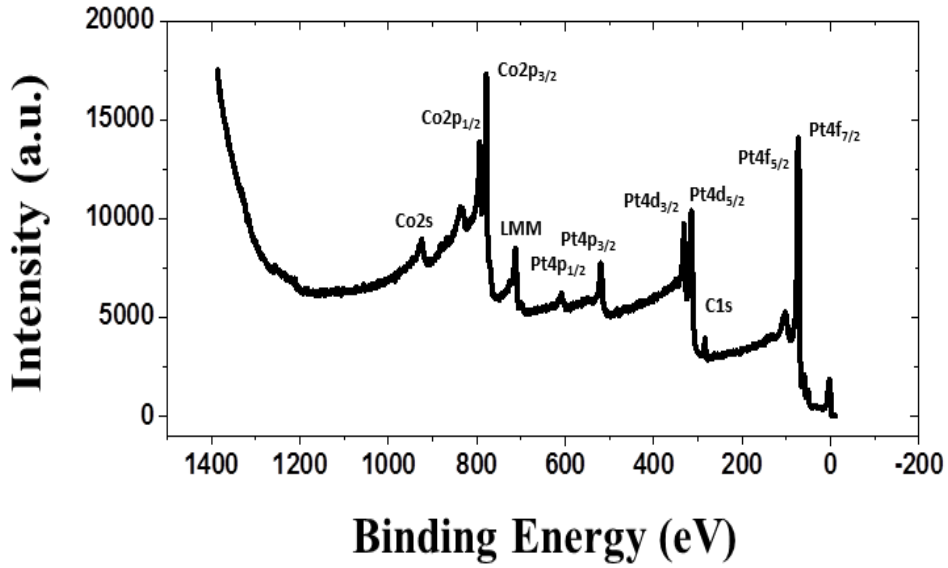

Figure (1.7) Example of a survey XPS scan of a Pt/Co/graphene stack. From this spectrum, it is possible to study the chemical composition of the surface by comparing the binding energy position of the peaks with respect the tabulated values. To note that we can recognize the photelectron peaks originated in the orbitals of carbon, belonging to the graphene layer, cobalt and platinum atoms.

The spectrum in Figure (1.7) Example of a survey XPS scan of a Pt/Co/graphene stack. From this spectrum, it is possible to study the chemical composition of the surface by comparing the binding energy position of the peaks with respect the tabulated values. To note that we can recognize the photelectron peaks originated in the orbitals of carbon, belonging to the graphene layer, cobalt and platinum atoms. is dominated by the photelectron peaks originating in the orbitals of carbon cobalt and platinum atoms. It can be also noticed the presence of the line produced by the valence band, i.e., low intensity peak in the low binding energy region, and the series of the lines due to Auger electron emission, in the high energy binding region.

Quantitative analysis. The spectrum of a XPS measurement of a given material contains peaks related to the various elements present on the

surface. Furthermore, the peaks intensity contains information on chemical stoichiometry of the body surface, and it is possible to carry out quantitative analyses since the intensity of the peaks, as well as peaks area, is related to the amount of each element. For instance, the number of electrons recorded for a given transition is proportional to the number of atoms at the surface. In general, assuming that the elemental concentrations are homogeneous within the XPS sampling depth, the intensity peak I_i yielded by electrons with kinetic energy E_{KE} , which are originated from an electron level of element i, can be described by the equation [4]:

$$l_i = n_i K T_{KE} L_{ij} \sigma_i \lambda cos\theta \left(1 - exp\frac{-d}{\lambda cos\theta}\right) \quad (1.5)$$

being K an instrumental constant, T_{KE} the transmission function of the analyzer, L_{ij} the angular symmetry factor for orbital j of the element i, ni the concentration of the element i, σi the photoionization cross section, λ is inelastic mean free path of electrons (IMFP), and finally θ the emission angle of the photoelectrons measured with respect to the surface normal. The XPS sampling depth d is about 10 nm, which is usually 3 ÷ 5 times bigger than the IMFP of most photoelectrons with a kinetic energy in the range from 10 to 1000 eV. Therefore, the exponential in equation (1.5) is very small and it can be neglected. Thus, the former equation becomes:

$$l_i = n_i K T_K L_{ij} \sigma_i \lambda cos\theta \quad (1.6)$$

and it possible to determine the relative concentration *ci* of element *i*:

$$c_i = \frac{n_i}{\Sigma_i n_i} = \frac{{l_i}/{(\sigma_i \lambda)}}{\Sigma_i {l_i}/{(\sigma_i \lambda)}} \quad (1.7)$$

where Σ_i is the summation over all the surface elements which give contribution to the spectrum. In equation (1.7), the peak area *I* can be calculated from XPS spectra whereas the photoionization cross-section σ and the inelastic mean free path λ can be obtained from literature or databases.

Background. In order to estimate the relative concentrations of the elements on the surface, it is essential to recognize the background contribution which

is always present and, eventually, correct the XPS spectra accordingly. Background has risen from the scattering interaction of the photoelectron with other electrons in the solid. Thus, this effect is responsible of the characteristic staircase like structure observable in the XPS spectra. Moreover, at low kinetic energy, ≈100 eV, the intensity of continuous background can result very high due to successive electronic excitation induced by photoelectrons (secondary electrons). Inelastically-scattered electrons have lost all coherence with their initial state and this background is discarded using a adequate subtracting procedure. Analytically different kinds of background functions are usually employed to correct measured spectra. The most common choice is to subtract a simple linear background, or more sophisticated like Shirley type background [5] used in this thesis, and a Tougaard type background [6].

Auger. The ejection of an inner core electron leads to secondary processes. After the ionization of the atom the created core holes will be filled after a very short time through different relaxation processes. As shown Figure (1.8), an electron from a higher energy level may fill the newly formed vacancy (white arrow), causing the emission of a second electron, called "Auger", in order to conserve energy. In this process, the kinetic energy

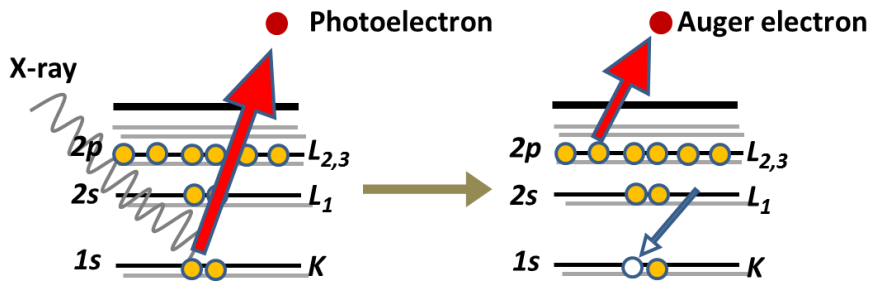

Figure (1.8) After a relaxation time from the photoionization an electron from an outer shell fills the formed vacancy and an Auger electron is emitted. Specifically for this picture it is shown a "KLL" Auger process.

of emitted electron is again directly related to the binding energy of the electron of the atom. The energy value of the emitted Auger electron is independent from the energy of the incident radiation. For this reason, by changing the ionizing sources, it is possible to notice that the Auger lines have fixed values, in the kinetic energy scale, whereas the other peak lines show an energy shift. Together with the direct electron photoemission, the

Auger effect is also used to identify the elements in the sample. In XPS measurements is possible to observe four main Auger series: *KLL*, *LMM*, *MNN* and *NOO*. Such a nomenclature identifies the specific transitions involved in the electron Auger emission. The first letter indicates the inner shell filled by a second electron at higher electron shell (second letter). The latter leads, for the energy conservation, to the emission of a second electron belonging to the shell indicated by the third letter.

"X-ray" satellite peaks. An XPS spectrum may also show additional photoemission peaks generated by minor X-ray resonance lines. These X-ray lines, such as the main radiation line, are characteristic of the anode employed. The satellite peaks produced by the minor lines can be suppressed by means of a monochromator (a quartz crystal) which provides a very narrow energy width, improving the resolution of the photoelectric peaks in the XPS spectrum as well.

"Shake-up" satellites. Shake-up peaks are observed as the peaks having a kinetic energy of about some eV lower (higher binding energy) than those of the primary peaks. Shake up satellites result from two-electron interaction. Once it is emitted, a photoel- ectron can interact with an electron in the valence band promoting it to an unoccupied level. In organic molecules this phenomenon usually occurs from HOMO and LUMO. Therefore, the emitted electron outcomes with a lower kinetic energy that has higher binding energy with respect to the main peak. The shake up satellites often occur in the presence of transition metal ions, aromatic systems or unsaturated bonds. They have an intensity that is 5 − 10% of the main peak and show a binding energy 6 − 7 eV higher. The shifts and the relative intensities can be taken into account to identify the chemical state of the element since the energy transfer is orbital specific, although the energy difference between the shake-up and the main peak does not correspond exactly to the energy gap of the material analysed. Furthermore, in some cases, an additional electron may be promoted from the valence band above the vacuum level. The corresponding peak in the photoemission spectrum is called "shake-off ".

Chemical shift. The binding energy of a particular peak does not depend only on the element but also on the chemical environment and energy state of the atoms. Any change that perturbs the energy level of the atom, or its bond configuration, will cause a corresponding energy variation (between 0:1 − 5

eV) in the XPS spectrum. This variation in binding energy is called "chemical shift".

Photoelectron Spectrocopy (UPS)

In UPS spectroscopy the electrons are photoemitted by means of ultraviolet (UV) irradiation of the sample. In this technique usually a gas (H, He, Ne, Ar) discharge-lamp or synchrotron radiation are employed as source to generate UV radiation. The helium discharge lamps lead to two radiation lines of 21:2 eV and 40:8 eV, for He I and He II respectively. Due to such low energies, UPS is very suitable for the investigation of the valence electronic structure of the materials. In Figure (1.9) the main differences in the electron emission mechanisms that have place in XPS and UPS are shown.

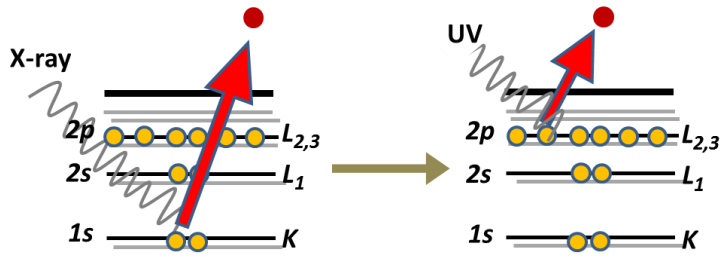

Figure (1.9) Sketch of substantial differences in XPS and UPS spectroscopy techniques. With UPS only the electrons of the valence level are excited, whereas with XPS also core electrons are excited.

The UV-photoelectron spectroscopy allows also to measure the density of states and the adsorbate induced electron density distribution in the valence band. Furthermore, it is particularly suitable for the study of electronic structure of adsorbed molecules at surface. For instance, the valence orbitals are responsible for the formation of chemical bonds. Unlike XPS, UPS is not a quantitative method, because at low photon energies the cross sections for different energy levels vary greatly. Furthermore, the low kinetic ener- gies may lead to diffraction effects of the electrons. However, UPS can be employed very usefully in the characterization of solids determining the work function of the material.

Experimental setup: analisys system

The study of the epitaxial and graphene-based nanostructure surfaces was carried out in the mentioned UHV system.

The experimental equipment shown in Figure (1.10) is currently located in the Nanomagnetism laboratory at IMDEA Nanociencia.

The system consists in an independent chamber where it is possible to achieve in situ Photoemission Spectroscopy (PES) analysis of the samples. Each chamber is provided with a small-volume chamber for an independent fast introduction of samples. The MBE and PES chambers are connected through a UHV linear transfer arm and are separated by two UHV valves that make possible the independent employment of both of them.

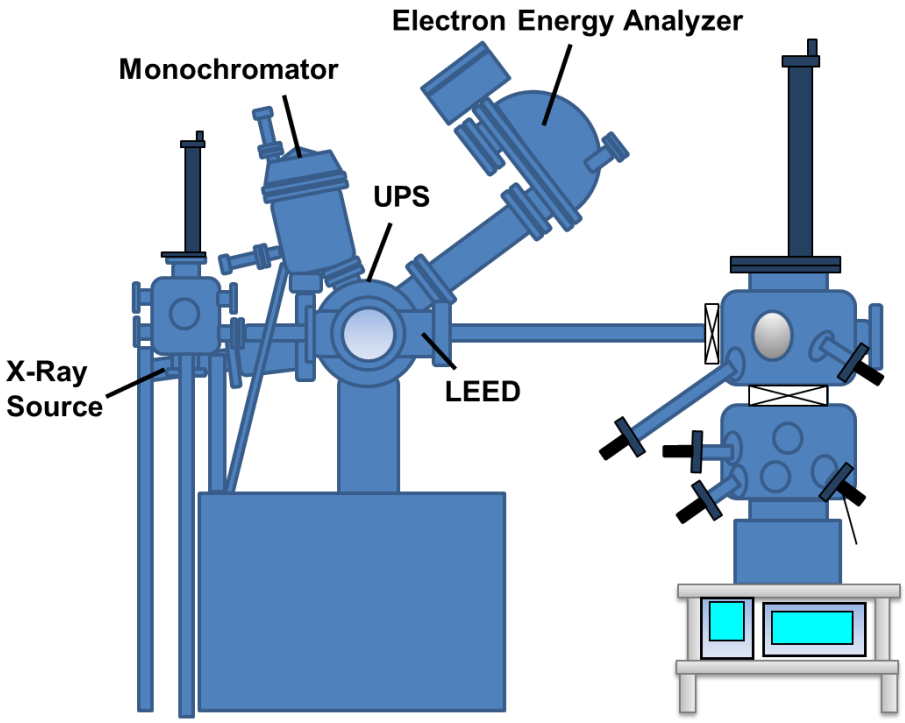

Figure (1.10) Photograph of the experimental setup consisting in two main UHV chambers. On the right side is found the MBE growth chamber whereas on the left side is located the XPS-UPS analysis chamber.

The vacuum in the chambers is achieved using two autonomous pumping systems consisting in turbo pumps, backed by a rotary pump for pressure down to 10^{-8}mbar range, an ion pump and a titanium sublimation pump for lower pressures. The base pressure in the two system stages is in the range of 10^{-11} mbar.

The analysis UHV chamber is devoted to in-situ surface characterizations, made possible by means of a monochromatized X-ray source plus a SPHERA II analyser, both from Omicron Nanotechnology, and a helium discharge lamp (VG scienta) as UV-source. Moreover, an ion gun and a LEED (Omicron) are implemented for the cleaning of the sample surface and the monitoring of its surface structure. The samples are mounted on a horizontal manipulator having four degrees of freedom. The samples can be resistively heated up to 900 K and cooled down to liquid nitrogen temperatures.

In the following, I describe some of the characteristics of the main components that implement the analysis chamber that were employed to collect the measurements discussed in this thesis.

X-ray source. In Figure (1.11) is shown a schematic diagram of the X-ray source. It consists on a filament (cathode), which emits thermal electrons, generated through Joule heating of the filament, and an anode, toward which the electrons are accelerated by applying an high voltage of typically 9 ÷ 15 k V . Generally, the operation emission current is about 20 mA. Hereby, the anode atoms are exited and emit X-ray radiation during the relaxation.

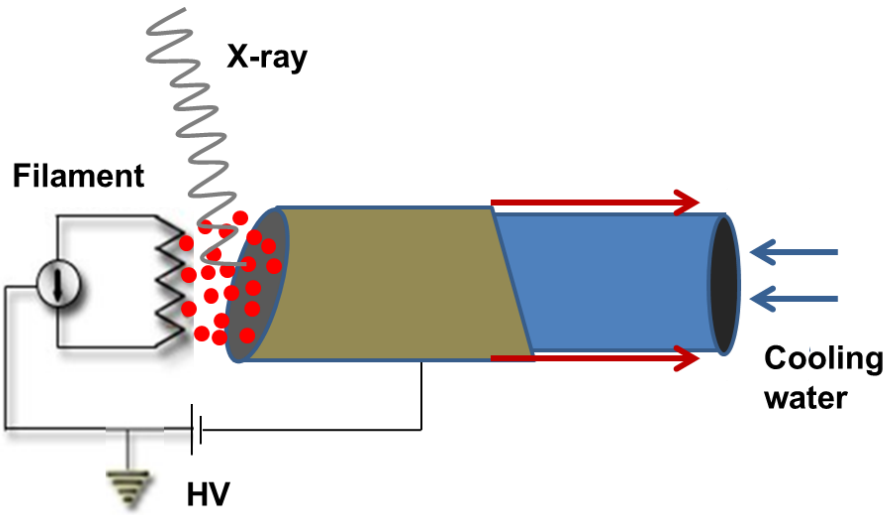

Figure (1.11) Simplistic diagram of the XPS source. A high voltage bias accelerates the emitted thermal electrons toward the anode leading the X-ray emission. The water-cooling (blue and red arrows indicate the flowing of the water in and out, respectively) avoids the overheating of the anode during the process.

The source used in our lab employs an aluminium anode, which provides a photon energy of 1486.6 eV by the Al K α-transition. During the

photoemission process, the overheating of the anode is avoided by a water-cooling (fixed at 18◦C by a refrigerator chiller).

Monochromator. The XPS system mounted in our chamber is equipped with a monochormator. The use of monochromatic X-rays ensures different advantages compared to standard XPS. Firstly, the distribution of the photon energies is narrower compared to the unfiltered X-ray line. This improves the resolution, making possible to identify and measure more precisely different chemical structures and eventual chemical shifts. A further benefit of a previous filtering of the X-rays that irradiate the sample is that satellite lines and additional lines from anode impurities are removed. Moreover, by emplying a monochromator we can improve the signal noise ratio, since it eliminates the continuous background at all energies due to the Bremsstrahlung radiation.

As displayed in Figure (1.12), a monochromator employs a toroidal mirror of quartz crystal to "select" the X-rays with a given wavelength. Its physical principles are based on Bragg's Law:

$$n\lambda = 2dsin\theta \tag{1.8}$$

where d is the distance of the planes of the crystal employed for the diffraction (2d ≈8:5 Å), λ is the X-ray wavelength (λE=1486:6 eV ≈ 8:34 Å) and θ (≈ 78:53◦) is the Bragg angle. The X-ray source, the toroidal quartz crystal and the sample have to lie in the Rowland circle [7], as shown in Figure (1.12) panel b. This identifies the correct locations of the source and the sample in order that the beam is correctly focused on the sample. In fact, if the source is anywhere on the circle, then the specular beam, and the dispersed beams in all orders, will be focused at other points on the same circle.The final energy resolution of an XPS spectrometer is usually measured using the full width at half-maximum intensity (FWHM) of the Ag 3d5/2 peak from sputter cleaned silver. The instrumental resolution is affected by the analyser pass energy, slit widths and the line width of the incident X-rays. In our case the resulting resolution was found to be ≈ 0:5 and 0:7 eV at pass energy of 20 and 50 eV respectively. On the other hand, for a pass energy of 5 eV , the energy resolution in UPS was found to be about 0:1 eV.

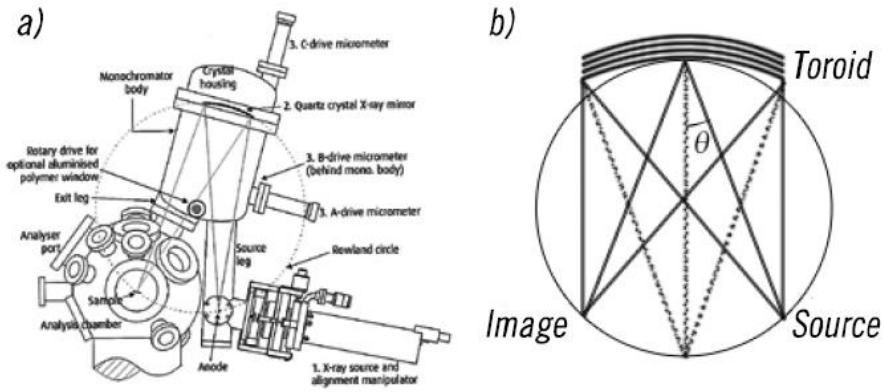

Figure (1.12) a) Plan of X-ray source setup, by Omicron manual [7]**, where are reported several components of the monochromator. The source, the quartz crystal and the sample have to lie in the Rowland circle, as shown in b), in order to focus on the sample surface all the diffraction orders of the x-ray light coming from the source.**

UPS source. The UV source is a helium gas discharge lamp (VG SCIENTA, model 22-101) in which the discharge is confined by a quartz capillary tube. The lamp generates light by sending an electrical discharge through the helium gas. The electrons of atom orbitals of the helium, due to the collision with the electrons of the discharge, are excited to higher energy states. When the excited atoms relax to a lower energy state, the photons, in the ultraviolet range, are emitted. The purity of the gas is essential to have good results and sharp emission line, particularly in the case of He II line at 40:8 eV. Since the capillary is directly introduced in the analysis chamber, it is employed a two stage differential pumping in order to preserve the optimal vacuum level in the chamber. For the discharge process the power supply provides up to 50 mA and a voltage of 500 V .The predominant emission of the He I (at 21.2 eV) is obtained by finding the good values of the He pressure in the lamp (typically≈ 10^{-6}mbar). By reducing the helium gas pressure it is possible to notice a change in the color of the bulb, that pass to be from yellowish orange to greenish blue, indicating that the HeII emission is predominant.

Electron energy analyser. The detection system is a spherical capacitor electron energy analyser coupled with a 7-channel electron amplifier detector. Specif- ically our system is equipped with the EAC2000 energy analyser controller (Omicron-Nanotechnology) that operate over the kinetic energy range 0 − 2000 eV. The detector is employed for both types of PES measurements. Figure (1.13) shows the main components of a hemispherical

analyser. It consists of an electrical lens system and two metallic hemispheres. Crucial parameter of such a setup is the electrostatic fields within the hemispheres, the so-called "Pass Energy". It has, in fact, influence on the resolution and the background noise. The two concentric hemispheres are biased negative and positive with respect to the selected pass energy of the analyser. For instance, the hemispherical analyser can be considered as an energy filter. In fact, once established such a value the hemispherical analyser allows electrons of a given energy E_k > Epass to be measured.

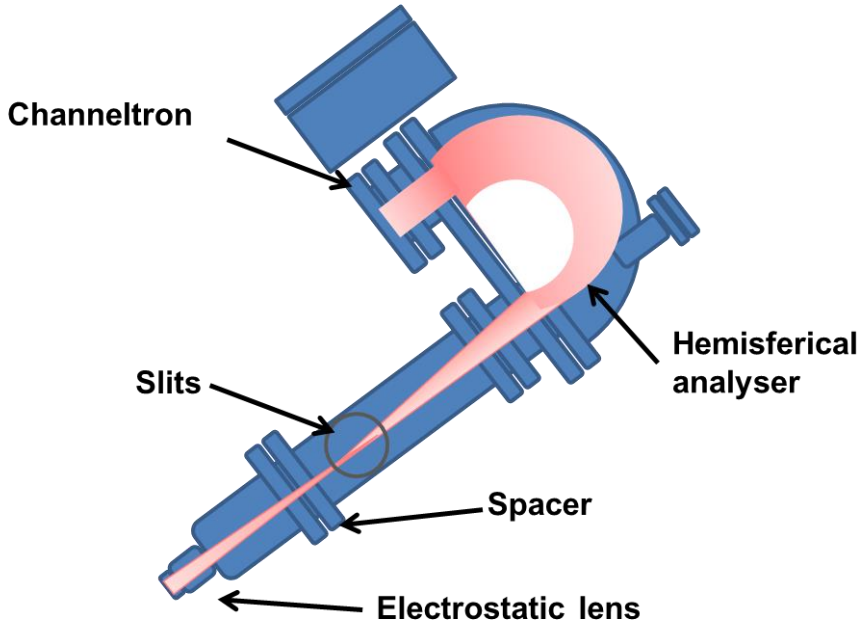

Figure (1.13) Draft of main components of hemispherical analyser. Once photoemitted, the electron are first focused by electrostatic lens and then selected by the energy pass in the analyser. Finally, the electrons are detected by the channeltron placed across the exit plane of the analyser.

The photoemitted electrons are earlier focused onto the entrance of the analyser by the electrostatic lens and their energy is adjusted according to the pass energy. Finally, the electrons are detected by the detector, which consists in a channeltron with a multiplication level of $10^7 \div 10^8$.

Low energy electron diffraction (LEED)

Low energy electron diffraction is a commonly used method in order to determine the structure of surface adsorbates. It is a suitable method to probe the structure of regular organic monolayers such as SAMs. The initial observation of low energy electron diffraction was made by Davisson and

Germer in 1927 [8]. However, it took nearly 50 years until it could be used to determine atomic positions [9] because of the lack of an adequate UHV setup and a proper scattering theory. The basic principle of this method relies on the wavelike behavior of the electrons. Low energy electrons (between 20 – 500 eV) have a deBroglie wavelength of several Å, according to

$$\lambda = \frac{h}{m_e v} \tag{1.9}$$

These electrons are suitable to probe crystalline structures as their wavelengths are in the same order of magnitude as the inter-atomic distances in a solid. Due to their low energy and their strong interaction with the atomic potentials, the electrons are backscattered within the first few layers. A scheme of a typical experimental setup for LEED is shown in Figure (1.14). Electrons are accelerated from a cathode filament towards the sample, where some of them are backscattered elastically. The scattered electrons typically reach a hemispherical grid arrangement. The first and third grids are on earth potential in order to guarantee a field free space. On the second grid, a negative bias is applied which is several volts below the acceleration voltage. Thereby only elastically scattered electrons go through the second grid and finally are accelerated towards the fluorescent screen where they produce a diffraction pattern.

A complete description of the positions and intensities of diffraction spots requires a dynamic theory that accounts for multiple scattering from all the layers that contribute to the scattering. The description of this sophisticated theory is out of scope in this thesis and can be found in literature [10]. An adequate description of the observed diffraction pattern can frequently be obtained by the simpler kinematic theory.

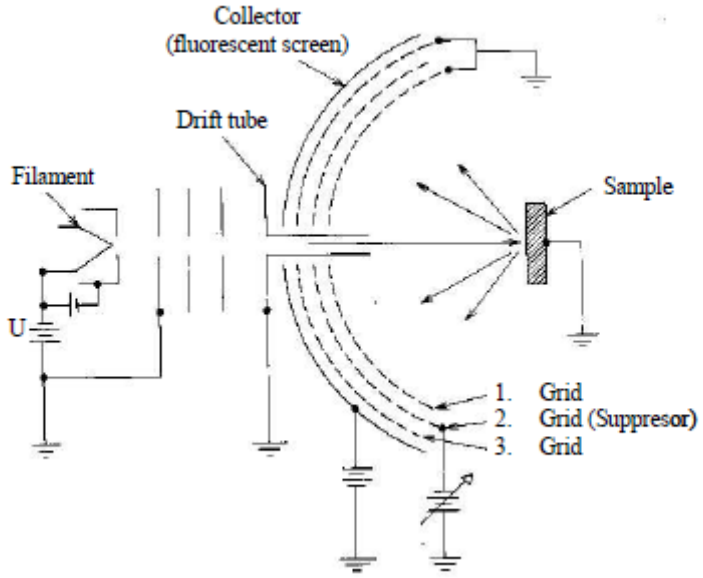

Figure (1.14) Scheme of the experimental setup for LEED, as reported in [11]**.**

The kinematic theory only accounts for single scattering processes of the primary electrons with the periodic surface structure [11]. The basic equations can be obtained by several geometrical considerations: The diffraction condition for a lattice of periodicity is a

$$\mathrm{a} \cdot (sin\varphi - sin\varphi_0) = n \cdot \lambda \tag{1.10}$$

Where φ and φ_0 are the angles of the scattered and of the incident beam, respectively, and *n* denotes the diffraction order. Tipically normal incidents is set as $\lambda[\text{Å}] \approx \sqrt{\frac{150}{U[V]}}$, one obtains:

$$\sin\varphi = \frac{n}{a} \cdot \sqrt{\frac{150}{U}} \tag{1.11}$$

This equation forms the basis of kinematic LEED analysis.

In analogy to the geometrical consideration, the condition for constructive scattering can be expressed by the Laue–condition and visualized by the Ewald-sphere [12]. It can be shown that constructive interference occurs when the change of the incident wave vector kΔ during the scattering process corresponds to a reciprocal lattice vector. This yields the Laue-equations:

$$\begin{aligned} \boldsymbol{a}_1^* \cdot \Delta\boldsymbol{k} &= 2\pi h \\ \boldsymbol{a}_2^* \cdot \Delta\boldsymbol{k} &= 2\pi h \end{aligned} \tag{1.12}$$

In order to visualize the Laue condition for constructive scattering, one can use the Ewald construction as shown in Figure (1.15).

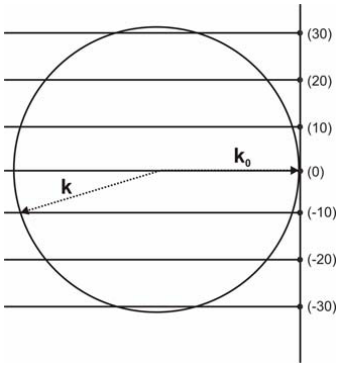

Figure (1.15) The Ewald construction for electron scattering on a surface

The reciprocal lattice is infinitively expanded in the direction orthogonal to the surface, one therefore typically draws rods. The wave vector of the incident wave k_0 is drawn in such a way that it ends up with the (0,0) point. A sphere with radius k of the scattered vector is designed around the origin of k_0. Diffracted beams produce spots where the Ewald sphere intersects with the reciprocal lattice rods.

1.2 Vectorial-Kerr magnetometry

When a beam of polarized light reflects off a magnetized media, the plane of polarization of the light can slightly rotate and its intensity can slightly change. This phenomenon is known as the magneto-optic Kerr effect (MOKE), named after Reverend Sir John Kerr who discovered the effect in the 19th Century [13]. Both effects, i.e. polarization rotation and reflectivity changes, result from the off-diagonal components of the dielectric tensor, as described below. The MOKE technique is a pure photon-based technique (photon-in/photon-out) and can be used easily to trace out magnetic hysteresis loops of ferromagnets. While known for more than 100 years, the magneto-optical Kerr effects were fully exploited for the first time in surface magnetism studies (SMOKE) on ultrathin Fe films grown on a Au(100) substrate [14] in 1985. Nowadays the MOKE technique is one of the most widely used due to its simplicity [15].

Magnetic information obtained by MOKE concerns much more to the surface/thin film behavior than to the bulk/substrate, as long as the light interaction with matter is subjected to a limited penetration depth of about several tens of nanometers. The technique allows studying magnetic properties such as magnetic ordering, magnetic anisotropy, exchange coupling, among others in systems as thin films, exchange-bias systems, multilayers such as tunnel junctions or spin valves, or last but not least nanoparticles. Different setup geometries can be used to exploit the magneto-optic effects to obtain the magnetic information of a given material (see Figure (1.16)). The first publication on magneto-optical effects was probing an out-of-plane magnetization in a setup where the magnetic field was applied normal to the sample, referred as Polar configuration. Two more setup configurations are possible, depending on the relative orientation of the applied field vector **B**, the surface plane P_I, and the reflection plane P_R. Consequently, there are three configurations:

Longitudinal:

$$\vec{\boldsymbol{B}} \in \boldsymbol{P}_I \wedge \vec{\boldsymbol{B}} \in \boldsymbol{P}_R \tag{1.13}$$

Transversal:

$$\vec{\boldsymbol{B}} \perp \boldsymbol{P}_I \wedge \vec{\boldsymbol{B}} \in \boldsymbol{P}_R \tag{1.14}$$

Polar:

$$\vec{\boldsymbol{B}} \in \boldsymbol{P}_I \wedge \vec{\boldsymbol{B}} \perp \boldsymbol{P}_R \tag{1.15}$$

Usually, the different MOKE geometries exploit different magneto-optics effects and provide different magnetization components. Within a first order approximation, Longitudinal and Polar geometries can provide information on the magnetization components M_y and M_z, respectively, by measuring their corresponding polarization rotations. In turn, M_x can be determined by using transversal geometry by measuring the reflectivity changes. Therefore, vectorial information on the magnetization can be obtained by performing three measurements in the three different MOKE geometries. In practice, however, there are difficulties to overcome, such as second order terms and angular accuracy when both sample and field angles must be rotated simultaneously to get the different geometries.

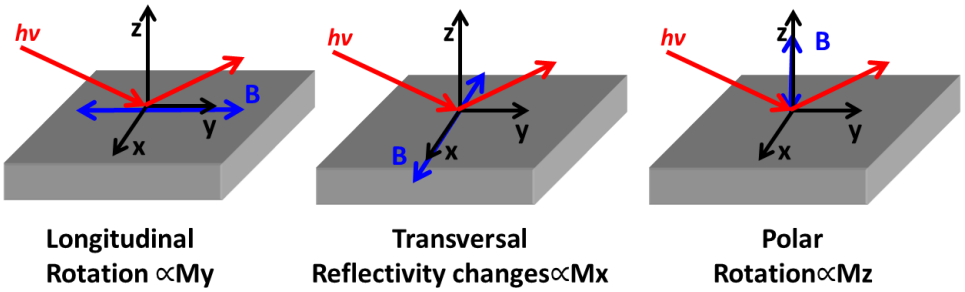

Figure (1.16) Standard MOKE geometries. *Longitudinal*: the magnetization vector is parallel to both the surface and the reflection plane. *Transversal*: the magnetization vector is parallel the surface but perpendicular to the reflection plane. *Polar*: the magnetization vector is perpendicular to the surface and parallel to the reflection plane. Note that, usually, Longitudinal and Polar geometries exploit the polarization rotations while the Transversal geometry used the reflectivity changes.

A vectorial-Kerr setup where the two in-plane components of the magnetization vector are acquired simultaneously during the reversal process has been used in this thesis. This setup has unique features that allows quantitative vector magnetometry to be performed.

1.2.1. Experimental setup

The vectorial-MOKE setup can be explained in three parts, the optical path, the mechanical sample stage, and the control unit. The optical part consists of (see Figure (1.17)): Laser, polarizer, lens, sample, lens, ƛ/2-retarder, Wollaston-prism and photodiodes.

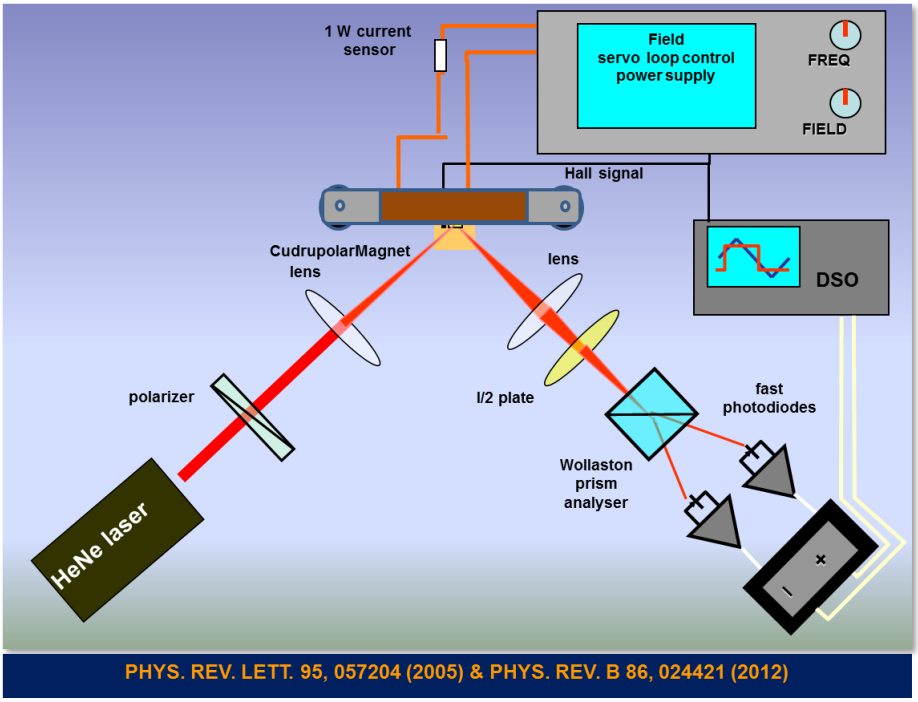

Figure (1.17) Scheme of the v-MOKE setup. Optical part of the setup. Light from a HeNe laser is polarized, focused by a lens, and reflected at the sample surface. The reflected beam is focused by a second lens and crosses a ƛ/2-retarder, to intermix the s- and p-wave. The two components are then split by a Wollaston prism. The corresponding intensities of the beams are measured using photodiodes.

The 5 mW HeNe laser (ƛ = 632 nm) is intensity stabilized, but has an undefined polarization such that a Glen-Thompson polarizer with extinction coefficient $1x10^{-5}$ is introduced. In the typical configuration, it is set to *p*-polarization, although it also allows for measurements with incident s-polarization. Lenses are used to focus the light beam onto the sample as well as to focus the divergent beam after reflection. The ƛ/2 retarder, set to 22.5 of the optical axes, intermixes the outgoing s- and p-. Finally, the s- and p-waves are split into two separate beams using a Wollaston prism with extinction coefficient $1x10^{-5}$. The intensities of the two waves are measured by two fast photodiodes. These are incorporated into a proper amplification electronics developed at SEGAINVEX, which also contains some circuits for data post processing, ending up with three outputs channels for the difference DC, sum DC and the sum AC signals of the two orthogonal polarization components of the reflected beam. These signals are read with a digital oscilloscope.

The positioning stage in combination with the focused beam and a microscope allows investigating specific areas of microstructured samples. Spot sizes down to 20 µm are possible. The sample is placed on a eucentric goniometer head to ensure a fixed plane of reflection upon sample rotation, so that the absolute values of the magnetization determined in different measurements can be compared. The whole head can be rotated by a stepping motor in steps of 0.9º. The applied magnetic fields can be simultaneously calibrated with a Hall micro-probe placed in the middle of the gap close to the sample.

The control unit is formed by a computer, an arbitrary function generator and current source, and a digital oscilloscope. The set-up is pc-controlled via a home made software that drives the stepping motors and the applied magnetic field, as well as reads out the signals from the oscilloscope. A commercial arbitrary function generator connected to a bipolar power supply, developed at SEGAINVEX, are used to generate the sinusoidal shape magnetic field. All the measurements presented here were performed at 3.21 Hz (quasi-static conditions). A 4-channel fast digitizing oscilloscope (200 MHz BW, 1GS/s), triggered to the applied field frequency, reads:

1. I_{Σ}^{DC}:the sum of intensities of the two orthogonal polarization components of the reflected beam (i.e. ∝ total refelectivity)
2. I_{Δ}: the difference of the intensities (i.e. ∝ polarization changes)
3. I_{Σ}^{AC}: the AC component of th sum of intensities (i.e. ∝ refelectivity changes)
4. The voltage applied to the electromagnet, which, after calibration, can be directly transformaed into applied field.

where I_{Δ} and I_{Σ}^{AC} are usually 10^{-4} times I_{Σ}^{DC}. The total reflectivity, i.e., (I_{Σ}^{DC}), is used to normalize the data. Statistical noise is greatly reduced by averaging some measurements taken in the same condition. In a first approximation,

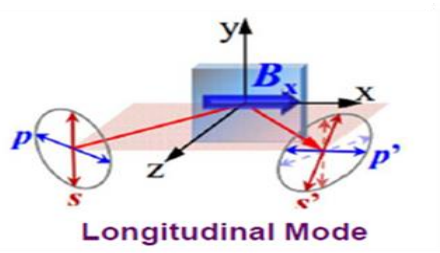

$$M_{||} = m_x \, \alpha \, \frac{I_\Delta}{I_\Sigma^{DC}}$$

$$M_\perp = m_y \, \alpha \, \frac{I_\Sigma^{AC}}{I_\Sigma^{DC}}$$

Figure (1.18) Scheme of longitudinal mode. Two types of polarization p and s. $M_{//}$: in-plane component parallel to applied magnetic field. $M_\perp$: in-plane component perpendicular to applied magnetic field. I_Δ: Polarization rotation, I_Σ^{AC}: Total reflectivity. I_Σ^{DC}: Total reflectivity

the difference of the intensities I_Δ is proportional to polarization rotations (i.e. longitudinal or polar component), while the alternating component of the sum of intensities (I_Σ^{AC}) is proportional to reflectivity changes (i.e., transversal component). Both Kerr effects are measured at the same time, providing the simultaneous determination of the two in-plane magnetization components. Therefore, in a single automated measurement procedure it is possible to acquire the hysteresis data—transverse and longitudinal—of a sample for the whole in-plane angular range.

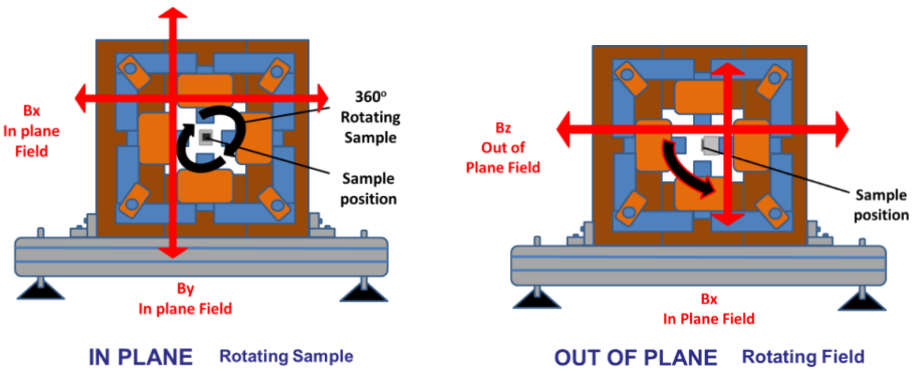

Figure (1.19) In-plane and out-of-plane configuration for longitudinal (transversal) and polar geometry, respectively.

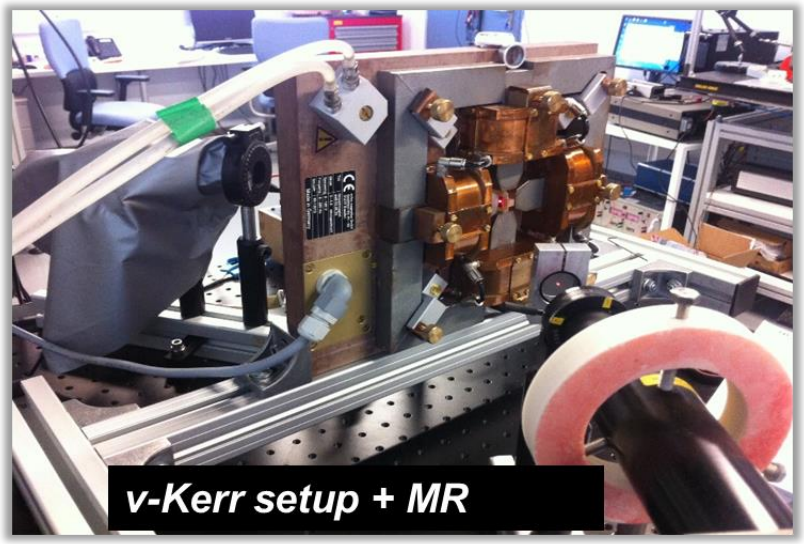

Figure (1.20) MOKE set-up in Polar Configuration.

1.3 Simultaneous field dependent MR and magnetization loops: MR-OKE set-up

The MOKE set-up has been upgraded for simultaneous MR capabilities measurements during my thesis. This set-up combines the high resolution vectorial-resolved Kerr magnetometry, which provides the simultaneous measurements of both in-plane magnetization components, with the additional capability to acquire at the same time the magnetoresistive signals. It allows hence for the understanding of the magnetoresistance (MR) responses as related to the magnetization reversal pathways, in any kind of magnetic material. This is done by experimentally disclosing the resistance changes occurring during (and simultaneously to) the magnetization reversal processes in many magnetic systems, ranging from metals to half-metallic oxides with unprecedented accuracy, as discussed in detail in the Chapter 3.

To measure MR, we have employed an ac technique varying the applied current direction from parallel to perpendicular to K_U, i.e., $\theta_J = 0^o$ and $\theta_J = 90^o$, respectively. The samples were contacted using Al-wire bonding in four probe current-in-plane (CIP) geometry. The measurements were performed using a lock-in amplifier with an ac current typically of the order of 50-100 μA, with a frequency in the range of 33-200 kHz through a load resistance of $R_L \approx 1k\Omega$-$1M\Omega$, depending on the samples resistance. $MR(H) = \frac{R(H)-R_m}{R_m}$, where R_m is the resistance at saturation field (sample magnetization aligned

to current direction), was hence derived from the experimental R(H) curves. The magnetization loops were measured by high-resolution vectorial-Kerr magnetometry by using p-polarized light focused between the inner electric probes and analyzing the two orthogonal components of the reflected light.

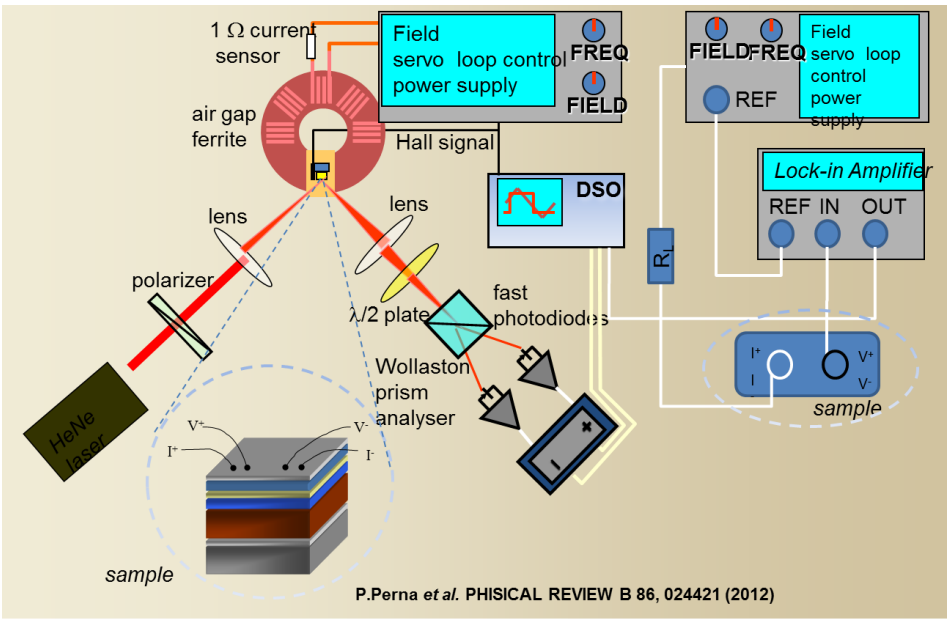

Figure (1.21) Scheme of the experimental M(R)OKE set-up, which allows magnetic field- and angular- dependent measurements acquiring simultaneously both in-plane magnetization components and the MR signals.

1.4 KERR Microscopy

Different techniques have been developed to image magnetic domains. The first one was presented by Francis Bitter in 1931, who used what we now call Bitter colloids (ferromagnetic microparticles) to reveal the stray field of a polished ferromagnet, using an optical microscope [17]. In a presence of an external magnetic field, even with low magnetic field, Bitter could invert completely the structure of a “Bitter” pattern [18]. Kerr effect could, in theory, reveal magnetic patterns too, but such small changes in amplitude (induced by a variation in polarization) were impossible to be observed by the naked eye. MOKE microscopy was hence developed with digital cameras and digital data processing.

This technique is explained in a scheme presented in Figure (1.22). Where the illumination and image-formation ray paths are illustrated separately for convenience. Light emitted from a lamp is focused onto the plane of the

aperture diaphragm by the lamp collector lens, passes through the opening of a variable field iris diaphragm, and is then plane polarized and deflected downward into the objective lens. After the reflection from the sample, the light is captured by the objective and then passes through the half-mirror again.

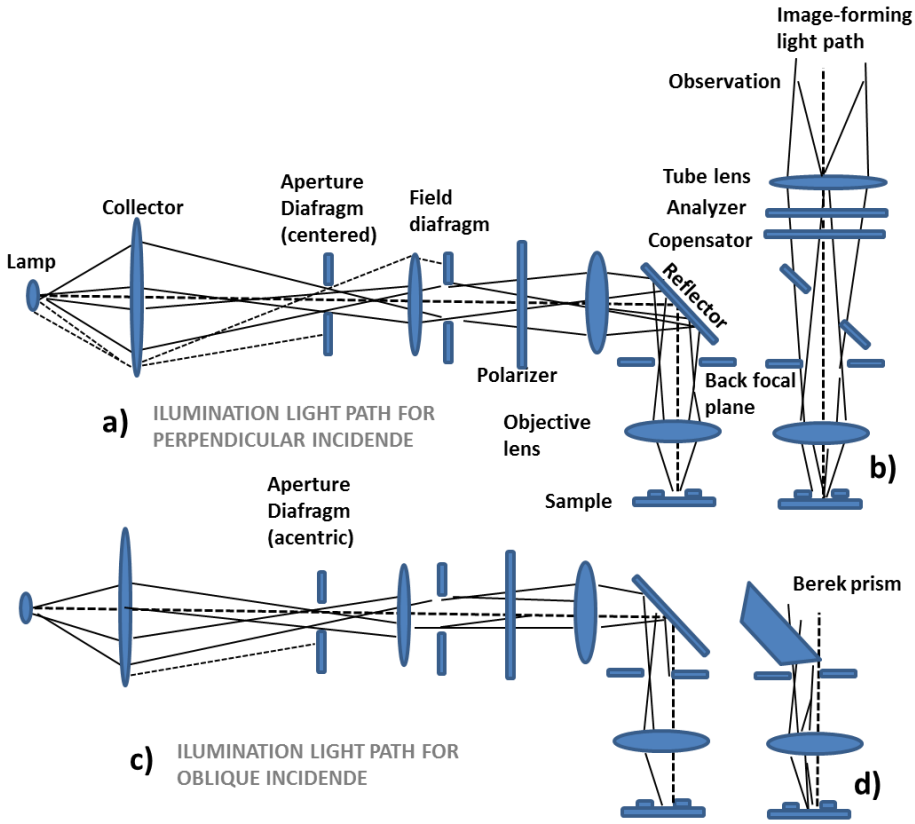

Figure (1.22) The essential components and light paths of a wide-field Kerr microscope. a) Illumination path for perpendicular light incidence, and b) image-forming path. c) Oblique incidence requires splitting slit and d) can also be optined with a Berek prism. Draw based on Schäfer manual.

1.4.1 Image processing

The procedure to get images starts with a digitized, averaged image of the magnetically saturated state, where in an external dc magnetic field all domains are eliminated. Alternatively, an alternating field of moderate amplitude can be applied, which mixes up the domains during averaging with the advantage that forces on the ample may be smaller than in the high saturating field. This domain-free background (reference) image is then

substracted from a state containing domain information, so that in the difference image a clear micrograph of the domain pattern is obtained, which can be improved by averaging and digital contrast enhancement, free of topographic contrasts. A schematic representation is shown in Figure (1.23).

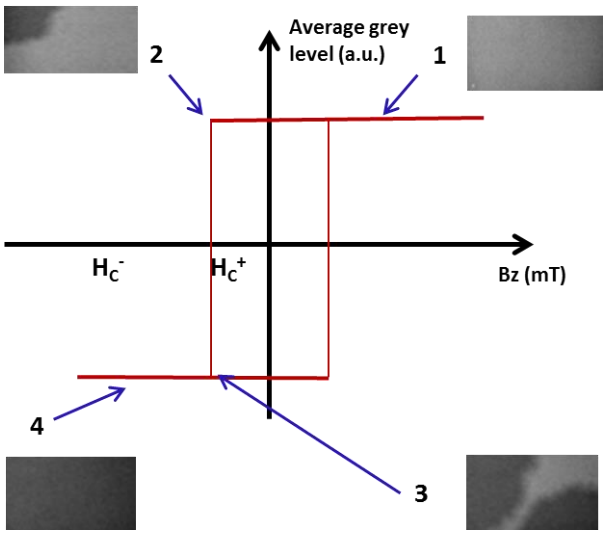

Figure (1.23) Schematic hysteresis loop (Average grey level / Bz) 1) sample saturated with pointing up magnetization. 2) Nucleation of domain walls with opposite direction (magnetization pointing down) black contrast. 3) Expansion of the magnetic domain wall up to down. 4) Sample saturated with pointing down magnetization

Kerr microscopy is a valuable tool for the characterization of magnetic structures, giving information about the nucleation and propagation of magnetic domain walls.

1.5 Other techniques: XAS-XMCD

X-ray absorption spectroscopy (XAS) utilizes the energy dependent absorption of x-rays to obtain information about the elemental composition as well as on the chemical environment of the atoms and their magnetic state. In the following, the description is focused on the spectra of the magnetic 3d transition metal elements Fe, Co and Ni. Core electrons are excited in the absorption process into empty states above the Fermi energy and thereby probe the electronic and magnetic properties of the empty valence levels. Their magnetic properties are largely determined by the 3d valence electrons. Since x-ray absorption spectra are governed by dipole selection rules the d-shell properties are best probed by L-edge absorption studies (2p to 3d transitions). For a magnetic material the d shell has a spin

moment that is given by the imbalance of spin-up and spin-down electrons or equivalently (except for the sign) by the imbalance of spin-up and spin-down holes. In order to measure the difference in the number of d holes with up and down spin, the x-ray absorption process must be spin dependent. This is done by use of right or left circularly polarized photons, which transfer their angular momentum to the excited photoelectrons. In a ferromagnetic material the d-bands are split into spin-up and spin-down bands.

Considering the selection rules of the transition and the corresponding transition matrix elements, the resonant absorption for circular polarized light depends on the angle between photon angular momentum and magnetization. Consequently, the absorption spectra of a ferromagnetic material for left and right circular light are, in general, different, as can be seen in Figure (1.24). By closely analyzing the difference in the XMCD spectrum, information can be obtained on the magnetic properties of the atom, such as its spin and orbital magnetic moment. In particular, XMCD probes the projection of the magnetization onto the photon k-vector. In addition, quantified information with element selectivity can be obtained with the XMCD analysis. In fact, two sum rules have been developed to relate the amplitude of the XMCD signal to the spin and orbital momenta of the 3d states. The sum of the XMCD values at the L3 and L2 edges is related to the orbital momentum while the difference is related to the spin momentum. Finally, in order to understand element-selective hysteresis loops or the origin of magnetic contrast in holography imaging, it is worth to emphasize that the quantization axis of the magnetic band is given by the magnetization direction. In fact, the size of the dichroism effect scales as cos ϕ, where ϕ is the angle between the direction of photon propagation (defining the photon angular momentum) and the magnetization direction. The maximum dichroism (absorption difference) is observed for their parallel and antiparallel orientations, whereas for the perpendicular directions the difference is zero for both magnetization orientations. In absorption spectroscopy, it is equivalent whether the photon polarization is changed and the magnetization direction is kept fixed or whether the magnetization direction is changed and the photon helicity is fixed. This means that the XMCD signals obtained for magnetic domains of opposite magnetizations will be opposite.

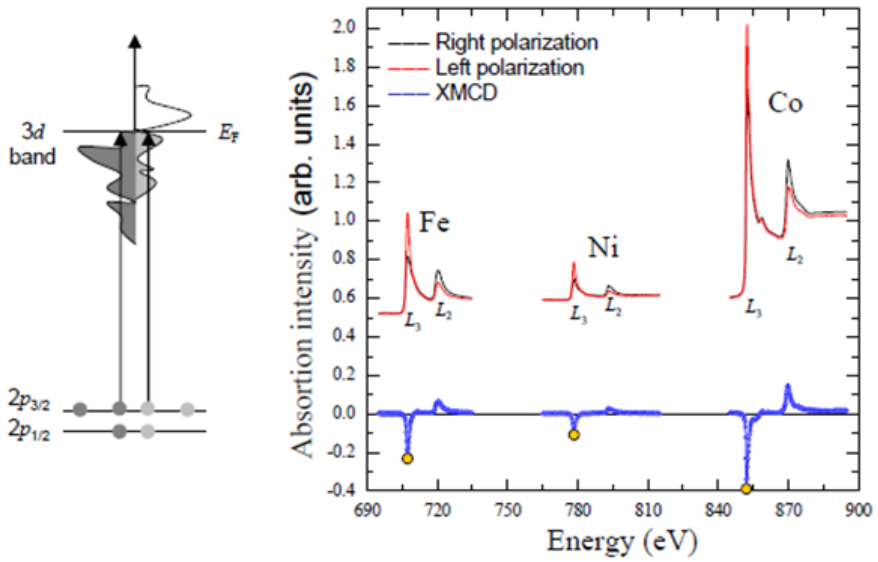

Figure (1.24) Concept of XMCD. Left: Scheme of a resonant electron transition from 2p states to 3d states (left). Due to the d-band splitting in ferromagnets and the selection rules for transitions, the photon cross section is different for left and right circular light. Furthermore, the energy of the transition is strongly element dependent, such that element specific absorption asymmetries can be recorded. Right: XAS spectra for right (black) and left (red) x-ray polarization and corresponding XMCD (blue) spectra of a FeNi/Cu/Co trilayer system saturated in the direction of x-ray beam. Image couresy of J. Camarero.

Nowadays XMCD has become a well established experimental tool in advanced magnetism. This is because at modern synchrotron sources XMCD is a rather simple technique.

1.6 References

[1] A. P. Guimarães, “The Basis of Nanomagnetism,” *Princ. Nanomagnetism*, pp. 1–20, 2009.

[2] “Structure and dynamics at graphene interfaces: from metal substrates to adsorbed molecules.”

[3] M. P. Seah and W. A. Dench, “Quantitative electron spectroscopy of surfaces: A standard data base for electron inelastic mean free paths in solids,” *Surf. Interface Anal.*, vol. 1, no. 1, pp. 2–11, 1979.

[4] J. E. Castle, “Practical surface analysis by Auger and X-ray photoelectron spectroscopy. D. Briggs and M. P. Seah (Editors). John Wiley and Sons Ltd, Chichester, 1983, 533 pp., £44.50,” *Surf. Interface Anal.*, vol. 6, no. 6, p. 302, 1984.

[5] D. A. Shirley, “High-Resolution X-Ray Photoemission Spectrum of the Valence Bands of Gold,” *Phys. Rev. B*, vol. 5, no. 12, pp. 4709–4714, Jun. 1972.

[6] S. Tougaard, “Practical algorithm for background subtraction,” *Surf. Sci.*, vol. 216, no. 3, pp. 343–360, 1989.

[7] “Omicron-Nanotechnology XM 1000 MkII:X-ray Source and Monochromator 2010.”

[8] C. Davisson and L. H. Germer, “Diffraction of Electrons by a Crystal of Nickel,” *Phys. Rev.*, vol. 30, no. 6, pp. 705–740, 1927.

[9] D. W. Jepsen, P. M. Marcus, and F. Jona, “Low-Energy-Electron-Diffraction Spectra from [001] Surfaces of Face-Centered Cubic Metals: Theory and Experiment,” *Phys. Rev. B*, vol. 5, no. 10, pp. 3933–3952, May 1972.

[10] H. Ibach, “No Title,” *Surf. Sciece Reports*, vol. 35, p. 71, 1999.

[11] G. . K. Ertl, *Low Energy Electrons and Surface Chemistry*. 1974.

[12] L. Bergmann and C. Schäfer, “Bergmann · Schaefer Lehrbuch der Experimentalphysik Band 1 Mechanik · Akustik · W¨ arme,” *New York*.

[13] J. K. LL.D., “XLIII. On rotation of the plane of polarization by reflection from the pole of a magnet,” *Philos. Mag.*, vol. 3, no. 19, pp. 321–343, 1877.

[14] E. R. Moog and S. D. Bader, “Smoke signals from ferromagnetic

monolayers: p(1×1) Fe/Au(100)," *Superlattices Microstruct.*, vol. 1, no. 6, pp. 543–552, 1985.

[15] J. Fassbender, "Magnetization Dynamics Investigated by Time-Resolved Kerr Effect Magnetometry," in *Spin Dynamics in Confined Magnetic Structures II*, B. Hillebrands and K. Ounadjela, Eds. Berlin, Heidelberg: Springer Berlin Heidelberg, 2003, pp. 59–92.

[16] P. Perna *et al.*, "Magnetization reversal signatures in the magnetoresistance of magnetic multilayers," *Phys. Rev. B*, vol. 86, no. 2, p. 24421, Jul. 2012.

[17] F. Bitter, "On Inhomogeneities in the Magnetization of Ferromagnetic Materials," *Phys. Rev.*, vol. 38, no. 10, pp. 1903–1905, Nov. 1931.

[18] W. F. B. Jr., "Domains, micromagnetics, and beyond: Reminiscences and assessments," *J. Appl. Phys.*, vol. 49, no. 3, pp. 1937–1942, 1978.

[19] J. L. Erskine and E. A. Stern, "Calculation of the M_{\rm 23} mageto-optical absorption spectrum of ferromagnetic nickel," *Phys. Rev. B*, vol. 12, no. 11. pp. 5016–5024, 1975.

[20] B. T. Thole, G. van der Laan, and G. A. Sawatzky, "Strong Magnetic Dichroism Predicted in the ${M}_{4,5}$ X-Ray Absorption Spectra of Magnetic Rare-Earth Materials," *Phys. Rev. Lett.*, vol. 55, no. 19, pp. 2086–2088, Nov. 1985.

[21] F. De Bergevin and M. Brunel, "Observation of magnetic superlattice peaks by X-ray diffraction on an antiferromagnetic NiO crystal," *Phys. Lett. A*, vol. 39, no. 2, pp. 141–142, 1972.

[22] G. Van Der Laan *et al.*, "Experimental proof of magnetic x-ray dichroism," *Phys. Rev. B*, vol. 34, no. 9, pp. 6529–6531, 1986.

[23] G. Schütz *et al.*, "Absorption of circularly polarized x rays in iron," *Phys. Rev. Lett.*, vol. 58, no. 7, pp. 737–740, Feb. 1987.

[24] C. T. Chen, F. Sette, Y. Ma, and S. Modesti, "Soft-x-ray magnetic circular dichroism at the ${\mathit{L}}_{2,3}$ edges of nickel," *Phys. Rev. B*, vol. 42, no. 11, pp. 7262–7265, Oct. 1990.

II. Overview of micromagnetic energies and magnetoresistive effects

The basic concepts in magnetism required to understand the experimental results of the thesis are briefly introduced. In general, the significance of the (magnetic) geometry of a system to its physical behavior is emphasized. In particular, the different energies existing in magnetic nanostructures, the basics of the magnetotransport phenomena, and the characteristics of the dynamic of domain wall motion under magnetic fields will be presented. In addition, the state of the art of (tailored) magnetic nanostructures will be given. The structure of the thesis, according to the technological and scientific advances, is briefly introduced at the end of this chapter.

2.1 Spin-Orbit Interaction (SOI)

As its name already implies, spin-orbit interaction (SOI) gives rise to a coupling between the spin dynamics of an electron and its (orbital) motion in space. The relativistic nature of this coupling can be understood by alow velocity approximation to the Dirac equation [1].This approach yields, among other fine-structure corrections to the non-relativistic Schrödinger equation, the Pauli SO term:

$$\hat{H}_{SO} = -\frac{\hbar}{4m_0^2c^2}\boldsymbol{\sigma}\cdot(\mathbf{p}\times\boldsymbol{\nabla}V(r)) \qquad (2.1)$$

Where $\hbar$ is Planck's constant, m_0 the bare mass of the electron, c the velocity of light, and $\boldsymbol{\sigma}$ the vector of Pauli matrices. V(r) is the electrostatic potential in which the electron propagates with momentum p. (Coulomb potential of the atomic core).In the classical approximation, it is possible to present the SO in function of the electron induction (B) created in the system:

$$\widehat{H}_{SO} = -\frac{1}{2}\mu \cdot \mathbf{B} \tag{2.2}$$

Where (1/2) factor is the relativistic Thomas-Wigner factor, μ the huge moment of electron being, $\mu = \frac{-e\hbar}{2mc}\boldsymbol{\sigma}$and $= \frac{-\boldsymbol{v}\times\boldsymbol{E}}{c}$. The presence of this effective magnetic field that the electron feels in its rest frame affects both the dynamics of the spin and the total energy of the electron. One should keep in mind that the only possible interaction for the spin degree of freedom is with a magnetic field, whose source can be either an externally applied magnetic field, or the effective field generated by the spin-orbit interaction. The static electric field causing the spin-orbit interaction can have different physical origins, for example being the electric field of the atomic nucleus, or related to the crystal or band structure of the solid. In crystal with large Z, the relativistic correction is relevant. It is possible to present the SOI with the last equation:

$$\widehat{H}_{SO} = -\frac{Ze^2}{2m_e^2c^2r^3}\mathbf{L}\cdot\mathbf{S} \tag{2.3}$$

Where the orbital momentum is given by **L** = **r** × **p**, m_e is the electron's mass, Z is the atomic number of the nucleus and r is the radius of the electron orbital Equation (2.3) reveals the coupling between spin (S) and orbital (L) angular momentum.

2.2 Magnetic Anisotropy

A strong spin-orbit coupling interaction makes the band structure sensitive to the direction of the magnetization which gives rise to magneto-crystalline anisotropy. In all the ferromagnetic thin films, the magnetization prefers to orient along certain direction termed as easy axis (e.a.). The direction along which a maximum energy is required to saturate the magnetization is termed as hard axis (h.a.), see Figure (2.1). This excess energy required to change the orientation of the magnetization from easy to hard axis is termed as the effective magnetic anisotropy energy (K_{eff}).

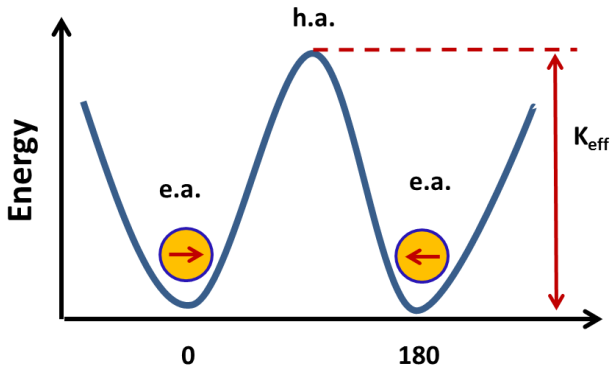

Figure (2.1) Schematic illustration of the effective anisotropy energy associated with a ferromagnetic thin film. Easy axis (e.a.) is the direction along which magnetization prefers to orient, whereas hard axis (h.a.) is the direction along which a maximum energy is required to orient the magnetization.

2.2.1 Shape Anisotropy

Magnetic shape anisotropy is the consequence of long-range dipolar interaction. The surface divergence of the magnetization gives rise to a demagnetization field. H_d is given by:

$$\widehat{\boldsymbol{H}}_{\boldsymbol{d}} = -\boldsymbol{N}_{\boldsymbol{D}} \cdot \boldsymbol{M} \tag{2.4}$$

Where, M is the magnetization vector and N_D is the demagnetizing tensor depends on the shape of the sample. In the case of thin films, the tensor elements $N_{xx}=N_{yy}=0$ and $N_{zz}=1$ i.e. $N_D=1$. Then, the demagnetizing energy associated with the influence of demagnetizing field on the direction of magnetization in thin films can be written as:

$$\mathrm{E_A} = \frac{\mu_0}{2} {M_S}^2 cos^2\varphi \tag{2.5}$$

Where, M_s is the saturation magnetization which subtends an angle θ with the film normal. According to this equation, the demagnetizing energy contribution favors the orientation of the magnetization along the sample plane. However, the roughness of the thin film samples significantly influences the demagnetizing factor N_D.

2.2.2. Magnetocrystalline (surface/interface) anisotropy

The microscopic origin of magnetocrystalline anisotropy is the SO coupling. This interaction causes the alignment of the magnetic moment due to the spin of the electron with the magnetic moment due to the orbital motion of the electron. These are then coupled to the crystallographic axis by means of electrostatic field by the overlapping of the wave functions associated with neighboring atoms in the crystal lattice.[2] This causes a preferred orientation of the magnetization along certain crystallographic direction. The anisotropy is hence an intrinsic property of a crystalline ferromagnetic material and it reflects the symmetry of the crystal. Néel in 1954 predicted that the reduced symmetry at the surface of the thin films would result in a different anisotropy compared to that of the bulk crystalline anisotropy.[3] Therefore in the case of thin films, the total magnetocrystalline anisotropy energy has the contribution from the bulk or volume anisotropy, Kv per unit volume and the contribution from the surface anisotropy, Ks per unit area.[4]Similar situation is also encountered in the ferromagnetic/noble metal multilayers due to a lowered symmetry at the interface [5] [6]. A general expression for the total anisotropy energy in terms of the volume and the interface contributions describing the angular orientation of the magnetization in the case of polycrystalline thin film can be written as:

$$\mathrm{E} = -K_{eff} cos^2\theta \tag{2.6}$$

Where:

$$K_{eff} = K_v + \frac{K_s}{t} \tag{2.7}$$

Here, $\theta \equiv (\widehat{M,K})$ is the angle between **M** and anisotropy axis, t is the thickness of the ferromagnetic thin films. The interfacial/surface anisotropy would make a significant contribution only in the case of ultrathin ferromagnetic layers, we define a critical film thickness t_{cr} = Ks/Kv where transition from in-plane to out-of-plane magnetization occurs. Kv is an energy density per volume and Ks is an energy density per surface.

2.2.3 Uniaxial Anisotropy

The simplest case of magnetocrystalline anisotropy is uniaxial anisotropy. The crystalline structure of the film induces an additional anisotropy due to the spin-orbit interaction. If there are no other anisotropy contributions the magnetocrystalline anisotropy makes the magnetization align along a defined direction with respect to the crystal structure. This type of anisotropy is manifested, e.g., in hexagonal, tetragonal, and rhombohedral structures. The anisotropy energy in those cases has the form (up to fourth-order terms):

$$E_K = K_{u_1} sin^2\theta + K_{u_2} sin^4\theta \qquad (2.8)$$

Where, Ku_1 and Ku_2 are the first and second order energy density constants, or magnetocrystalline anisotropy constants. In zero applied field the free energy of the uniaxial system is such that it is minimized when the magnetization lies along the easy axis.

2.2.4 Unidirectional Anisotropy

The unidirectional anisotropy is an additional energy contribution towards the effective magnetic anisotropy of the FM layer (as mentioned in the previous section) and thereby influences the resulting orientation of the corresponding magnetization direction. This anisotropy arises from the interfacial phenomena of exchange coupling across the FM and the AFM layers termed as the exchange bias effect. This effect causes a displacement of the FM hysteresis loop along the field axis. This type of anisotropy was first observed by Meiklejohn and Bean in Co-CoO system.[7]

The shift in the hysteresis loop due to the exchange bias effect can be qualitative understood assuming an exchange coupling between the FM and AFM spins at the interface. Let T_N and T_C be the Néel temperature of AFM layer and the Curie temperature of the FM layer, respectively. At the temperatures higher than T_N and lower than T_C, all the FM spins align along the direction of the applied field, whereas the AFM spins are randomly oriented as shown in Figure (2.2). Upon reducing the temperature below T_N with an external field (field cooling), the AFM spins in the plane next to the FM layer at the interface, align ferromagnetically or antiferromagnetic (depending upon the exchange coupling energy) with the FM spins.

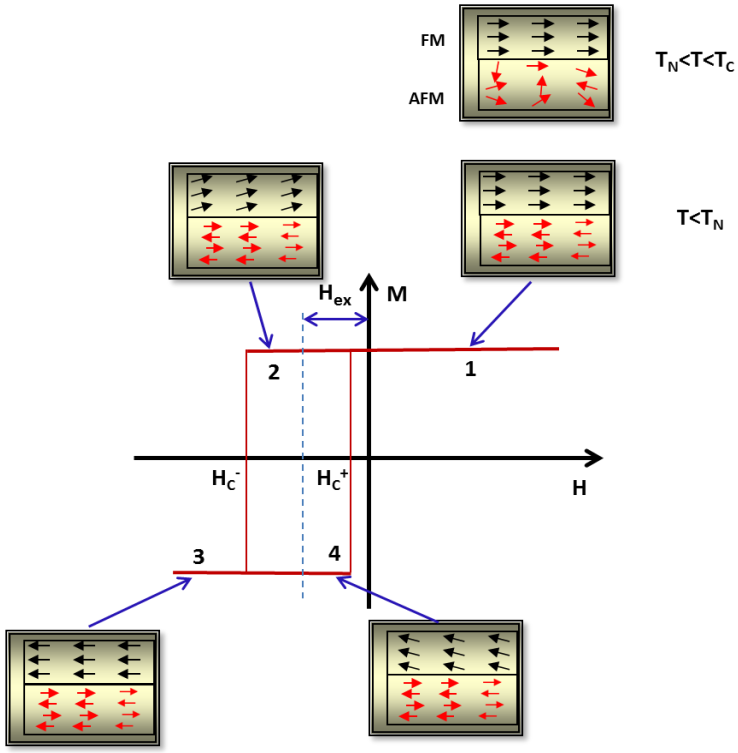

Figure (2.2) Schematic diagram depicting the response of exchange biased FM and AFM spins at various stages (1-4) of the negative shifted hysteresis loop after field cooling procedure. (Illustration was based on the reference [8]**).**

The AFM spins in the next layer align in the opposite direction to follow the AFM order to produce zero net magnetization. When the applied field is reversed, the FM spins start to rotate to align themselves along the direction of the applied field. But the AFM spins with sufficiently large AFM anisotropy (K_{AFM}) will not respond to the applied field. Due to the exchange coupling at the AFM/FM interface, the AFM spins exerts a torque on the FM spins. This holds the FM spins in the direction of the field cooling and it results in an induced unidirectional anisotropy. Because of this effect the FM spins switch only at a large reverse field, which is sufficient to overcome the torque exerted by the AFM layer. Therefore, in this case the transition field (H_c^-) is larger than the field (H_c) required to switch the FM spins in the absence of exchange coupling at the FM/AFM interface. The field (H_c^+) at which the FM spins switch back to their original direction is also reduced due to the exchange interaction at the interface, which acts as an internal field. As a result, the FM hysteresis loop is shifted in the field axis. The corresponding

exchange-bias (H_{ex}) and coercive field (H_c) can be calculated using the formula:[9]

$$H_E = \frac{H_C^+ + H_C^-}{2} \tag{2.9}$$

$$H_C = \frac{H_C^+ - H_C^-}{2} \tag{2.10}$$

2.3 Domains and domain walls

A straightforward consequence of energy minimization is the formation of domains.[10], [11]If the magnetization were homogenous throughout the sample, there would be a high cost of magnetostatic energies due to the formation of free poles. This could be avoided if the magnetization is divided into regimes known as domains and arranged in a way to minimize the stray field energy Figure (2.3).In the process, boundaries are formed between adjacent domains having different magnetization directions. Abrupt transitions, however, are not favorable due to the strong exchange interaction in the ferromagnets. Instead these boundaries spread out into a region of finite thickness known as domain walls (DWs), in which the magnetization directions twist and form relatively smooth transitions between two domains.

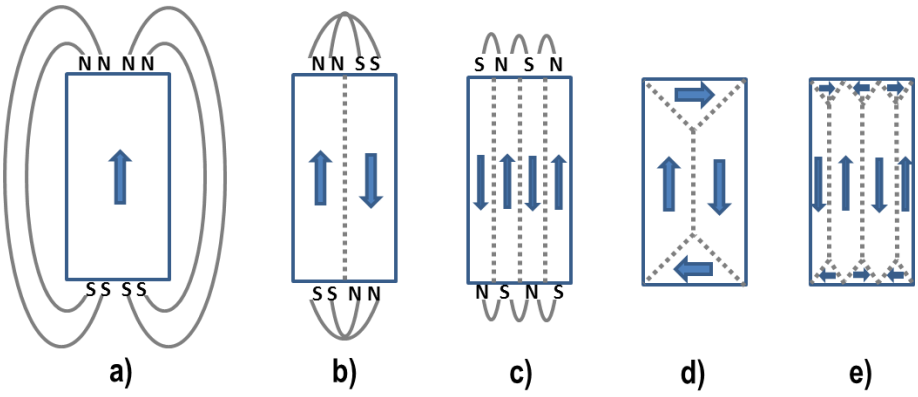

Figure (2.3) Origin of domains, after Kittel[12].

Figure (2.4) a) shows a Bloch domain wall [13] containing smoothly rotating moments, which minimizes the energy cost due to the exchange interaction. For the case of thin films (that do not show significant surface anisotropy),

the 'magnetic charges' formed by the Bloch wall moments rotating out of plane would cost a high magnetostatic energy, hence it is more favorable for the moments to rotate in the plane of the film. A Néel wall [3] Figure (2.4) a) is formed in preference to a Bloch wall in this way. The width of the domain wall is strongly dependent on the material and its anisotropies, but is typically of the order of tens to 100 nm. The width and the energy of a wall can be calculated (in absence of an external applied magnetic field) by minimizing the total energy of the system. Let us consider a Bloch wall

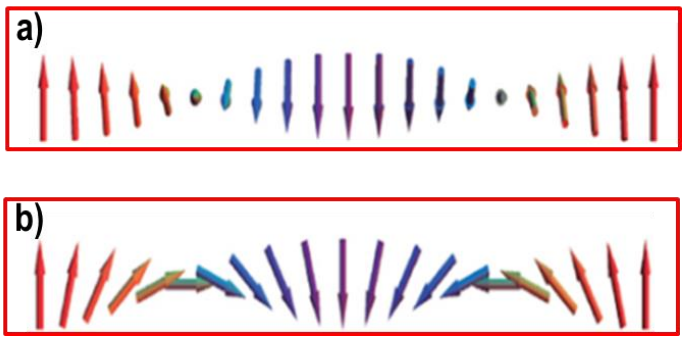

Figure (2.4) Schematic diagrams showing (a) a Néel wall and (b)a 180° Bloch wall

and assume that Ox is the axis perpendicular to the DW. The moments make an angle θ with the Oz axis and the angle between two successive moments along the x-axis will be Δθ. The total energy of the wall (with unit surface area) will be:

$$\mathrm{E}(\theta) = \int_{-\infty}^{+\infty} \left[A\left(\frac{d\theta}{dx}\right) + e_{an}(\theta) \right] dx \qquad (2.11)$$

Where A is the exchange stiffness and $e_{an}(\theta)$ is the anisotropy energy density, which will be assumed to be zero along the easy directions of magnetization. θ(x) must take the values that minimize the integral. For this, if at each point x, θ(x) varies by a small amount δθ(x), the modification in configuration of the spins does not provoke, to first order, any variation δE, thus, after some calculus we can extract the following expressions.

$$e_{an}(\theta) = A\left(\frac{d\theta}{dx}\right)^2 + const \qquad (2.12)$$

When x→ ±∞ (within the domain), $e_{an}(\theta)$= 0 and ∂θ/∂x = 0, indicating that const is zero.

Hence:

$$e_{an}(\theta) = A\left(\frac{d\theta}{dx}\right)^2 \tag{2.13}$$

which reads: at all point of the domain wall the cost in anisotropy energy and in exchange energy balance each other. In other words, inside the domain wall, where the anisotropy energy is most costly, the angle between adjacent spin is greater, and vice versa. The domain wall energy is:

$$\mathrm{E}(\theta) = 2\int_{-\infty}^{+\infty} e_{an}(\theta)dx \tag{2.14}$$

Extracting dx from eq. (2.11):

$$dx = \sqrt{\frac{A}{e_{an}(\theta)}} \tag{2.15}$$

one can write the general energy expression for a Bloch wall For a 180° wall (θ_i = -π/2 and θ_f = π/2) and assuming a uniaxial anisotropy ($e_{an}(\theta)$= $K\cos^2\theta$):

$$\mathrm{E}(\theta) = 4\sqrt{AK} \tag{2.16}$$

various definitions have been proposed for the DW width Δ. One widely accepted is that that consider the angular deviation constant and equal to the value at the center of the wall, which yields:

$$\Delta = \pi\left(\frac{\partial x}{\partial\theta}\right)_{x=0} = \pi\sqrt{A/K} \tag{2.17}$$

Where θ_f–θ_i = π has been assumed. In the case of a Néel wall, energy minimization will vary the angle θ from -90 to 90 by changing the magnetization parallel to the surface in order to restrict the demagnetization effects created by the proximity of the planes. The characteristic length of a Néel wall can be calculated to be:

$$\Delta = \pi \sqrt{A/K_U} \tag{2.18}$$

where Ku is the out-of-plane shape anisotropy constant. It is worth mentioning that, while reducing the thickness of a film, the transition from Bloch wall to Néel wall is not sharp. In a certain region of film thicknesses, a third type of wall is observed that is named cross-tie wall. This kind of wall is not of interest for the present work. The reader is remanded to Ref. 20 for more information.

2.4 Exchange energy

In solids, the electronic orbitals of neighboring atoms overlap, which leads to the correlation of electrons. These results in the interatomic exchange interaction that makes the total energy of the crystal depend on the relative orientation of spins localized on neighboring atoms. The exchange interaction is the largest magnetic interaction in solids (≈1eV) and is responsible for the existence of parallel, i.e. ferromagnetic, and antiparallel, i.e. antiferromagnetic, spin alignment. The exchange interaction might be mediated by different mechanisms depending on the material system under consideration. The most important mechanisms are described below.

2.4.1 Direct exchange

The direct exchange arises from a direct overlap of electronic wave functions of the neighboring atoms and the Pauli exclusion principle, which requires different symmetry properties from the spatial and spin parts of the electronic wave function. In a two-spin system, the exchange energy is defined as the energy difference between the parallel and antiparallel spin configuration. For a many electron system, the exchange energy is given by the expectation value of the Heisenberg Hamiltonian:

$$\mathcal{H}_{ex} = -\sum_{i \neq j} J_{ij}\, \hat{\boldsymbol{S}}_{\boldsymbol{i}} \cdot \hat{\boldsymbol{S}}_{\boldsymbol{j}} \tag{2.19}$$

Where J_{ij} is the exchange integral describing the coupling between two spins or magnetic moments represented by the spin operators $\hat{\mathbf{S}}$i and $\hat{\mathbf{S}}$j. Depending on the interatomic distances (i.e. orbital overlap) the values of J_{ij} might have a positive or negative sign, resulting in the parallel or antiparallel ground state configuration of spins, respectively. The direct exchange is a

short-range interaction. If the interatomic distance is too large (i.e. wave function overlap too small) the direct exchange coupling is not strong enough to overcome thermal excitations, giving rise to paramagnetism.

2.4.2 Antisymmetric exchange: Dzyaloshinskii-Moriya interaction

The antisymmetric part of the exchange interaction knows as Dzyaloshinskii-Moriya interaction (DMI) can be written as follow:

$$E_{ex}^{a} = -\frac{1}{2}\sum_{i\neq j} \mathbf{S}_i \widehat{\mathbf{A}}_{ij}^{a} \mathbf{S}_j = -\frac{1}{2}\sum_{i\neq j} \mathbf{D}_{ij} \cdot (\mathbf{S}_i \times \mathbf{S}_j), \tag{2.20}$$

Where,

$$D_{ij}^{x} = \frac{A_{ij}^{yz} - A_{ij}^{zy}}{2}, \qquad D_{ij}^{y} = \frac{A_{ij}^{zx} - A_{ij}^{xz}}{2}, \qquad D_{ij}^{z} = \frac{A_{ij}^{xy} - A_{ij}^{yx}}{2} \tag{2.21}$$

The antisymmetric term was first proposed by Dzyaloshinskii [14] in 1958 and Moriya [15] in 1960. Dzyaloshinskii predicted, purely on grounds of symmetry, that the combination of low symmetry and spin-orbit couplings gives rise to antisymmetric exchange interactions. Moriya found a microscopic mechanism which leads to such a term in systems with spin-orbit couplings.

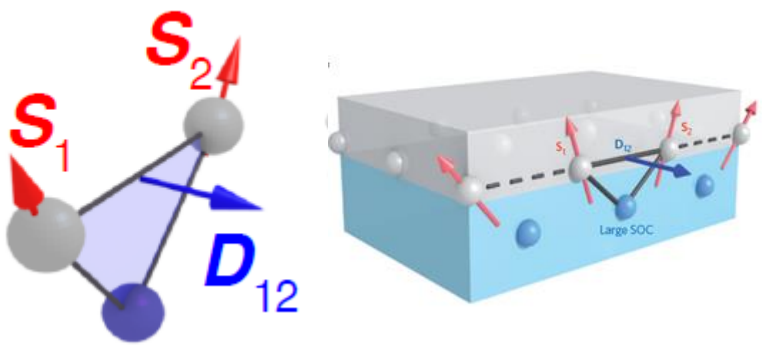

Figure (2.5) Dzyaloshinskii-Moriya Interaction for a single trilayer composed of a magnetic layer (grey) and heavy metal (blue) in the Fert-Lévy picture. Courtesy of V. Cros.

In Figure (2.5), it is shown DMI emerging from the interplay of two atomic spins with a neighboring atom having a large spin-orbit coupling in a thin film.

The resulting DM-vector appears in plane, parallel to the surface, pointing outwards from the plane of the spins. Starting with a ferromagnetic state where all the spins are aligned: $S_1 \| S_2$, we then assume a strong spin-orbit coupling that induces a DMI. The resulting magnetic strength depends on the direction of the D-vector, which depends on the way the symmetry is broken at the interface. Thereby, positive and negative helicities can be obtained for the inversion of the magnetization vectors. The resulting configuration of two spins S_1 and S_2,is a tilt around D_{12} This rotation eventually results in the configuration showed in Figure (2.5).

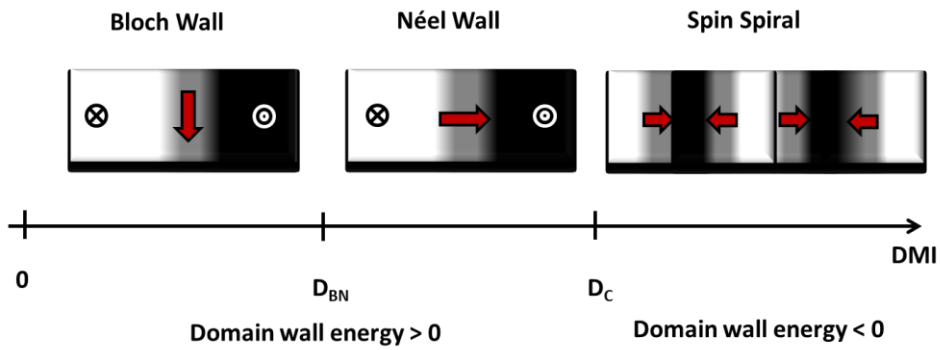

Figure (2.6) Domain wall chirality depending on the DMI strength.

DMI shows significant effects when SOC have an important role. This is manifested e.g. in perpendicularly magnetized Pt/Co ultra-thin films or multilayers [16], [17], where the interfacial DMI constitutes an effective in-plane magnetic field which stabilizes the Néel domain wall configuration which otherwise would be energetically unfavorable [18] (Thiaville et al., 2012) (Figure (2.6)). DMI field (H_{DMI}) appears only inside the DW and acts along the length of the wall. This also induces a specific chirality to the Néel wall which is dependent on the sign of D_{ij}[18], [16]. Indeed, as seen in Figure (2.6), there is a transition between Bloch and chiral Néel domain wall for lower value of DMI. Above a threshold value Dc, it is more energetically favorable to tilt the spin so we can expect spiral state or skyrmionic lattices.

2.4.3 Other exchange mechanisms

Itinerant exchange

In metallic 3d systems, like Co, Fe or Ni, both the atomic moments and the exchange interaction are due to the delocalized, also called itinerant,

electrons. It is thus not possible to describe the magnetic properties of metals in terms of atomic or ionic moments coupled by the intersiteexchange interaction, and one has to rely on the band model of electrons. As a consequence of the Coulomb repulsion of electrons and their kinetic energy, the bands with opposite spin orientation are exchange split giving rise to a non-zero total magnetic moment, and the appearance of ferromagnetism. This exchange splitting is commonly described using the Stoner model where the exchange splitting energy is given by $\Delta E_{ex} = IM$. Here, I is the so-called Stoner exchange parameter and M is the averaged atomic magnetization. Within this model, the stability of the spontaneous magnetic order is given by the Stoner criterion where $N(E_F)$ is the density of states at the Fermi level (E_F). A high density of states at the Fermi level and strong exchange splitting thus favor metallic ferromagnetism. The total magnetic moment is not fixed by atomic rules.

RKKY exchange

RKKY indirect exchange interaction (named after Rudermann, Kittel, Kasuya and Yoshida [19]) can play an important role when there is no direct overlap of the wave functions with unpaired electrons. In this case the interaction between two magnetic moments at sites i and j is mediated by the polarization of the conduction electrons. Characteristic for this coupling mechanism is an oscillatory behavior of the exchange integral J which changes its sign as a function of distance between the localized moments. Amongst others, this mechanism explains the coupling of 4f electrons in rare earth materials and is responsible for the oscillatory interlayer exchange coupling in multilayer structures, called spin-valve. In contrast to the direct exchange interaction, this type of interaction is long-range.

Superexchange

Superexchange is another kind of indirect exchange interaction and is important in ionic solids such as the transition metal oxides and fluorides. The most prominent example is MnO. The interaction between the magnetic Mn atoms is mediated by the diamagnetic oxygen though the overlap of the 3d metals and 2p oxygen orbitals, and a partial delocalization of the involved electrons. In the case of a parallel orientation of the magnetic moments located at the metal centers, no delocalization occurs, which makes the antiferromagnetic alignment energetically favorable. Generally, the size of the superexchange depends on the magnitude of the magnetic moments on

the metal atom, the orbital overlap between the metal, and the non-metallic element and the bond angle.

2.5 Magnetoresistive effects

Magnetoresistance (MR) is the change in resistance in a conductor due to an applied external magnetic field. Various and much different physical origins can be responsible of the effect in the different systems, although all of them are important candidates for technological applications. We will here review some MR effects with particularly emphases on those of interest in this work.MR effect can be divided into two categories: intrinsic and extrinsic MR effects. The only MR effect that cannot be strictly catalogued as either intrinsic or extrinsic is the domain wall resistivity that will be treated apart.

2.5.1 Lorentz Magnetoresistance (LMR)

This effect occurs in conducting films (not necessarily magnetic) and is due to the Lorentz force F affecting the trajectories of the conduction electrons when a magnetic field B is applied perpendicular to the electric field (see Figure (2.7):

$$\mathbf{F} = -e\mathbf{v} \times \mathbf{B} \tag{2.22}$$

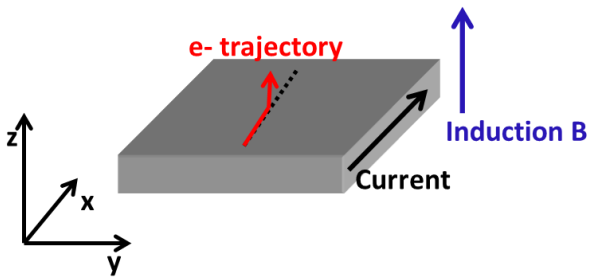

Figure (2.7) Fig. 2.1: Effect of the Lorentz force on the electrons trajectory when a magnetic field B is applied along the direction z perpendicular to the electric field E direction x.

Where, *v* is the electron velocity. The effect of the Lorenz force is twofold. The induced non-uniform electron distribution along z gives rise to the so-called Hall voltage, which varies linearly with B, and hence of great interest for magnetic sensing. On the other hand the non-uniform electron distribution gives rise to an increase of the resistance along x whose quadratic dependence from B can be easily understood: the conduction electrons see a reduced effective cross-section $A_{eff} < A$. From Ohm's law: R =

$(l/A_2)\rho$, hence the quadratic dependence is straight forward. This effect is not much of use for several reasons. First of all, *it is neither linear nor sign-dependent*, while the Hall effect is. Moreover, the effect is much weaker than the Hall effect: in normal metals changing of resistance of 1% require fields up to 1 Tesla. Since the OMR comes along with the Hall effect, it is obviously the latter to be exploited for practical applications.

2.5.2 Anisotropic MR (AMR)

The resistance of ferromagnetic metals or alloys under a magnetic field is anisotropic and changes according to the relative orientation of the magnetization to the measuring current (Figure (2.8). The resistance is maximum when the current is parallel to the magnetization direction and minimum when the current is perpendicular to the magnetization direction. A measure for the size of this effect is the MR ratio, which is defined by:

$$\mathrm{AMR} = \frac{\rho_{\parallel} - \rho_{\perp}}{\rho_{\parallel}} \tag{2.23}$$

At intermediate angles θ between the current and the magnetization direction, the resistivity is given by:

$$\rho(\theta) = \rho_{\perp} + (\rho_{\parallel} - \rho_{\perp})cos^2\theta = \rho_{\perp} + \Delta\rho_{max}cos^2\theta \tag{2.24}$$

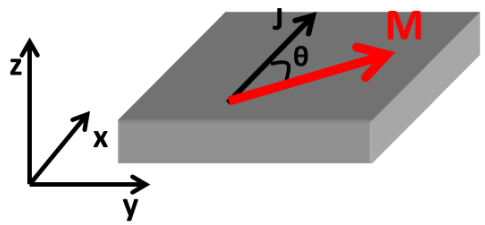

Figure (2.8) Plain view of the AMR effect.

The AMR effect was already discovered in 1857 by Thomson[20] but it took a century to explain the phenomenon [21]. This is because the explanation requires quantum mechanics. AMR effect arises from the SOI which is a relativistic effect as seen before.

2.5.3 Colossal MR (CMR)

Colossal MR refers to the large change of resistance observed in manganites when a high magnetic field is applied. In 1993 von Helmholt et al.

[22]observed an ((R(7T)-R(0))/R(0) ratio of 60% at room temperature in $La_{0.67}Ba_{0.33}MnO_3$ thin film. In the following year, Jin et al. [8] reported an MR effect of millions percent at 77K in $La_{0.67}Ca_{0.33}MnO_3$ thin film. The effect is believed to arise from the close correlation between the magnetic phase

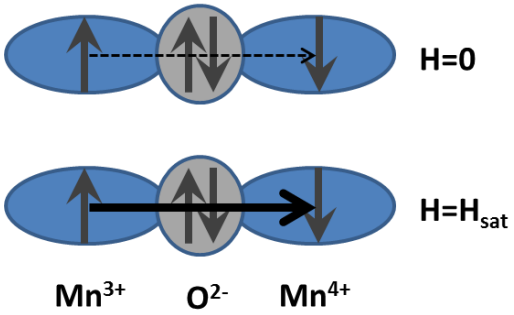

Figure (2.9) Schematic picture of the CMR effect. Theexternal magnetic field aligns spinparallels, forcing a transition frominsulating to metal phase.

transition and the electronic phase transition near the Curie Temperature T_{Curie}, though the fundamental physics is yet to be understood. A qualitative explanation of the phenomenon is that pictured in Figure (2.9): close to the transition temperature, a high magnetic field forces the spin to align parallel, therefore forcing the transition from insulating to metal phase. Because the CMR effect requires large magnetic fields (several Tesla) near T_{Curie}, imminent technological applications are largely limited at the moment. As will be shown in the following paragraph, manganites can be used for low-field applications by using extrinsic MR effects.

2.5.4 Giant magnetoresistive effect (GMR)

Giant magnetoresistance (GMR) occurs in ferromagnetic/non-magnetic (FM/NM) multilayers when the current is applied either in the plane or perpendicular to the plane of the structure. GMR was discovered in 1988 [23] in a superlattice multilayer with alternating Fe and Cr layers. As shown Figure (2.10), the resistance of such a superlattice structure is high at zero field, decreases when a magnetic field is applied in both directions along the sample surface, and finally saturates at a field of about 2T. The MR ratio of superlattices with an $[Fe(3nm)/Cr(0.9\ nm)]_{60}$ structure was measured to be about 45% at 4.2 K, which is much larger than the AMR effect. It was proved soon afterward that the resistance of the superlattice structure depends on

the relative orientation of the magnetization of the adjacent magnetic layers. In a F/N multilayer, the nearest neighbor adjacent F layers can spontaneously align either parallel (P) (ferromagnetic coupling) or antiparallel (AP) (antiferromagnetic coupling)according to the N spacer thickness.

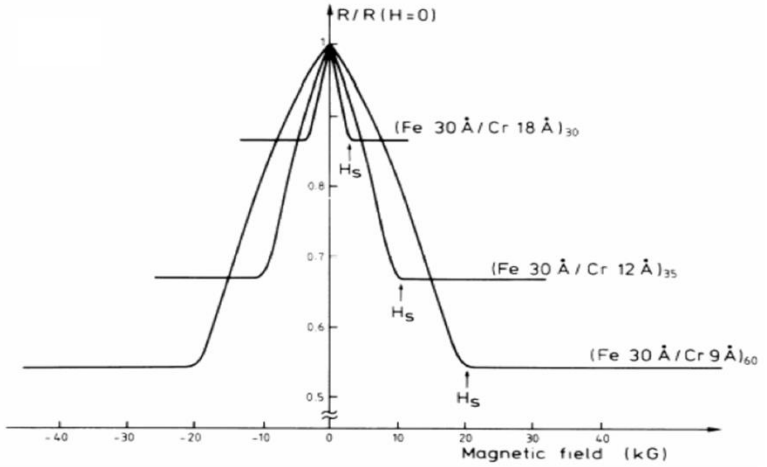

Figure (2.10) Magnetoresistance of Fe/Cr superlattices. Both the current and the applied field are along thes ame [110] axis in the film plane. Taken from [23]**.**

In Figure (2.10) the resistance is detected by applying the current in the plane (CIP configuration). Larger MR ratio can be achieved by making the current pass perpendicular to the planes (CPP configuration). In both cases the resistance can be written, considering a trilayer structure, in the following form [24] comparable to equation (2.24):

$$R(\theta) = R_0 + \frac{\Delta R_{GMR}}{2}(1 - cos\theta) \qquad (2.25)$$

with θ is the angle between the magnetization directions of the F-layers. It remains the question why the resistance is higher in the AP configuration as compared to the case of P configuration. The main idea behind all the models proposed is the difference of resistivities between the spin up and spin down electron channels, first proposed by Mott [25].

The mechanism of GMR can be understood using the simple two-current model [26].Consider a trilayer with two magnetic layers separated by a non-magnetic metallic spacer layer. Assume that the thickness of the N-layer is much smaller than the spin diffusion length λ_{sd} that is the length scale over

which the spin accumulation (that decay exponentially from the F/N interface) is conserved. We can thus assume that electrical current in the trilayer flows in two channels, one corresponding to electrons with spin up and the other to electron with spin down. Since the up- and down-spin channels are independent (spin is conserved)they can be regarded as two wires connected in parallels. The electron with different spin polarization are scattered in a different way when the yenter an F-layer. Given that electrons obey the Pauli Exclusion Principle, an electron can be scattered from an impurity only to quantum states that are not occupied by other electrons. At zero (low) temperatures, all the states with energy E below the Fermi energy E_F are occupied and those with $E > E_F$ are empty. Since scattering from impurities is elastic (energy conservation), electrons at the Fermi level (which carry the current) can be scattered only to states in the immediate vicinity of the Fermi level. It follows that the scattering probability is proportional to number of states available for scattering at E_F, i.e. to the density of states$N\uparrow\downarrow(E_F)$. Different $N\uparrow(E_F) \neq N\downarrow(E_F)$ implies different scattering probability.

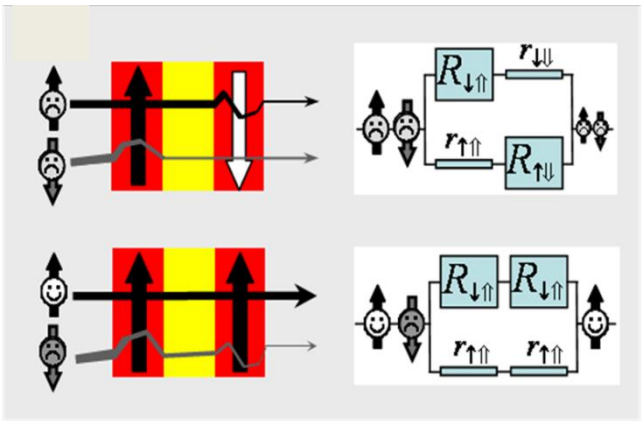

Figure (2.11) Resistor model of GMR. Picture courtesy of J. Camarero.

This is modeled by two small resistors in the ↑ channel and by two large resistors in the ↓ channel, in the equivalent resistor network shown Figure (2.11). Since the ↑ and ↓ channel are connected in parallel, the total resistance is determined by the low resistance↑ spin channel that shorts the high-resistance ↓ spin channel and is given by:

$$\rho_\rho = \frac{\rho_{\uparrow\uparrow} - \rho_{1\downarrow}}{\rho_{\uparrow\uparrow} + \rho_{1\downarrow}} \tag{2.26}$$

On the other hand, ↓ spin electrons in the AP configuration are strongly scattered in the first F-layer but weakly scattered in the second F-layer. The ↑ spin electrons are weakly scattered in the first F-layer but strongly scattered in the second F-layer. This is modeled in Figure (2.11). There is no shorting now and the total resistance is much higher:

$$\rho_{AP} = \frac{\rho_{\uparrow\uparrow} - \rho_{1\downarrow}}{2} \tag{2.27}$$

The MR ratio is thus given by:

$$\rho_\rho = \frac{\rho_P - \rho_{AP}}{\rho_{AP}} = -\left(\frac{\rho_{\uparrow\uparrow} - \rho_{1\downarrow}}{\rho_{\uparrow\uparrow} + \rho_{1\downarrow}}\right)^2 \tag{2.28}$$

The negative sign indicates that the resistivity at saturation state is lower than that at the zero-field state.

2.6 References

[1] E. M. L. L. D. Landau, *Relativistic quantum theory Vol. 4 of Course of theoretical physics*, Pergamon P. Oxford, 1971.

[2] J. H. van Vleck, "On the Anisotropy of Cubic Ferromagnetic Crystals," *Phys. Rev.*, vol. 52, no. 11, pp. 1178–1198, 1937.

[3] L. Néel, "Anisotropie magnétique superficielle et surstructures d'orientation," *J. Phys. Radium*, vol. 15, no. 4, pp. 225–239, 1954.

[4] C. Chappert and P. Bruno, "Magnetic anisotropy in metallic ultrathin films and related experiments on cobalt films (invited)," *J. Appl. Phys.*, vol. 64, no. 10, pp. 5736–5741, 1988.

[5] F. J. A. den Broeder, W. Hoving, and P. J. H. Bloemen, "Magnetic anisotropy of multilayers," *J. Magn. Magn. Mater.*, vol. 93, pp. 562–570, 1991.

[6] M. F. Thomas, J. Bland, G. S. Case, J. A. Hutchings, and O. Nikolov, "Magnetic anisotropy in multilayers," *Hyperfine Interact.*, vol. 126, no. 1, pp. 377–386, 2000.

[7] W. H. Meiklejohn and C. P. Bean, "New Magnetic Anisotropy," *Phys. Rev.*, vol. 105, no. 3, pp. 904–913, Feb. 1957.

[8] J. Nogués and I. K. Schuller, "Exchange bias," *J. Magn. Magn. Mater.*, vol. 192, no. 2, pp. 203–232, 1999.

[9] J. P. King, J. N. Chapman, M. F. Gillies, and J. C. S. Kools, "Magnetization reversal of NiFe films exchange-biased by IrMn and FeMn," *J. Phys. D. Appl. Phys.*, vol. 34, no. 4, p. 528, 2001.

[10] L. Landau and E. Lifshits, "on the Theory of the Dispersion of Magnetic Permeability in Ferromagnetic Bodies," *Phys. Zeitsch. der Sow.*, vol. 169, no. 14, pp. 14–22, 1935.

[11] C. Kittel, "Physical Theory of Ferromagnetic Domains," *Rev. Mod. Phys.*, vol. 21, no. 4, pp. 541–583, Oct. 1949.

[12] O. Céspedes, E. Clifford, and J. M. D. Coey, "Magnetoresistance of magnetite point contacts and nanoconstrictions," *J. Appl. Phys.*, vol.

97, no. 6, p. 64305, 2005.

[13] F. Bloch, “Zur Theorie des Austauschproblems und der Remanenzerscheinung der Ferromagnetika,” *Zeitschrift f{ü}r Phys.*, vol. 74, no. 5, pp. 295–335, 1932.

[14] I. Dzyaloshinsky, “A thermodynamic theory of ‘weak’ ferromagnetism of antiferromagnetics,” *J. Phys. Chem. Solids*, vol. 4, no. 4, pp. 241–255, 1958.

[15] T. Moriya, “Anisotropic Superexchange Interaction and Weak Ferromagnetism,” *Phys. Rev.*, vol. 120, no. 1, pp. 91–98, Oct. 1960.

[16] S. Emori, U. Bauer, S.-M. Ahn, E. Martinez, and G. S. D. Beach, “Current-driven dynamics of chiral ferromagnetic domain walls,” *Nat Mater*, vol. 12, no. 7, pp. 611–616, Jul. 2013.

[17] A. Hrabec *et al.*, “Measuring and tailoring the Dzyaloshinskii-Moriya interaction in perpendicularly magnetized thin films,” *Phys. Rev. B*, vol. 90, no. 2, p. 20402, Jul. 2014.

[18] A. Thiaville, S. Rohart, É. Jué, V. Cros, and A. Fert, “Dynamics of Dzyaloshinskii domain walls in ultrathin magnetic films,” *EPL (Europhysics Lett.*, vol. 100, no. 5, p. 57002, 2012.

[19] K. Yosida, “Magnetic Properties of Cu-Mn Alloys,” *Phys. Rev.*, vol. 106, no. 5, pp. 893–898, Jun. 1957.

[20] W. Thomson, “On the Electro-Dynamic Qualities of Metals:--Effects of Magnetization on the Electric Conductivity of Nickel and of Iron,” *Proc. R. Soc. London* , vol. 8, pp. 546–550, Jan. 1856.

[21] R. I. Potter, “Magnetoresistance anisotropy in ferromagnetic NiCu alloys,” *Phys. Rev. B*, vol. 10, no. 11, pp. 4626–4636, 1974.

[22] R. von Helmolt, J. Wecker, B. Holzapfel, L. Schultz, and K. Samwer, “Giant negative magnetoresistance in perovskitelike La2/3Ba1/3MnOx ferromagnetic films,” *Phys. Rev. Lett.*, vol. 71, no. 14, pp. 2331–2333, Oct. 1993.

[23] M. N. Baibich *et al.*, “Giant Magnetoresistance of (001)Fe/(001)Cr

Magnetic Superlattices," *Phys. Rev. Lett.*, vol. 61, no. 21, pp. 2472–2475, Nov. 1988.

[24] R. Coehoorn, J. C. S. Kools, T. G. S. M. Rijks, and K.-M. H. Lenssen, "Giant magnetoresistance materials for read heads," *Philips J. Res.*, vol. 51, no. 1, pp. 93–124, 1998.

[25] N. F. Mott, "Electrons in transition metals," *Adv. Phys.*, vol. 13, no. 51, pp. 325–422, 1964.

[26] J. Mathon, *Spin Electronics*, Eds., Spri. Berlin, 2001.

III. Universality of AMR in spintronics systems

Despite the enormous market moving around the spintronic technologies, the microscopic understanding of magnetoresistive effects in low dimensional structures has not been fully addressed experimentally so far. Here it is shown that anisotropic magnetoresistance effects are generic notion and that only detailed angular-dependent studies combining magnetoresistive and vectorial-resolved magnetic hysteresis loops provide its origin in spintronic systems. The magnetoresistive response presents different fingerprints that depend sensitively on the details of the magnetic field value and orientation, for both single and multilayered systems, and on the current direction in the case of single films. The data show that the different MR responses at different angles originate from the anisotropic angular dependence of the magnetization reversal, ultimately dictated by the effective magnetic anisotropy of the system. In this sense, systems having a unidirectional magnetic anisotropy contribution show chiral asymmetry in both transport and magnetic behaviours. Remarkably, all this is shown in spintronic systems with magneto-resistive processes of different origin (AMR and GMR) and in ferromagnetic systems of different nature (metallic and oxides). The study illustrates the universality of the phenomenon of anisotropic magneto-resistance in spintronic systems.

The understanding of the magnetoresistance (MR)responses as related to the way how the magnetization reverses in any kind of magnetic material is of great interest, not only for fundamental study, but importantly also for the improvement of the current spintronics technology. Especially in new systems, it results of extremely great importance to disentangle the MR

responses and correlate them to the mechanisms of magnetization reversal. For instance, the actual sensing and storage (recording/reading) devices exploit MR effects, as AMR and GMR, respectively. However, widely different field-dependent magnetoresistive behaviors, including positive or negative MR values and curve shapes, are unexpectedly found for magnetic systems with similar structures.

In this chapter, I will show experimentally that the magnetoresistive signals are imposed by the system magnetic anisotropy and applied current direction in different spintronics systems, as single FM layer, AFM/FM bilayer, and exchange-biased spin-valve. In particular, by measuring simultaneously angular- and field-dependent vectorial-resolved magnetization and MR loops, we can disclose the resistance changes occurring during (and simultaneously to) the magnetization reversal processes.

I will thus show that:

1. The MR behaviors are strictly related to the magnetization reversal pathways. This has been experimentally proven in three model systems: single FM layer, FM/AFM bilayer and spin valve.
2. The unidirectional (one-fold) magnetic anisotropy induces chiral asymmetries in the MR curves around the magnetization hard-axis direction. In particular, I will present the case of exchange-bias FM/AFM bilayer and exchange-bias spin-valve, where even though the MR responses are due to different transport phenomena, namely anisotropic magnetoresistance (AMR) and giant magnetoresistance (GMR), similar (chiral) effects of the unidirectional anisotropy are found.
3. The AMR presents a universal behavior. I will demonstrate this by comparing the MR (and magnetization reversals) responses of a conventional 3d FM and a half-metallic perovskite oxide ($La_{0.7}Sr_{0.3}MnO_3$) thin film. In addition, I will display evidences that by engineering the magnetic anisotropy of$La_{0.7}Sr_{0.3}MnO_3$,it is possible to tune the AMR signal despite other MR contributions (such as, LMR, CMR).

3.1 Angular and field dependent transport and magnetic properties

As I have discussed in Chapter 2, the magnetic anisotropy of a system is due the spin-orbit (SO) interaction[1][2],and its effects influence both magnetic and transport properties. With the aim to improve the signal outputs in spintronics devices, it is important to achieve the full understanding of the MR phenomena, which can be done by correlating the MR responses with the magnetization reversal processes.

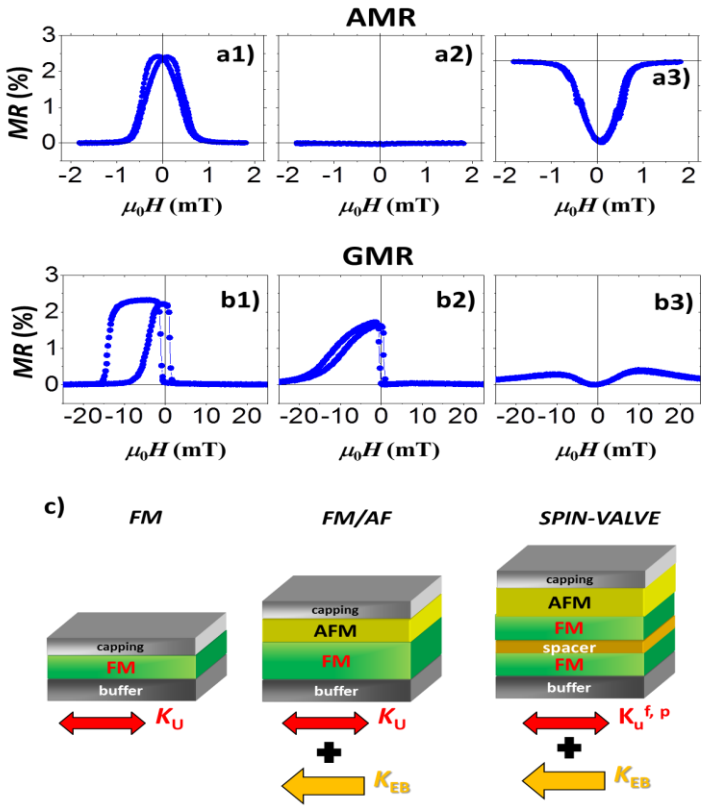

Figure (3.1) Examples of different field-dependent MR behaviors in dingle FM layer with uniaxial magnetic anisotropy and exchange-biased spin valve. The sketches of the structures are shown in panel a. Panels b and c present the AMR and GMR of FM layer and spin-valve respectively. In particular, panels a1-a3 show positive, zero and negative MR changes in single FM layer obtained by varying the relative angle between magnetization M and injected electrical current J. Panels c1-c3 present the case of the exchange biased spin-valve, in which by changing the angle between the magnetization direction of the two FM layers composing the structure (i.e., free and pinned layers) very well defined GMR plateaus or minimum MR changes can be obtained.

We were motivated by the observation of widely different field-dependent magnetoresistive behaviors, including positive (negative) or maximum (minimum) MR values and curve shapes (squared or smooth), even for systems with very similar (if not identical) structures. In Figure (3.1), I present an example of two magnetic systems, namely single FM layer and spin-valve (sketched in panel c), in which the MR signals are dominated by AMR and GMR respectively. In the first case (panel a), we can see that it is possible to obtain positive (a1), zero (a2) or negative (a3) AMR in the same system. In the second (panel b), we can get sharp and abrupt transitions with defined plateaus and maximum MR jumps (b1) or smooth transitions (b2) with minimum MR (b3), again in the same system.

It is clear hence that the MR output, and hence the device performance, can be modified depending on both measuring configuration (direction of the injected current and magnetic field) and magnetic anisotropy of the system under test. With the purpose to disclose the magnetization reversal signatures of the MR responses, I have studied the "model" cases of i) a single FM layer with defined uniaxial (two-fold) magnetic anisotropy; ii) a FM/AFM bilayer where an additional unidirectional (one-fold) magnetic anisotropy is at place and determine a break of magnetic symmetry that results in chiral AMR responses; and iii) an exchange-biased spin-valves, where the MR is due to the spin-dependent scattering in the FM (GMR), but the unidirectional anisotropy imposed by the FM/AFM core determines chiral MR response too.

It is convenient to recall what discussed in Chapter 2 regarding the various MR effects. In particular, AMR(that arises from the SO [3], [2])is proportional to $\cos^2\theta$, with θ being the angle enclosed by the magnetization vector **M** and the injected electrical current **J**. The GMR, instead, is due to bulk spin dependent scattering processes in the FM layers[4]. It follows a cos ϕ law, where ϕ is the angle between the magnetization vectors of two FM layers separated by a NM metal.

3.1.1 Uniaxial system

Let us discuss first the case of a single FM film with defined uniaxial (two-fold) magnetic anisotropy (K_U). The sample, which consists in 10 nm thick FM layer of $Ni_{80}Fe_{20}$ (Py)capped with a 2-nm thick Ta buffer [5], has been grown by dc magnetron sputtering at room temperature (RT) on thermally oxidized Si substrates. To set the uniaxial magnetic anisotropy K_U of the FM layer we

applied an in-plane magnetic field of 200 mT (larger than the anisotropy field H_K) during the deposition. The sketch of the sample structure and its anisotropy configuration are shown in Figure (3.2).

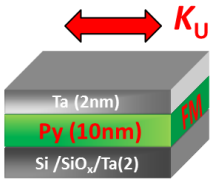

Figure (3.2) Scheme of the FM sample. The structure consists in 10 nm thick FM layer of $Ni_{80}Fe_{20}$ (Py) capped by 2 nm of Ta to prevent oxidation. To set the uniaxial magnetic anisotropy K_U of the FM layer we applied an in-plane magnetic field of 200 mT during the sputtering deposition. Red arrow represents the uniaxial (two-fold) magnetic anisotropy.

The *angular dependence* of the magnetic and transport properties have been studied at RT by means of a home-made magneto-resistance -optical Kerr effect (M(R)OKE).This unique setup (see chapter 1) allows us to determine simultaneously magnetoresistive responses and magnetization reversal processes[6],[7] . The schematic diagram of the set-up is shown in Figure (3.3).M(R)OKE combines the capabilities of both four-probes MR and high resolution vectorial-Kerr techniques [6], [7]. The magnetization reversal processes and the magnetoresistance (MR) outputs are hence acquired simultaneously by measuring in-plane vectorial-resolved magnetization hysteresis loops and the corresponding resistance changes, as function of the sample in-plane angular rotation angle H keeping fixed the external magnetic field direction. $\alpha_H = 0^o$ is taken when the external field is aligned parallel to the direction of K_U, i.e. along the easy-axis (e.a.) of the system. The samples are mounted in a stepper motorized eucentric goniometer head, which ensures a constant plane of reflection for all measurements performed. In magnetoptical measurements this is important to be able to compare the values of the magnetization components measured at different rotation angles and between different samples [8]. The whole angular range was probed every 1.8^o, with 0.5^oangular resolution. To measure MR, we have employed an ac technique varying the applied current direction from parallel to perpendicular to K_U, i.e., $\theta_J = 0^o$ and $\theta_J = 90^o$, respectively.

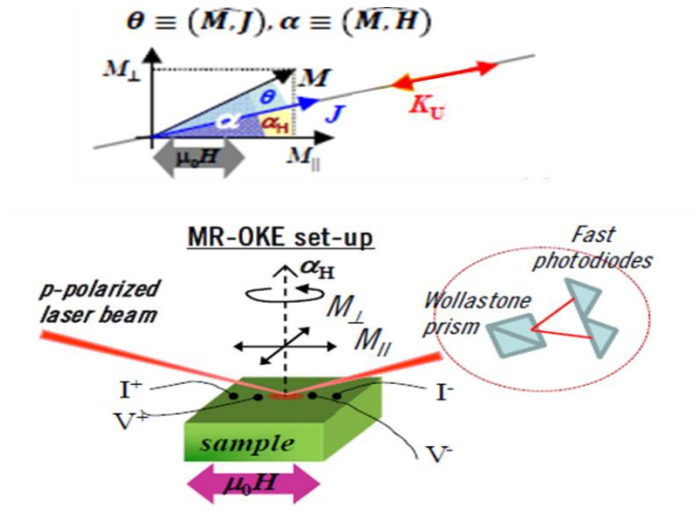

Figure (3.3) Scheme of the experimental configuration. The anisotropy (K_U), current direction(J), external field ($\mu_0 H$), magnetization vector, and magnetization components (parallel, M∥ and transverse, M⊥) are represented with arrows in the top graph. The angles between the external magnetic field and the anisotropy axis (α_H), between the magnetization and the external field, and between the current and magnetization (θ) are also indicated. The bottom panel displays the scheme of the experimental M(R)OKE set-up, which allows magnetic field- and angular- dependent measurements acquiring simultaneously both in-plane magnetization components and the MR signals.

The samples were contacted using Al-wire bonding in four probe current-in-plane (CIP) geometry. The measurements were performed using a lock-in amplifier with an ac current of 50 μA, with a frequency of 33 kHz through a load resistance of RL≈1kΩ, whereas the samples resistance was about 20Ω.$MR(H) = \frac{R(H)-R_m}{R_m}$, where R_m is the resistance at saturation field (sample magnetization aligned to current direction), was hence derived from the experimental R(H) curves [6], [7].The magnetization loops were measured by high-resolution vectorial-Kerr magnetometry by using p-polarized light focused between the inner electric probes and analyzing the two orthogonal components of the reflected light.

The experimental results of angular dependence experiments are conclusive, since they relate clearly the magnetization reversal processes with MR phenomena. In Figure (3.4) a,I show the magnetic hysteresis loops around the magnetization e.a. The black curves represent the field loops of the parallel-to-field (in-plane) magnetization component $M_{\parallel}$ (normalized to the saturation magnetization M_S), the red curves are the normalized

perpendicular-to-field (in-plane) magnetization component $M_{\perp}$. The acquisition of both in-plane magnetization components allows for disclosing the specific magnetization reversal pathways.

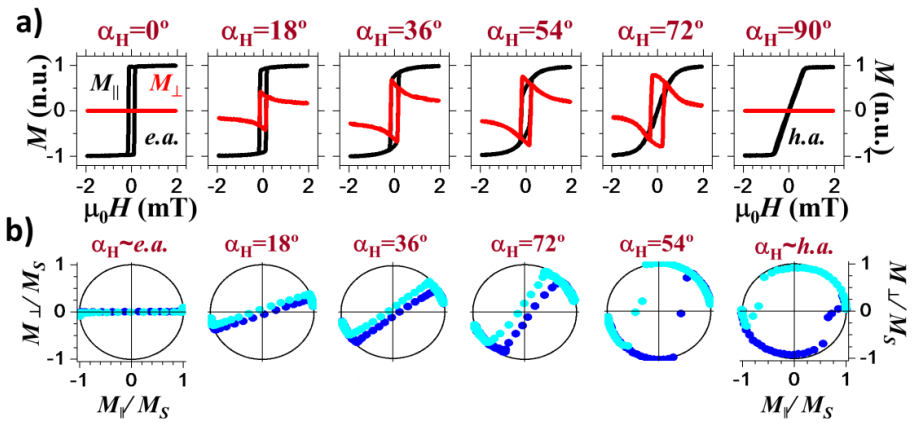

Figure (3.4) Vectorial resolved M-H loops at selected angles α_H from e.a. (α_H=0°) to h.a. (α_H=90°) magnetization direction. In panel a), black curves are the parallel-to-field (in-plane) magnetization component $M_{\parallel}$ normalized to the saturation magnetization M_S, while red curves are the perpendicular-to-field (in-plane) magnetization component $M_{\perp}$ normalized to M_S. Note that the vanishing perpendicular component at α_H=90° turns out after averaging many successive iterations in which for each one the magnetization can rotate along the positive and negative values of $M_{\perp}$. Panel b) presents $M_{\perp}$ vs. $M_{\parallel}$ vectorial-plots at selected angles α_H. These plots allow for directly visualizing the reversal mechanisms: It is clearly seen that the sample magnetization always follows the anisotropy axis: at e.a. the magnetization can only lie parallel to the external magnetic field, whereas close to h.a. $M_{\perp}$ vs. $M_{\parallel}$ presents a quasi-circular loop describing the rotation of the magnetization vector during the reversal.

At the e.a., $M_{\parallel}(H)$ curve presents square loop with sharp transitions at coercive field H_C, whereas $M_{\perp}(H)$ is negligible. This is an indication that the reversals occur via nucleation and further propagation of domain walls and the magnetization switches from one saturated state to the other (parallel to the external field) with no rotation mechanisms. Rotating the sample around e.a. $\alpha_H = 18^{\circ}$ the hysteresis loop sharp transitions looks more reversible, and $M_{\perp}(H)$ starts to show non-negligible variations. This tendency becomes more pronounced when $\alpha_H = 36^{\circ}$and $\alpha_H = 54^{\circ}$, and $M_{\parallel}$ becomes fully reversible near the h.a. The vanishing perpendicular component at $\alpha_H = 90^{\circ}$turns out after averaging many successive iterations in which for each one the magnetization can rotate along the positive and negative values of $M_{\perp}$ .By

looking at the vectorial-plot $M_\perp$ vs. $M_\parallel$ representation in Figure (3.4) b) from e.a. toh.a.at same angles $\alpha_H$than panel a, it is possible to directly envisage the direction of the magnetization vector as well as disclose the reversal mechanisms. The sample magnetization always follows the anisotropy axis: at e.a. the magnetization can only lie parallel to the external magnetic field, whereas close to h.a. $M_\perp$ vs. $M_\parallel$ presents a quasi-circular loop describing the rotation of the magnetization vector during the reversal. The simultaneous transport measurements have been performed for both current parallel (θ_J=0°), and perpendicular(θ_J=90°) to K_U direction, as shown in Figure (3.5) panels b) and c),respectively.

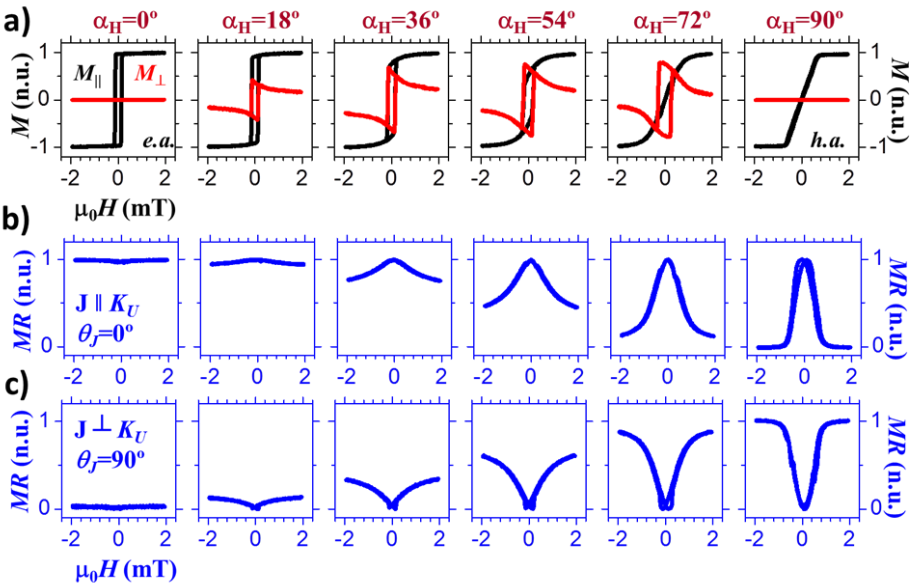

Figure (3.5) Comparison of the vectorial resolved M-H and MR-H loops at selected angles α_H from e.a. (α_H=0°) to h.a. (α_H=90°) magnetization direction. M∥ and M⊥ field loops are shown in panel (a). Panels (b) and (c) show the simultaneous MR-H loops with current flowing parallel to e.a. (θJ=0°) and h.a. (θJ=90°), respectively. M⊥ and M∥ are normalized to M_S and MR to the maximum (2.4%).

From a first view, we notice that the MR-H curves acquired at α_H=0° are flat in whole magnetic loops, whereas present the largest variation at α_H=90°, being the maximum MR jump 2.4%.If the current is injected parallel to the e.a. direction, i.e.,θ_J=0°(b), the maximum MR values is obtained atα_H=0°, i.e., when **J//M**. MR is constant because the sample magnetization is forced, by the intrinsic anisotropy of the system, to be parallel to the external magnetic

field, that is, parallel or antiparallel to the applied current. Increasing α_H, the MR shape changes and decreases smoothly for higher magnetic field. The MR jump becomes larger and larger approaching to h.a. (α_H=90°), where **J**⊥**M**. At h.a. in fact, M rotate sin-plane during the reversal, whereas at the saturation field it points perpendicularly to the current direction. In clear contrast, different behavior is found when **J** is injected parallel to the h.a. direction, i.e., θ_J=90°(panel c). The maximum MR is obtained at α_H=90°, which corresponds to **J**// **M**. The MR curve shows the maximum change at high magnetic field [5],[7], where **M**⊥**J**. Approaching to e.a., MR progressively diminishes and, at θJ=0°, becomes flat assuming its minimum value, i.e., **M**⊥**J**. It is worth noting that the angular-dependent study shows unambiguously that the *MR values* are always comprised within a ***maximum value***, obtained when the ***current is parallel*** to the magnetization direction, and a ***minimum value***, when the ***current and the magnetization vector are orthogonal.*** For a given α_H, the MR maximum value and shape can be controlled therefore by the applied current direction.

3.2 Interfacial exchange-coupling induced chiral symmetry breaking of spin-orbit effects

3.2.1 FM/AFM bilayer

What happened if we induce an additional magnetic anisotropy in our FM system? As we have discussed before, *uniaxial systems* present symmetric magnetization reversal pathways and hence ***symmetric MR responses***. In this sense, a magnetic symmetry breaking could promote non-symmetric reversals and MR responses. The exchange biased systems, where a FM layer is coupled with an antiferromagnet (AFM) layer presents an additional(one fold) unidirectional magnetic anisotropy (K_{EB}) [9], which is generally revealed through a shift of the hysteresis loop of the FM layer[Figure (3.7) central graph of panel a)], called the exchange-bias (EB) field, and an enhancement of the coercivity. From a technological point of view, EB is largely exploited in spintronics because it satisfies the need for stable and controlled MR outputs in magnetic recording, processing, and sensing devices. Systematic studies have shown how this interfacial exchange coupling modifies the magnetization reversal pathways [10][11]. The transport properties have also been studied, but only for several fixed magnetic field values and/or field directions [12].We are going to present that the interfacial exchange coupling

in *FM/AFM systems* strongly influences the SO effects[13], thus promoting ***chiral asymmetric MR responses***, with respect to the h.a. direction, as Figure (3.6) illustrates. Angular- and field-dependent measurements of the MR and the magnetization reversal pathways (measured simultaneously)have been performed, showing the symmetry-breaking of the MR response.

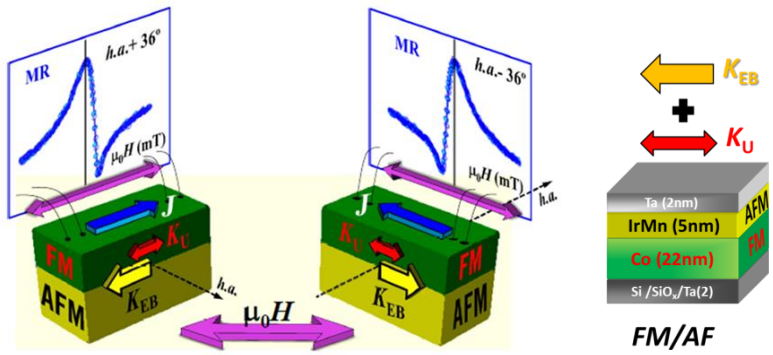

Figure (3.6) Schematic representation of the chiral asymmetric transport behavior in FM/AFM system (as described in the text), which arises from interfacial exchange coupling. The intrinsic (two-fold) K_U and interfacial-induced (one-fold) K_{EB} anisotropies are indicated with arrows. The top graphs display the corresponding MR curves acquired around the h.a. direction.

The sample structure and the anisotropy configuration are schematically represented in Figure (3.6) panel b). The ferromagnetic FM/AFM structures consist in 22nm of Co and 5nm IrMn bilayer. The samples were fabricated by dc magnetron sputtering at RT on thermally oxidized Si substrates and then capped with2 nm thick Ta layer to prevent oxidation. The samples were grown in a 0.2 T in-plane external magnetic field, to promote uniaxial anisotropy (K_U) in the FM layer and to induce a collinear anisotropy configuration in the FM/AFM system, i.e., collinear K_U and K_{EB}. Figure (3.7) compares representative vectorial-resolved magnetization (panel a)) and magnetoresistance (panel b)) hysteresis loops acquired simultaneously at selected α_H around the e.a. At $\alpha_H = 0^o$ (central panel), $M_{\parallel}$-H presents a shifted ($\mu_0 H_{EB}$ = +5 mT) (only difference with FM sample studied previously) squared shape hysteresis loop with a sharp irreversible jump at 7.2 mT, whereas the $M_{\perp}$-His negligible in the whole field loop. Away from the e.a., $M_{\perp}(H)\neq 0$ and reverses only in one semicircle, and above a critical angle, which depends on the ratio K_U/K_{EB}[10], the magnetization reversal becomes fully reversible.

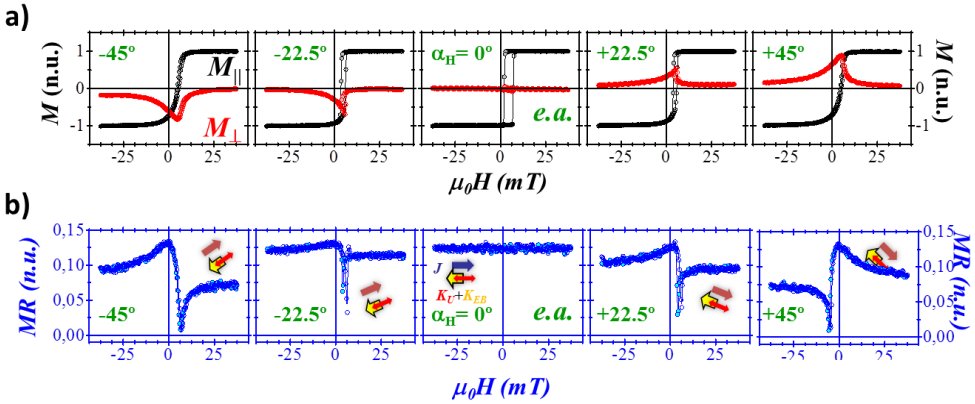

Figure (3.7) Magnetic and transport study at selected α_H around the e.a. direction. The left column panel shows the $M_{\parallel}$/MS and $M_{\perp}$/MS hysteresis field loops whereas the right column panel displays the corresponding MR loops. Solid (open) symbols refer to the descending (ascending) branch. The insets show schematically the specific current-anisotropy-field configuration. Notice the identical behavior of the MR(e.a. ± 22.5◦)-H curves.

Therefore, close to the e.a. direction, nucleation and propagation of magnetic domains are the relevant processes. Panel b) displays the corresponding transport measurements. At the e.a., the MR-H curve is symmetric (and flat) in the whole field loop, whereas non-symmetric curves are found for$\alpha_H \neq 0$. Figure (3.8) shows a similar study close to the h.a. In general, both $M_{\parallel}$ and $M_{\perp}$ loops show smooth reversible transitions, indicating that magnetization rotation is the relevant processes during reversal, so that the angle between M and Jis continuously changing as the field is sweeping. At the h.a. (central graph of panel a), **M** displays a nearby linear behavior, with an anisotropy field $\mu_0 H_K$ = 12 mT, whereas MR shows the maximum variation, which yields 0.13%. In addition, the $M_{\parallel}$-H curve shows rotational symmetry whereas $M_{\perp}$-H and MR-H curves are mirror symmetric with respect to zero field. However, these symmetric features are lost away from the h.a. direction. Around the characteristic directions, different symmetry relationships are identified. For instance, for α_H = ±22.5◦that is, around the e.a.

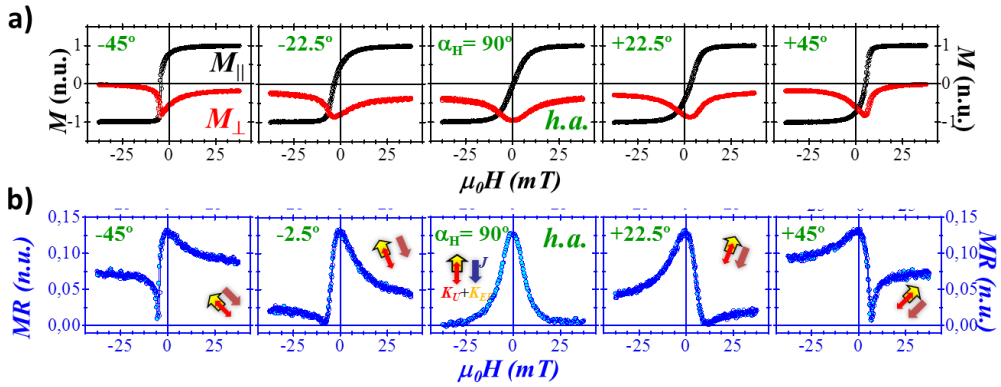

Figure (3.8) Magnetic and transport study at selected α_H around the h.a. with relevant magnetization rotation reversal. The left column panel shows the $M_{\parallel}/MS$ and $M_{\perp}/MS$ hysteresis field loops whereas the right column panel displays the corresponding MR loops. Solid (open) symbols refer to the descending (ascending) branch. The insets show schematically the specific current-anisotropy-field configuration. Note the chiral asymmetry behavior of the MR(h.a. ± 22.5◦)-H curves.

direction (Figure (3.8) panel b)), $M_{\parallel}$ and MR loops display identical field-dependent evolutions, i.e., $M_{\parallel}(\alpha_H,H) = M_{\parallel}(-\alpha_H,H)$ and $MR(\alpha H,H) = MR(-\alpha H,H)$,whereas the $M_{\perp}$ experiences a sign change $M_{\perp}(\alpha_H,H) = -M_{\perp}(-\alpha_H,H)$. In turn, around the h.a. direction, e.g., for$\alpha_H = 90◦ \pm 22.5◦$ [Figure(3.8) panel b)], the hysteresis curves of the parallel component are identical under rotation around the origin, i.e., $M_{\parallel}$(h.a. + 22.5◦,H) = $-M_{\parallel}$(h.a. − 22.5◦,-H), whereas the hysteresis curves of the perpendicular component and the MR display chiral asymmetry, i.e., $M_{\perp}$(h.a. + 22.5◦,H) =$M_{\perp}$(h.a. − 22.5◦,-H) and MR(h.a. + 22.5◦,H) = MR(h.a. −22.5◦,-H). This [two-dimensional (2D)] chiral asymmetry is schematically illustrated in Figure (3.6).The chiral asymmetry is not only found close to the h.a., where the magnetization reversal is governed by magnetization rotation processes, but is extended in the whole angular range.

3.2.2 Exchange-biased Spin spin-valve

With the aim to generalize the chiral effects due the breaking of magnetic symmetry imposed by the additional unidirectional anisotropy, I show the case of an exchange-biased SV in which the MR response has a different origin from the AMR, i.e. it is GMR.

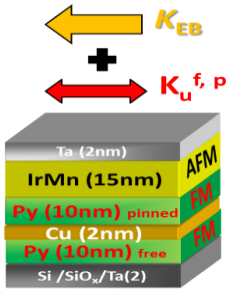

Figure (3.9) Scheme of the spin-valve sample. The structure consists in 10 nm FM layer of $Ni_{80}Fe_{20}$ (Py) as free layer, 2nm of NM Cu layer as spacer, 10 nm FM layer of $Ni_{80}Fe_{20}$ (Py) as pinned layer and 15nm AFM layer of IrMn capped by 2 nm of Ta to prevent oxidation. To set the uniaxial magnetic anisotropy K_U of the FM layers we applied an in-plane magnetic field of 200 mT during the sputtering deposition. Red arrow represents the uniaxial (two-fold) magnetic anisotropy.

As we have seen above, the exchange-biased spin-valve is composed bytwo FM electrodes, one of them pinned with an AFM layer, and separated by a NM spacer [14]. The entire magnetic structure is FM (free)/NM/FM(pinned)/AFM. In these structures, the overall MR response is due to GMR, which originate from the spin-dependent scattering in the FM layers. Therefore, for some specific field values and directions, the free FM layer can reverse its magnetization while the magnetization of the FM adjacent to the AFM remains fixed.[6]

The layer sequence $Ni_{80}Fe_{20}$(9 nm)/Cu(2 nm)/$Ni_{80}Fe_{20}$(9 nm)/FeMn (15 nm) was grown at RT by sputtering on an oxidized Si substrate precovered with a 2nm-thick Ta buffer layer. The structure was then capped with a2-nm-thick Ta layer to prevent oxidation. The sample was heated up to 420 K for 30 min and then field-cooled (FC) to RT in a magnetic field of 250 mT. This procedure locks the magnetization of the pinned-FM layer along the FC direction via the induced unidirectional anisotropy arising from the interfacial exchange coupling with the adjacent AFM FeMn layer, and it defines the magnetization e.a. direction of the system.

By acquiring simultaneously the MR and the magnetization curves for any field value and direction, we can experimentally provide evidence that i) GMR depends on the relative angle ϕ between the magnetization vectors of two FM layers separated by a NM metal, that is GMR ~ cos ϕ; ii) chiral MR asymmetric response are found with respect to the h.a., as we have found in the FM/AFM bilayer.

Let us discuss first the former point. When the magnetic field is applied along the collinear anisotropy axes of the two FM layers, the resulting M-H is loop presents squared hysteresis with sharp and abrupt transition Figure (3.10) upper part). From the curve, it is possible to discriminate two distinctive hysteresis due to the free-FM reversal (with smaller coercivity), and the one due to the pinned-FM shifted towards negative field value ($\mu_0 H_{EB}$ = -7 mT). The simultaneous MR-H loops in panel b, present plateaus and maximum MR changes in correspondence of the antiparallel alignment between the two FM layers (high resistance state), whereas the MR is zero when the magnetization of the FMs are parallel (low resistance state).

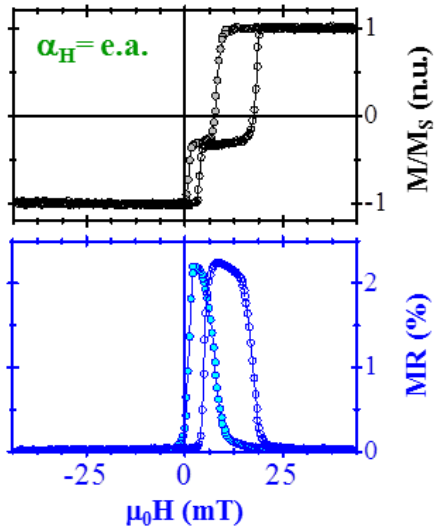

Figure (3.10) Field-dependent MR and magnetization ($M_{\parallel}/M_S$, where M_S is the saturation magnetization) loops of the exchange-bias spin-valve at α_H = e.a. The MR curve presents sharp transitions between low and high resistance states, a well-defined plateaus corresponding to the parallel and antiparallel magnetization configuration of the two FM electrodes, as demonstrating by the simultaneous M-H loop (bottom-panel). In the latter, the hysteresis curve with smaller coercivity is ascribed to the free-FM, whereas the shifted loops is due to the pinned-FM. Filled (empty) symbols refers to descending (ascending) branch.

By applying the external field at 90^o (i.e., at the h.a. of the system) the behaviors of both M-H and MR-H completely change. In contrast to the sharp transitions found around e.a, smoother transitions occur. In fact, at h.a. (Figure (3.11) top panels) the magnetization reversal processes are dominated by rotation mechanisms. Therefore, **M** rotates in plane only in

one semicircle during the reversal, like the FM/AFM system. Panel b presents the simultaneous MR variations. Exactly at h.a., the MR value is minimum since the angle ϕ is continuously changing during the field loop. To note that, around the h.a., e.g.at α_H = h.a.±27◦, ***chiral behavior*** in the GMR are observed.

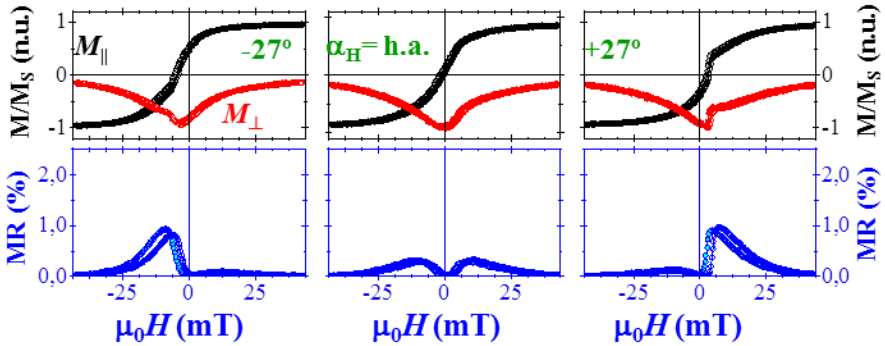

Figure (3.11) Field-dependent magnetization (top-graphs) and MR (bottom-graphs) loops of spin-valve around h.a., i.e. at α_H = h.a.±27◦. In contrast to the sharp transition found in the e.a. region, smoother transitions (in both MR and magnetization loops) become progressively more relevant as approaching to the h.a. direction (reversal dominated by magnetization rotation mechanisms). As consequence ,the maximum MR value is minimum exactly at h.a. Filled (empty) symbols refers to descending (ascending) branch. Note the chiral asymmetry displayed by the MR and $M_\perp$ curves around the h.a., i.e. αH = h.a.±27◦.

Such a chirality is hence due to the symmetry-breaking induced by the unidirectional (one-fold) anisotropy imposed by the AFM layer.

In conclusion, even though the MR output has a different origin from the FM / AFM case (due to AMR), the exchange biased spin-valve, where the MR is GMR, displays similar chiral asymmetric features too. This experimental evidence proves that the chiral asymmetries in the MR response is due to the unidirectional magnetic anisotropy.

3.3 Engineering large anisotropic magnetoresistance in $La_{0.7}Sr_{0.3}MnO_3$ films at room temperature

In section 3.1 I have shown that the mangetic anisotropy dictates the magnetization reversal processes and the AMR. It was discussed for the case of 3d transition metal films, i.e. Py. To generalize the AMR behaviors I consider the case of a half-metallic manganese based oxide epitaxial films,

namely LSMO. I will demonstrate along this section, that apart from its sign (opposite to the metals case), the AMR in manganites behaves similar to the AMR in metals, hence suggesting a similar underlying physics despite the complexity of the magnetic interactions in correlated oxides. In addition, I will show that it is possible to tune the AMR response in LSMO films through the engineering of their (uniaxial) magnetic anisotropy.

Perovskite half-metallic manganites are considered very promising materials for next generation spintronics because of their high spin-polarization (almost 100%) [15] and large magnetoresistance (MR) response [16], [17], [18]. The wide variety of ground states and in most cases the common perovskite structure, exhibited by complex transition metal oxides allows their combination in highly perfect epitaxial heterostructures. Moreover, interesting device concepts have resulted from multilayer structures where half-metallic manganites are combined with other (multi)ferroic layers.[19], [20]. In spite of that, the technological promise of manganite-based devices has not been fulfilled [21], [22], mostly due to the complexity of the physical scenarios governing the interplay between a wide variety of coupled interactions[23]. Harnessing the magnetotransport responses is essential for device design and operation, yet important questions remain on the physical origin of the low-field MR in manganites [24].

In manganites, transport is coupled to magnetism by a double exchange mechanism [25] and by the spin polarized nature of conduction electrons. *Colossal magnetoresistance* (CMR) is very large close to the metal-to-insulating transition (MIT) [16]. Typically it *overshadows* other magnetoresistance contributions such as anisotropic magnetoresistance (AMR) due to spin–orbit (SO) coupling and largely the small Lorentz magnetoresistance[1], governed by the electronic structure (which is several orders of magnitude smaller). In addition, due to the high spin polarization of the conduction band, spin-dependent scattering at grain-boundaries[26], domain-walls [27], and other magnetic inhomogeneities [28], can be significant. Several types of MR concurring the measurements, and generally it is difficult to get a clear picture of its dependence on magnetization and/or current direction. Disentangling the origin of MR in manganites requires clear cut experiments to isolate the various contributions. A problem for the application of the CMR inspintronics is its isotropic character at low magnetic fields. CMR depends monotonically on magnetic field independently of its

direction and as a consequence it is non switchable. This is contrary to AMR which depends on the direction of magnetization with respect to current, and is thus intrinsically switchable and more amenable for spintronic applications. Signatures of switchable magnetoresistance at coercivity in magnetic field sweeps of manganites are typically very weak, and are due to the AMR which is mostly overshadowed by the CMR[26]. For this reason, AMR has remained poorly understood in manganites. However, important applications could be envisaged if we succeed to tailor the nano and microstructure of the sample and to disentangle AMR from CMR. We show that by inducing an extrinsic anisotropy (through the use of vicinal surfaces) a large AMR can be engineered in half-metallic $La_{0.7}Sr_{0.3}MnO_3$ (LSMO) films at room temperature (RT), as schematically shown in Figure (3.12). By combining simultaneous magnetization (vectorial Kerr) and transport measurements, we disentangle the different contributions to the total MR response and demonstrate that AMR is in fact the dominant contribution. As such, it can be tuned in sign and intensity by conveniently choosing the magnetization current configuration.

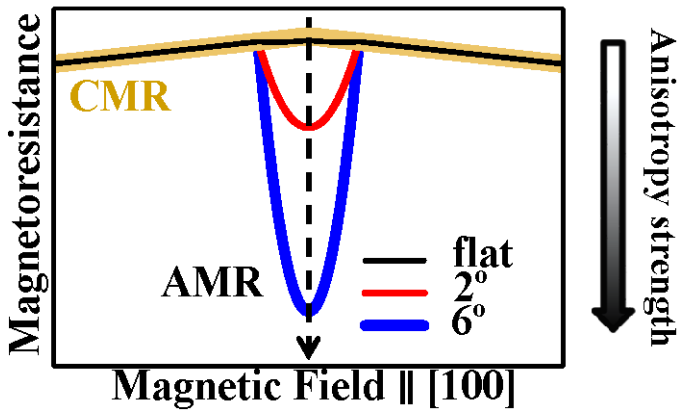

Figure (3.12) Schematic representation of engineering large AMR in LSMO films.By tailoring the magnetic anisotropy strength of LSMO (sidearrow), through the use of substrates with progressively larger miscut angles [from 0◦ (flat) to 6◦], despite the CMR contribution (yellow line) we are able to magnify over one order of magnitude the AMR signal.

AMR results from the SO interaction and its effect on the scattering between carriers and magnetic ions. Therefore, the sample resistivity depends on the angle between the sample magnetization and the applied current. In ferromagnetic 3D transition metal films, the AMR, which is computed as $[\rho_{\parallel} - \rho\perp]/[(1/3)\rho_{\parallel} + (2/3)\rho\perp]$, with $\rho_{\parallel}$ and $\rho\perp$ being the in-plane resistivities for current parallel and perpendicular to the external magnetic field, largely

dominates the overall MR response [1]. The two-current model based on SO interaction[29] that incorporates s–d electron scattering satisfactorily describes the AMR in metals, but it partially fails in reproducing the more complex scenario for manganites. In particular, while the AMR in metals is positive and monotonically dependent on temperature [1], in manganites it is generally found to be negative [26] and non-monotonic [30] with temperature. In the latter compounds, AMR also has its origin in SO coupling ($H_{SO} = \lambda L*S$), [26] although the complex interplay between electron, orbital, spin, and lattice degrees of freedom may affect the properties of the system near the phase transition. In fact, the orbital moment is completely quenched and for symmetry reasons, the matrix elements of the orbital momentum operator functioning on the e_g states are zero (although they can be nonzero for t_{2g} states as in the case of titanates). The SO coupling acts to second order in $\lambda/\delta E$, where λ is the on-site SO interaction of Mn and δE is the excitation (transfer) energy of t_{2g} into e_g levels[26].

In order to engineer a specific in-plane magnetic anisotropy we employed on purpose designed $SrTiO_3$ (STO) (001) vicinal surfaces, with miscut angle of 0◦, 2^o, and 6^o from the [001] toward [100] crystallographic direction, as substrates for the 30nm thick LSMO epitaxial pulsed laser deposition growth. These substrates are intentionally misoriented to a (near) low index surface, thus inducing terraces with edges along the [010] direction. The resulting surface symmetry-breaking favors preferential anisotropy directions, defining a twofold (uniaxial) in-plane magnetic anisotropy along the steps with anisotropy constant K_U.[31]

The LSMO epitaxial thin films, with thickness of 30 nm, were deposited by pulsed laser deposition (PLD) from a stoichiometric target onto STO (001) single crystal substrates. We have employed both flat (with nominal 0º miscut) and vicinal (with miscut of 2º and 6º from the [001] towards [100] crystallographic direction) STO surfaces [Figure (3.13) panel a]. For the LSMO growth we used a laser fluence of 1-2 Jcm^{-2}, target-to-substrate distance of 50 mm, oxygen pressure of 0.35 mbar and substrate temperature of 720 ºC [31]. The crystal structure of the films has been investigated by means of X-ray Diffraction (XRD). Standard θ-2θ scans Figure (3.13) panel b shows the representative case of the LSMO on 6º STO] around the (002) crystallographic peak have been used to determine the out-of- plane lattice parameter (=0.386 nm), whereas the crystalline quality of the films was checked by

measuring the Full-Width-Half-Maximum (FWHM) of the corresponding (ω-scan) rocking curve (=0.14º) [inset of Figure S1(b)]. Measurements of temperature dependent resistivity [ρ(T)], performed in a four-square contacts geometry showed low residual resistivity [ρ(10 K) ≈ 10^{-6} Ωm] (which confirms a high crystal quality) and a Metal-to-Insulating transition (MIT) temperature of ≈ 320 K (Figure (3.13) panel c).

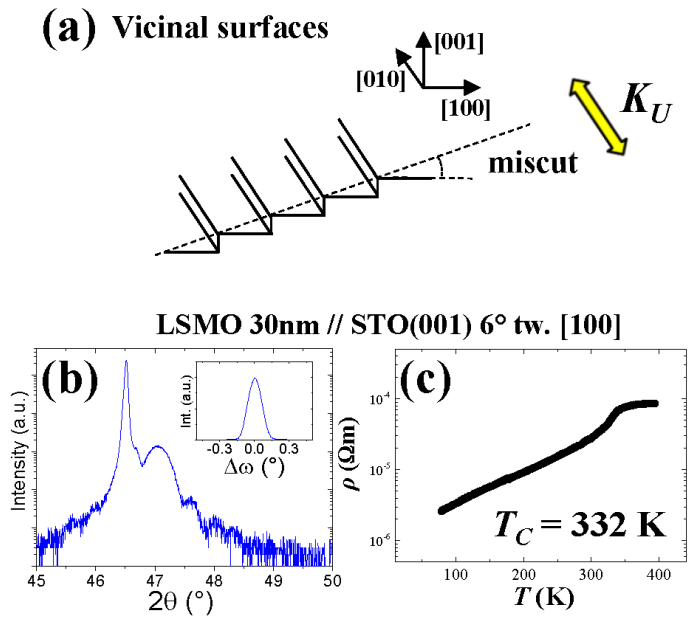

Figure (3.13) a) Structural characterization of 30 nm thick LSMO films grown onto STO (001) surface with miscut angle of 6º surface from the [001] towards [100] crystallographic direction. XRD θ-2θ scans and ω-scan (inset) around the (220) crystallographic peaks. Panel b) shows the dependence of the films resistivity. All films show a Curie temperature above RT.

To investigate the correlation between the magnetic and transport phenomena I have performed measurements of the field driven magnetization and MR loops simultaneously, as done in the precedents sections. The sketches of the LSMO /STO (001) vicinal surface and of the combined vectorial-Kerr and MR measurement configuration are presented in Figure (3.14).

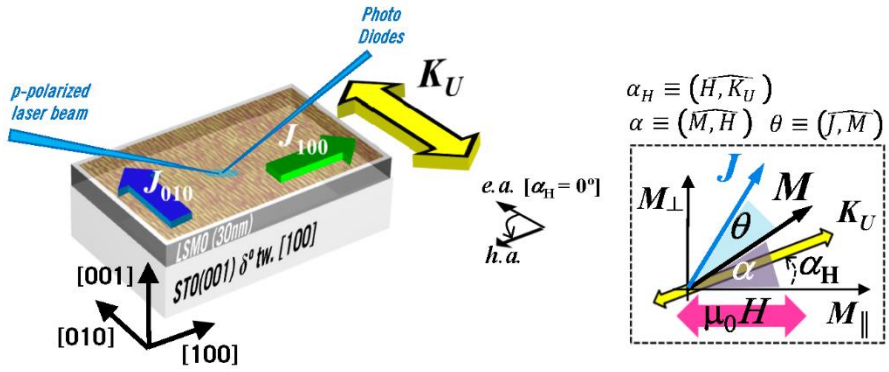

Figure (3.14) Schematic representation of the LSMO film grown onto STO(001) substrate with miscut angle δ◦ = 0◦, 2◦, and 6◦ (from the [001] toward [100] crystallographic direction) and of the combined vectorialKerr and MR measurement configuration. In the left panel, an adapted atomicforcemicroscopy(AFM)image(500×500 μm^2)oftheLSMOvicinal surface that shows typical film grains elongated toward the direction of the substrate step-edges, i.e., along the [010]. The twofold symmetry of the film morphology determines a defined twofold (uniaxial) magnetic anisotropy with anisotropy constant K_U. The magnetization easy-axis (e.a.) is parallel to the [010] direction, whereas the hard-axis (h.a.) results perpendicular to it. In the box, the illustration of the measurements configuration is sketched for clarity.It defines the angles between the magnetic field and the anisotropy direction$\alpha_H \equiv (\widehat{H,K_U})$,the magnetic field and the magnetization of the system $\alpha \equiv (\widehat{M,H})$ (i.e., magnetic torque), and injected current and magnetization $\theta \equiv (\widehat{J,M})$. Note that in our measurements, the magnetic field is kept fixed and the sample is rotated. The two orthogonal in-plane magnetization components are parallel ($M_\parallel$) and perpendicular ($M_\perp$) to the magnetic field *H*.

The electrical current vector has been set either parallel or perpendicular to the anisotropy axis, i.e., J_{010} and J_{100}, respectively. In Figure (3.15), we have compared the RT MR responses (left panel) with the corresponding magnetization curves (right panels) of the LSMO films grown onto substrates with different miscut angles. We clearly observe that by increasing the miscut angle we get an enhancement of the MR signals, with magnetic field applied perpendicularly to the step edges (i.e., along [100]). In particular, the largest MR variation (≈0.28%) was obtainedinthefilmsdepositedonto6◦ miscut substrate (light-blue curve in panel a1), whereas the smallest MR (light-blue curve in panel c1) was measured in the flat films (0^o miscut). The corresponding Kerr rotation field loops (proportional to the parallel

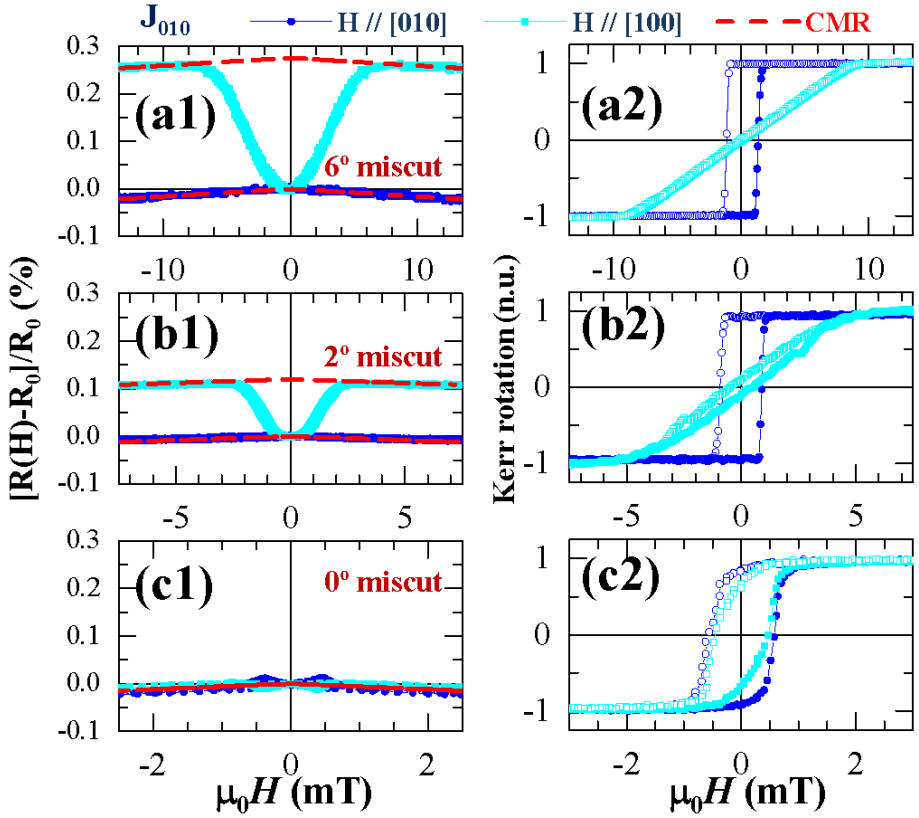

Figure (3.15) Left panels:RT magnetoresistance responses of the LSMO films grown onto a1) 6◦, b1) 2◦, and c1) 0◦ miscut STO (001) substrates with magnetic field applied along the [010] (blue curve) and [100] (cyan curve) direction. The MR curves are obtained by injecting the current along the anisotropy direction, i.e., along [010]. Red dashed curves are the fits of the CMR contribution. Right panels: corresponding M–H loops with magnetic field applied along the [010] (blue curve) and [100] (cyan curve) direction. The anisotropy field HK is measured with magnetic field along the magnetization hard-axis, i.e., the [100] crystallographic direction.

to-field magnetization component) [8] with magnetic field applied parallel (perpendicular) to the step-edges indicate that the films deposited on larger miscut angle substrate, present larger anisotropy field H_K, and larger MR. In contrast, the magnetic anisotropy of LSMO film deposited onto nominally flat substrate (i.e., 0^o miscut) presents a weak magnetic anisotropy at RT, with a total MR one order of magnitude smaller (≈0.03%). The small peaks at coercivity of MR curves in panel (c1) result from magnetization switching under the weak residual fourfold (biaxial) magnetocrystalline anisotropy.[31] From the resistance changes loops in Figure (3.15)withfield applied along the [010] (blue) and [100] (light-blue) of stepped LSMO (panels a1 and b1), it is

possible to envisage two main regimes. At high magnetic fields, the film resistance varies linearly with H ($\propto -\mu_0 H$) independently to the direction of the magnetic field. At low fields, the two curves are completely different: for $\mu_0 H \parallel [010]$ [i.e., easy-axis(e.a.)], R(H) shows the same linear behavior observed at high field, while for $\mu_0 H \perp [100]$ [i.e., hard-axis (h.a.)] it presents a huge variation upon sweeping the field from positive to negative values, being minimum at zero field and maximum at high field ($\geq \mu_0 H_K$). The behavior at high magnetic fields, i.e., a linear drop of the resistivity as the magnetic field increases, is due to CMR effect. It does not depend on the direction of the external field and is maximum at the Curie temperature (above RT in our films). Note that a Lorentz magnetoresistance contribution to the measured MR can be discarded since it may produce a parabolic field-dependent resistance[1] that is not observed in our measurements. The behavior at low magnetic fields is dominated by AMR, which is due to the mixing of spin-↑ and spin-↓ states because of SO interaction. It depends on the relative orientation between the magnetization M and the injected electrical current J, and is generally described by a $\cos^2\theta$,[29] with θ (H) ≡ $(\widehat{M,J})$(H). The sign of the AMR in manganites, which is opposite to what found in 3D ferromagnetic metals, derives from the $L_z S_z$ term of the SO interaction that leads to e_g states splitting. [26] On the basis of aforementioned considerations, since M at the e.a. always lies parallel to the magnetic field (Figure (3.15) a2,b2), the corresponding R(H) (Figure (3.15)a1,b1) should not show any AMR variation (M ∥ J, thus constant AMR). In clear contrast, at the h.a. M rotates during the field loop (M–H is fully reversible), and consequently the AMR contributes the most to R(H) changes. For applied fields larger than $\mu_0 H_K$, M is forced to be parallel to the field and, therefore, perpendicular to J. As the field decreases, the magnetization rotates and the angle θ changes continuously. At zero-field, M is oriented along the anisotropy axis, thus aligned to J. Note that for large magnetic field the CMR has the same slope for any field angle (red dashed line in Figure (3.15)a1,b1,c1). This means that CMR is independent to the field direction, allowing the discrimination from the AMR contribution. It is worth remarking that in the case of flat film (i.e.,0◦ miscutinpanelc1) the AMR is completely overshadowed by the CMR signal. We compare the R(H) curves measured at RT by injecting the electrical current (and probing the voltage drop) in-plane either along the [010] (i.e., parallel to K_U) or along [010] (i.e., perpendicular to K_U), i.e., J_{010} and J_{100}, respectively. This is reported in Figure (3.15) in which we immediately see that: (i) the sign of the resistance variation changes depending on the current

direction; (ii) the CMR contribution does not depend neither to the current nor the field direction. In order to gain further insight into the origin of the magnetotransport properties and to elucidate the role of the AMR in manganites, we have studied accurately the magnetization reversal pathways for any magnetic field values and directions αH ≡ $(\widehat{H, K_U})$.αH =0◦ refers to the external field $\mu_0 H$ parallel to the anisotropy K_U axis (i.e., [010] direction) (see sketch in Figure (3.13)). The magnetization components, parallel ($M_{\parallel}$) and perpendicular ($M_{\perp}$) to the external field, are derived from vectorial-resolved magneto optic Kerr effect measurements.[8] Figure (3.16) shows M– H and MR–H hysteresis loops (acquired simultaneously) at RT for selected directions of the magnetic field, from easy- to hard axis direction of the LSMO film deposited onto 6◦ vicinal STO (001). The CMR contribution ($\propto -\mu_0 H$) has been extracted from the measured MR(H) loops, by fitting the R(H) curves in the linear region obtaining ≈0.04% at 20 mT. In order to isolate the AMR from the CMR, we have subtracted such linear contribution from the MR(H) curves acquired in the whole angular range (Figure (3.15). From a simple inspection of the angular-dependent data, we notice that the MR–H curves change accordingly to the M–H, indicating their intimate correlation with the magnetic anisotropy of the system. We first focus on the field-driven magnetization behaviors in order to understand the influences of the magnetic symmetry on the magnetic properties of our system (Figure (3.16) a,b). Then, we correlate the reversal mechanisms to the MR–H loops (Figure 5c,d).

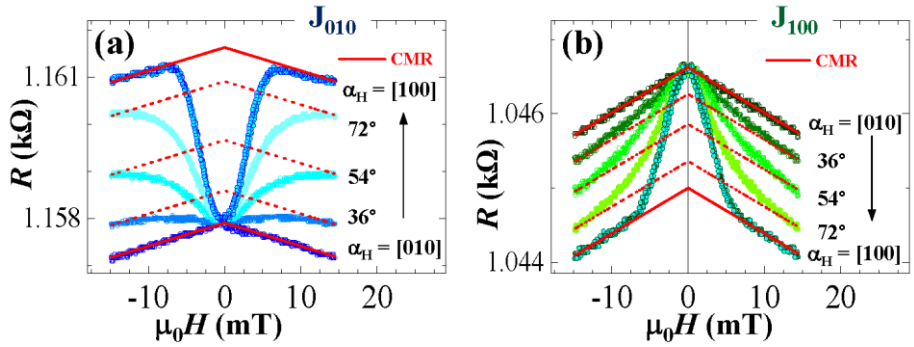

Figure (3.16) MRmeasurementsatRTofLSMOfilmdepositedonto6◦ vicinal STO(001) for different magnetic field directions, from the [010] (i.e., e.a.) to the [100] (i.e., h.a.) crystallographic directions. a) Corresponding to the case of current injected along the [010], J010; b) to the case of current injected along the [100], J100. The red continuous lines are fits of the measured MR in the linear regions, which highlight the CMR contribution. Note that the CMR has the same slope for any field and current direction.

With this aim we use two representations, standard M–H (Figure (3.17) a) and polar $M_\perp$ versus $M_\parallel$ (Figure (3.17) b) plots to identify the preferential magnetization direction, critical fields, domain wall angles, and magnetization reversal processes. Figure (3.17) shows $M_\parallel$–H and $M_\perp$–H loops (normalized to the saturation magnetization MS) for selected directions of the magnetic fieldαH.

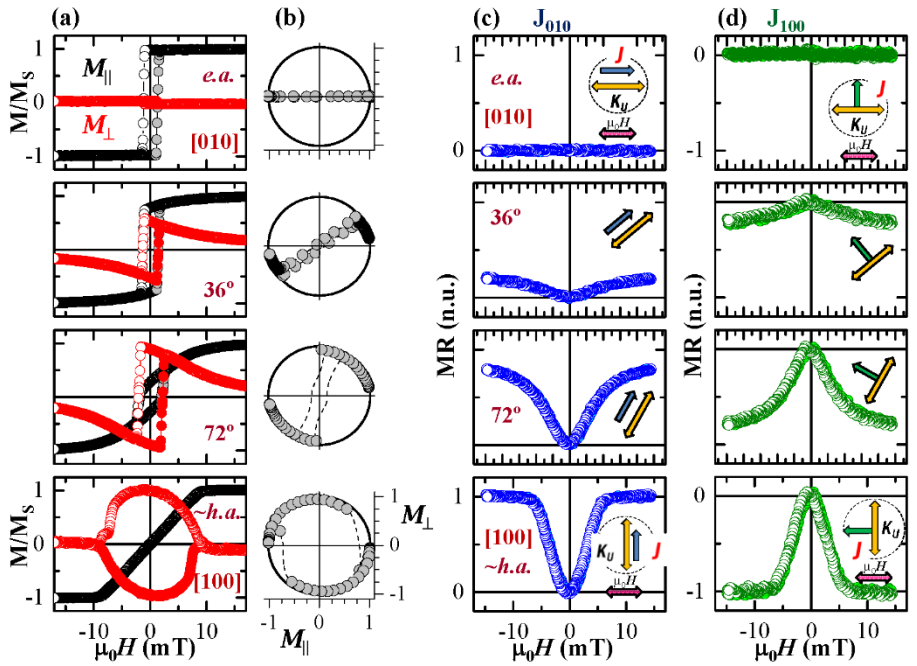

Figure (3.17) Simultaneous RT vectorial-Kerr and low-field MR curves of LSMO film deposited onto 6◦ vicinal STO(001), for selected direction of the magnetic field μ_0Hfrome.a.([010],α_H =0◦)to h.a.([100],α_H =90◦). a) The $M_\parallel/M_S$–H and $M_\perp/M_S$–H loops. At e.a., $M_\parallel$ presents a squared loop with sharp transitions, meanwhile $M_\perp$ is negligible. Approaching to the h.a., smoother transitions in both magnetization components become progressively significant. At the h.a., Mk is fully reversible and $M_\perp$ describes a quasi perfect circle. b)$M_\perp$ versus $M_\parallel$ at the corresponding $\alpha_H$are reported. These plots allow to clearly see that the sample magnetization always follows the anisotropy axis: at e.a., M can only lie parallel to H, whereas close to h.a., it rotates during the reversal. c,d) MR = [R(H) − R_0]/R_0 curves for current injected along the [010] direction, i.e., J_{010}, and along the [100], i.e., J_{100}, respectively. MR curves have been corrected for the presence of CMR (see text). When the field is applied along K_U the MR is constant in both cases, being minimum (maximum) for J_{010} (J_{100}). In both configurations, the largest MR variation occurs when the field is applied perpendicular to K_U (i.e., h.a.) because θ varies smoothly from 0◦ to 180◦. Note that positive and negative MR signals are obtained depending on the magnetization–current configuration.

As mentioned above, exactly at the e.a. (i.e., $\mu_0 H \parallel [010]$, $\alpha_H = 0^\circ$) $M_\parallel$ presents a squared loop with sharp transitions, whereas $M_\perp$ does not vary at all. This is because the magnetization of the system switches from one direction to the other, always following the external field. This is a typical behavior of an e.a. region where the reversal is dominated by the nucleation and further propagation of magnetic domains oriented parallel to the external field.[31] When the field is misaligned with respect to K_U, smoother transitions in both magnetization components appear (e.g., at $\alpha_H = 36^o$ and 72^oin Figure (3.17) a).

These signify that magnetization reversal processes become progressively more significant when approaching to the h.a. In other words, M tries to be aligned to the anisotropy direction, while it is parallel to the external field only if the latter is larger enough (at saturation). Close to the h.a., i.e., $\mu_0 H$ k [100] ($\alpha_H = 90^\circ$), $M_\parallel$ becomes fully reversible (with no hysteresis), whereas M⊥ describes a quasi-circular loop, meaning that magnetization rotation mechanisms are dominating the reversal.[32] The $M_\perp$ versus $M_\parallel$ polar-plots in Figure (3.17) b (normalized to M_S) allow for the visualization of the in-plane trajectory of the magnetization vector during reversal. In this way, the specific mechanism of the magnetization reversal is easily elucidated. The data lying on the circle of unit radius (solid line in panel b), represent rotation processes. Every time the data are off this circle, magnetic domains are present. As the field is decreased from saturation, the magnetization vector rotates reversibly along the circle, except for e.a. The rotation continues for negative fields until a new irreversible process occurs (this is indicated by the deviation from the circle of the magnetization vector). Both departure and return points are close to the anisotropy axis, which mean 180^o reversal. Hence, the sharp transitions correspond to reversal via nucleation of magnetic domains oriented along the anisotropy direction and further 180^o domain-wall propagation. In contrast, at h.a., M describes a quasi-perfect circle proving that the reversal is governed by rotation mechanisms. The corresponding MR curves are presented in Figure (3.17) c,d. Here, MR is defined as $[R(H)-R_0]/R_0$, where R_0 is the resistance at zero field. In panel (c), we show the case of J_{010} injected along K_U (i.e., along the [010] direction); in panel (d), the case of J_{100} perpendicular to K_U (i.e., along the [100]). These two configurations are sketched in Figure (3.13) for clarity. At first glance, we notice that for both current configurations, when the field is applied along the e.a. ($\mu_0 H \parallel [010]$, $\alpha_H = 0^\circ$) MR is constant in the field loop, but minimum

for J_{010} (because M and J are always parallel, as indicated in the side-sketch) and maximum for J_{100} (because M and J are always perpendicular). For $\mu_0 H \parallel$ [100] (i.e., h.a. direction), the MR–H loops show the largest variation (of the whole angular range) in both congratulations, although with inverted sign. These behaviors are due to the smooth changes (from 0◦ to 180◦) of θ (angle between M and J) during the field loop. Therefore, the angular range where magnetization rotation processes are more relevant (i.e., close to h.a. direction) correspond always to the largest MR changes. For the J_{010} case we found MR = +0.28%, while for J_{100} we obtained −0.16%. In summary, the shape of the MR–H loop depends on the specific magnetization reversal pathway, and its value can be tuned from positive to negative by modifying the measuring conditions. For field-direction in which no M rotation occurs (i.e., at the e.a.), the resulting MR is constant, and is maximum or minimum depending on the direction of J. For field-direction in which the magnetization rotates (i.e., away from the e.a.), since the angle between the magnetization and current vectors changes, MR also varies. The largest MR variation is found therefore when the magnetic field is applied along the h.a. direction. In this configuration, in fact, the angle θ varies gradually from 0^o to 180^o during the field loop.

By analyzing the anisotropy induced magnetotransport symmetry, i.e., the field direction dependence of the MR, we finally show that the low-field MR output in our system follows the $\cos^2\theta$ law, i.e., it is due to AMR. The 2D map representation of the angular MR evolution allows a clear picture of the MR dependence with field for both J_{010} (Figure (3.18, top) and J_{100} (Figure (3.18, bottom) current configurations. By cutting the map vertically, we get a MR–H loop at given field -direction, whereas the angular evolution of the low- field anisotropic MR at fixed values of the magnetic field is obtained by cutting the map horizontally. The latter is shown in the insets (c,d) for different field values. For $\mu_0 H > |\mu_0 H_K|$ = 9 mT, the curve resembles the $\cos^2\alpha_H$ behavior [e.g., at $\mu_0 H$ = −13 mT, black-circles in the insets (panels c,d) of Figure (3.18), with inverted sign depending on the chosen magnetization–current configuration. At smaller field (e.g., at $\mu_0 H$ = −3.7 mT, orange-squares in insets) such a dependence is no longer satisfied, similarly to the case of 3D metals,[7] although the $\cos^2\theta$ dependence is still valid.

In conclusion, we have exploited vicinal surfaces to engineer an extrinsic (uniaxial) magnetic anisotropy in LSMO which dominates magnetotransport

at RT. By simultaneously measuring the magnetization and magnetoresistance hysteresis loops we have established the link between magnetization reversal pathways and anisotropic resistance changes. We have found that AMR dominates over CMR and any other spin-dependent contribution due to grain-boundaries, domain-walls, inhomogeneities, etc. Apart from its sign (opposite to the metals case), the AMR in manganites behaves similar to the AMR in metals, hence suggesting a similar underlying physics despite the complexity of the magnetic interactions in correlated oxides.

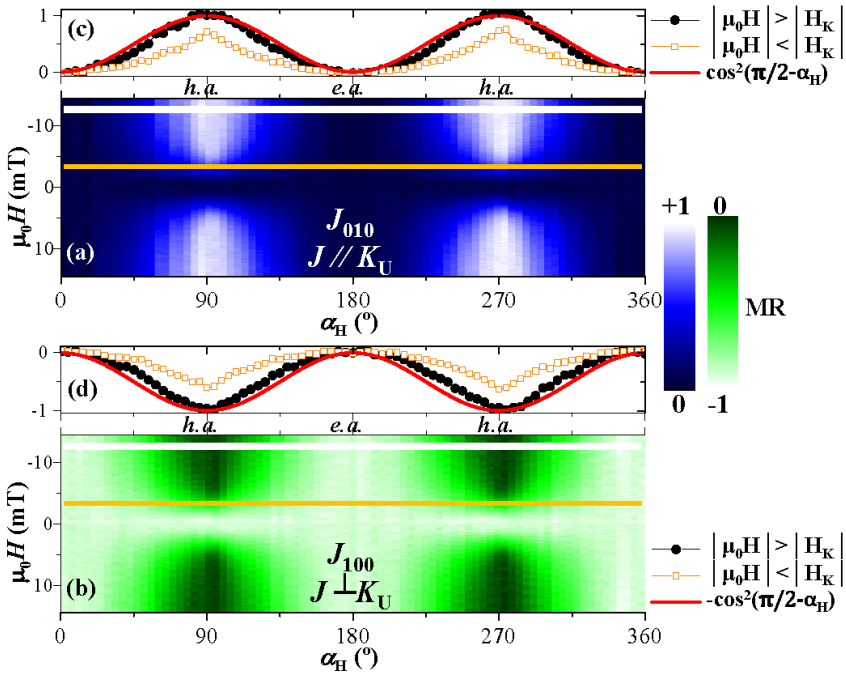

Figure (3.18) 2D map representations of the RT angular evolution of the forward branches of the MR curves of LSMO film deposited onto 6◦ vicinal STO(001). a) The case of current injected along the [010] direction (J010), b) the case of current injected along the [100] (J100). This graphic representation allows the identification of twofold (uniaxial) symmetry with 180◦ periodicity. By cutting the maps horizontally, we get an angular evolution of MR at fixed magnetic field. c,d) By doing so, at field larger than the anisotropy field [μ0H = −13mT,black-circles in insets (c,d)],we obtain a good agreement with cos2αH, whereas for smaller field [μ0H = −3.7 mT, orange-squares in insets (c,d)] such a dependence is not valid.

The ability to engineer a switchable magnetoresistance in manganites at room temperature could open the way to new applications as high-resolution low field magnetic sensors in a future oxide electronics or spintronics.

3.4 References

[1] T. McGuire and R. Potter, “Anisotropic magnetoresistance in ferromagnetic 3d alloys,” *IEEE Transactions on Magnetics*, vol. 11, no. 4. pp. 1018–1038, 1975.

[2] G. W. Fernando, *Metallic Multilayers and their Applications,*. Elsevier, Amsterdam, 2008.

[3] T. R. Mcguire and R. I. Potter, “Anisotropic Magnetoresistance in Ferromagnetic 3D Alloys,” *IEEE Trans. Magn.*, vol. 11, no. 4, pp. 1018–1038, 1975.

[4] C. Dorner, M. Haidl, and H. Hoffmann, “Giant magnetoresistance of Co/Cu multilayers with and without Fe buffer layers,” *J. Appl. Phys.*, vol. 74, no. 9, pp. 5886–5888, 1993.

[5] P. Perna *et al.*, “Interfacial exchange-coupling induced chiral symmetry breaking of spin-orbit effects,” *Phys. Rev. B - Condens. Matter Mater. Phys.*, vol. 92, no. 22, pp. 1–5, 2015.

[6] P. Perna *et al.*, “Magnetization reversal signatures in the magnetoresistance of magnetic multilayers,” *Phys. Rev. B*, vol. 86, no. 2, p. 24421, Jul. 2012.

[7] P. Perna *et al.*, “Direct experimental determination of the anisotropic magnetoresistive effects,” *Appl. Phys. Lett.*, vol. 104, no. 20, pp. 0–4, 2014.

[8] J. L. F. Cuñado *et al.*, “Note: Vectorial-magneto optical Kerr effect technique combined with variable temperature and full angular range all in a single setup,” *Rev. Sci. Instrum.*, vol. 86, no. 4, pp. 1–3, 2015.

[9] J. Nogués and I. K. Schuller, “Exchange bias,” *J. Magn. Magn. Mater.*, vol. 192, no. 2, pp. 203–232, 1999.

[10] J. Camarero *et al.*, “Origin of the Asymmetric Magnetization Reversal Behavior in Exchange-Biased Systems: Competing Anisotropies,” *Phys. Rev. Lett.*, vol. 95, no. 5, p. 57204, Jul. 2005.

[11] E. Jiménez *et al.*, “Emergence of noncollinear anisotropies from interfacial magnetic frustration in exchange-bias systems,” *Phys. Rev.*

B, vol. 80, no. 1, p. 14415, Jul. 2009.

[12] B. H. Miller and E. D. Dahlberg, “Use of the anisotropic magnetoresistance to measure exchange anisotropy in Co/CoO bilayers,” *Appl. Phys. Lett.*, vol. 69, no. 25, pp. 3932–3934, 1996.

[13] A. N. Bogdanov and U. K. Rö\ssler, “Chiral Symmetry Breaking in Magnetic Thin Films and Multilayers,” *Phys. Rev. Lett.*, vol. 87, no. 3, p. 37203, Jun. 2001.

[14] B. Dieny, V. S. Speriosu, S. S. P. Parkin, B. A. Gurney, D. R. Wilhoit, and D. Mauri, “Giant magnetoresistive in soft ferromagnetic multilayers,” *Phys. Rev. B*, vol. 43, no. 1, pp. 1297–1300, 1991.

[15] J.-H. Park, E. Vescovo, H.-J. Kim, C. Kwon, R. Ramesh, and T. Venkatesan, “Direct evidence for a half-metallic ferromagnet,” *Nature*, vol. 392, no. 6678, pp. 794–796, Apr. 1998.

[16] A.-M. Haghiri-Gosnet and J.-P. Renard, “CMR manganites: physics, thin films and devices,” *J. Phys. D. Appl. Phys.*, vol. 36, no. 8, p. R127, 2003.

[17] A. P. Ramirez, “Colossal magnetoresistance,” *J. Phys. Condens. Matter*, vol. 9, no. 39, p. 8171, 1997.

[18] A. M. Haghiri-Gosnet, T. Arnal, R. Soulimane, M. Koubaa, and J. P. Renard, “Spintronics: perspectives for the half-metallic oxides,” *Phys. status solidi*, vol. 201, no. 7, pp. 1392–1397, 2004.

[19] F. A. Cuellar *et al.*, “Reversible electric-field control of magnetization at oxide interfaces,” *Nat. Commun.*, vol. 5, p. 4215, Jun. 2014.

[20] A. Chanthbouala *et al.*, “A ferroelectric memristor,” *Nat Mater*, vol. 11, no. 10, pp. 860–864, Oct. 2012.

[21] C. Israel, M. J. Calderón, and N. D. Mathur, “The current spin on manganites,” *Mater. Today*, vol. 10, no. 10, pp. 24–32, 2007.

[22] S. Gariglio, M. Gabay, and J.-M. Triscone, “Oxide materials: Superconductivity on the other side,” *Nat Nano*, vol. 5, no. 1, pp. 13–14, Jan. 2010.

[23] E. Dagotto, “Complexity in Strongly Correlated Electronic Systems,” *Science (80-.).*, vol. 309, no. 5732, pp. 257–262, 2005.

[24] P. K. Siwach, H. K. Singh, and O. N. Srivastava, “Low field magnetotransport in manganites,” *J. Phys. Condens. Matter*, vol. 20, no. 27, p. 273201, 2008.

[25] C. Zener, “Interaction between the d-Shells in the Transition Metals. II. Ferromagnetic Compounds of Manganese with Perovskite Structure,” *Phys. Rev.*, vol. 82, no. 3, pp. 403–405, May 1951.

[26] M. Ziese and S. P. Sena, “Anisotropic magnetoresistance of thin La 0.7 Ca 0.3 MnO 3 films,” *J. Phys. Condens. Matter*, vol. 10, no. 12, p. 2727, 1998.

[27] J. Wolfman *et al.*, “Large domain wall magnetoresistance up to room temperature in La0.7Sr0.3MnO3 bridges with nanoconstrictions,” *J. Appl. Phys.*, vol. 89, no. 11, pp. 6955–6957, 2001.

[28] R. Di Capua *et al.*, “Direct observation of spectroscopic inhomogeneities on La 0.7 Sr 0.3 MnO 3 thin films by scanning tunnelling spectroscopy,” *J. Phys. Condens. Matter*, vol. 18, no. 35, p. 8195, 2006.

[29] I. A. Campbell, A. Fert, and O. Jaoul, “The spontaneous resistivity anisotropy in Ni-based alloys,” *J. Phys. C Solid State Phys.*, vol. 3, no. 1S, p. S95, 1970.

[30] I. C. Infante *et al.*, “Anisotropic magnetoresistance in epitaxial (110) manganite films,” *J. Appl. Phys.*, vol. 99, no. 8, p. 08C502, 2006.

[31] P. Perna *et al.*, “Tailoring magnetic anisotropy in epitaxial half metallic La0.7Sr0.3MnO3 thin films,” *J. Appl. Phys.*, vol. 110, no. 1, p. 13919, 2011.

[32] S. J. Zhu *et al.*, “Exchange bias effect and enhanced magnetoresistance in La0.67Sr0.33MnO3/SrTiO3 superlattices,” *Appl. Phys. Lett.*, vol. 90, no. 11, p. 112502, 2007.

IV. Tuning chiral effects in PMA metallic trilayers systems

A new branch technology that exploits the creation and displacement of chiral domain walls (DWs) induced by spin-orbit coupling (SOC) effects has been proposed recently its potential for next generation magnetic-based information technology applications, promising smaller sizes, higher speeds, and lower power consumption. Here it is presented the first steps to engineer interfacial SOC chiral effects in multilayered perpendicular magnetic anisotropy (PMA) metallic systems by using asymmetric interfaces and by tuning PMA and an effective interfacial (chiral) Dzyaloshinskii-Moriya interaction (DMI). These spin-orbitronic systems combine ferromagnetic (FM) films and heavy metals (HM) with large SOC. A detailed study of the influence of the buffer layer, number of repetitions, FM thickness, and HM type has been carried out in multilayer stacks, mainly asymmetric HM1/FM/HM2 trilayers. Averaged and imaging information derived from different magnetometries have been used to identify the parameters controlling both PMA and DMI.

The actual technology for magnetic data storage is based on rotating magnetic hard drives which are intrinsically limited in speed and dimension. To fulfill the industry demand of smaller, faster devices with reduced power consumption, novel concepts of apparatus with improved capabilities have to be designed.

Some years ago, a new spintronics technology that exploits the domain walls (DWs) creation and displacement demonstrated its potential for next generation of magnetic read/write and processing applications[1]. Compared with the traditional technology, researchers are now able to nucleate DWs in specific positions (mainly by resorting to nanoconstrictions) and to move them using relatively small spin-polarized current pulses at velocities a few

hundreds of m/sec. However, such a promising technology is not yet mature for market since many drawbacks as reliability and complexity of structures (requiring nanolithography processes) has hard solutions. A new strategy relying on Néel-type Chiral DW stabilized by the Dzyaloshinskii-Moriya interaction has been proposed in order to achieve high speed and low consumptive devices. As discussed in the precedents chapters, the DMI is originated by the SOC[2]at the interface between a ferromagnetic material (such as Co, Fe, Ni…) and a heavy-metal (e.g., Pt, Ir…). It worth notice that the nucleation and stability of DWs depend strongly on a subtle balance between magnetic anisotropy (PMA) and DMI [3][4] (which are both due to SOC). In the following, I will discuss on the different strategies adopted in this thesis to obtain optimized chiral Néel-type DWs, and on the possibility to tune their speed by employing different stacks (i.e., with different DMI). In view of the large DMI of some of these materials, they are also good candidates to contain magnetic skyrmions, which are magnetic stable chiral features recently placed in the center of the magnetic research[5] A series of thin film systems, in which the magnetic layer is deposited on top of a thick Pt layer with (111) texture have been grown, in order to study the effect of anisotropy and DMI on the domain wall dynamics. In addition, we have focused on epitaxial structures (with controlled interface/surface) canceling out (or at least minimizing) spurious effects due to disorder.

In this chapter, I discuss on the possibility to tune both PMA and DMI and thus how to engineer chiral DWs and improve its motion. In particular, I focus on:

1. Polycrystalline magnetic structures in which the PMA has been tuned by varying thickness of a Ta buffer and the number of the stack repetitions (n=2, 6, 10, 12…).
2. Epitaxial symmetric (NM1/FM/NM1) and asymmetric (NM1/FM/NM2) trilayers, with controlled interfaces and different DMI, grown onto (111)-orientated MgO substrates.

Determination of DMI effective values and sign of chirality of DWs in polycrystalline and epitaxial structures.

4.1 Tuning Perpendicular Magnetic Anisotropy in thin film systems

FM thin films with PMA have been widely investigated for practical applications in nanoscale spintronic devices such as spin-transfer-torque magnetic random access memories (STT-MRAMs). PMA-based systems were demonstrated to have great advantages over the in-plane ones for real applications, because they normally display strong thermal stability,[6], low critical switching current density [7]and more efficient current-induced DWs motion [7]. To keep the magnetization of the system out-of-plane and in remanence, it is required strong enough PMA in order to overcome the shape anisotropy of the thin film[8] (see Chapter 2 Section 2.2.2 eq. (2.7)).Such a strong PMA can be achieved by engineering (ultra) thin films with symmetric interfaces (e.g. [Co/Pt]n multilayers) with Co layer thickness typically limited to a range of 3-7 Å[9][10].In the 90s, Ferré *et al.*or Rodmarcq *et al.*found an increase of the magnetic volume extending vertically through the multilayer, in Pd/Co, Fe/Cr *etc*. As result, a huge magnetic signal was obtained, favoring therefore the detection of the magnetic properties and the presence of PMA.

4.1.1 Polycrystalline samples

The polycrystalline samples described in this section are all fabricated by dc magnetron sputtering in high-vacuum (with base pressure of $\sim 3\times10^{-8}$mbar, sputtering system described in Chapter 1) and grown onto precut Silicon substrates with $\sim 5\times5$ mm^{2}dimension. The commercial Si wafer present <100> orientation and an oxide layer 285nm thick. Before the insertion into the vacuum chamber, the substrates were routinely cleaned by acetone and isopropanol in an ultrasound bath and dried with Nitrogen. All the metallic layer (Pt, Ta, Co, Ir, ...) were grown from polycrystalline commercial targets by dc magnetron sputtering. We used a partial Ar pressure in the range of2-8×10^{-3}mbar, parallel face-to-face target and substrate configuration (target-sample distance was kept at 5 cm). The deposition rates were calibrated for every material prior the deposition.

PMA vs. Ta buffer layer in Pt/Co/Pt trilayers

As described in the Chapter 2, the magnetic anisotropy depends strongly on the FM layer thickness and its crystallographic orientation. In ultra-thin FM films, in fact, the surface anisotropy term overcomes the volume anisotropy in Equation 2.7, thus favoring a perpendicular alignment of the magnetization. In addition, the increase of PMA can be achieved by the

presence of a Pt (111) [11][12] and Ta (111)[7]seed layers that induce a preferential (111) orientation for the Co deposited on it.

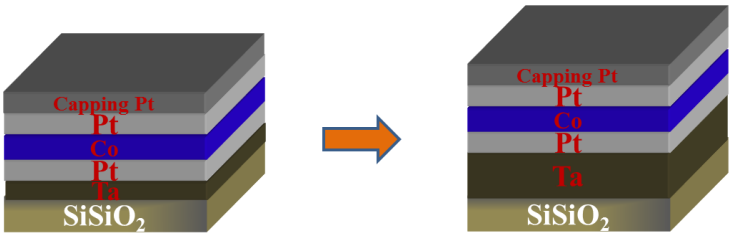

Figure (4.1) Illustration of the sample structures used in this section. The Pt/Co/Pt stacks are deposited onto Si-SiO_2 (285nm)substrate with a T abuffer layer with thickness of 3, 5, 10, 15nm.

In order to achieve strong PMA, we have employed the structures illustrated in Figure (4.1). The Pt (2nm) /Co (0.8nm) /Pt (4nm) stacks have been deposited onto commercial Si substrates with controlled 285nm thick SiO_2. To tune the PMA we have inserted a Ta buffer layer with different thickness (i.e., 3, 5, 10 and 15nm). The stacks were finally capped with 2 nm Ta to prevent oxidation/contamination.

With the aim to study the field-dependent magnetization reversals and to evaluate the magnetic anisotropy we have acquired M-H loops with the external magnetic field applied along the normal-to-sample surface direction ($\hat{z}$) by Kerr magnetometry in polar configuration(the set-up has been described in Chapter 1 section 1.2). In this geometry, the Kerr rotation is directly proportional to the magnetization component along $\hat{z}$, i.e. M_z.

In Figure (4.2), I show the dependence of the hysteresis loop shapes as function of Ta thickness (scheme in Figure (4.1). The structure with the thinnest Ta buffer presents fully reversible magnetization reversal, whereas the ones having thicker buffer show squared loops and progressively sharper transitions, which indicates a stronger perpendicular anisotropy. Panel d)

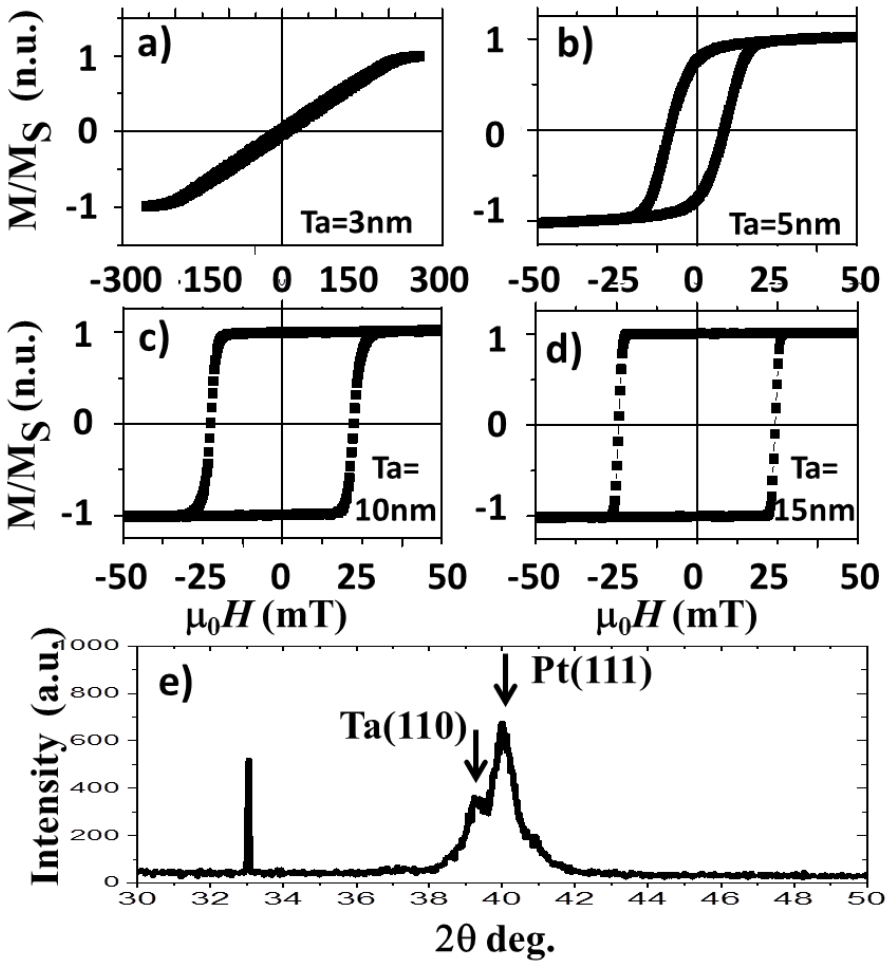

Figure (4.2) Polar Kerr hysteresis loops of stacks with different thickness of the Ta buffer. Panels a-d) present vectorial resolved Mz-Hz loops normalized to the saturation magnetization M_S with a) 3nm, b) 5 nm, c) 10 nm, and d) 15 nm thick Ta buffer. To note that fully reversible magnetization reversal is obtained for the thinnest Ta layer, whereas squared loop with sharp transition is found for the thickest case. Panel e) shows θ-2θXRD measurement around the (111) crystallographic peak of the Pt of sample with 5 nm buffer layer.

displays finally θ-2θ XRD measurement around the (111) crystallographic peak of Pt. The data indicates a dominant (111)-texture in all samples, with a minor contribution of the (110) phase of Ta (peak centered at 39.2º) [13]. The peak at the left side is due to the Si (100). A careful observation of the hysteresis loops we can argue that samples with reduced Ta thickness present lower perpendicular anisotropy, which can be ascribed to a poorer

interface. In fact, larger coercive fields and remanence magnetization is found for the systems with 10 and 15 nm thick Ta buffer, whereas the 3 and 5 nm thick samples present smoother transitions. Even though more experiments are needed to elucidate the weight of crystallographic phases and the roughness of each interfaces, it is clear that a strong anisotropy is achieved by increasing the Ta buffer up to 15 nm. This was the purpose of this study.

PMA vs. number of repetition in Pt/Co multilayers

We have shown that the hysteresis loop shapes and, as consequence, the anisotropy fields, can be varied by modifying the buffer layer thickness while keeping fixed the (symmetric) trilayer structure. What happens in [Pt/Co]x (with x being the number of repetition) stacks? In these systems (sketched in Figure (4.3)a), the Co layers are ferromagnetically coupled via the Pt ones.

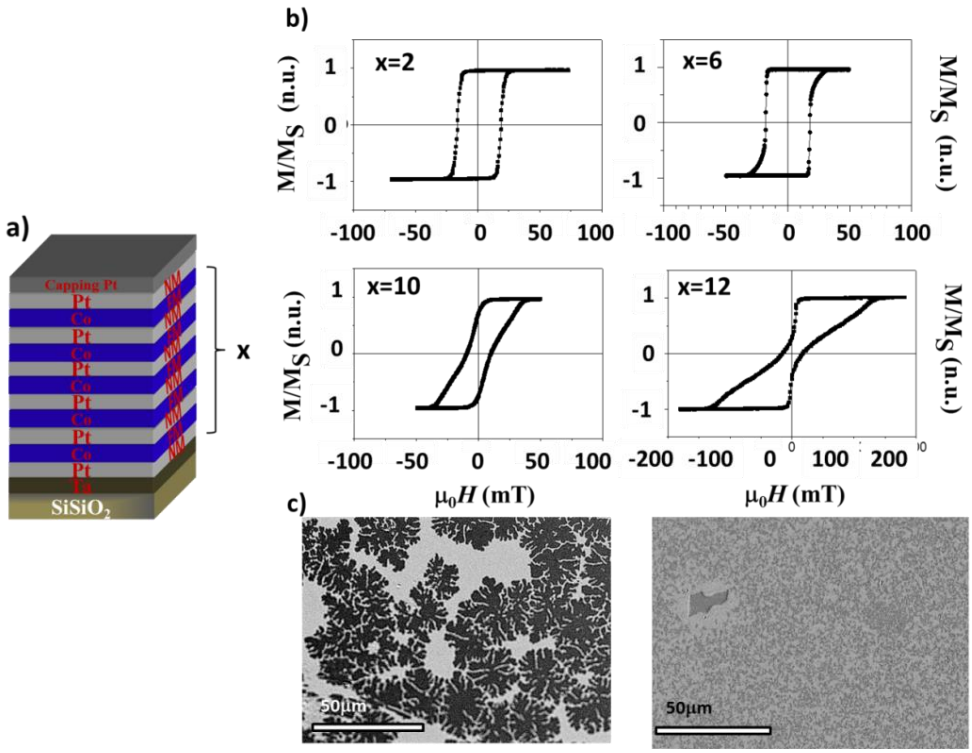

Figure (4.3) a) Scheme of sample. The structure consists in $SiSiO_2$ substrate with varying the number of repetitions $[Co(0.6nm)Pt(1nm)]_x$ b) MOKE hysteresis loops of perpendicular multilayers for different number of repeats x as indicated in the plots. c) MOKE microscopy images of sample with x=2(left), and with x=12(right). In both cases the dendritic expansions of DW with large size for x=2.

The balance between exchange anisotropy [14] and dipolar energies determines PMA, and often results in stripe domain patterns as first described by Kittel [15].This has also an effect on the magnetization reversal processes and on the nature of domain formation. In Figure (4.3)b, I present M-H loops of [Co(0.6nm)/Pt(1nm)]x multilayers with a progressive larger number of repetitions (x). The stack with x=2 shows a square hysteresis loop with sharp transitions. Increasing the number of repetitions, the loops present progressively smoother (and rounded) transitions accompanied by smaller coercive fields. The changes in the reversal processes are reflected in the magnetic domains arrangements as demonstrated by the polar Kerr microscopies in panel c. The latter are performed in the remanence magnetization state of samples with x=2 (left image) and x=12 (right image). The black/white contrast indicates magnetic domains oriented parallel or antiparallel to the external magnetic field (applied along the normal-to-sample surface direction). From the microscopies, it appears clear than smaller up/down magnetic domains are obtained increasing the number of repetitions. In the following I will make use of single crystal oxide substrates with (111) crystallographic orientation in order to fabricate epitaxial structures with larger PMA strength and better interface properties than the polycrystalline samples. Moreover, with the aim to isolate the contribution of DMI coming from the interfaces with Co, I will focus onto trilayer systems only where the Co is sandwiched between two identical or different non-magnetic metals.

4.1.2 Epitaxial PMA stacks

It is worth noting that the interface anisotropies observed for samples grown on single crystals are generally larger than those observed for polycrystalline samples. This indicates the importance of the interface quality. A novelty introduced in this study, is the selection of commercially available (111)-oriented MgO oxide single crystals, instead of metallic buffer single crystals. This isolated substrate allows us to develop future experiments passing current through the sample, avoiding the substrate current leaks.

Growth process

The fabrication of high quality epitaxial PMA stacks is slightly more complex than the one used for polycrystalline samples. I have employed a three-step process that consists in the:

- Growth of epitaxial metallic Pt(111) buffer at high temperature.
- Growth of epitaxial NM1, FM, NM2 sandwiches at RT on the Pt buffer.

Deposition of capping layer.

Substrate characterization

I have used commercial Magnesium oxides (MgO) and strontium titanates (STO) ($SrTiO_2$) with (111) orientation or sapphire (Al_2O_3) with hexagonal (0001) as substrates for the PMA stack epitaxial growth. The quality of these oxides in fact is generally good, with atomically flat surface and with average roughness typically of the order of few unit cells. In particular, along this thesis I will focus on the MgO (111). It consists of a lattice of Mg^{2+} ions and O_{2-} ions held together by ionic bonding. The surface is quite unstable [16] in (111) orientation with characteristic stacking (abc) FCC along the [111] direction. In Figure (4.4) panel a) is shown a schematic crystal, top and side

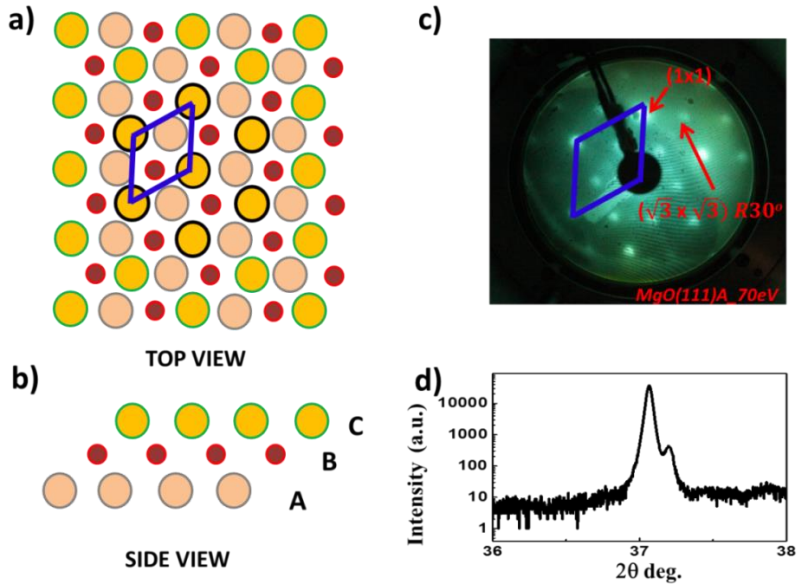

Figure (4.4) a) Top view of an ideal MgO(111) crystallographic plane, where the oxygen surface layer is represented with orange spheres, whereas red spheres correspond to Mg second layer and pink spheres to bottom oxygen layer. Blue lines represent the 1x1 unit cell. b) Side view of the FCC (111) with ABC staking. c) LEED patterns of MgO(111) substrates. The six spots of top oxygen layer more brilliant at 70eV. Blue line represents the 1x1 unit cell. The second layer of the Mg atoms is rotated by 30°, which corresponds to a √3 x √3 electronic reconstruction. d) θ-2θXRDmeasurements performed around 37°showing the (111) crystallographic peak of MgO.

(panel b)) view. The 1x1 unit cell with lattice parameter a = 0.4212 nm is marked with a blue line. The top O^{2-} layer is represented by orange spheres, remarked with black line the pattern LEED. The substrates used in the following experiments were 10 mm thick, 5 x 5 mm^2 pre-polished MgO (111) oriented single crystals of Crystal GmH Company. The LEED pattern of the single crystal showing the six spots of the (111) plane (1x1) is depicted in panel c).The picture shows at 70eV the principal spots O_{2-} belong to the top layer are surrounded by six additional spots ((√**3** x √**3**) R30º) turned 30 degrees belong to Mg^{+} of the second layer. [17] Panel d) shows the θ-2θXRD spectrum of the (111) crystallographic peak of MgO. The narrow peak centered at 37º confirms the good crystallinity of the substrate. Before its insertion in UHV, the substrates were routinely treated ex-situ at high temperature in a controlled air-atmosphere. This thermal treatment, performed in quartz cylinder oven at 800°C during 1 hour, improved the surface morphology as demonstrated by atomic force microscopy (AFM) study. The result of the annealed surfaces is shown in Figure (4.5) panel b).

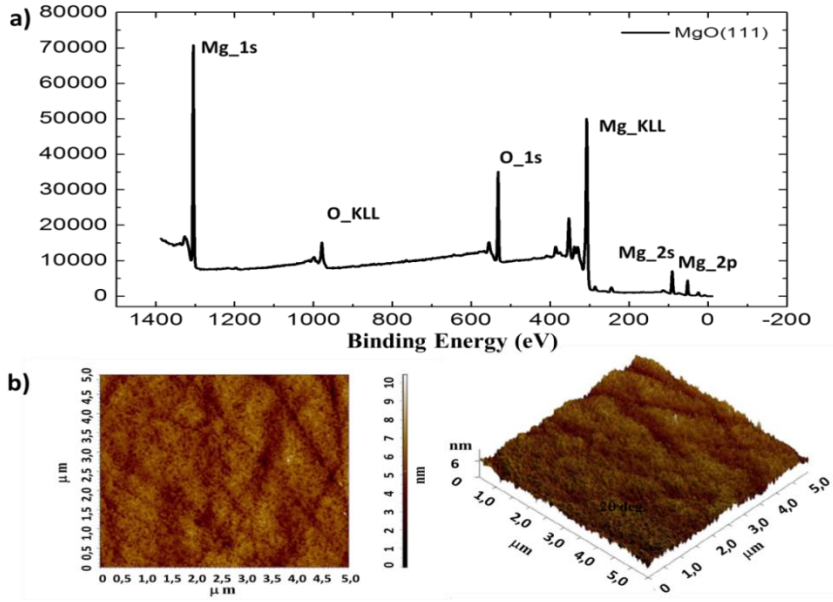

Figure (4.5) a) XPS Survey spectrum of MgO(111) substrate. The chemical composition analysis shows the presence of Mg and O atoms. b) AFM image of 5x5µm^2.of MgO(111) substrate after heat treatment. The contrast covers amplitude variation in the 1-5nm range showing flat terraces and deep scratches. The root mean square (rms) surface roughness of 0.5 nm. The AFM measurements were performed at IMDEA by Patricia Pedraz and Almudena Inchausti.

10 x 10 μm^2 roughness plot, reveal smooth surfaces with a root mean square (rms) surface roughness of 0.5 nm for the (111) face. There are big flat plateaus and deep dislocations. The electronic and chemical surface analysis was performed by XPS measurements Figure 4.5 a). The survey spectrum after the thermal treatment shows indicates a free of contaminant surface of the MgO substrates.

Buffer layer

The substrates were glued to the molybdenum plate with carbon paste without OH solvents to homogenize the heat transfer through the plate in contact with the sputtering heater system [chapter 1]. The deposition of the buffer layer of Pt was performed at high temperature in the sputtering chamber (T $\cong 450^{o}C$) (Figure (4.6) panel b). After one hour of heat treatment at $450^{o}C$, 30 nm of Pt has been deposited by dc magnetron sputtering using$6x10^{-3}$ mbar Ar+ pressure and 20W magnetron power. The layer thickness was routinely calibrated by a quartz balance (QB) installed in the sputtering chamber. Once the buffer was deposited, I checked surface quality in-situ by low electron energy diffraction technique (LEED). LEED patterns acquired in the same condition of MgO(111) and MgO(111)/Pt are shown in panel a), left and right picture respectively. After the deposition (right image), the spots appear better defined, indicating good surface quality with hexagonal reconstruction. In contrast, the spots are larger for the single crystal (left image) suggesting a poorer reconstruction (more disorder surface). In addition, the distance between the peaks is larger in the substrate, suggesting that the Pt lattice parameter is smaller than the one of the MgO(111). In the next chapter I will discuss more in detail the crystal properties of Pt(111) on MgO compared to the Ir(111) case. [Chapter 5]

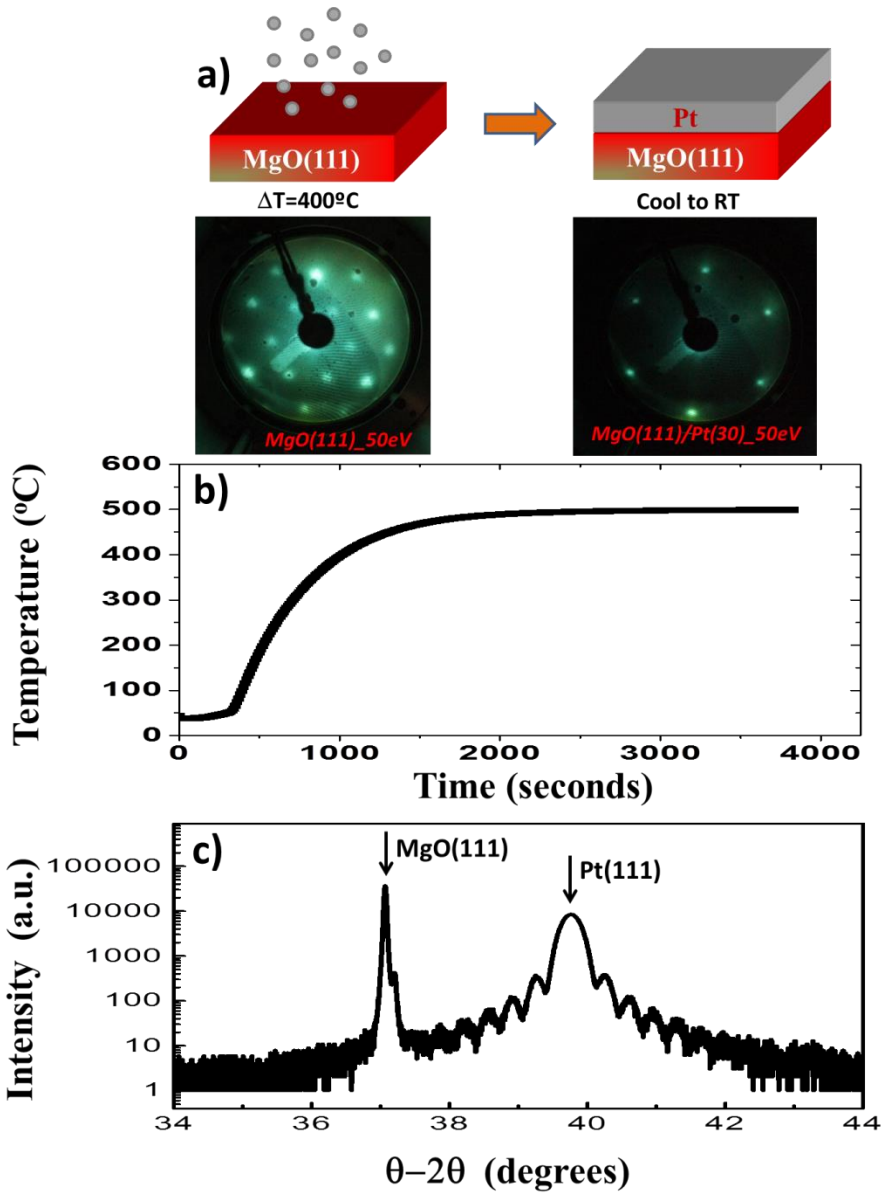

Figure (4.6) a) (Top) Schematic process of Pt layer growth. (Bottom) LEED patterns of MgO substrate (left) and Pt (111) layer (right). b) Ascending temperature ramp during the annealing. c) XRD theta 2theta scans around the FCC (111) Bragg-peaks of sputtered Pt/MgO(111) with pure [111]-growth. The XRD measurements were performed at CNRS-GREYC lab in Caen by Sandeep Kumar Chaluvadi.

Panel c) shows θ-2θXRD scans covering the region of the FCC Pt(111) crystallographic peak. It results clear that only a single-phase FCC with [111]

orientation is present, with no other structural domains coexisting. The other intense peak belongs to the MgO(111) substrate.

RT depositions

To avoid intermixing in the trilayer, the NM1/Co/NM2 sandwiches were deposited at RT.(Figure (4.7)upper part of panel a))

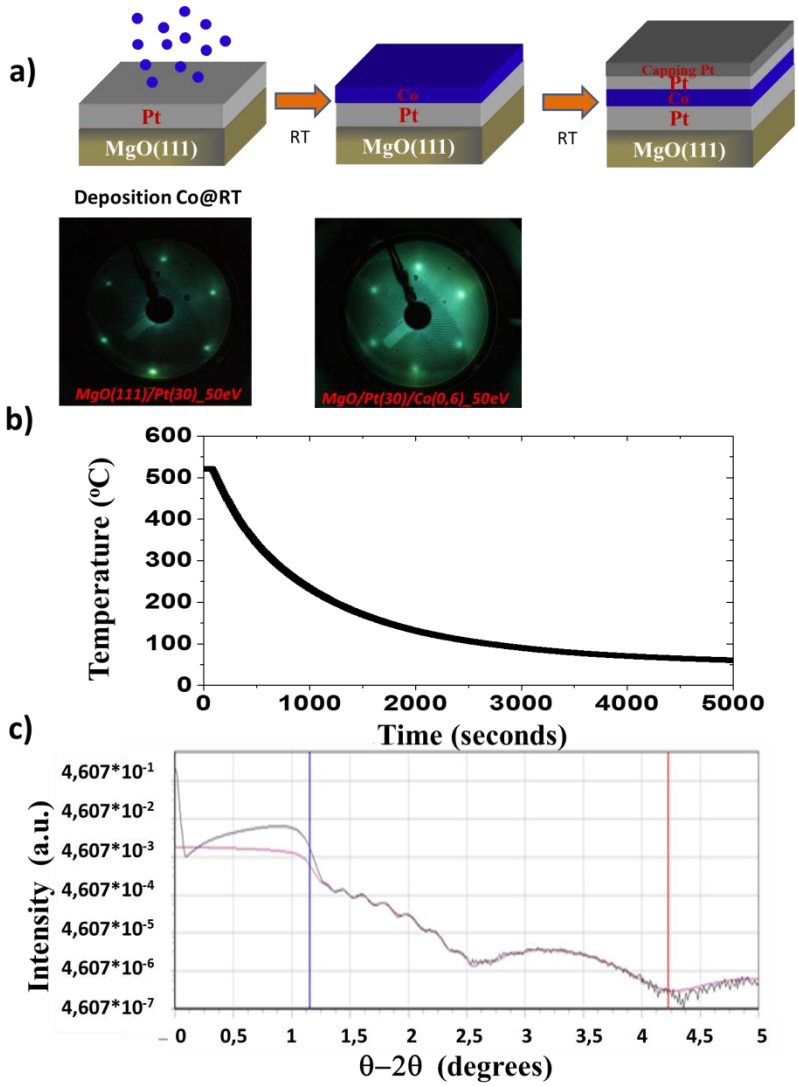

Figure (4.7) a) (upper part) Schematic process of Pt layer growth. (bottom part) LEED patterns of Pt(111) layer (left) and epitaxial Co placed on Pt layer (right). b) Descending ramp during the cooling down sample to RT. c) XRR theta 2theta scans of Pt/Co/Pt epitaxial sample. Red line is the fit with good agreement with experimental data.

Once the buffer layer was deposited, the sample was cooled down to RT (panel b) in 10^{-3}mbar Ar^{+} pressure. To prove the epitaxy of the structures I have checked by LEED the surface reconstruction of the Co layer (shown in panel a). Finally, X-ray reflectivity (XRR) experiments were performed in order to evaluate the thicknesses of each layer of the stack (by fitting the experimental curves), and compared with the nominal values obtained by the QB.

Magnetic characterization

The magnetic properties of the stacks were studied by Kerr magnetometry. In Figure (4. 8) the comparison between the M-H of a polycrystalline (black dots) and epitaxial (red dots) samples with stacks, $SiSO_2$/Ta/Pt/Co(0.6)/Pt and MgO(111)/Pt/Co(0.6)/Pt, respectively. It is immediately seen that, the epitaxial system shows a coercive field (52 mT) much larger than the one of the polycrystalline sample (18 mT).Both of them present a similar hysteresis shape, with abrupt and sharp transitions.

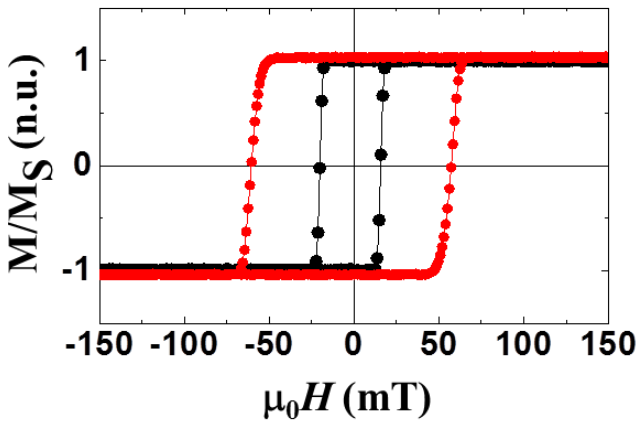

Figure (4. 8) Vectorial resolved M-H loops normalized to the saturation magnetization M_S. Black dots belongs to polycrystalline sample $SiSiO_2$/Ta/Pt/Co(0.6nm)/Pt (Hc=18mT). Epitaxial sample MgO(111)/Pt/Co(0.6nm)/Pt is represented by red dots (H_C=52mT). Both hysteresis loops present square shape with sharp transitions in the reversal processes.

In order to elucidate the role of the intermixing, I compare in Figure 4.9 a stack in which the Co was deposited at 110ºC (blue dots) with one where the growth of the Co was done at RT (red dots). It results clear that the intermixed sample shows a larger anisototropy.

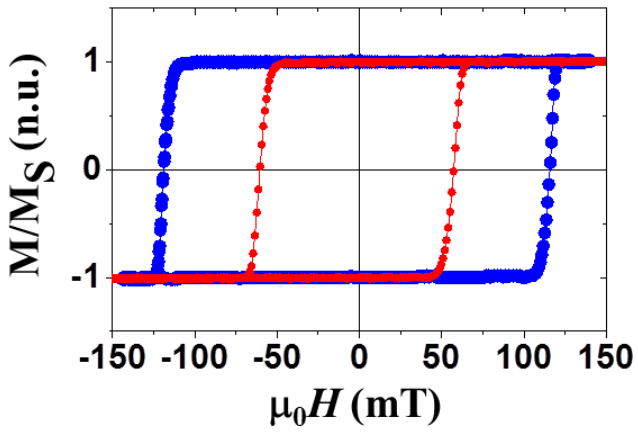

Figure (4.9) Vectorial resolved M-H loops normalized to the saturation magnetization M_S. Red dots belongs to epitaxial sample MgO(111)/Pt/Co(0.6)/Pt (H_C=52mT). Blue dots represents an epitaxial MgO(111)/Pt/Co(0.6)/Pt with Co layer grown at 110°C (H_C=115mT) Both hysteresis loops present square shape with sharp transitions in the reversal processes.

An additional magnetic characterization of the sample Pt/Co(110°C)/Pt were performed with synchrotron light source .Element selectivity X-ray absortion spectra (XAS)and x-ray magnetic circular dichroism (XMCD)spectra were acquired with field applied along and perpendicular to the surface normal direction, at the CoL_3, L_2 absorption edges to probe the electronic state as well as the magnetic properties. This allows us to obtain information on both the spin and the orbital part of the magnetic moments. The measurements were carried out by acquiring the total electron yield (TEY) signals at the BOREAS beamline of the ALBA synchrotron (Cerdanyola del Vallés, Barcelona, Spain). Magnetic field up to 6 T was used to align the moment of magnetic spins parallel to the photon beam and to saturate the magnetization of Co atoms. The results are shown in Figure (4.10) panel a) XMCD (blue line) give us the magnetic information which are obtained from the difference between two XAS spectra acquired with opposite photon helicities; one taken with left circularly polarized (red line) light, and one with right (black).

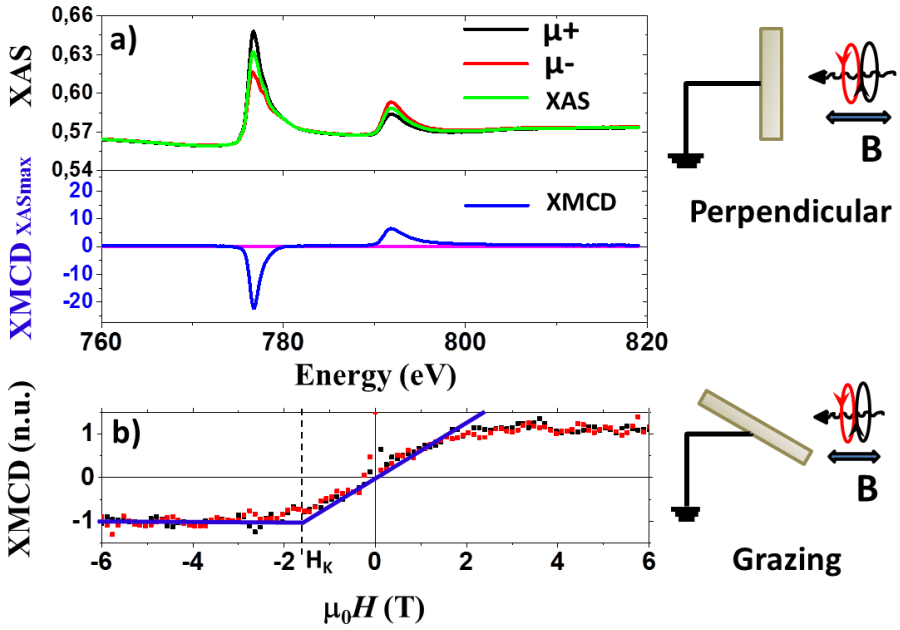

Figure (4.10) a) Co $L_{III,II}$-edge circularly polarized positive and negative (black and red lines respectively) and XMCD (blue line) spectra of 0.6nm Co grown at 110°C. The angle between surface normal and the x-ray electric field is theta=90 deg. correspond to normal x-ray incidence. b) Hysteresis loop around h.a. measuring by XMCD normalized to the saturation magnetization. Blue lines remark the slopes of the curve. Dashed lines mark the H_K value.

Panel b) shows the element-specific grazing hysteresis loop measured at the h.a. by using positive (black) and negative (red) helicities with the photon energy set to the maximum dichroism of the Co-L_{III} absorption edge (778 eV). The two branches of the curve are depicted with filled symbols for increasing and decreasing fields, respectively. From this measurements we have extracted the anisotropy field H_K=1.6T.

By performing angular study (from oop to ip) of M-H loops with polar Kerr magnetometry (using a vectorial magnet) we have studied the evolution of the transition field. As the external field approaches to the in plane direction, in fact, the transition fields present a similar behavior thus allowing a suitable scaling of the anisotropy values.

In the panel a of Figure (4.11) the angular evolution (from out of plane to in-plane) of the transition field of three Pt/co/Pt systems: epitaxial intermixed (blue), epitaxial (blue) and polycrystalline (black). To note that angle = 0º is taken for H // to the normal to the simple surface (90º in plane direction). It

is seen that the polycrystalline samples has Hk of about 270mT that is 1/3 of the Hk of the epitaxial systems with no-intermixing.

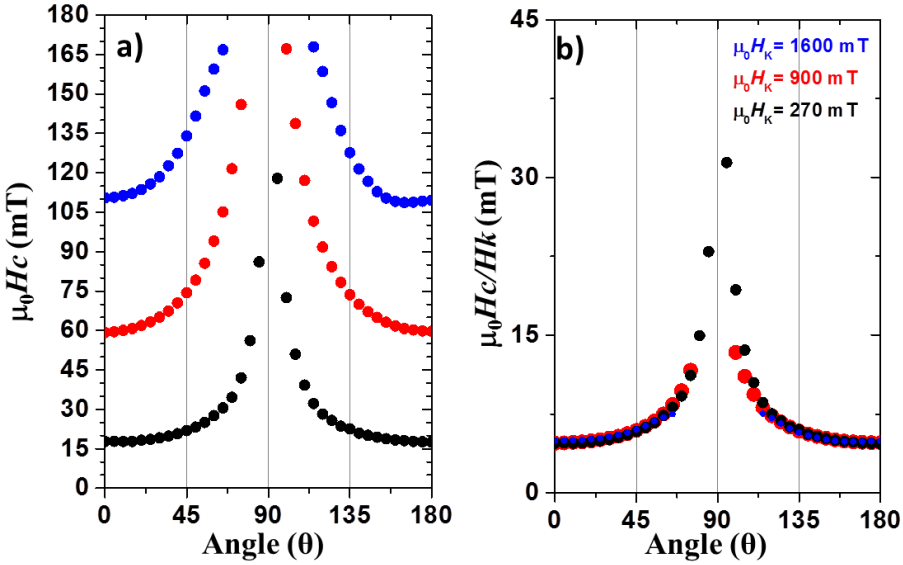

Figure (4.11) Anisotropies comparison: polycrystalline vs epitaxial RT vs epitaxial 100°C. a) angular field evolution of polycrystalline (black dots), epitaxial RT (red dots) and epitaxial 110°C (blue dots). Each curve evolution start at e.a. with Hc to h.a (90°C). b) angular evolution in function of Hc normalized by Hk. The three samples present the same evolution in the reversal process, adjusting the other curves is possible to extract the anisotropies.

4.2 Tuning Dzyaloshinskii-Moriya Interaction in thin film systems

As we have extensively discussed above, DMI resulting from the SOC between the FM and HM and localized at the interfaces of the magnetic layer, stabilizes chiral Néel-type DWs. In order to modify such a interaction, we have designed asymmetric trilayer structures by replacing one of the layer adjacent to the FM one. The resulting general stack reads NM1/FM/NM2. Studies of current induced DW motion in the case of asymmetric Pt/Co/AlOx trilayers [10]confirmed that DMI is present at the Pt/Co interface and this is at the origin of chiral Néel-type DWs and revealed an increase of the walls displacement. It results relevant to improve the fundamental understanding of the DMI effects, and to evaluate its strength in different type of asymmetric structures also in view of device fabrication and optimization.

The final idea is in fact to employ chiral DWs and magnetic skyrmions as carriers of binary information [5].

4.2.1 Asymmetric trilayers

In order to induce an enhancement of DMI, we replace one of the layer composing the asymmetric structure (e.g., NM1) with a different material (NM2). Symmetric samples Pt/Co/Pt generate in both interfaces (heavy metal/Co) the same effective DMI but with opposite sign, thus the total DMI in the system is zero and the DW internal structure is of Bloch type. Using for example Cu as NM2 we are changing the strength of the DMI on the top interface compared to bottom interface.

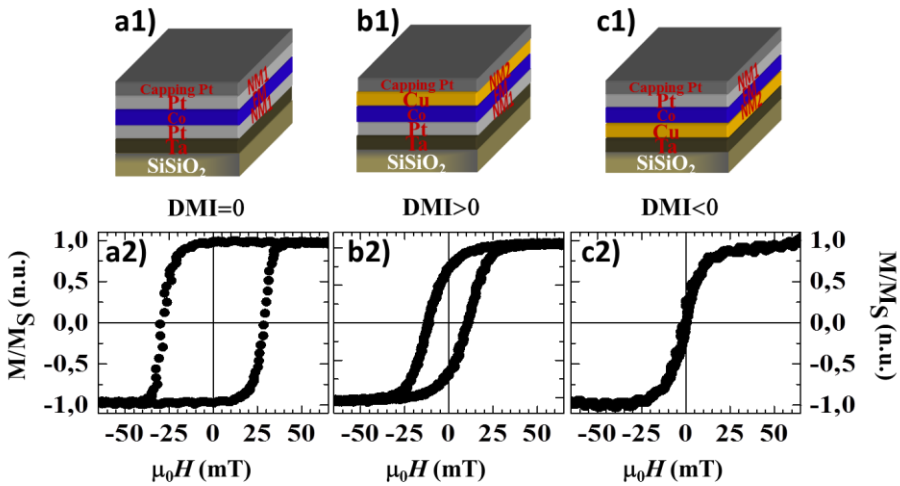

Figure (4.12)Overview of symmetric vs. asymmetric interfaces. a1) Scheme of symmetric interface structure Pt/Co/Pt, and a2) hysteresis loop (Hc=25mT). b1) Scheme of asymmetric interface structure Pt/Co/Cu sample, andb2) hysteresis loop (Hc=13mT). c1) Scheme of the (inverted) asymmetric interface structure Cu/Co/Pt, andc2) hysteresis loop (Hc=0mT). By comparing symmetric (zero DMI) and asymmetric (non-zero DMI) interfaces, it results evident the change of the magnetization reversals upon the introduction of a non-zero effective DMI.

The result is an effective DMI strength in the system that stabilizes chiral Néel walls. In Figure (4.12) are shown three polycrystalline samples grown onto buffered Si substrates in similar condition and with the Co thickness set to 0.6nm. The symmetric Pt/Co/Pt interface (panel a1) shows a well-defined PMA with squared loop and ~25mT coercive field (panel a2). The asymmetric Pt/Co/Cu structure (panel b1) presents instead a reduced (of about 50%)

coercive field, indicating poorer PMA. Finally, the inverted asymmetric Cu/Co/Pt system(panel c1) displays a fully reversible loop (with no hysteresis, and zero coercive field), indicating a weak PMA.Apart from thereduced PMA in Cu-based asymmetric interfaces, by employing asymmetric interfaces we introduce an effective DMI, which affects the reversal behavior via the modification of PMA/DMI ratio [5]].The investigation of such inverted structures gives us the possibility to determine the sign of the effective DMI. To do so, we have chosen to focus on epitaxial systems, since their improved interfaces allows us to neglect spurious effects due to interface disorder.

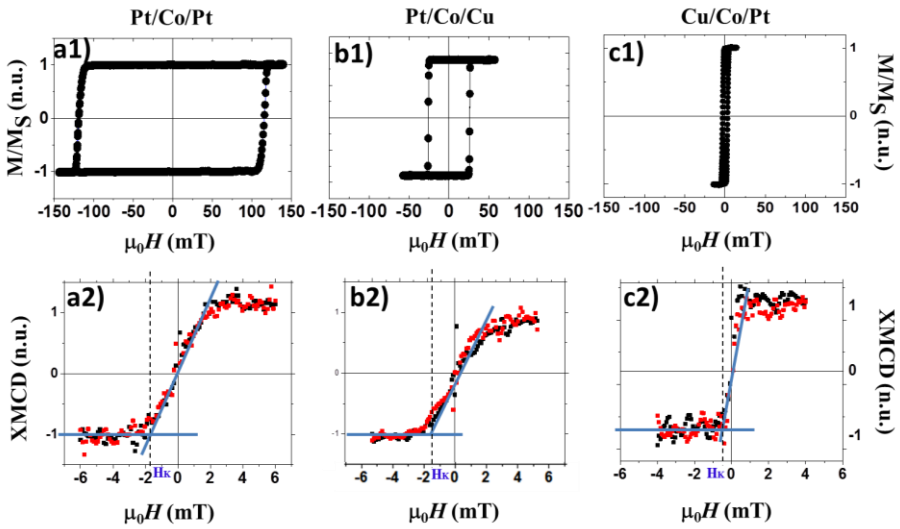

Figure (4.13) a1-c1) Vectorial resolved M-H loopsnormalized to the saturation magnetization M_S of symmetric and asymmetric samples. a1) Pt/Co/Pt H_C=120mT. b1) Pt/Co/Cu Hc=25mT. c1) Cu/Co/Pt Hc= 5mT- a2-c2) Hysteresis loop around h.a. measuring by XMCD normalized to the saturation magnetization. Blue lines remark the slopes of the curve. Dashed lines mark the HK value. A2) Pt/Co/Pt Hk=1600mT. b2) Pt/Co/Cu Hk=1500mT. c2) Cu/Co/Pt Hk= 500mT.

Let's now discuss first the general magnetic behavior of the epitaxial Pt/Co/Pt, Pt/Co/Cu and Cu/Co/Pt (whose growth procedure is discussed later). Polar Kerr and XMCD hysteresis loops spectra have been acquired with the external field normal and parallel to sample surface respectively, as shown in Figure (4.13). As it occurs in polycrystalline systems, we notice a reduction of the coercive (polar Kerr Mz-Hz loops in top panels) and anisotropy fields(XMCD-Hx loops in bottom panels) in the asymmetric interfaces. In particular, the system with Cu on the bottom interface displays the lowest H_K value. The XMCD measurements were performed by acquiring

the dichroic signal with positive (black) and negative (red) helicity with the photon energy set to the peak of the Co-L_{III} absorption edge (778 eV). We found H_K=1600mT in the case of symmetric Pt/Co/Pt, H_K=1500mT for Pt/Co/Cu and H_K= 500mTin Cu/Co/Pt.

4.2.2 Engineering additive DMI

Ab initio and DFTcalculations predict an inverted sign of the DMI for Co/Ir and Fe/Ir interfaces [18]. Hence, it is possible to engineer structures with additive DMI However, the difference between Co/Ir and Fe/Ir cannot be explained by simple arguments and requires further analysis, and it was showed in [18]. As illustrated in Figure (4.14)b for Pt and Ir (when both are below or above the Co layer) the resulting opposite chirality leads to the potential additive effects and, therefore,to the achievement of a large DMI when Co is sandwiched between Pt and Ir. This finding is also reported by other authors for Pt/Co/Ir (panel a) multilayers.[19]In particular, Moreau-Luchaire et al.estimated a DMI value in 1.6 ± 0.2mJ/m^2 for asymmetric Ir/Co/Pt multilayers or 0.2 ± 0.2mJ/m^2 for symmetric Pt/Co/Pt sample.

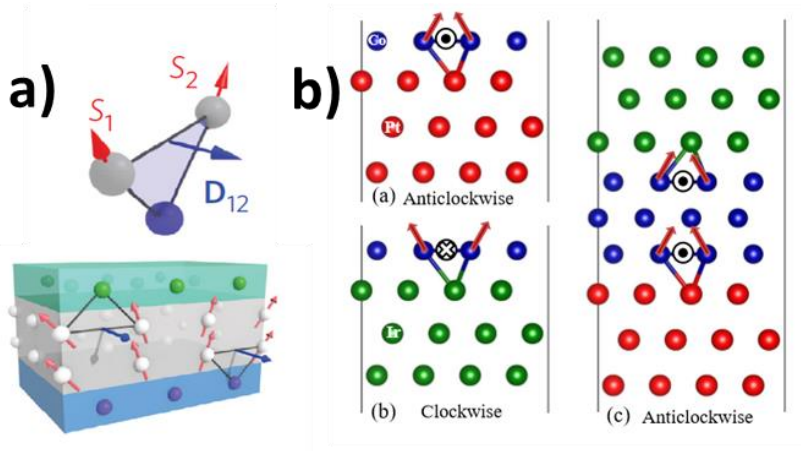

Figure (4.14) a) Schematic representation of trilayer Pt/Co/Ir with additive DMI. In the upper part of the panel schematic representation of DMI resulting of Pt/Co interface. b) (left)Pt/Co anticlockwise and Ir/Co clockwise scheme representation. (right) Pt/Co/Ir anticlockwise chirality with additive DMI. Pictures adapted from [19] **and** [18]**.**

Besides, further ab-initio calculations have been published by Yang, Thiaville et al.[20],. The authorsdiscussed on the additive effectsin Ir/Fe/Co/Pt, and on the different mechanism for enhancing DMI in oxides [18]. These calculations are represented in Figure (4.15) panel b), showing a high SOC in the last layer

of Pt, (Pt/Co interface), and Ir (Fe/Ir interface) and opposite DW chirality between Pt/Co and Ir/Fe or Pb/C, leading to a reinforcement of the total D strength. Recent experimental results, as well as calculations[21]confirmed an additive DMI in multilayers Ir/Fe/Co/Pt (panel a). However,there exists discrepancy on the results. Kim et al., for example, have investigated experimentally the Ir/Co system by performing Brillouin light scattering [22]. Contrary to previous reports, they suggested that the sign of the DMI at the Ir/Co interface is the same as in the case of the Pt/Co interface, but the magnitude of the DMI energy density is relatively smaller than in the case of the Pt/Co interface. In the same direction Han et al., obtained conflicting results, which were attributed to a lack of knowledge of the origin of this effect. The reason for the not convergent results may lie in the different sample stacks and growth conditions, which strongly influence the interfacial quality that can be reflected in changes of the DMI [23].

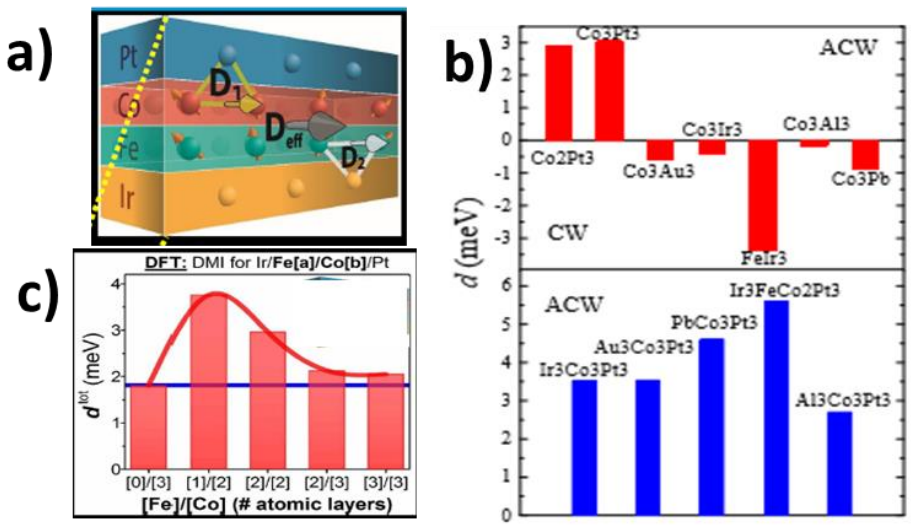

Figure (4.15) a) Schematic representation of a quatrilayer block with additive DMI due to Pt/Co and Ir/Fe interfaces [extracted from [21]**]. b) DMI values of different interfaces calculated by ab-initio simulations**[20]**and c)DFT calculations for Ir/Fe[a]/Co/[b]/Pt atomic layers** [21]**.**

Soumyanarayanan et al. presented DFT calculations of the DMI (d_{tot}, in meV) Figure (4.15) panel c) for Ir[3]/Fe[a]/Co[b]/Pt [3] [21] stacks with varying Fe/Co composition predicting an enhancement of DMI with Fe[1]/Co[2] compared to Fe[0]/Co[3] [ML]. To elucidate this issue we have grown simple

epitaxial quatrilayer system and analyzed the effective DMI. This allowed to disentangle the DMI contribution and sign coming from each interface.

4.2.3 Growth and characterization process of inverted trilayers and quatrilayer systems

As discussed above, the Pt buffer layer promotes a PMA. By replacing Pt with Ir (or Cu) the PMA can result reduced because of the different mismatch with Co. To grow better interface I choose to deposit the Ir layer on a buffer of Pt. In such a way, the quality of the interface and PMA remains unchanged and the DMI is varied. In addition, from a technical point of view, a drastic reduction of the remanence magnetization results in a poorer contrast in the Kerr microscopy contrast.

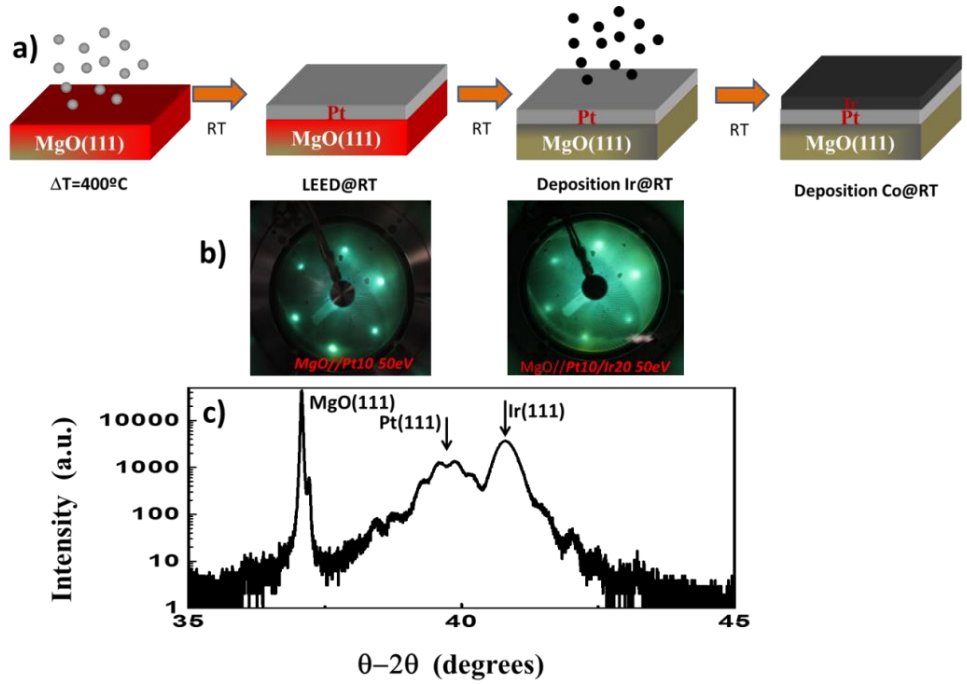

Figure (4.16) a) Schematic representation of epitaxial growth process of inverted trilayers Pt/Ir/Co/Pt. 10nm of Pt was deposited at 400°C. To avoid intermixing Pt/Ir the following layers were deposited at RT. b) LEED patterns at 50eV of Pt 10nm (left) and Pt/Ir(20nm) (right). c) θ-2θscans around the FCC (111) Bragg-peaks of the sputtered Ir/Pt/MgO(111) super lattices. The XRD measurements were performed at at CNRS-GREYC lab in Caen by Sandeep Kumar Chaluvadi.

Quatrilayers

The samples were grown by sputtering with the opposite order, compared to the Soumyanarayanan et al work, i.e. Pt/Co(0.3nm)/Fe(0.3nm)/Ir and Pt/Co(0.4nm)/Fe(0.2nm)/Ir capped by2nm Pt. The results were compared with Pt/Co/Ir trilayer (with 0% of Fe). At each step of the growth, I have characterized in-situ the interfaces by LEED and ex-situ by XRR. Figure (4.13) shows high crystal and surface quality of the epitaxial samples and the XRR fits allowed to extract the layer thicknesses.

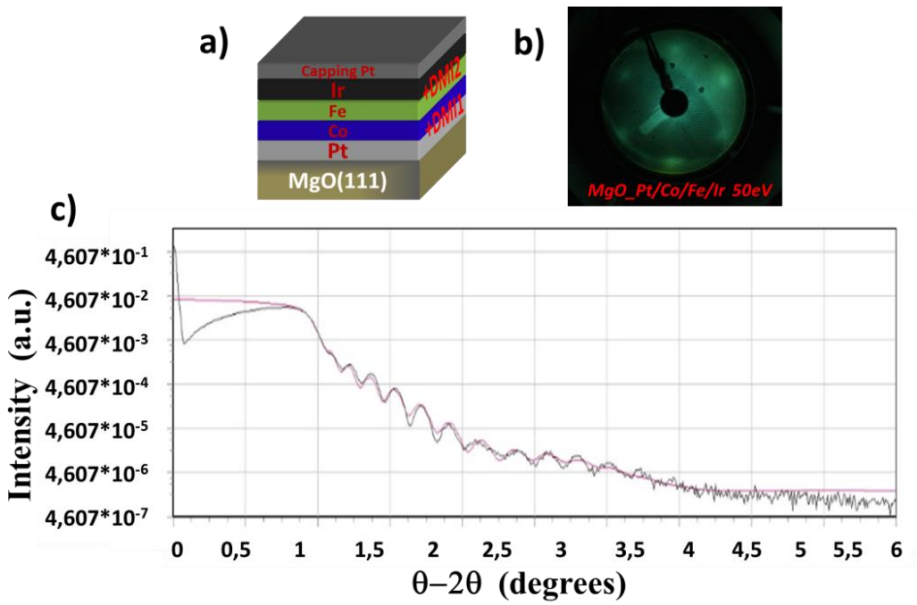

Figure (4.17) a) Schematic representation of epitaxial quatrilayer Pt/Co/Fe/Ir. b) LEED patterns at 50eV of Pt/Co/Fe/Ir after Fe deposition. c) XRR theta 2theta scans of Pt/Co/Fe/Ir epitaxial sample. Red line is the fit of the reflectivity curve showing good agreement with experimental data.

I tried to grow a good epitaxial inverted sample Ir/Fe/Co/Pt and try to compare with Ir/Co/Pt trilayer, but finally I didn't manage to get one with well define PMA. Ir layer was epitaxial but after Fe deposition LEED patterns becomes too fuzzy, with big spots indicating, that there is a problem with the epitaxial Fe deposition. Optimize this and others growth parameters to obtain best quality samples as possible is future work outside this thesis.

4.3 Dzyaloshinskii-Moriya interaction determination

The goal of this part of the thesis is to quantify and determine the effective DMI strength and sign, determining the internal structure and chirality of the DWs and the influence of intermixing in the interfaces on the DMI, by measuring a set of samples with different stack configuration. The sputtering system allows us to use a six different materials [chapter1]to build asymmetric trilayer samples with appropriate magnetic properties (H_c, H_k, etc.)

Summarizing, the epitaxial samples that have been grown were:

- Pt/Co/Pt symmetric sample, characterized by a negligible DMI.
- NM1/Co/NM2, (NM1 is Pt and NM2 Ir and Cu) and inverse NM2/Co/NM1 (as shown in Figure (4.18)), displaying a non-zero DMI.
- Pt/Co/Al, Pt/Co/Cu and Pt/Co/Ir, in which we determined the DMI depending on the top interface.
- Pt/Co(0.3)/Fe(0.3)/Ir, Pt/Co(0.4)/Fe(0.2)/Ir, evaluating the enhancement of the effective DMI.

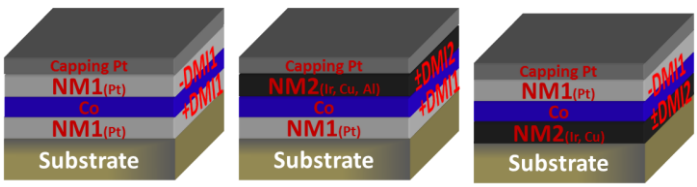

Figure (4.18) Schematic representation of symmetric (left) asymmetric (center) and inverted asymmetric (right) systemsconsidered to determine the DMI value.

The understanding of the DWs dynamics is a nice challenge that I have found during the development of my PhD. In the following I discuss on the key role of the Dzyaloshinskii-Moriya interaction to stabilize chiral DWs. The PMA was determined using polar magneto-optic Kerr effect [Chapter1] in IMDEA nanoscience. All the measurements performed by means of MOKE microscopy and VSM-SQUID were realized at Institut Néel (Grenoble-France) in theMicro and Nano Magnetism group under the supervision of Dr. Stefania Pizzini.

4.3.1 Regimes of magnetic DW motion

To move DWs it is necessary to apply either an external field or an electrical current. In our case, the motion is promoted by pulses of out of plane external magnetic field. During the motion the DW goes through three main regimes of motion, creep, depinning and flow. This was predicted theoretically [24] and experimentally reported by Metaxas et al. for Pt/Co/Pt trilayers. There is a field dependence on the velocity to pass through the three regimes. In the transition between a thermally activated creep regime and a viscous flow regime, the internal wall dynamics plays an important role. [25] The ***creep regime*** is a very low-velocity regime, see Figure (4.19) panel a). If T=0,and below the depinning force (f_{dep}),all the elastic interface will be pinned. In the case of finite temperature (e.g. at RT), the depinning transitions are despicable and the presence of a small velocities ≠0 are expected. In this region, the DWs show not smooth definition (are rough), appears fingers and non-symmetric displacements.

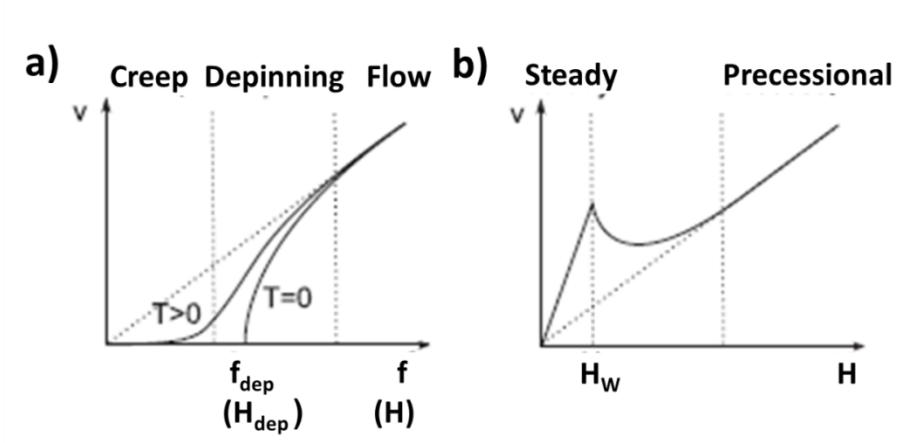

Figure (4.19) a) Theoretical variation of the velocity (v), of a domain wall 1D interface in a 2D weakly disordered medium submitted to a driving force, f (magnetic field, H), at zero and finite temperature, T. b) Regimes of domain-wall flow motion in an ideal ferromagnetic film without pinning. The steady and precessional linear flow regimes are separated by an intermediate regime which begins at the Walker field, HW. Picture adapted from [25]**.**

If f >>>f_{dep} the disorder becomes irrelevant hence resulting in a dissipative viscous flow motion with v ∝ f[26]. This region is known as ***depinning*** and presents an exponential behavior. The determination of H_{dep} is not easy because the two main factors that drive the transitions are temperature dependent. These two factors are: the thermal smearing of depinning

transition, and the magnetic anisotropy. In the high-velocity field regime, that is outside from the creep wall, these effects become smoother, indicating a reduced relevance of the disorder. This regime is called ***flow regime***, and the dissipation limits of DW velocity dominate over the disorder. This regime is characterized by the damping parameter (α) which is related to the wall mobility (m). Two different regimes of linear flow regime are expected (panel b) with different mobilities due to a change in the internal dynamics near of the critical field (Walker field (H_W)). Below H_W,DW motion is steady, above exists a second linear flow regime with the magnetization within DW precesses [25].

4.3.2 Domain walls dynamics. determination of DMI energy density

The DMI strengths have been obtained from two different experiments, which consist in the study of domain wall dynamics:

i) Study of DW velocity driven by an out-of-plane field. In systems with DMI, the velocity saturates after the Walker field [10][27], and the saturation speed can be related to the DMI strength.

ii) Study of the DW velocity driven by an out of plane field, measured as a function of a constant in-plane field applied perpendicular to the domain wall direction. The Hx field for which the velocity is minimum corresponds to the H_{DMI} field that stabilizes chiral Néel walls. The strength of this field can also be related to the DMI strength.

Similar experiments have been carried out in symmetric and asymmetric systems. First the sample is saturated with out of plane magnetic pulse. An opposite magnetic-field pulse is then applied to nucleate some reverse domains. From these first nucleations, by applying more pulses is possible expand the DW. Measuring the expansion and knowing the duration of the applied pulse, the velocity of the expansion can be extracted. To saturate the sample, an external electromagnet was used. For the generation of the bubble domains in high fields, up to 500mT was used micro-coils with 200 µm diameter connected to a current source and a function generator able to send pulses down to 30ns duration.

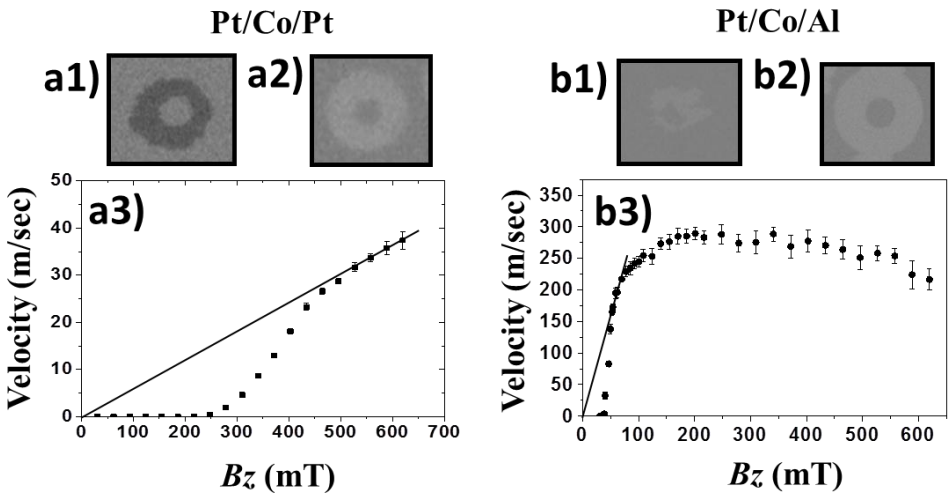

Figure (4.20) Panel a) Symmetric Pt/Co/Pt sample. Panel b) Asymmetric Pt/Co/Al. Differential Kerr images showing the expansion of a domain during the application of an out-of-plane field Bz during a1) and b1) creep regime. And a2) b2) flow regime. a3) DW velocity vs. Bz for Pt/Co/Pt with absence of DMI b3) and Pt/Co/Al with presence of DMI. The thin lines in a3) b3) emphasize the slope of the linear regime.

Figure (4.20) a3shows the DW velocity as a function of Bz of the symmetric sample Pt/Co/Pt. The behavior of this sample is similar to other reported in literature [25][10] with polycrystalline symmetric stacks. The main difference is the larger depinning field in our sample, that is around 250mT. We believe that this large depinning field is related to the larger perpendicular magnetic anisotropy of our epitaxial samples compared to the previous works on polycrystalline samples below the flow regime, the domain profile is rough, as expected for the thermally activated creep regime in panel a1).Once the applied field is higher than the H_{dep} the bubbles becomes rounded and symmetric like panel a2). In the high-field regime the velocity increases exponentially the velocity up to 250mT with constant DW mobility and following a linear function never reaching saturation. The Walker field in this sample is hidden by the creep regime, especially with this huge depinning field. This behavior is promoted by Bloch DWs, more stables than Néel walls in symmetric stacks. The confirmation of the presence of Bloch walls is presented in Figure (4.21) panel a2) the graph shows the DW behavior under the presence of in plane magnetic field, and absence of DMI. Symmetric curves are measured for Pt/Co/Pt and identical dynamics for up/down and

down/up DWs, are found. The bubble expansion (panel a1) is identical for positive and negative in plane field.

Returning back to Figure (4.20) b3, which shows that the Pt/Co/Al sample strongly differs from the symmetric one, we DW velocity reaches a maximum with 280m/s (v_W) under 200mT (Hw) Bz field after which the velocity stays almost constant up to the largest fields. The depinning field in this sample is six times smaller than Pt/Co/Pt, and comparing the coercivity fields, the high dependence Hc-anisotropy-depinning field is clear. In this case, the expected presence of an effective DMI in the he asymmetric stack promotes chiral Néel DWs and under the in plane field the DW propagation is anisotropic in the direction of Bx. The speed-vs.-Bx curve Figure (4.21) panel b2) is proof of it. Shows two minima for $\pm$200mT respectively, up/down and down/up DWs for Hx fields applied in opposite directions. H_{DMI} is present through Dzyaloshinskii-Moriya interaction[10]. The DW velocity presents a minimum when the applied in-plane field compensates the H_{DMI} and the DW magnetization reaches the Bloch orientation [9]. The images show more clearly this chirality, in panel b1) the asymmetric expansion of the DW under external in plane field.

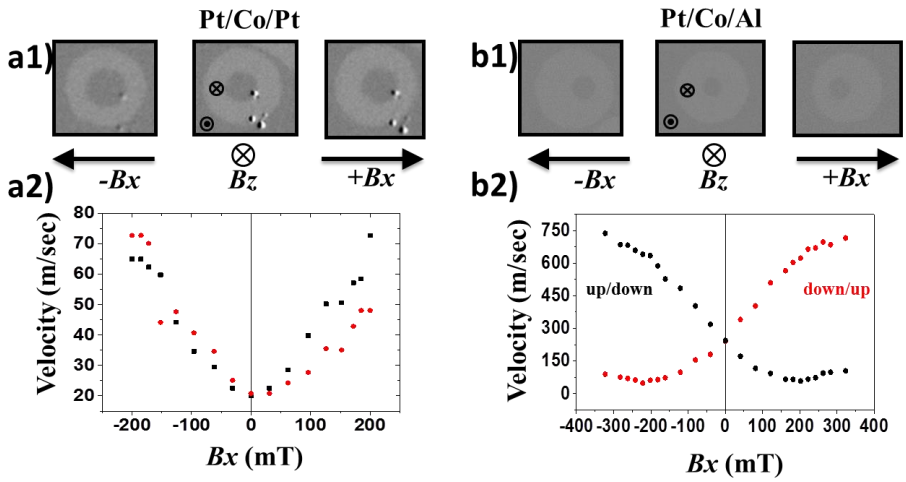

Figure (4.21) a1), b1) differential Kerr images showing the expansion of a domain during the application of an out-of-plane field Bz, without (central panel) and with the simultaneous application of an in-plane field positive (right) and negative (left), in Pt/Co/Pt a1) and Pt/Co/Al b1), a2) b2) DW velocity vs. in-plane field Bx for Pt/Co/Pt (Bz = 400mT) (a2) and Pt/Co/Al (Bz = 100mT) (b2). Black squares: up/down DWs, red dots: down/up DWs.

Once presented the two experiments will be easier explain the dynamics of DWs and how is deduced the effective D energy density. The field for which the DW reaches a minimum corresponds to the$\mu_0 H_{DMI}$field, which is equal to:

$$\mu_0 H_{DMI} = \frac{D}{Ms\Delta} \tag{4.1}$$

D (mJ/m^2) is DMI strength, Ms(MA/m) the spontaneous magnetization and Δ (nm) the DW parameter. Δis obtained by the following relation:

$$\Delta = \sqrt{A/K_0} \tag{4.2}$$

Where A (pJ/m) is the Exchange stiffness and K_o(MJ/m^3).The effective anisotropy energy is given by: $K_0 = K_{u,eff} = K_u - \frac{1}{2}\mu_0 Ms^2$. Ms and Keffare obtained by means of VSM-SQUID measurements.So, the DMI strength can be obtained ones the magnetization and A are known. Note that while Ms can be obtained from VSM-SQUID measurements, A is difficult to obtain and we have used values in the literature for similar Co thicknesses.

In addition, the Walker field allow us to get D using other parameters[28].

$$H_W = \frac{\alpha M_s N_{NDW}}{2} \tag{4.3}$$

whereα is the dumping parameter and N_{NDW} is demagnetization vector of a Néel wall (its value is reported by Metaxas et al., and it is of the order of 12.5 mT inside the creep regime). It is possible to obtain the damping parameter due to the mobility. The DW mobility depends on the regime. In the precessional flow mobility is given by: $m = \frac{\gamma_0 \Delta}{(\alpha + 1/\alpha)}$ and in the steady flow$m = \frac{\gamma_0 \Delta}{\alpha}$.
Thiaville et al. defined the field H_D as:

$$H_D = \frac{(\pi/2)D}{\mu_0 Ms\Delta} \tag{4.16}$$

Substituting the values in the formula, knowing the H_{DMI} expression (Equation (3)) we obtain $H_D = (\pi/2)H_{DMI}$. Continue with the predictions, Thiaville et al. related the Walker field with H_D:

$$H_W \approx \alpha H_D = \frac{\pi \alpha H_{DMI}}{2} \tag{4.5}$$

Thus, extracting α from other linear regime of the DW mobilities, showed before, is possible to relate experimental and calculated data from both experiments, which give back the value of D. The speed around and above the Walker field and how is related with $H_{DMI}\Delta$ and is proportionaltoD/Ms.

$$v_W = \gamma_0 \frac{\Delta}{\alpha} H_W \approx \frac{\pi}{2} \gamma_0 H_{DMI} \Delta = \frac{\pi}{2} \gamma_0 \frac{D}{Ms} \tag{4.6}$$

The predictions are experimentally demonstrated [10] and indicate how critical is the ratio between D and Ms and the importance of the magnetization in this samples.

The DMI strength is obtained from the analysis of the two DW dynamics measurements through equations (4.2) and (4.7). To note that the SQUID measurements gave back a value of Ms surprisingly higher than bulk Co, which can be attributed to proximity effect as reported by Parkin et al. in Ir.based stacks(around 1,65 x 10^6 A/m in agreement with our values).[29]To avoid any possible misinterpretation of the obtained values, we have chosen to extract the Ms and D as function of the film thickness, i.eMs*t and Ds=D*t.

$$v_{max} = \frac{D}{M_S} = \frac{D * t}{M_S * t} = \frac{Ds}{Ms * t} \tag{4.7}$$

We consider a sign convention for which the positive values are anticlockwise rotation, and negative for clockwise rotation.

In table (4.1) Ilistthe characterization results:the coercivity field (Hc), the in-plane saturation field (Hs) thatis used to extract the effective anisotropy energy (K_0)and the DW parameter (Δ).Maximum velocity after Walker field and the DMI effective field is given by $v_W$and H_{DMI} respectively. D_S values are obtained by the two different methods.

Sample	Hc (mT)	Hs (mT)	Ms*t (A)	K_0 (J/m^3)	Δ (nm)	v_W (m/s)	H_{DMI} (mT)	D_s^V (pJ/m)	D_s^H (pJ/m)
Pt/Co/**Al**	20	1295	$1.3x10^{-3}$	$6.9x10^5$	4.8	280	212	1.32	1.33
Pt/Co/**Cu**	25	1780	$0.75x10^{-3}$	$9.5x10^5$	4.1	230	200	0.82	0.85
Pt/Co/**Ir**	14	1405	$7.5x10^{-4}$	$7.5x10^5$	4.6	100	96	0.27	0.33
Ir/Co/Pt	10	559	$9.0x10^{-4}$	$3.0x10^5$	7.3	240	106.5	-0.78	-0.70
$Pt/Co_{0.4}$**$Fe_{0.2}$**/**Ir**	29	1650	$8.4x10^{-4}$	$8.8x10^5$	4.3	180	215	0.77	0.55
$Pt/Co_{0.3}$**$Fe_{0.3}$**/**Ir**	9	1146	$8.6x10^{-4}$	$6.1x10^5$	5.1	260	167	0.74	0.81

Table (4.1) Coercive field Hc, in-plane saturation field Hs, spontaneous magnetization in function of thickness Ms*t, effective anisotropy energy K0, DW parameter Δ, Walker velocity v_W, DMI field $\mu_0 H_{DMI}$, DMI surface energy, Ds^v extracted from the Walker speed, and Ds^H extracted from the DMI field.

Figure (4.22) shows that the saturation DW velocity Pt/Co/NM2 are strongly depending on the NM2 metal and are in general larger than that obtained for the Pt/Co/Pt stack. The symmetric sample (Pt/Co/Pt) shows the minimum speed with non-saturated curve, indicating a negligible DMI. Pt/Co/Al displays a Ds = 1.3±0.2pJ/m and gives back the maximum values of H_{DMI} and v_{max}. DMI is the largest of all samples, which seems to confirm that the Co/Al interface does not contribute to DMI. This is the clearest result in addition to the Cu sample which shows lower speed than Al; the effective DMI is lower than the previous case so the top interface induces an effective D in opposite direction than Pt/Co interface showing a Ds=0.8±0.2pJ/m. The v_W in Pt/Co/Ir sample (around 100m/s) almost three times smaller than Pt/Co/Al. This indicates that the DMI in the top interface is ***not additive***, the sign of the DMI is opposite than the Pt/Co interface and large. But is difficult to quantify the DMI value in this sample, the magnetization Ms*t is much smaller than all the other samples, in particular to the intermixed sample Pt/Co/Ir measured at Institut Néel as well. An approximate value could be Ds=0.3±0.2pJ/m, in our opinion the smaller value is due to the smaller difference between the DMI of the two interfaces.

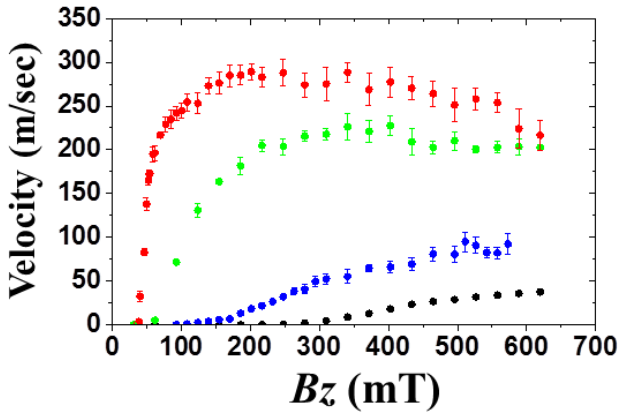

Figure (4.22) Velocity vs Bz. Saturation DW velocity Pt/Co/NM2 are strongly depending on the NM2 metal (Al= red dots, Cu green dots, Ir blue dots), are larger than that obtained for the Pt/Co/Pt (black dots).

In panel a of Figure (4.23) is shown the Pt/Co/Fe/Ir velocity behaviors. For the two samples with different Co/Fe composition Co0.4/Fe0.2 and Co0.3/Fe0.3 Ds = 0.8±0.2pJ/m.

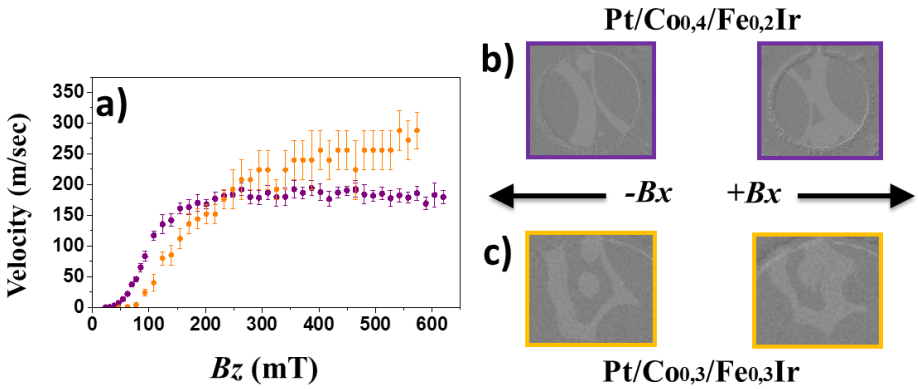

Figure (4.23) a) velocity in function of Bz field of $Pt/Co_{0.4}/Fe_{0.2}/Ir$ (purple) and $Pt/Co_{0.3}/Fe_{0.3}/Ir$ (orange) b) and c) are presented differential Kerr images showing the asymmetric expansion of DWs during the application of an out-of-plane field Bz with the simultaneous application of an in-plane field positive (right) and negative (left), in $Pt/Co_{0.4}/Fe_{0.2}/Ir$ (b) and $Pt/Co_{0.3}/Fe_{0.3}/Ir$ (c) demonstrating the presence of Néel type DW.

The first conclusion and contrary what was published is clear, the DMI are ***not additive*** (otherwise DMI values should be bigger than for Pt/Co/Al).

Assuming due to the possible intermixingbetween Co and Fe there are not the best samples, the only thing clear is that DMI is similar to Pt/Co/Ir, so that we can assume that in this case the Fe/Ir give the same contribution to total DMI than Co/Ir. If it was opposite the DMI would grow much more. In panel b) and c) are presented differential Kerr images showing the asymmetric expansion of DWs during the application of an out-of-plane field Bz with the simultaneous application of an in-plane field positive (right) and negative (left), in Pt/Co/Fe/Ir (b) and Pt/Co/Fe/Ir (c) demonstrating the presence of Néel type DW.

4.3.3 Sign of DMI in Pt/Co/NM and NM/Co/Pt stacks

As commented above, in this section I determine the sign of the chirality of the DWs in the asymmetric interfaces.

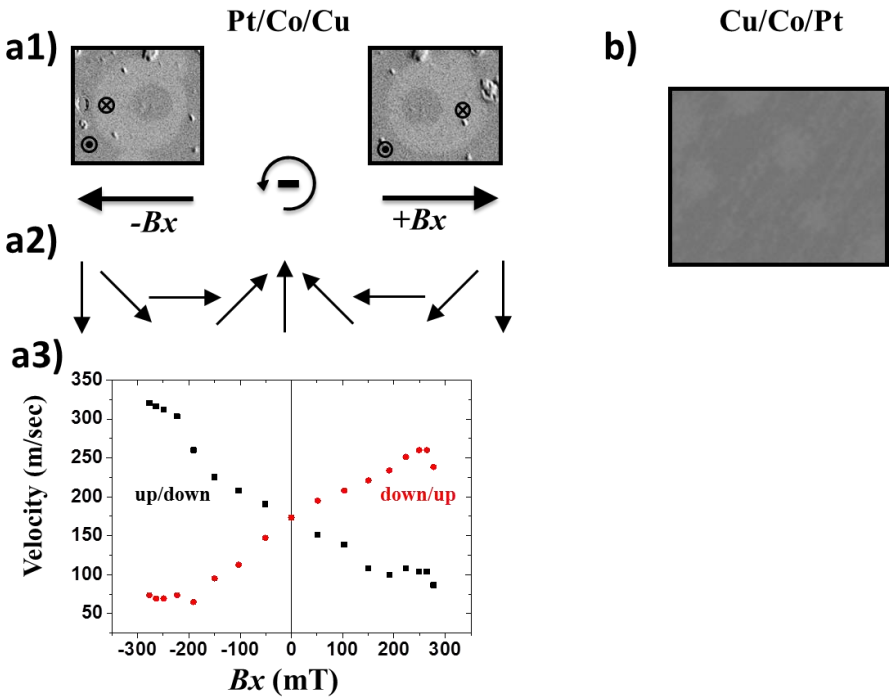

Figure (4.24)a1) Differential Kerr images showing the asymmetric expansion of DWs during the application of an out-of-plane field Bz with the simultaneous application of an in-plane field positive (right) and negative (left), in Pt/Co/Cu. a2)anticlockwise chirality direction. a3) DW velocity vs. in-plane field Bx for Pt/Co/Cu (Bz = 220mT). Black squares: up/down DWs, red dots: down/up DWs demonstrating the presence of Néel type DW. b) Kerr image showing not good magnetic contrast and small nucleation center points.

In panel a1) is shown the asymmetric expansion of the DW under in plane field, positive +Bx (right) and negative –Bx (left). The direction of the expansion is favorable to the direction of the external field. In this case (same behavior than Pt/Co/Al) the chirality follows anticlockwise direction, positive value in our sign convention (panel a2)). Asymmetric sample DW propagation is anisotropic in the direction of Bx. The speed-vs.-Bx curves show a minimum for ∓200mT respectively for down/up and up/down DWs, and the trend for up/down and down/up DWs is similar for Hx fields applied in opposite directions. This is the due to the presence of chiral Néel walls stabilized by the Dzyaloshinskii-Moriya interaction.

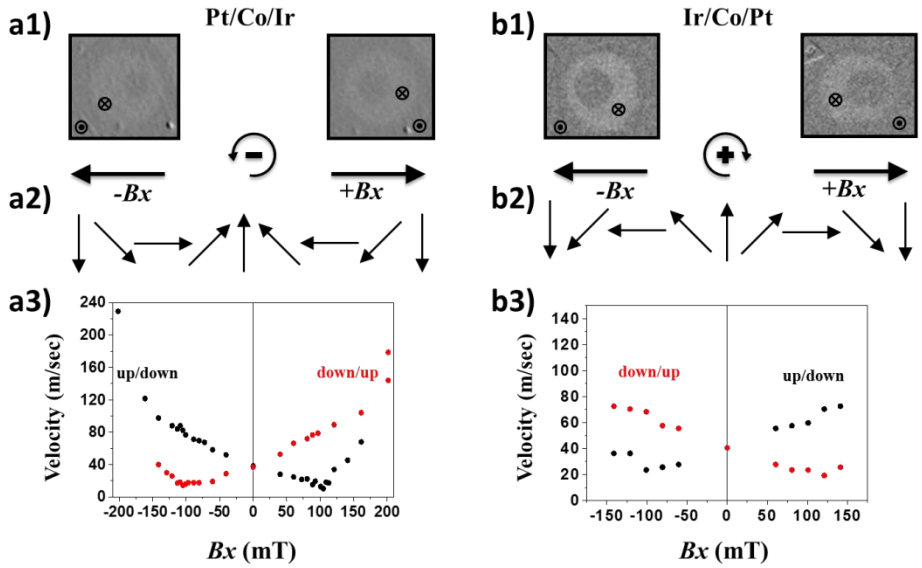

Figure (4.25) a1) and b1) Differential Kerr images showing the asymmetric expansion of DWs during the application of an out-of-plane field Bz with the simultaneous application of an in-plane field positive (right) and negative (left), in Pt/Co/Ir (a1) and Ir/Co/Pt (b1). a2) anticlockwise chirality direction.). b2) clockwise chirality direction. a3)and b3) DW velocity vs. in-plane field Bx for Pt/Co/Ir (Bz = 180mT). Black squares: up/down DWs, red dots: down/up DWs demonstrating the presence of Néel type DW anticlockwise direction. b3) DW velocity vs. in-plane field Bx for Ir/Co/Pt (Bz = 190mT). Black squares: up/down DWs, red dots: down/up DWs demonstrating the presence of Néel type DW clockwise direction.

After the impossibility of the measurement of the Cu inverted sample because of the poor magnetic contrast, the second stack of inverted trilayers, Pt/Co/Ir and Ir/Co/Pt was measured in the same way to try to achieve a good result. The Hc of both samples are quite similar, ($Hc_{Pt/Co}$=14mT and

$Hc_{Ir/Co}$=10mT) that allow us to apply the in plane field which was not possible with the previous samples. After the application of out of plane external field pulses, the Ir/Co/Pt sample shows a high V_W speed 240m/s and a Ds^V value -0.7±0.2pJ/m. The determination of the sign is showed in Figure (4.25) panels a2) and b2). Under the same external in plane field, the expansion of the magnetic bubble occurs in opposite direction (panel a1) and a2)).

When the Ir layer is placed at the bottom, the DMI is opposite therefore, the DW chirality is opposite, i.e.clockwiserotationb2). The symmetry inversion is shown in the Bx speed graphs. Where the inversion of up to down and down to up DW is opposite as well, the color of the branches facilitate the understanding.

In conclusion, I have demonstrated the absence of DMI in symmetric Pt/Co/Pt samples. It showed how the Al interface enhances the DMI effect in the Pt/Co interface more than Cu or Ir interfaces. In the case of additive DMI, it has been shown how Ir/Co or Fe/Ir interfaces have not the same sign and there are not additives. In both cases, the sign of the upper layer is opposite to Pt/Co and provide large DMI.

4.3.4 DMI sensibility: Epitaxial vs polycrystalline and interface intermixing

It has been demonstrated, the enhancement of the v_{max} in the epitaxial samples compared to polycrystalline ones Figure (4.26) panel a). The velocity reached by the epitaxial Pt/Co/Al is three times larger than the velocity in the polycrystalline Ta/Pt/Co/Al on Silicon (sample grown by Stefania Pizzini). This enhancement is driven by an enhancement of the DMI due to a better quality interfaces. In panel b) is shown how in the case of the epitaxial sample (filled dots) the external in plane field necessary to compensate the H_{DMI} (212mT) is almost double than the polycrystalline (empty dots) with 100mT.

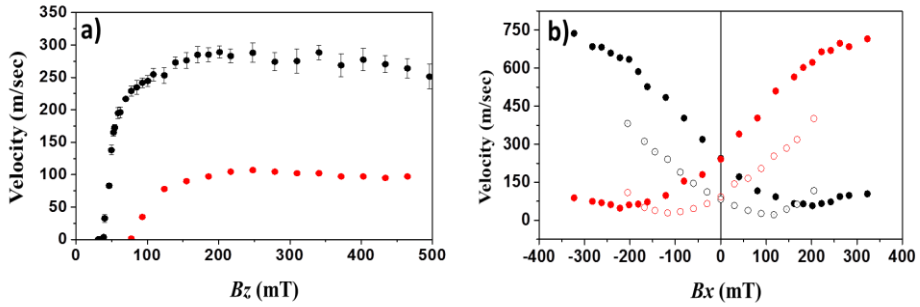

Figure (4.26) a) Velocity vs Bz comparison between epitaxial sample (black dots) $v_{max=}$280 m/sec and polycrystalline sample (red dots) $v_{max=}$100 m/sec. b).

On the other hand and in the same direction than Moore et al. [30]is shown the influence of the interfacial intermixing on the total DMI.

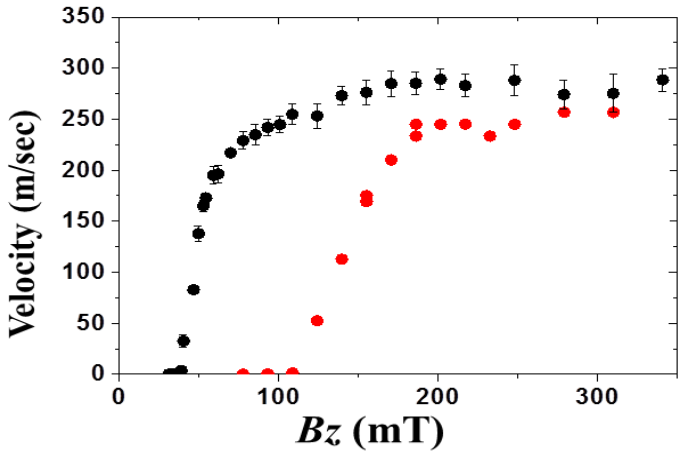

Figure (4.27) Velocity vs Bz graph. Comparison epitaxial sample (black dots) with v_{max}280m/sec grown at RT with epitaxial grown at 110°C (red dots) with v_{max}220m/sec.

In our case we compare two samples, Pt/Co/Al where the Co deposition was at RT with Ds = 1.3±0.2 pJ/m and Pt/Co/Al with Co deposition at 110°C Ds=0.8±0.2 pJ/m. This is the first observation, weaker DMI for intermixed Co/Al interface, 30% less Ds. The other effect is the increase of depinning field.

4.4 References

[1] M. H. and L. T. Stuart S. P. Parkin, "Magnetic Domain-Wall Racetrack Memory," *Am. Assoc. Adv. Sci.*, vol. 320, no. 5873, pp. 190–194, 2008.

[2] P. Perna *et al.*, "Two-dimensional chiral asymmetry in unidirectional magnetic anisotropy structures," *AIP Adv.*, vol. 6, no. 5, 2016.

[3] G. Z. J. Ping Liu, Zhidong Zhang, *Skyrmions: Topological Structures, Properties, and Applications*. .

[4] C. P. Chui, F. Ma, and Y. Zhou, "Geometrical and physical conditions for skyrmion stability in a nanowire," *AIP Adv.*, vol. 5, no. 4, pp. 0–10, 2015.

[5] A. Fert, V. Cros, and J. Sampaio, "Skyrmions on the track," *Nat Nano*, vol. 8, no. 3, pp. 152–156, Mar. 2013.

[6] S. Fukami, T. Suzuki, K. Nagahara, N. Ohshima, and N. Ishiwata, "Large thermal stability independent of critical current of domain wall motion in Co/Ni nanowires with step pinning sites," *J. Appl. Phys.*, vol. 108, no. 11, pp. 7–11, 2010.

[7] S. Mangin, D. Ravelosona, J. A. Katine, M. J. Carey, B. D. Terris, and E. E. Fullerton, "Current-induced magnetization reversal in nanopillars with perpendicular anisotropy," *Nat Mater*, vol. 5, no. 3, pp. 210–215, Mar. 2006.

[8] L. Néel, "Anisotropie magnétique superficielle et surstructures d'orientation," *J. Phys. Radium*, vol. 15, no. 4, pp. 225–239, 1954.

[9] S. G. Je, D. H. Kim, S. C. Yoo, B. C. Min, K. J. Lee, and S. B. Choe, "Asymmetric magnetic domain-wall motion by the Dzyaloshinskii-Moriya interaction," *Phys. Rev. B - Condens. Matter Mater. Phys.*, vol. 88, no. 21, pp. 1–5, 2013.

[10] T. Ha Pham *et al.*, "Very large domain wall velocities in Pt/Co/GdOx and Pt/Co/Gd trilayers with Dzyaloshinskii-Moriya interaction," *EPL (Europhysics Lett.*, vol. 113, no. 6, p. 67001, 2016.

[11] S. Wei, B. Li, T. Fujimoto, and I. Kojima, "Surface morphological modification of Pt thin films induced by growth temperature," *Phys.*

Rev. B, vol. 58, no. 7, pp. 3605–3608, 1998.

[12] Y. Xie and J. A. Blackman, “Theory of enhanced magnetic anisotropy induced by Pt adatoms on two-dimensional Co clusters supported on a Pt(111) substrate,” *Phys. Rev. B*, vol. 74, no. 5, p. 54401, Aug. 2006.

[13] M. H. Read and D. H. Hensler, “X-ray analysis of sputtered films of beta-tantalum and body-centered cubic tantalum,” *Thin Solid Films*, vol. 10, no. 1, pp. 123–135, 1972.

[14] W. Heisenberg, “Zur Theorie des Ferromagnetismus,” *Zeitschrift f{ü}r Phys.*, vol. 49, no. 9, pp. 619–636, 1928.

[15] C. Kittel, “Theory of the Structure of Ferromagnetic Domains in Films and Small Particles,” *Phys. Rev.*, vol. 70, no. 11–12, pp. 965–971, 1946.

[16] M. Baudin, M. Wójcik, and K. Hermansson, “A molecular dynamics study of MgO (111) slabs,” *Surf. Sci.*, vol. 375, no. 2–3, pp. 374–384, 1997.

[17] P. F. Lyman, S. T. King, W. Han, and K. Pradhan, “Reconstructed surfaces of binary polar oxides: MgO (111) and ZnO (000-1),” no. 111.

[18] H. Yang, O. Boulle, V. Cros, A. Fert, and M. Chshiev, “Controlling Dzyaloshinskii-Moriya Interaction via Chirality Dependent Layer Stacking, Insulator Capping and Electric Field,” *Arxiv Prepr.*, p. 1603.01847, 2016.

[19] C. Moreau-Luchaire *et al.*, “Additive interfacial chiral interaction in multilayers for stabilization of small individual skyrmions at room temperature,” *Nat. Nanotechnol.*, no. January, pp. 1–6, 2016.

[20] H. Yang, A. Thiaville, S. Rohart, A. Fert, and M. Chshiev, “Anatomy of Dzyaloshinskii-Moriya Interaction at Co/Pt Interfaces,” *Phys. Rev. Lett.*, vol. 115, no. 26, pp. 1–5, 2015.

[21] A. Soumyanarayanan *et al.*, “Tunable Room Temperature Magnetic Skyrmions in Ir/Fe/Co/Pt Multilayers,” *arXiv*, p. 1606.06034, 2016.

[22] N. H. Kim *et al.*, “Interfacial Dzyaloshinskii-Moriya interaction, surface anisotropy energy, and spin pumping at spin orbit coupled Ir/Co

interface," *Appl. Phys. Lett.*, vol. 108, no. 14, 2016.

[23] D. S. Han *et al.*, "Asymmetric hysteresis for probing Dzyaloshinskii-Moriya interaction," *Nano Lett.*, vol. 16, no. 7, pp. 4438–4446, 2016.

[24] S. Brazovskii and T. Nattermann, "Pinning and Sliding of Driven Elastic Systems: from Domain Walls to Charge Density Waves," *Adv. Phys.*, vol. 53, no. 2, pp. 177–252, 2004.

[25] P. J. Metaxas *et al.*, "Creep and Flow Regimes of Magnetic Domain-Wall Motion in Ultrathin Pt = Co = Pt Films with Perpendicular Anisotropy," vol. 217208, no. November, pp. 1–4, 2007.

[26] M. Kataja and S. Van Dijken, "Magneto-optical Kerr effect susceptometer for the analysis of magnetic domain wall dynamics," *Rev. Sci. Instrum.*, vol. 82, no. 10, 2011.

[27] Y. Yoshimura *et al.*, "Soliton-like magnetic domain wall motion induced by the interfacial Dzyaloshinskii-Moriya interaction," *Nat Phys*, vol. 12, no. 2, pp. 157–161, Feb. 2016.

[28] E. Jué *et al.*, "Domain wall dynamics in ultrathin Pt/Co/AlOx microstrips under large combined magnetic fields," *Phys. Rev. B - Condens. Matter Mater. Phys.*, vol. 93, no. 1, pp. 1–11, 2016.

[29] K. S. Ryu, L. Thomas, S.-H. Yang, and S. S. P. Parkin, "Chiral spin torque at magnetic domain walls.," *Nat. Nanotechnol.*, vol. 8, no. 7, pp. 527–33, 2013.

[30] A. W. J. Wells, P. M. Shepley, C. H. Marrows, and T. A. Moore, "Effect of interfacial intermixing on the Dzyaloshinskii-Moriya interaction in Pt/Co/Pt," *arXiv*, p. 1607.06405, 2016.

V. Towards gr-based spin-orbitronic PMA systems

Novel active graphene (gr) based spin-orbitronic systems could benefit from the outstanding properties of gr, as high electronic mobility, large spin lifetimes and long spin diffusion length, and potentially large (and tuneable) SOC. In this chapter it is introduced the methodology to prepare high quality gr-based spinorbitronic systems, i.e., epitaxial asymmetric HM/Co/gr trilayers grown on (111)-oriented oxide substrates. The methodology includes epitaxial growth and intercalation (via heating) processes monitored in-situ by XPS and LEED. This allows to confirm the quality of the trilayers as well as to find the optimum temperature range for Co-gr intercalation and the critical temperature for Co-HM intermixing. The magnetic characterization shows that the gr-based trilayers result with well-defined PMA and exhibit an effective DMI. Remarkably, both chiral effects and very large PMA (up to 15 monolayer thick Co films) are demonstrated. The results open the way for the development of the next generation of (low-power, faster and smaller) gr-based spin-orbitronic devices in 21st century.

A major challenge for future spintronics is to develop suitable spin transport channels with superior properties as long spin lifetime and propagation length. Graphene can meet these requirements, even at room temperature. On the other side, magnetic skyrmions can satisfy the demands for highly dense data storage, low power consumption and high processing speed. We realized epitaxial asymmetric HM/Co/graphene nanostructures grown on (111)-oriented oxide substrates, with large perpendicular magnetic anisotropy and Dzyaloshinskii–Moriya chiral interaction (DMI), and investigated the growth mechanisms by surface science analysis and the magnetic properties by Kerr magnetometry, microscopy and X-ray magnetic circular dichroism (XMCD) measurements. We provide evidences of a large

perpendicular magnetic anisotropy (H_K~2T) and DMI (Ds=0.3±0.2pJ/m) for Cobalt thickness up to 16 MLs (4 nm) at room temperature in structures grown onto oxide substrates. This discovery enables practical applications for future spintronics based on graphene.

In this chapter, I will present hence the growth process study and the magnetic characterizations of epitaxial asymmetric trilayer system with large PMA and DMI, based on graphene. In addition, I will provide evidence of fast Néel-type chiral domain walls motion in such hybrid structures. This finding may enable practical applications for future spintronics based on graphene.

However, there are some practical issues to overcome regarding the fabrication of epitaxial gr-based PMA stacks with atomically flat interfaces. This makes it more complicated than the epitaxial all-metallic systems. First, the synthesis of epitaxial graphene requires high temperature, and this may cause interfacial intermixing. Second, the evaporation of metals on graphene typically forms disordered clusters with no defined anisotropy [1] [2]. To circumvent these problems, we employed an intercalation process to prepare homogeneous epitaxial cobalt layers, sandwiched between a (111)-oriented metallic buffer (Pt, Ir) and a monolayer of graphene. The epitaxial buffer is grown on commercially available oxide substrates. The sketch of the structure is shown in Figure (5.1).

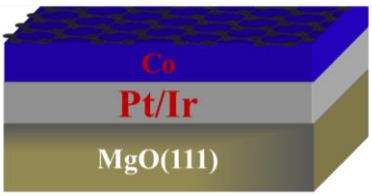

Figure (5.1) Structure of the sample model. MgO(111) oxide substrate where is grown the (111) oriented metallic buffer (Pt, Ir) layer. The Co layer have been intercalated underneath the graphene monolayer sheet.

5.1. Graphene spin-orbitronics

Due to its exceptional high electrical conductivity, carrier mobility, thermal conductivity, optical transparency, inertness, passivation and super hydrophobicity [3] [4] properties, graphene, a single atomic layer of graphitic carbon, is expected to play an important role in nanoscience and spintronics. It offers great opportunities in the relentless race toward smaller, faster and low consumptive electronics [5].

For this purpose, graphene can be employed to achieve of room-temperature spin transport with long spin diffusion lengths of several micrometers [6] [7] [8] [9]. However, the development of all-graphene spintronic devices requires that, in addition to its passive capability to transmit spins over long distances, other active properties be incorporated to graphene. So far, the search of novel magnetic functionalities to graphene is scarce. Only few theoretical and experimental works have been implemented magnetic functionalities in graphene-based system through the introduction of defects (vacancies or adatoms) [3], as well as by the introduction of giant spin-orbit coupling (SOC) in the electronic bands of graphene [10]. Together with the passivating properties, inertness and impermeability [11], it was also reported that graphene may affect the tunnel magnetoresistance [12] [13], spin injection efficiency [14] [15], Rashba [16] [17], quantum spin-Hall effect [18] and perpendicular magnetic anisotropy (PMA) [19].

Very recent studies argued that the graphene in contact with a FM Co layer might be responsible for the enhancement of the PMA even though, as said, it experiences an almost negligible SOC [6]. The large PMA in gr/Co has been ascribed to the hybridization of the graphene and Co electron orbitals [11], whereas the unusual DMI found at the gr/Co interface was proposed to be a Rashba-like DMI [14].

This work is part of an EU project, named SOgraphene, coordinated by IMDEA Nanociencia, which involves four research institutions (IMDEA, UMPHY, Soleil and IPM) (reference). The aim of the project is the creation, characterization, imaging, and testing all-graphene spin-orbitronic systems/devices functional at RT by exploiting the advantages of combining ferromagnetic (FM) and non-magnetic (NM) heavy metals and graphene [10] From one side, interface-induced tailored SOC, and therefore DMI, is achieved by artificially stacking ferromagnetic (FM) with non-magnetic (NM) metals, namely MgO(111)/Pt or Ir (111)/Co/gr. On the other side, we modify the top-interface SOC by inserting a different metal as Pb, namely and MgO(111)/NM/Co/Pb/gr.

5.1.1 2D materials. Graphene, state of the art

Graphene is one of the allotropic forms of elemental carbon consisting of sheets that have the thickness of one atom. The atoms are arranged in a honeycomb pattern (= a pattern of shapes with six sides) [20]. The characteristic honeycomb-like lattice structure of graphene is shown in Figure

(5.2) a) The planar monolayer of carbon atoms is arranged on two dimensional hexagonal lattices with a carbon–carbon bond length of 0.142 nm [21]. Graphene is also the conceptual building block for some of these allotropes, including graphite, which is layered graphene, as well as nanotubes, which are graphene sheets that are seamlessly rolled up into cylinders with nanometer-scale diameters, and fullerene, which are graphitic molecular cages (Figure (5.2). While the existence of graphene has been known for some time, the name ‘‘graphene’’ was formally adopted by IUPAC only in 1997 as a replacement for the term ‘‘graphitic layers’’ in their Compendium of Chemical Technology. Was in 2004 when an explosive growth in graphene research began with several publications, pioneered by a group at Manchester [5], [22], [23] and the Georgia Institute of Technology [24].There are several reasons for this worldwide interest in graphene, but above all the remarkable electronic, mechanical, optical, and transport properties [4] that have generated many avenues for applications in spintronics [25].

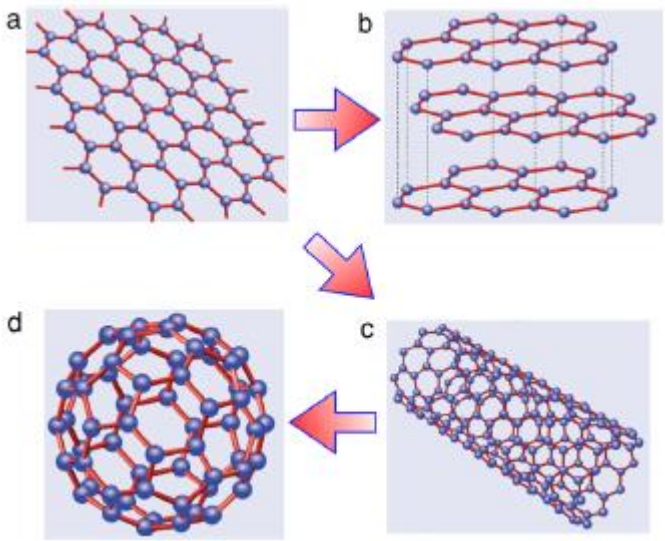

Figure (5.2) Graphene monolayer sheet (top left) consisting in a 2D hexagonal lattice of carbon atoms. Each atom is covalently bonded to three others; but since carbon has four valence electrons, one is left free allowing graphene to conduct electricity. Other well-known forms of carbon all derive from graphene: graphite is a stack of graphene layers (top right); carbon nanotubes are rolled-up cylinders of graphene (bottom left); and a buckminsterfullerene (C60) molecule consists of graphene balled into a sphere by introducing some pentagons as well as hexagons into the lattice (bottom right). Adapted from [26]

Since the beginning, many research groups were aware of the potential of this material, but the way to get high quality graphene over large areas slowed down its development. The most used technique was the "scotch–tape method" that utilizes common cellophane tape to remove layers from a graphite flake [22]. One year later, new techniques based on the cleavage from strongly layered materials as molybdenum disulphide (MoS2), Niobium diselenide (NbSe2), hexagonal boron nitride (BN) and (Bi2Sr2CaCu2Ox) have been developed to obtain also new families of 2D material., Such exfoliated materials were hence studied away from their bulk counterparts for first time [23].

Unique properties of graphene.

The properties of graphene are unique. This explains why the initial interest of the solid-state physicists was promptly followed by the attention of material scientists, chemists and biologists. So far researchers of various disciplines have been studying the fundamental properties of this material and exploring the ways to incorporate it into devices for new electronic technologies.

The ***electronic properties*** of graphene are described as the unique zero-gap semiconductor, the Fermi energy is localized at E = 0 where the two bands cross at K point (see Figure (5.3)). The electronic energy dispersion of graphene near the vertices of hexagonal Brillouin zone is written as $E = \pm vF|k|$, where *vF* is the Fermi velocity, about 106ms^{-1} [5].. In addition, very large ***current density*** can be applied through graphene, 10^8A/cm2 [27] and the highest known in plane conductivity at room temperature (2000−4000 Wm^{-1}K^{-1} for freely suspended samples [28]) and the highest carrier mobility (200.000 cm^2/V s [29]) were observed.

By applying an external electric field, it is possible to modulate the electrical conductivity (***electric field effect)*** of the graphene. In such a way, it might be possible to increase ten times the carrier concentration [22].

In addition to its unique electronic structure, graphene shows peculiar ***optical properties too***. In fact, it was demonstrated in graphene an optical absorbance of about 2:3% per monolayer independently of the wavelength from infrared to visible light [30]. Finally, due to its almost negligible spin–orbit coupling, the spins in graphene can be diffused over very long distances (***spin diffusion length***, between 1.5 and 2 μm at room temperature [31]).

Another unique phenomena observed in graphene is the Klein paradox, that leads to unity probability of tunnelling through arbitrarily high and wide barriers [4].

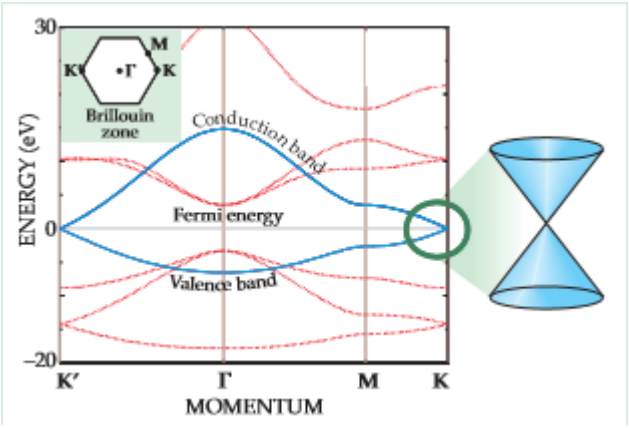

Figure (5.3) Band structure of graphene obtained within the tight-binding approximation. In red (blue) the bands with σ (π) symmetry. In the circle the "K" point is highlighted. (Picture adapted from [32]**).**

The remarkable ***electronic properties*** of graphene are due ultimately to its crystal structure of a honeycomb lattice of carbon atoms, which can be regarded as two interpenetrating triangular lattices. The s^2p^2 configuration of atomic carbon hybridizes in graphene into a configuration in which the 2s, $2p_x$, and $2p_y$ orbitals of each carbon are sp^2-hybridized to form in-plane σ bonds with its three nearest neighbors. The remaining p_z orbital is oriented along the z-direction, perpendicular to the graphene plane, and forms π-bonds which merge with neighboring $2p_z$ orbitals to form delocalized states across the graphene plane. The ease of movement of electrons in these π states is responsible for the extraordinary electrical conductivity of graphene. The graphene unit cell has two π orbitals forming two bands that may be thought of as bonding (the lower energy valence band) and anti-bonding (the higher energy conduction band) in nature. These are referred to as π and π∗ bands, respectively.

The gap between the π and π∗ bands closes at the K-points of the Brillouin zone, resulting in an energy–momentum dispersion which is approximately linear around the K points. This behavior is one of the many fascinating properties of graphene and is largely responsible for much of the excitement about this material.

Crystal structure. Honeycomb lattice

The honeycomb lattice is described by an hexagonal Bravais lattice with unit cell forming a lozenge (a rhombus with acute angles) containing two atoms, A and B as it is seen in Figure (5.4). This structure is invariant under 120 rotations and belongs to *P6/mmm* space group of symmetry.

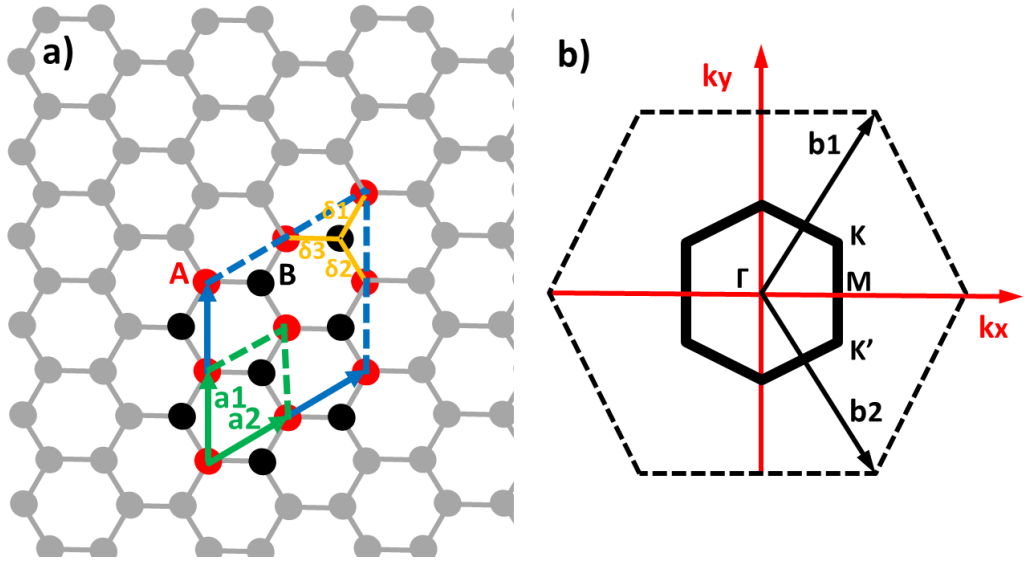

Figure (5.4) Honeycomb lattice and its Brillouin zone. a) Lattice structure of graphene, composed of two interpenetrating triangular lattices (a1 and a2 are the lattice unit vectors, and δi, i = 1, 2, 3 are the nearest-neighbor vectors). b) Corresponding Brillouin zone. The Dirac cones are located at the K and K' points

The adjacent carbon atoms are separated by 1:42 Å, the nearest neighbors vectors are:

$$\delta_1 = \frac{a}{2}(1,\sqrt{3}), \qquad \delta_2 = \frac{a}{2}(1,-\sqrt{3}), \qquad \delta_3 = -a(1,0) \tag{5.1}$$

where a is the C-C bond length. Graphene lattice constants have the value of a1 = a2 = a = 2:46 Å and the lattice vectors are defined as follow:

$$a_1 = \frac{a}{2}(3,\sqrt{3}), \qquad a_2 = \frac{a}{2}(3,-\sqrt{3}) \tag{5.2}$$

The unit vectors of the reciprocal lattice are:

$$b_1 = \frac{2\pi}{3a}(1,\sqrt{3}), \qquad b_2 = \frac{2\pi}{3a}(1,-\sqrt{3}) \tag{5.3}$$

And are related to lattice vector by the relation:

$$a_i b_j = 2\pi\delta_{ij} \qquad (i,j = 1,2) \tag{5.417}$$

Where ij is the Kronecker delta.

By restricting the reciprocal space to certain region called first Brillouin zone (IBZ), is possible to be built the primitive cell by translation of the reciprocal space vectors. In the IBZ, the two points, K and K', of particular importance for the physics of graphene, are located at the corners of the hexagon that outlines first Brillouin zone, right panel of Figure (5.4). Their positions in the reciprocal space are given by:

$$K = \left(\frac{2\pi}{3a}, \frac{2\pi}{3\sqrt{3}a}\right), \qquad K' = \left(\frac{2\pi}{3a}, \frac{2\pi}{3\sqrt{3}a}\right), \tag{5.518}$$

5.1.2 Growth techniques

Depending on the degree of perfection and size desired, graphene can be grown using different techniques.

The most used technique for the epitaxial growth of graphene on metallic surfaces is the ***chemical vapor deposition (CVD)***. This is based on deposition of molecules containing carbon onto a transition metal surface. The most used precursors are ethylene or methane [33] but it is also possible to grow graphene using a different carbon based molecules [34]. The sample is typically placed in a UHV chamber, with a base pressure of approximately 10^{-10} mbar and is annealing between 900 and 1100 K depending on the quality required. Afterwards, the gas is introduced into the chamber contacting with the hot surface. These surfaces could be of different nature, including foils, epitaxial layers deposited onto a bulk material, crystalline substrate, such as Pt(111) [35], Ir(111) [33],Cu(111) [36], Ni(111) [37], Ru(0001) [38],and more different materials as well as polycrystalline surfaces [39]. ***Temperature programmed growth (TPG)*** has also been used on transition metals. The main difference with the CVD method is that in TPG the carbon containing species are added to the 'cold' surface with subsequent annealing to stimulate the growth, while in CVD the species are added to the surface which is already 'hot'. In another method, to be called the ***segregation method*** hereafter, carbon is deposited on a surface maintained at such a high temperature that a proportion of C atoms are

absorbed into the bulk of the metal. Upon cooling, the absorbed carbon segregates from the bulk to the surface and becomes mobile forming graphene flakes, i.e. the segregated carbon in the bulk is used as a source. In addition to these methods where graphene is formed on metal surfaces, graphene can be ***grown on SiC***. The most widespread approach consists in heating SiC to a high enough temperature for silicon to sublimate from the surface, leaving behind carbon atoms that may then form graphene.

5.1.3 Interactions with transition metals.

The bottom metallic layer is known like buffer layer, affects the characteristics of graphene. In fact, most of the ideal properties for pristine graphene are modified by interactions at its interfaces. The interaction with metal substrates affects the intercalation of different elements between the graphene layer and the underlying buffer. Preparation of graphene on metallic buffers as Ir(111) or Pt(111), is achieved using CVD to decompound the ethylene (C_2H_4) molecule in a single layer. In the case of ***Ir (111) surface*** carbon has low solubility, is usually limited to just one layer. The Ir(111) surface gives rise to the growth of graphene with various orientations, see Figure (5.5), multiple domain phases which are rotated by various angles with respect to the R0 phase.

These domains each have different structural properties such as moiré repeat distance, gr–Ir separation and corrugation. The cause of these multiple domains is suggested to be due to the interaction strength between the graphene and the substrate surface. For Ir(111) the interaction with graphene is weak [40] and it is possible then that multiple orientations exist due to the limited influence of the surface. Compared to the Ir or Ru surface (with stronger interaction), the interaction between the ***Pt(111) surface*** and the graphene is considerably weaker [40]. As a result of this a main feature of graphene grown on Pt(111) is that there are many rotational domains [35]. Each of the domains has a moiré type structure with unit cells that are each sized differently [36] as shown in Figure (5.5). The super-structure of the moiré pattern panel.a) the effect is shown, where the pattern is generated by the superposition of two lattices rotated each other. In graphene, other regular superstructure, due to an incommensurate phase, is formed from the mismatch of the periodicity of the lattice of graphene and the underlying lattice of the metal. An example is given in Figure (5.5) panel c) which shows the moiré resulting from the slight mismatch of graphene on Ir(111) and in

panel b) the pattern showed is between graphene and Pt(111) 12 degrees rotated.

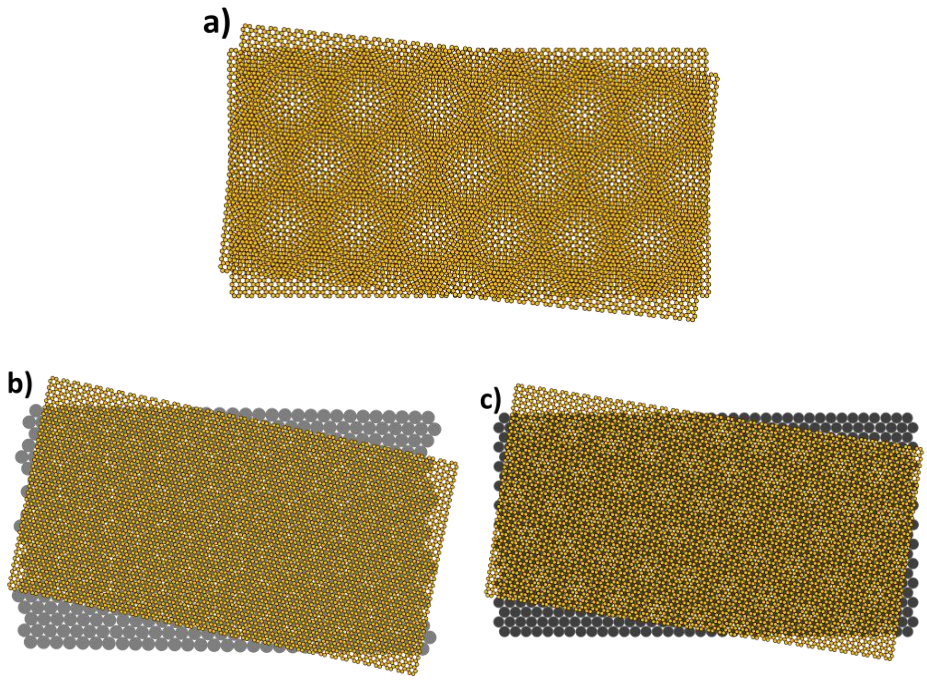

Figure (5.5): a) Moiré pattern obtained by stacking two honeycomb lattices with a relative angle. b) Moiré pattern obtained by stacking graphene (orange lattice) grown epitaxially on Pt(111) (grey lattice) 12 degrees rotated. c) moiré pattern of graphene (orange lattice) on Ir(111)(black lattice).

The interaction of the graphene varies by changing the position along the surface ordering of the carbon atoms rings with respect to the underlying atomic structure of the substrate

5.2 Growth process

The growth process is achieved in four stages:

- Growth of epitaxial metallic (Pt(111, Ir(111)) buffers on oxide single crystal substrates [(111)-oriented MgO and STO, and Al2O3 (0001)].
- Growth of epitaxial graphene on the epitaxial buffer.
- Evaporation of the ultrathin FM layer (Co) on the graphene surface
- Co film intercalation below graphene by thermal annealing.

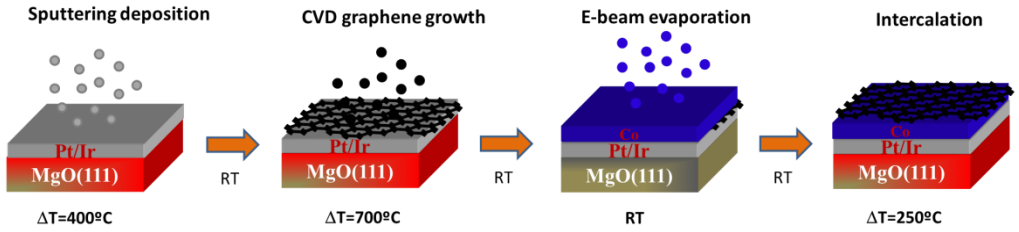

Figure (5.6) Schematic of the UHV growth process performed in four stages: i) buffer layer sputtering deposition at high temperature, ii) epitaxial graphene growth by CVD, iii) Co evaporation by molecular beam epitaxy on the graphene surface, iv) Co intercalation by thermal annealing in UHV underneath graphene at 250 °C.

In the case of the samples with lead layer, is necessary adding two more stages:

- Evaporation of Pb on the graphene surface
- Pb film intercalation below graphene by thermal annealing.

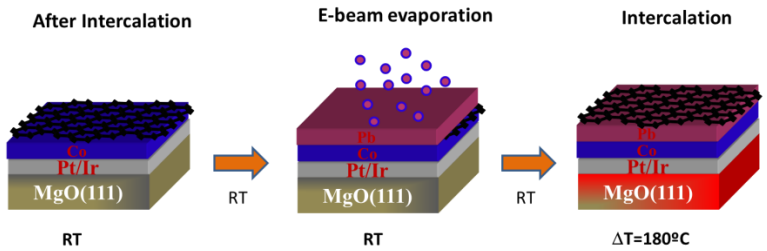

Figure (5.7) Schematic growth process of Pb samples achieved in two extra stages: i) evaporation of Pb by molecular beam epitaxy on graphene surface ii) Pb intercalation under graphene at 180 °C.

All the steps were developed in-situ in ultrahigh vacuum (UHV) with base pressure in the 10^{-10}mbar range. After each step characterization measurements were performed (LEED and XPS) to test the good development of the process and the quality of the film. In the followings subsections the whole process is detailed.

5.2.1 Buffer layer

The buffer layer was grown on MgO (111) substrate pre-treated ex-situ, following the procedure described in [Chapter 4 section 4.1.2]. Into the sputtering chamber in UHV ($1x10^{-8}$) the substrate was heated at 400°C during 1 hour.

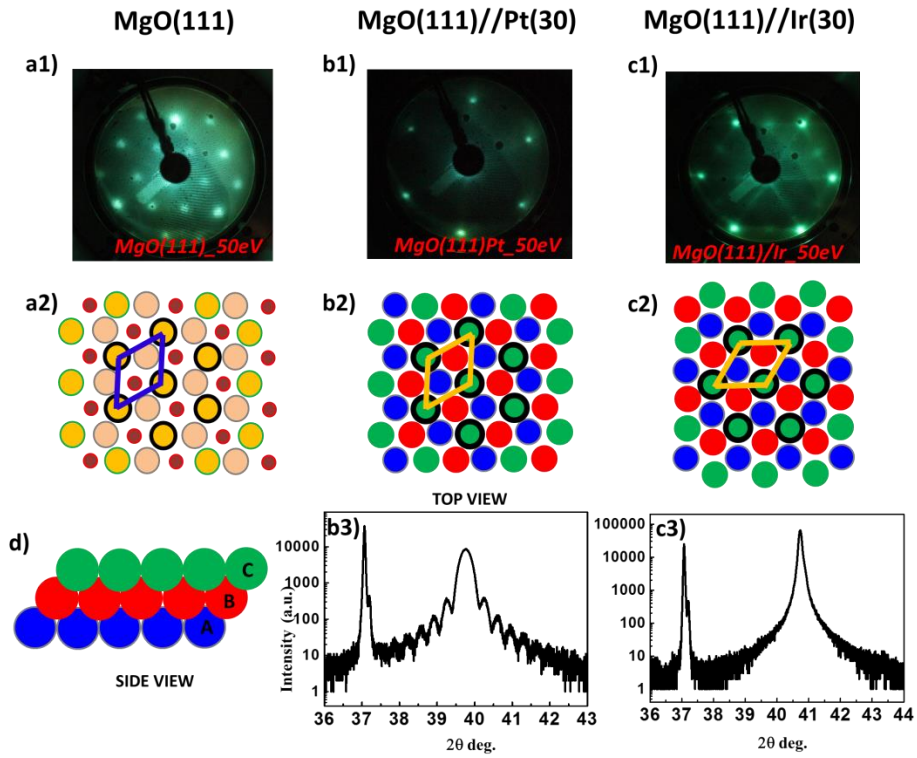

Figure (5.8) Overview of the structural characterization of MgO(111)-buffered systems. a1) LEED pattern of (111) surface of MgO(111) crystal acquired at 50eV. a2) Scheme of an ideal MgO(111) plane (top view), where the surface oxygen layer is represented with orange spheres, the second Mg layer with red spheres and the bottom layer of oxygen with pink spheres. Blue lines indicate the 1x1 unit cell. b1) LEED pattern of (111) surface of Pt buffer layer acquired at 50eV. b2) Scheme of an ideal Pt(111) plane (top view), where the surface top layer is represented with green spheres, the second layer of the stacking with red spheres and the bottom layer with blue spheres. Yellow lines indicate the 1x1 unit cell. b3) θ-2θ XRD scan around the FCC (111) Bragg-peak of sputtered Pt on MgO(111) ($2\theta=40^{o}$ corresponds to Pt(111) crystallographic peak). c1) LEED pattern of (111) surface of Ir buffer layer acquired at 50eV. c2) Scheme of an ideal Ir(111) plane (top view), where the surface top layer is represented with green spheres, the second layer of the stacking with red spheres and the bottom layer with blue spheres. Note the 30^{o} rotation of the Ir pattern with respect to the Pt(111) one (yellow lines represent the 1x1 unit cell). c3) θ-2θ XRD scan around the FCC (111) Bragg-peak of sputtered Ir on MgO(111) ($2\theta=41^{o}$ corresponds to Ir(111) crystallographic peak). d) Side view of a FCC (111) with ABC stacking.

The growth was performed by sputtering Ar^{+} deposition with partial gas pressure in the range of 10^{-3}mbar and 15W magnetron power, in parallel configuration between sample and target and 5cm distance. The rate was calculated by the in-situ QB. After the deposition, the heater was switched off and the sample was cooled down to RT. Two different buffer layers (Pt(111) and Ir (111)) have been grown to analyze the influence of the

bottom layer. In this step, the sign and the strength of the DMI at the bottom interface of the FM is tuned by using Pt(111) or Ir(111). In Figure (5.8) LEED pattern and a schemes of the stack are shown. The left panel shows the substrate crystallinity characterization of the (111) face. The scheme shows with yellow spheres the exposed face composed by $O_{-2,}$ the second Mg^{2+} layer (dark red) and the third oxygen layer (pink). The LEED pattern of Pt(111) (Ir(111)) in the center panel (right panel) shows the first difference between the two metallic buffers. The two patterns are rotated 30 degrees, although both of them have the same FCC structure (ABC stacking sequence) showed in panel d). Two schemes of the stacking are shown in the middle part of central and right panels, the size of the spheres has been reduced by one half for graphical convenience. The upper layer (in green) reproduces the LEED pattern with a thicker black line. It is possible to explain this rotation due to a different epitaxial growth place starting point. Pt radius is bigger than the Ir, so the atoms of Ir move to different sites of the MgO crystal ($(\sqrt{3} \times \sqrt{3})$ $R30^{o}$) rotated by 30 degrees. The XRD spectra in panel b3 and c3 confirm the epitaxial growth of both layers.

5.2.2 CVD graphene

The UHV growth of epitaxial graphene on metallic hexagonal single crystal surfaces has been reported in (Ir(111) [10]). The choice of an insulating substrate allow us to grow good quality (111) textured films and afterwards will be possible ex-situ experiments and transport characterization avoiding current leaks through the substrate.

The sample (MgO (111)/Pt(30)) was placed into the CVD chamber and annealed to 700^{o}C during one hour in UHV with base pressure in the range of 10^{-9} mbar. Once the surface is homogenously hot, ethylene (C_2H_4) is introduced by a leak valve increasing the pressure one order of magnitude to 10^{-8}mbar during 30 minutes. The sample was then cooled to RT.

The LEED measurements confirm the presence of epitaxial graphene. The pattern has changed compared to the buffer layer. It is shown in Figure (5.9), a1) (b1)) part is presented the graphene on Pt(111)[40] (Ir(111)) [41]. The very weak chemical bonding of graphene to Pt(111), can be deducted from the incommensurate structure in the LEED pattern that indicates a variety of preferred orientations (rotational domains).

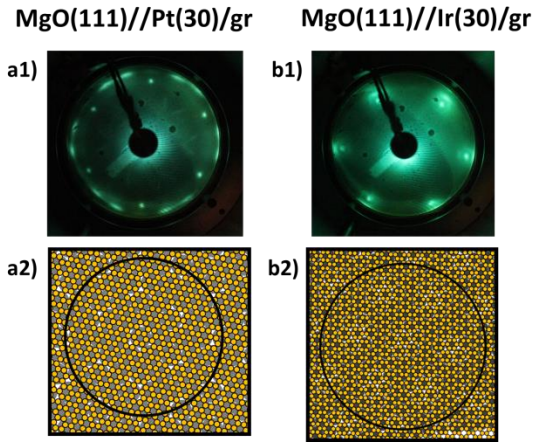

Figure (5.9) a1) LEED pattern acquired at 50eV of the epitaxial graphene sheet grown onto Pt(111) buffer layer. a2) Scheme of the moiré pattern formed between gr and Pt(111). b1) LEED pattern acquired at 50eV of the epitaxial graphene sheet grown onto Ir(111) buffer layer. b2) Scheme of the moiré pattern formed between gr and Ir(111)

Graphene on Ir(111) shows higher chemical bonding. The reduction in the 5d occupancy in going from Pt(d^9) to Ir(d^7) is probably the main reason for the higher covalent bonding for Ir [40]. Panels a2) and b2) reproducing the effects of the graphene on the different metals, Pt and Ir.

5.2.3 MBE Co evaporation

The next stage is the growth of the FM layer by molecular beam epitaxy (MBE). The sample was located with the surface parallel to the evaporator avoiding in this way an induced in-plane magnetic anisotropies. The deposition rate was calculated by a QB placed next to the sample holder, and it was 30 sec. per angstrom. Different FM thicknesses have been grown (Co6, Co2, Co1nm), in order to vary the PMA strength. The Co thickness was confirmed by acquiring XPS before and after the Co deposition and analyzing the Pt peaks.

5.2.4 Intercalation

The last step is the intercalation of the FM Co film below graphene by thermal annealing in UHV. Taking advantage of the defects and wrinkles created on the graphene after cooling the surface, the migration of the Co atoms bellow the carbon starts increasing the temperature of the sample. The thermal activation induces energy to the system, initiating the intercalation process.

To obtain a good quality interface between Co and Pt, and at the same time to avoid intermixing between Co and Pt, is very important to control accurately the temperature. The optimal intercalation temperature was found to be 250°C for Pt/gr and 350 °C for Ir/gr.

The intermixing process creates an irregular interface decreasing the total effective DMI and enhances the depinning field necessary to move DW. The intercalation was detected by acquiring fast XPS spectra at the C 1s, Co 2p and Pt 4d edges during the thermal annealing. In such a way, I was able to precisely determine the temperatures in which the intercalation and intermixing occur. As observed in Figure (5.10), both Pt(111) and Ir(111) buffered samples present the typical features due to the gr even after the Co intercalation.

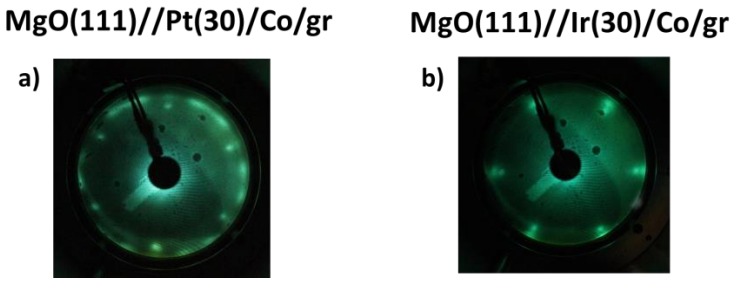

Figure (5.10) LEED patterns acquired at 50eV of the epitaxial Co layer intercalated underneath the graphene sheet on a) Pt on MgO(111) and b) Ir on MgO(111).

5.2.5 Samples with Pb layer

To grow Pb and intercalate it below graphene, the two last stages must be repeated adjusting some parameters. The evaporation is performed by MBE as Co in the same conditions with different evaporation rate. The intercalation process occurs at lower temperature around 180°C. There are not good images of LEED pattern after Pb intercalation. Is possible to see the graphene rings, but the spots belonging to the metallic layer have vanished. Further testing will be required to determine if the Pb layer is homogeneously expanded underneath graphene or not.

5.3 XPS study

The following part of the thesis presents the XPS characterization and spectra curve fitting procedures performed to quantitatively analyze each stage of the growth. Using a semi-empirical approach, the fitting procedures applied determine the sum of the photoelectrons for each chemical state. This can then be directly related to the relative percentage of each chemical state at the surface of a sample. The characterization was performed measuring first by means of a survey scan, once the peaks are identified, the following spectra were measured focus on the energy region of each core level corresponding to each component. C1s, Co2p, Pt4d and Pb4f are the binding energy levels analyzed. In Figure (5.11), the survey spectra of the four stages of the growth process are shown. In panel a) are overlapping Pt on MgO and gr on Pt. Both spectra have the same intensity and background, the only difference is the appearance of the carbon peak belongs to the presence of the graphene layer. It is shown in the capture into the panel a). After Co deposition the spectrum changes. In panel b) appears the two last survey corresponding to the deposition of Co and its intercalation. The photoelectron lines 2s and bigger $2p_{1/2}$ and $2p_{3/2}$ appearing at 924, 793 and 778 eV; it is the evidence of the presence of Co. Analyzing how much decrease the intensity of the Pt peaks is possible the estimation of the Co thickness. It will be shown in the following subchapter. After the intercalation, graphene is on the top again and the Co peaks intensity is reduced due to the attenuation due to top graphene layer. Blue spectrum (after intercalation) shows less intensity compared to the green one. Opposite behavior is shown by C1s peak, which increases its intensity after the intercalation.

XPS technique had been the key to understand and optimize the intercalation process. Unlike the scans after each stage, longer and with more number of scans (sweeps), during the intercalation fast scans were performed in real time analyzing the variations of the C1s, Co2p and Pt4d peaks taking into account the temperature in each scan.

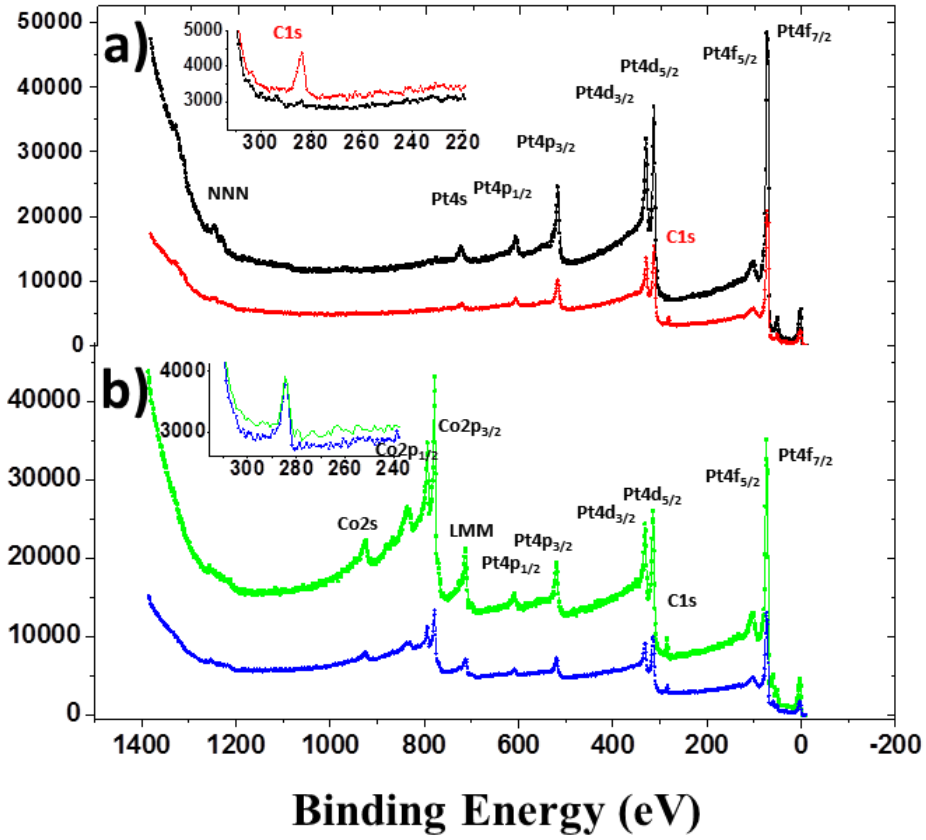

Figure (5.11) XPS survey spectra of the four stages of the growth process. a) Pt on MgO (black line) and gr on Pt (red line). Note the appearance of the C 1s peak after the graphene growth (inset panels). b) XPS survey spectra after the Co deposition (green) and after its intercalation (blue). The peaks centered at 793eV and 778eV correspond to metallic Co $2p_{1/2}$ and $2p_{3/2}$. After the intercalation, we notice a reduction of the Co peaks intensity due to the attenuation of the top graphene sheet. All spectra are vertically shifted for convenience.

Spectra were analyzed using CasaXPS software [42] (version 2.3.15). Gaussian (Y%)–Lorentzian (X%), defined in CasaXPS as GL(X). The best mixture of Gaussian–Lorentzian components is dependent on the instrument and resolution (pass energy), the average of the measurements have been fitted with a line shape of GL(70) while for spectra with broad peak shapes and/or satellite structure line shapes of GL(30) are used for the individual components. The C1s and metallic 2p and 4f core lines have been fitted using an asymmetric curve. This asymmetry was defined in the form of LA(α, β, m) where α and β define the spread of the tail on either side of the Lorentzian component. The parameter m specifies the width of the Gaussian used to

convolute the Lorentzian curve. A standard Shirley background is used for all reference sample spectra. The Binding Energies (BE) of the whole set of measurements are referred to the Fermi edge of each sample.

5.3.1 Pt/Co/gr systems

Many factors are involved in the intercalation process. The "receipt" to get the perfect, flat and homogenous sample requires deep and meticulous analysis of the experiments. Variations in the heating-up ramp, in the base pressure, quality of the graphene layer or even the substrate are important factors to take into account. I will present three kind of samples, i) homogeneous and completely intercalated, ii) sample with interdiffusion in the Co/Pt interface and iii) sample not completely intercalated. All the samples have been grown following the steps previously indicated.

Reference sample Pt/Co0.9/gr

The following sample will be considered as reference sample. All the stages and measurements were developed with positive results obtaining a homogenous sample and good process of intercalation without interdiffusion. Pt (30 nm) layer was grown by Ar sputtering deposition on annealed substrate (400^{o}C) with 10W plasma power and 0.23 Å/sec deposition rate. After the growth, the sample in-situ was analyzed by LEED Figure (5.8)) and XPS Figure (5.11) panel a). The survey spectrum shows the chemical species belongs to Pt layer. MgO substrate is not visible through the buffer layer. From now on the spectra are focused on the energy region of the core level corresponding to Pt4d, C1s and Co2p. In 2) the spectra of Pt $4d_{3/2}$ and $4d_{5/2}$ core levels in each stage of the growth process is shown. In panel a) the spectrum of the Pt layer on MgO (111) $4d_{3/2}$ and $4d_{5/2}$ core levels appears at BE=315 and 332eV.

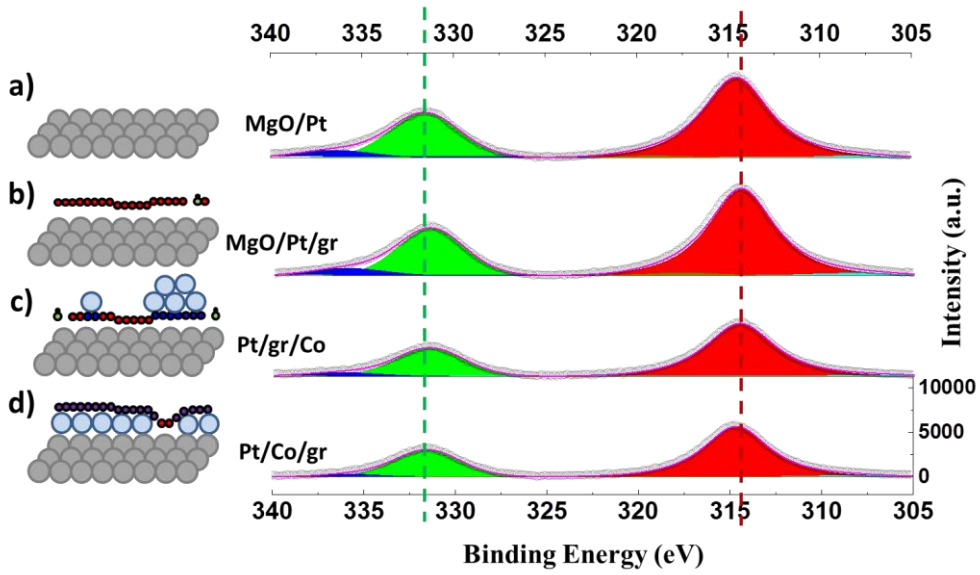

Figure (5.12) XPS spectra in the region of Pt $4d_{3/2}$ and $4d_{5/2}$ levels at each stage of growth process. The side panels indicate the stage of the growth: (a) grey spheres indicate the epitaxial Pt(111) buffer on MgO(111); (b) red spheres refer to C atoms of graphene; (c and d) light-blue spheres represent the Co atoms evaporated on top of graphene (forming islands or clusters) before and after the intercalation, respectively. In the sketches, the C atoms of graphene in contact with Co and Pt are in blue, whereas the C atoms in contact with the intercalated Co are in purple. The Pt_{4d} peaks are at B.E.=315 and 332eV. Note that the area of the peaks decreases after gr and Co growth, while it remains unchanged after (and during) the intercalation.

The left part of the panel shows the diagrams of the growth step where the XPS measurement was performed. Epitaxial graphene was grown on the Pt surface by CVD in a 10^{-8}mbar C_2H_4 gas pressure during 30 minutes, once the surface sample have been annealed at 700°C during one hour. The XPS measurement performed after the growth, confirms the good quality of graphene. A narrow and well define C1s core level (Figure (5.13)) appears at 284eV of BE [40] [43], it was able to fit with one asymmetric component corresponding to the sp^2 hybridization of the C-C bonding on Pt(111). Looking the Pt 4d core level panel b) of Figure (5.12) the total intensity is less than the previous stage, when only Pt layer was deposited on MgO(111) substrate. Therefore, the interaction between the graphene layer neighbor, placed bellow, changes from physisorption between the graphene layers in a high orientated pyrolytic graphite (HOPG) to weak chemisorption in Pt/gr and Ir/gr (will be shown later on) and growing to stronger chemisorption Ni/gr or Ru/gr systems. Since the Ir/gr bond is stronger than that of Pt/gr, the

corrugation of graphene is somewhat more pronounced on Ir(111) than on Pt(111) [40] The moiré patterns (explained in Chapter 5.2) create a periodic alternation, favorable and unfavorable adsorption sites results in this weak periodic corrugation of graphene. Ng et al, present in their two different active-bonding parts of graphene, less bonding parts called “wires” are the elevated parts and more bonding parts, the low lying called “pores”.[43]

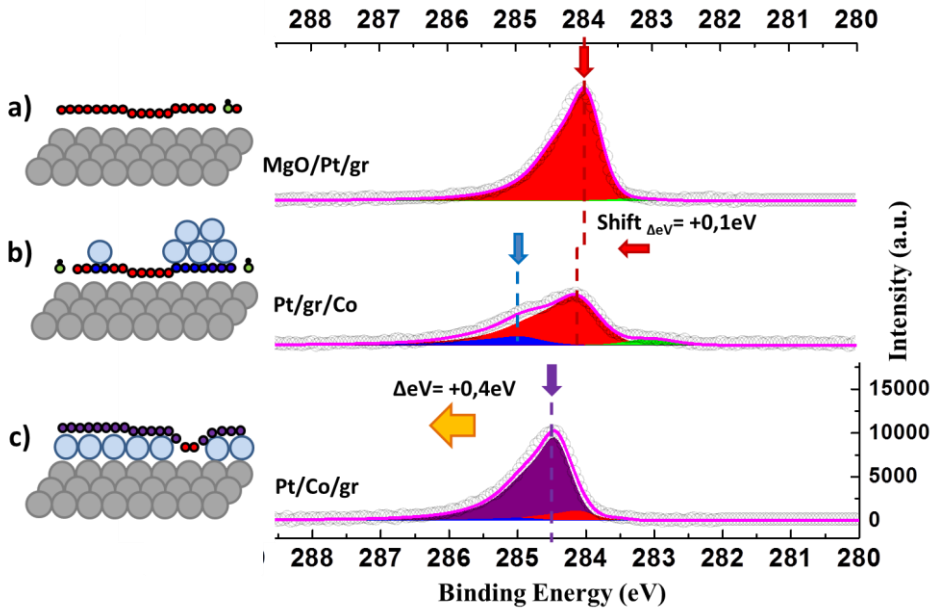

Figure (5.13) XPS spectra in the region of the C1s peak at each stage of growth process. The side panels indicate the stage of the growth: (a) grey spheres indicate the epitaxial Pt(111) buffer on MgO(111); (b) red spheres refer to C atoms of graphene; (c and d) light-blue spheres represent the Co atoms evaporated on top of graphene (forming islands or clusters) before and after the intercalation, respectively. In the sketches, the C atoms of graphene in contact with Co and Pt are in blue, whereas the C atoms in contact with the intercalated Co are in purple. The C1s peak appears at B.E.=284eV (red component in the fit). After the Co evaporation, a new component of C1s is found at 285eV (blue component). To note the chemical shift of about +0.1eV after the evaporation, whereas after the intercalation it shifts to 284.5eV (+0.4eV from the first peak).

C=C bonding are located in-plane (parallel to the surface) and belongs to σ^*_1 and σ^*_2 states and are full occupied due to the sp^2 carbon hybridization. π states are free to create new bonds with the Co atoms in the next stage of growth process. After the analysis of several XPS spectra is possible relate the behavior of the π bonds when the gr surface is covered with Co atoms relating it to other works in literature based on hydrogenated surfaces [43] . The evaporation was developed in UHV conditions in the higher 10^{-9} mbar

range at RT with 45 sec per angstrom rate, with an estimation of 1 nm Co thickness. The first XPS survey spectrum after the evaporation (Figure 5.11)b) confirms the presence of Co on the surface. Now Co2p core levels are the most intense, decreasing by more than a third the intensity in the Pt core levels due to the inelastic mean free path (IMFP) that the Pt electrons have to travel through the Co layer. IMFP is the key material parameter that has been used to describe inelastic scattering of the detected signal electrons in XPS and allow us to calculate the real thickness of the top layer. Co2p spectrum is shown in Figure (5.16), after de Co evaporation a well-defined asymmetric metallic peaks appear at Be 778.3eV ($2p_{3/2}$) and 793.3eV ($2p_{1/2}$) with Δ_{EB} 15eV [44]. On the other hand as have been said before, the intensity of the Pt 4d core level decrease (Fig.(5.14)c) and C1s not only decrease change the shape also. Due to the new chemical environment C1s peak shifts to higher BE 0.1eV (EB=284.1eV) due to the new interactions or new graphene corrugation, and another component appears at BE=285eV. It is assigned to sp^3 hybridized C atoms bonding with the Co atoms. At BE=283.2eV appears another component, due to the defects and C-H bondings. In the current stage of the growth process, the C atoms are bonded each other (sp^2) and bonded as well with Pt and Co by different BE. Have been deduced by carefully study of several evaporation processes that in this case Co was deposited on the surface forming islands (it is represented in the balls scheme in the right part of the XPS spectra). This explains why the new component (285eV) is only 20% of the total convolution area and the 284eV EB peak keep being mayor. The area analyzed by XPS is in the order of μm^2. Into this big region will be areas covered by more than 1nm of Co and others not covered. In the case of homogeneous evaporations blue component in Figure (5.13) b) should be at least identical to the red one.

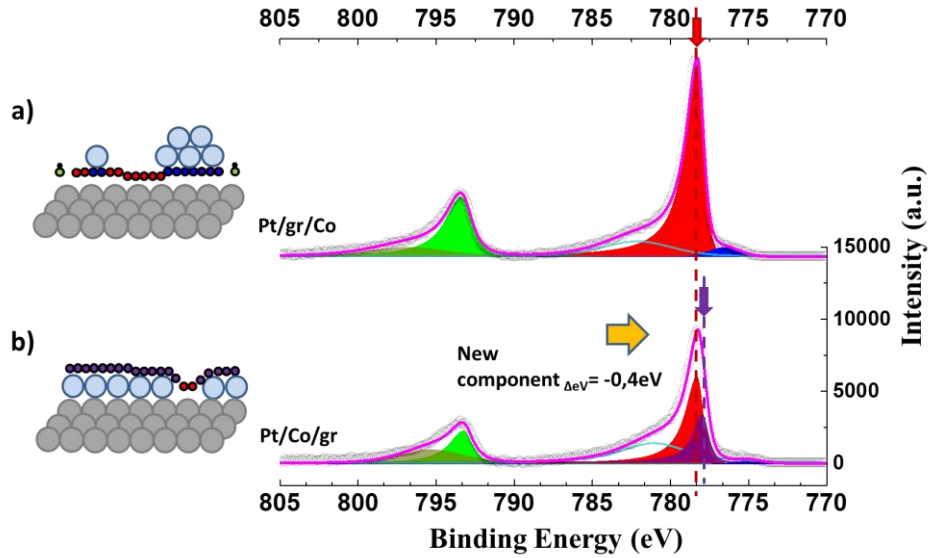

Figure (5.14) XPS spectra in the region of the Co2p peaks at each stage of growth process. The side panels indicate the stage of the growth: (a) grey spheres indicate the epitaxial Pt(111) buffer on MgO(111); (b) red spheres refer to C atoms of graphene; (c and d) light-blue spheres represent the Co atoms evaporated on top of graphene (forming islands or clusters) before and after the intercalation, respectively. In the sketches, the C atoms of graphene in contact with Co and Pt are in blue, whereas the C atoms in contact with the intercalated Co are in purple. The Co 2p 3/2 peak appears at B.E.=778eV (red component in the fit). After the Co evaporation, the peak shifts towards to lower binding energies (-0.4eV with respect to original peak).

After the Co intercalation process, C atoms will be in the last chemical environment. In the present case where is presented a complete intercalation of the film, the graphene is placed on the Co film. The interaction with the Co is higher than the Pt so the new component, purple in Figure (5.13) c), appears at BE= 284.5 eV. The total peak distance between the Pt/gr component (red) and the last Co/gr is +0.4eV at higher EB. This charge transfer is the clue that confirms the intercalation of the Co layer under the graphene. More than 93% of the total area of C1s core level is placed on the Co surface, 5% of the carbon atoms still are in contact with Pt layer and only 2% or the carbon have on top another Co atom. It is shown in the schemes adjacent to the XPS spectra. The decreasing of intensity and the broadening of the peak are the keys to know that the Co is placed below C and to extract the information of the $2p_{3/2}$ core level. The fit of the curve improves when the peak is fitted with two components, red and purple in Figure (5.14) panel b). The new component appears 0.4eV at lowest EB than

the previous component and belongs to the atoms of the surface in contact with the graphene layer and where the electron transfer is done. Finally to confirm the absence of interdiffusion in Pt/Co interface Pt4d core level have been analyzed before and after of the intercalation. After Co evaporation, the Pt area must be identical before and after. Only the Pt4d area will increase if atoms of Pt moving up due to the thermal energy on the Co atom. In this case both areas are identic. The intercalation and the growth process have been finished successfully.

Intercalation temperature analysis

The intercalation process was developed in the same position than the XPS measurements. The heater located in the manipulator allows us to increase the temperature under perfect control.

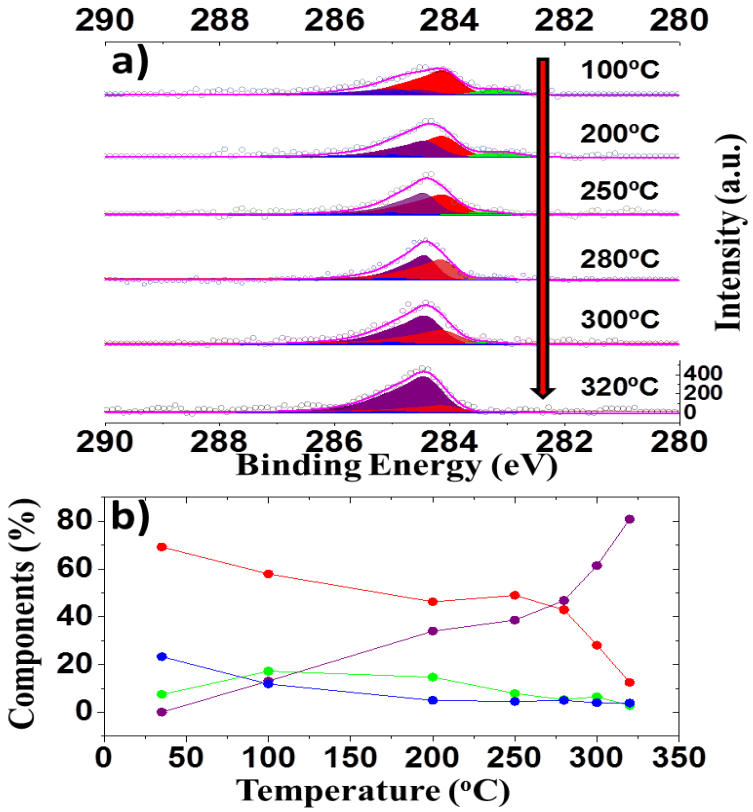

Figure (5.15) a) XPS spectra of C1s core level during the intercalation process. Four components are presented in all stages, Pt/gr (red component) at 284.1eV, at 284.5eV Pt/gr/Co (blue component), and at 283.2eV the component related to defects and rests of ethylene from the CVD. b) Components (%) as function of the temperature. Evolution of the components of C1s core level.

Consecutive scans were developed in sets of three ranges of energy belongs to C1s, Co2p and Pt4d core levels. Most represented steps of the C1s evolution is shown in Figure (5.16), from 100°C to 320°C. Four components were fitted in the first scan, BE=285eV (blue) corresponding to C atoms with Co on top and Pt bellow, 284.5eV intercalated areas wit Co bellow the graphene, 284.1eV is the C on Pt and at 283.2eV the component related to defects and rests of ethylene from the CVD. This last component will be disappeared at the end of the process due to the increasing of temperature. Figure (5.16) b shows the % of the components that conform the total convolution in function of the temperature. There are two exponential behaviors during the intercalation process; first, up to 250°C thermal energy induces energy to Co atoms to start the migration under the graphene layer using as drains the defects and wrinkles presented on the graphene.

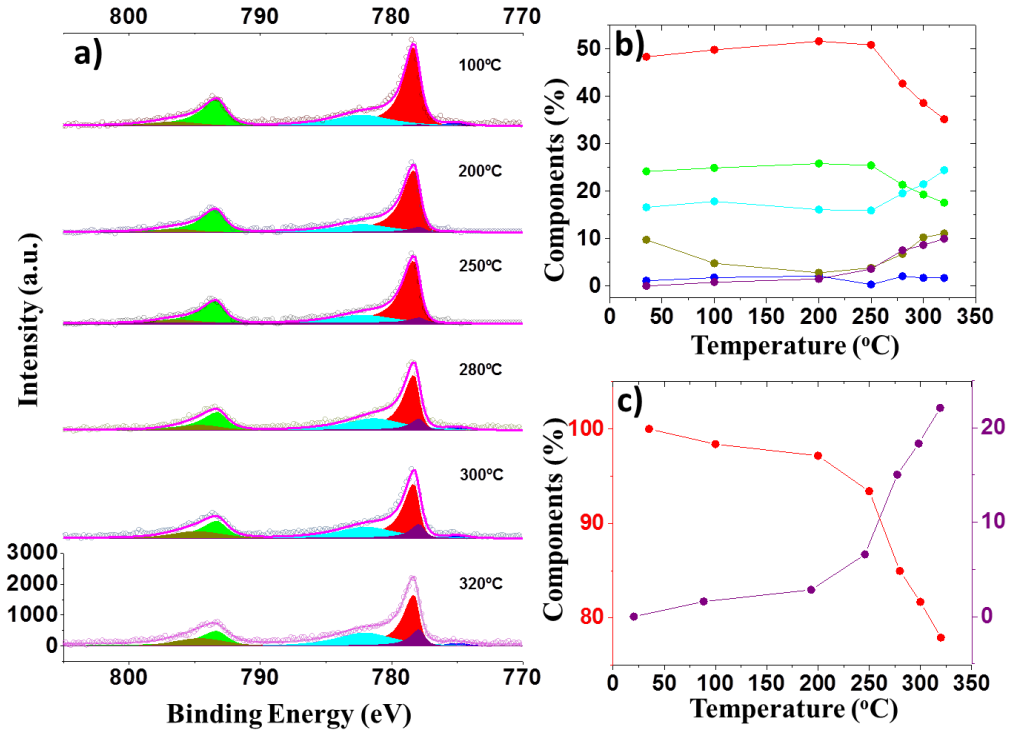

Figure (5.16) a) XPS spectra of Co2p core level during the intercalation process. A new component appears at 250°C (purple component) at lower B.E. (-0.4eV). b) Components (%) as function of the temperature. Evolution of the components of Co2p core level .c) Evolution of components of $2p_{3/2}$ core level.

During the Co intercalation, the C1s intensity increase almost recovering the total area prior to evaporation. The second part of the total intercalation could be considered as spreading completely as a continuous ML, it occurs from 250°C up to 320°C. The two components invert the areas exponentially being majoritarian the carbon atoms placed on Co layer. Looking the Co2p core level, once the temperature reach 150-200°C and atoms start to move under graphene, the new component (purple curve in Figure (5.18)a) appears. In panel b) is shown the temperature evolution of the total components and in panel c) the % variation of the two components of $Co2p_{3/2}$.

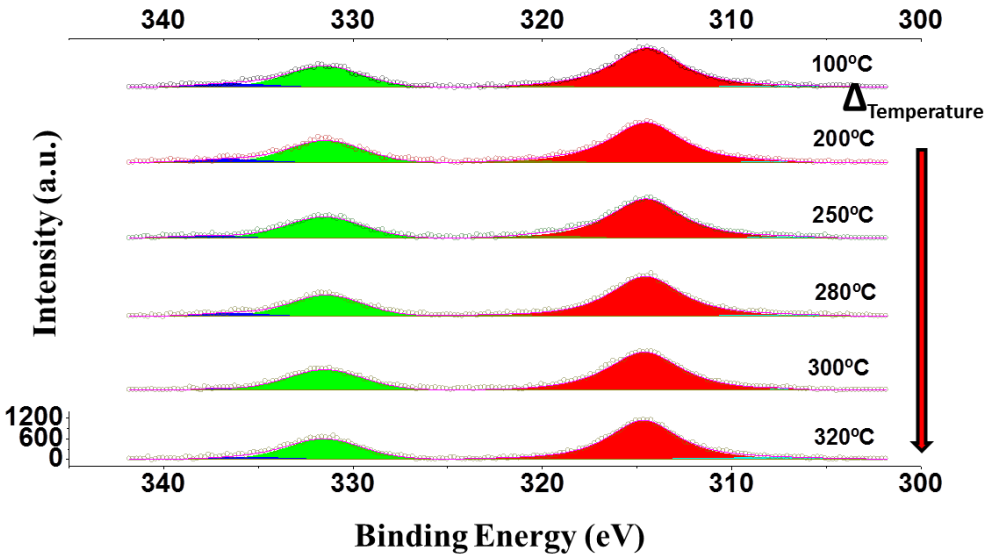

Figure (5.17) XPS spectra of Pt4d core level during the intercalation process. The Pt area is constant during the process. This indicates the absence of Co/Pt intermixing.

Finally as double check, the evolution of the Pt4d core level is shown in Figure (5.17). The area is constant during the experiment up to 320°C confirming the absence of interdiffusion.

Once the sample have been finished, was taken out from vacuum, and magnetically characterized by using M(R)OKE set-up. The hysteresis loop in panel b) of Figure (5.18) shows a very well define PMA with a huge coercive field, around 180mT. In the following chapter, the magnetic properties will be presented, but as first approximation is possible to say that graphene keep and induce PMA and protecting the FM layer from oxidation.

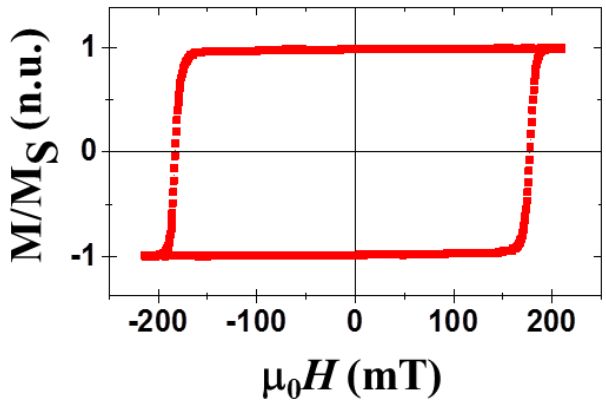

Figure (5.18) Vectorial resolved polar M-H loop normalized to the saturation magnetization M_S of epitaxial MgO(111)/Pt/Co(1)/gr, with Hc=180mT. The hysteresis loop presents square shape with sharp transitions.

Intermixed sample

The role of the interface is well known and repeated during past chapters of this thesis. Interdiffusion in the interface caused by an excess of temperature during the intercalation process, produced a raff interface not homogenous. Giving more thermal energy to the system, Co atoms move bellow the last ML of Pt. This intermixing increase Hc and the deepening field (Chapter IV), decreasing at the same time effective DMI and the homogeneity of the FM layer. The experimental results presented below, corresponding to an intermixed sample. It was grown following the same steps than the previous sample in the same conditions. The layer sequence in this case is MgO(111)/Pt(30)/Co(2)/gr increasing two times the thickness of Co layer to test the enhancement of PMA induced by the graphene top layer. After sputtering deposition of epitaxial Pt (111) (shown in Figure (5.19)c) graphene layer was grown by CVD on Pt buffer. XPS measurement shows a well define and narrow peak of C1s core level at BE= 284eV (Figure (5.19)a) and supported as well by LEED patterns. The deposition rate of the FM layer Co was estimated by QB and tested by XPS technic. The middle graph of panel a) shows the C1s peak after the evaporation of Co (Co2p is shown in panel c). In this case the evaporation was homogenous covering the entire surface; that is why the intensity in both C1s and Pt4d spectra has decreased. Using the Co IMFP index and the ratio between the Pt area before and after the evaporation the nominal thickness have been estimated:

$$d = \lambda * \ln\left({}^{A_1}/_{A_2}\right) \tag{5.6}$$

Applying Formula (5.6) the thickness obtained is closed to the nominal, 2.2nm. Due to the homogeneous Co deposition, the new component that appears at 285eV BE is closer than 50% of the total area convolution.

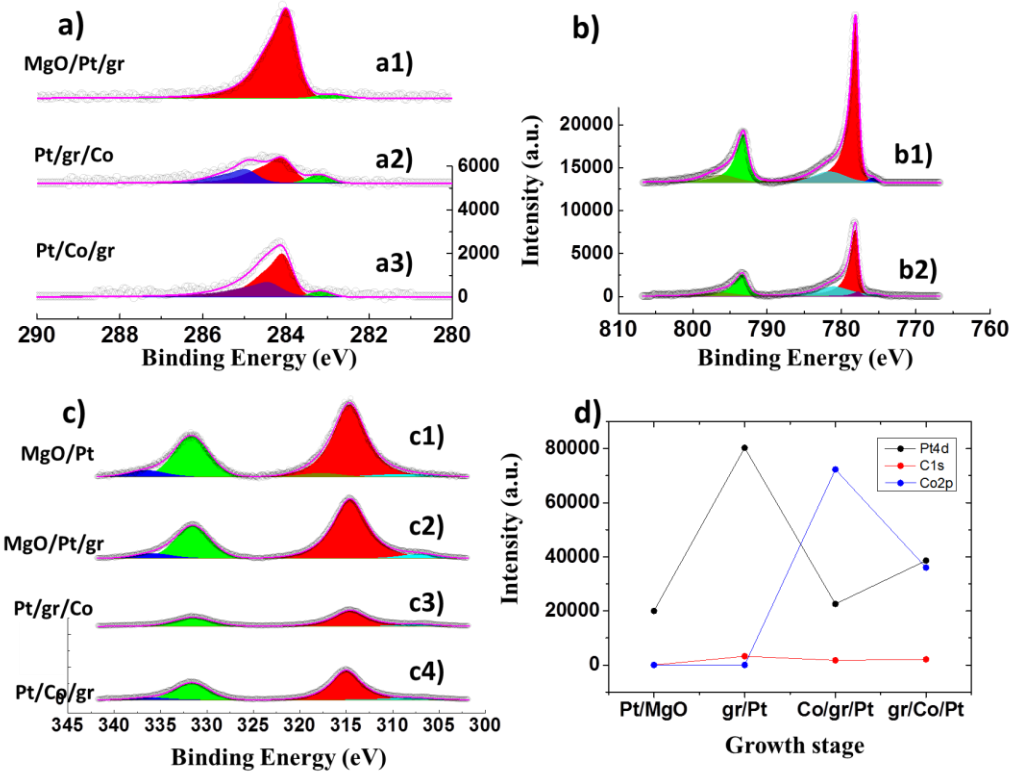

Figure (5.19) XPS spectra of a) C1s core level at each stage of growth process. a1) C1s peaks appears at B.E.=284eV (red component) before the evaporation of Co. a2) After the Co evaporation on graphene surface the spectrum presents a new component at 285eV (blue component). There is a chemical shift after the evaporation +0.1eV. a3) After the Co intercalation. The result of the intercalation is the appearance of a new component at 284.5eV (purple component), that is at +0.4eV from the original peak. b1) Co 2p core spectra present an asymmetric component at 778eV (red component). b2) After the Co intercalation a new component due to the atoms of the surface in contact with the graphene appears at -0.4eV from the first peak (i.e., opposite sign than C1s). c) XPS spectra of Pt $4d_{3/2}$ and $4d_{5/2}$ core levels in each stage of growth process. c1) Pt4d peaks appear at B.E.=315 and 332eV. c2) Pt4d core level shows a decreasing of the area due to the presence of the gr on the top. c3) After the Co evaporation, the Pt intensity decreases due to the presence of Co atoms on the top. c4) Increase of the total area of Pt 4d. It indicates the intermixing at the interface between Pt and Co. d) XPS peak intensities of Pt 4d (black), C 1s (red) and Co 2p (blue) peaks at different stage of the growth.

The maximum temperature applied during the intercalation of this sample has been higher than the interdiffusion limit, giving us the possibility to analyze its behavior.

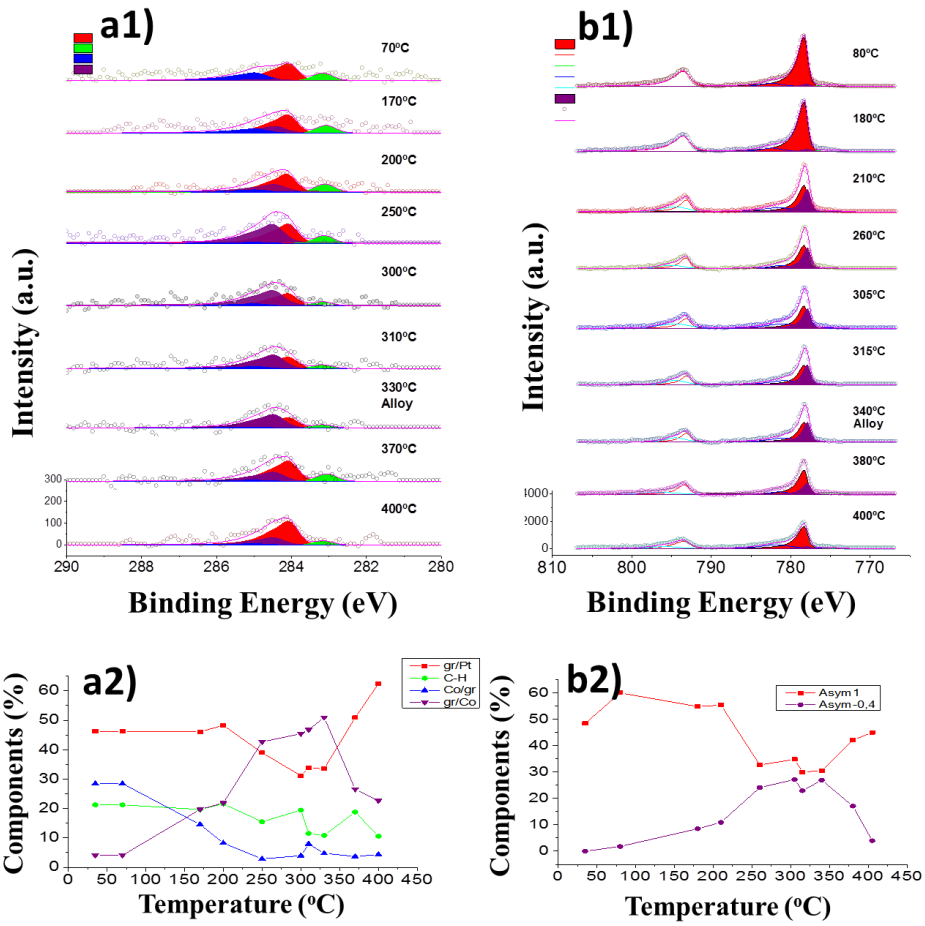

Figure (5.20) a) XPS spectra of C1s core level during the intercalation process. Four components are presented in all stages, Pt/gr (in red) at 284.1eV, at 284.5eV Pt/gr/Co (in blue), and at 283.2eV the component related to defects and rests of ethylene derived by the CVD growth. From 330°C starts the intermixing at the interface between Co and Pt. a2) Components (%) as function of the temperature. Evolution of the components of C1s core level .b1) XPS spectra of Co2p core level during the intercalation process. New component appears at 250°C (purple component) at lower B.E. (-0.4eV) b2) Components (%) in function of the temperature of $2p_{3/2}$ peaks.

A detailed study of the components during the intercalation is necessary. At first glance, analyzing the spectra after this process at RT, the intermixing at the interface between Co and Pt is evident. Looking at the C1s core level, is possible to say that the 100% of Co deposited have been intercalated,

because the component related to the carbon atoms placed between Pt and Co, Pt/gr/Co (blue component) has despaired and a new component appears at 284.5eV (purple component). But the major difference compared to the previous case Figure (5.15) is that the main component belongs to the carbon atoms on Pt not on Co. Pt4d and Co2p core levels confirms the intermixed behavior, Pt4d after the intercalation is bigger than the previous step because Pt atoms have placed on Co atoms. Due to the intermixing, the Co2p intensity has decreased more than the reference sample. Total intensities of each growth stages are shown in d). During the intercalation, C1s core level gives us accurate information about how the intercalation is developed. The evolution is shown in panel a) and b) of Figure (5.21). Up to 250^{o}C the process is identical to the reference sample the component at 285eV decrease while the component at 284.5eV related to the graphene on Co (purple) increases. From 250^{o}C to 300^{o}C at the same time, the intercalation and spreading mechanism occurs being majority the Co/gr component. Co2p spectra in panel c) confirm the intercalation, as the reference, a new component appears in $2p_{3/2}$ core level at 0.4eV lower BE. Intermixing process begins around 320^{o}C when Co atoms move below the Pt reverting the trend of both components. Before the alloying, more than 50% of the C atoms were placed on Co atoms being less than 30% which were located on Pt. At the end of the experiment when the temperature reached 400^{o}C, more than 60% of the graphene were place on Pt atoms and the charge transfer and peak shift did not occurs.

Unfinished intercalation process

The sample was prepared and grown following the same steps than previous experiments. In this occasion was evaporated 6nm of Co to analyze the enhancement of the PMA. Successfully evaporation was carried out and the surface was covered. Middle part of panel a) in Figure (5.21) shows how the intensity of C1s core level have been lost. In the insert graph is presented an enlargement of the spectrum. Three components as in previous samples appears at 283.2eV (C-H bonds), 284.1eV (Pt/gr) and 285eV (gr/Co)

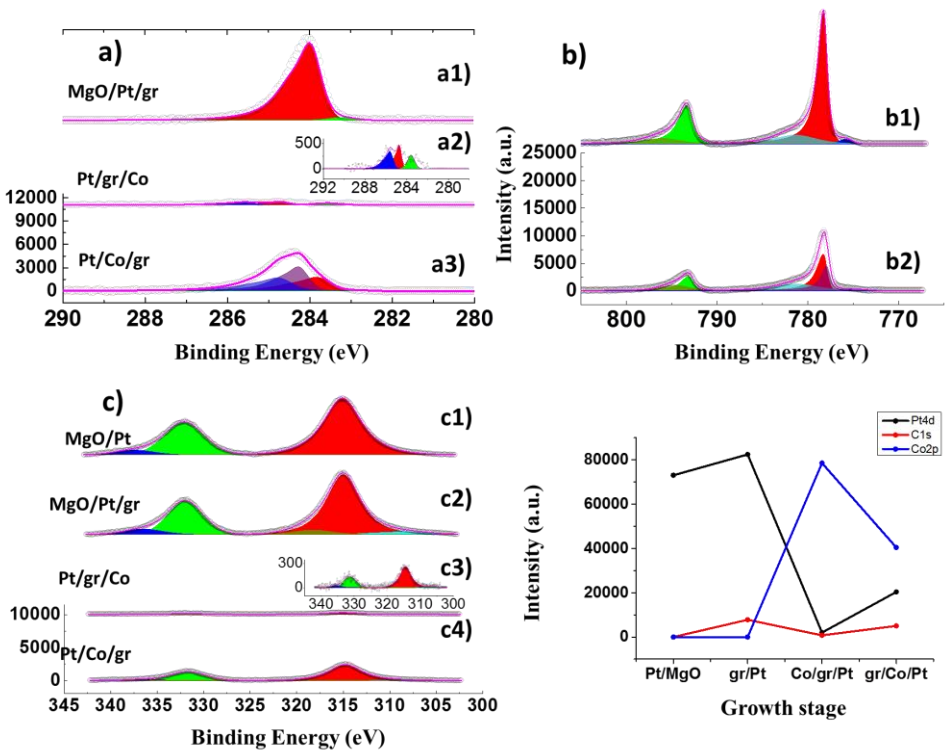

Figure (5.21) XPS spectra of a) C1s core level at each stage of growth process. a1) C1s core level at B.E.=284eV (red component) before and a2) After Co evaporation on graphene surface. C1s core spectra is almost disappeared under Co layer. In the sketch is presented a zoom of the components. a3) After the intercalation process a new component appears at 284.5eV (purple) (+0.4eV from the first peak). b1) Co 2p core spectra present an asymmetric component at 778eV (red). b2) After the Co intercalation a new component due to the atoms of the surface in contact with the graphene appears at -0.4eV from the first peak (i.e., the same value with opposite sign than C1s). c) XPS spectra of Pt $4d_{3/2}$ and $4d_{5/2}$ core levels in each stage of growth process. c1) Pt4d core level appears at B.E.=315 and 332eV c2) Pt4d core level shows a decreasing of the area due to the presence of the gr. c3) After Co evaporation the Pt intensity decrease due to the presence of Co atoms. c4) Increase of the total arear of Pt 4d. It indicates the interdifusion intermixing between Pt/Co. d) Growth stage as function of the total XPS intensity.

The bigger component (BE=284.5eV) indicates that the Co layer have been successfully intercalated and spread as complete ML in an order of 40% of the total surface analyzed. Other 28% of the surface is still covered by Co (blue component). In order to obtain 100% of intercalation, the temperature was increased up to 370°C intermixing the sample, due to this effect the remaining 30% of the total C1s area is considered like carbon placed on the Pt layer. Confirming the intermixed interface Pt4d core level after the intercalation have more intensity, bigger area, than the previous stage (panel c) and d))

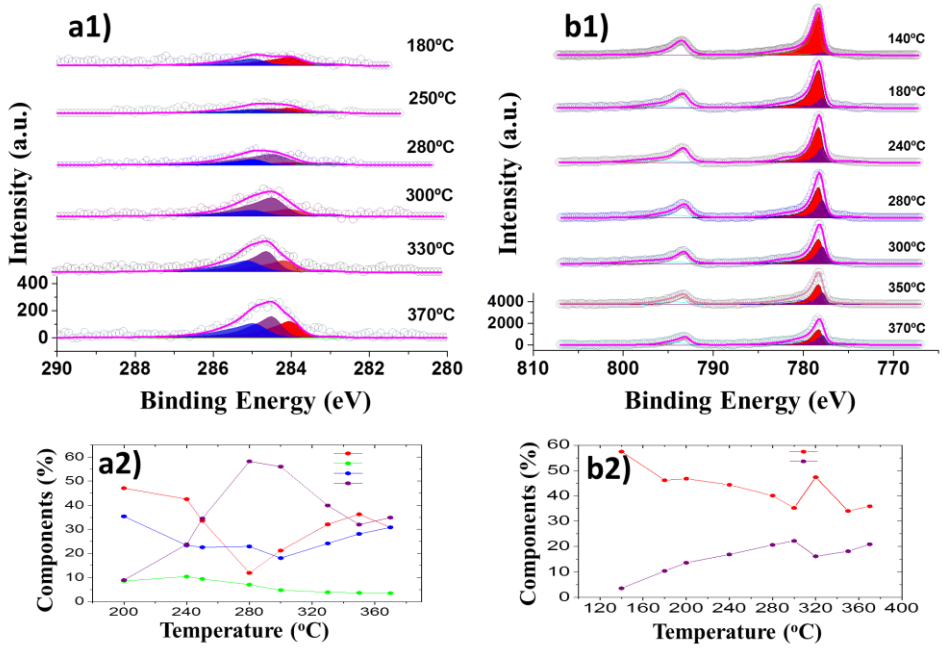

Figure (5.22) a) XPS spectra of C1s core level during the intercalation process. Four components are presented in all stages, Pt/gr (red component) at 284.1eV, at 284.5eV Pt/gr/Co (blue component), and at 283.2eV the component related to defects and rests of ethylene from the CVD. From 330°C starts the alloy in the interface. a2) Components (%) in function of the temperature. Evolution of the components of C1s core level .b1) XPS spectra of Co2p core level during the intercalation process. New component appears at 250°C (purple component) at lower B.E. (-0.4eV) b2) Components (%) in function of the temperature of components of $2p_{3/2}$ core level.

Analyzing more in detail the spectra during the intercalation is possible to determine the intermixing temperature and learn how develop the next procedures to intercalate FM layer as thick as possible. Around 280-300°C alloy temperature is reached, panel c) shows the slope change in the red curve (Pt/gr). It begins to increase and carbon on Co component (purple) begins to decrease. Thermal energy applied to the system induces mobility to the top Co atoms not intercalated, and the 3d islands on the graphene start to melt and spread on the carbon surface, increasing the area of the component related to Pt/gr/Co atoms (blue component). To avoid intermixed problems, once 280°C have been reached the temperature will be constant long enough to give energy to Co atoms making possible the migration under graphene. Why has not been possible to intercalate completely Co layer? As have been said previously, “drain” defects in graphene and thermal energy are necessary to intercalate Co. If graphene are strongly pinned on the Pt

surface around the defect, once the drain is full the Co mobility is impossible. In the other hand, if an island of Co is located far from defects, thermal energy will be not enough to move Co atoms below graphene.

5.3.2 Pt/Co/Pb/gr samples

The aim in these sample systems is to induce bigger SOC in graphene using lead. The additional intercalation has been developed at lower temperature than the Co intercalation to avoid the interdiffusion problems. The growth process has been done following the stages of previous samples. The structure of the samples with nominal thicknesses in nm is: MgO(111)/Pt(30)/Co(1)/Pb(1)/gr The evaporated cobalt was deposited forming islands in the graphene surface, reproducing the same behavior than the reference sample with 1nm of Co. But in this occasion the islands intercalated have not spread under graphene and more than 70% of carbon atoms are in touch with Pt. C1s core level is shown in Figure (5.23) panel a), before and after the intercalation the majority component of the total area is Pt/gr at BE=284.1eV. There is a partial charge transfer (0.4eV higher BE) but it is not majoritarian. It is confirmed looking the new component in $Co2p_{3/2}$ in Figure (5.24) panel a). This new component due to the interaction between Co and graphene interface is very small compared to the other samples analyzed, confirming the existence of Co island. Panel b) of Figure (5.24) represents the % of the peak composition in function of the temperature in the two intercalations. Lead evaporation has been performed in UHV in the range of 10^{-9} mbar at RT in the same chamber and conditions than Co evaporation. The upper part of panel b (Figure (5.24)) contains the doublet Pb4f core level at 142eV and

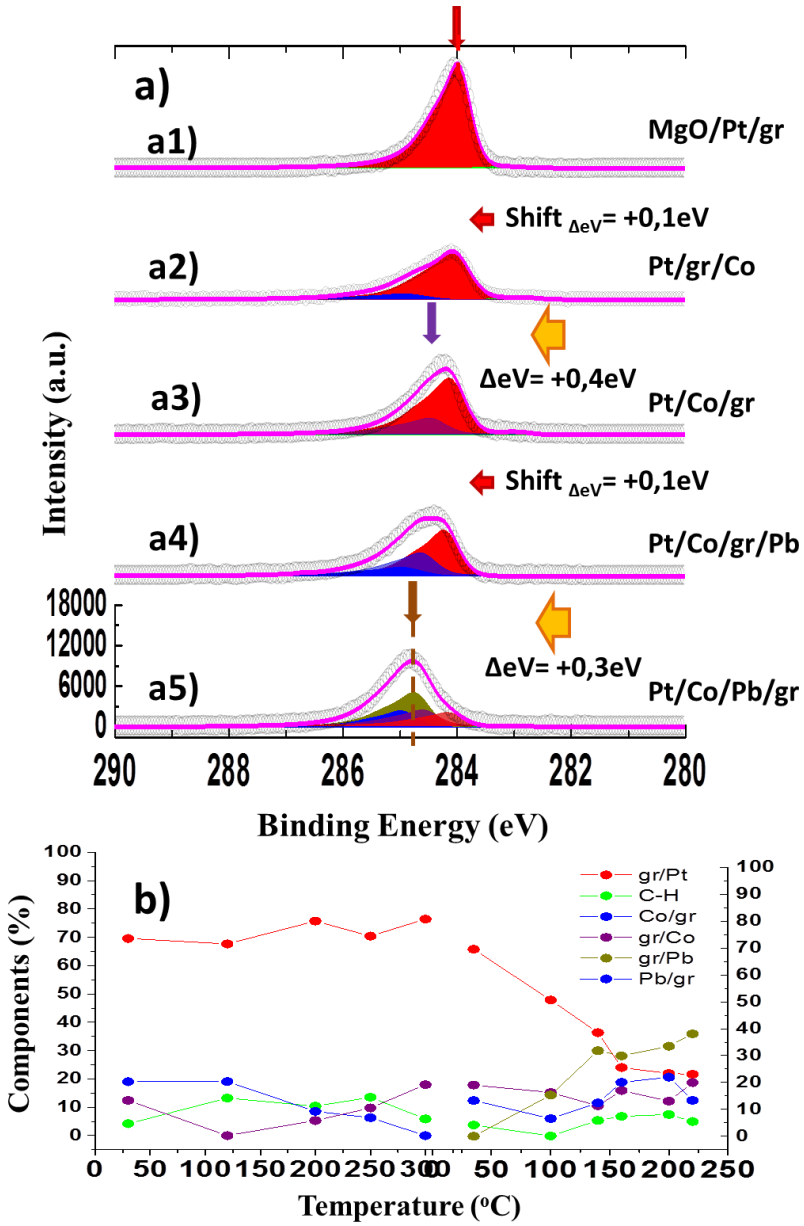

Figure (5.23) a) XPS spectra of C1s core level at each stage of growth. a1) C1s core level appears at B.E.=284eV (red component). a2) After Co evaporation on graphene surface, C1s spectrum presents a new component at 285eV (blue component), i.e. shifted of +1.0eV. a3) After the Co intercalation, C1s shifted to 284.5eV, i.e. at +0.4eV from the original peak. a4) After Pb evaporation, C 1s shifts to +0.1eV and a new component at 285eV appears (blue). a5) After Pb intercalation, the main peak is centered at 284.7eV. b) Components (%) in function of the temperature of both intercalation process.

137eV demonstrating the presence of lead on graphene. No other materials have been found in the survey spectrum.

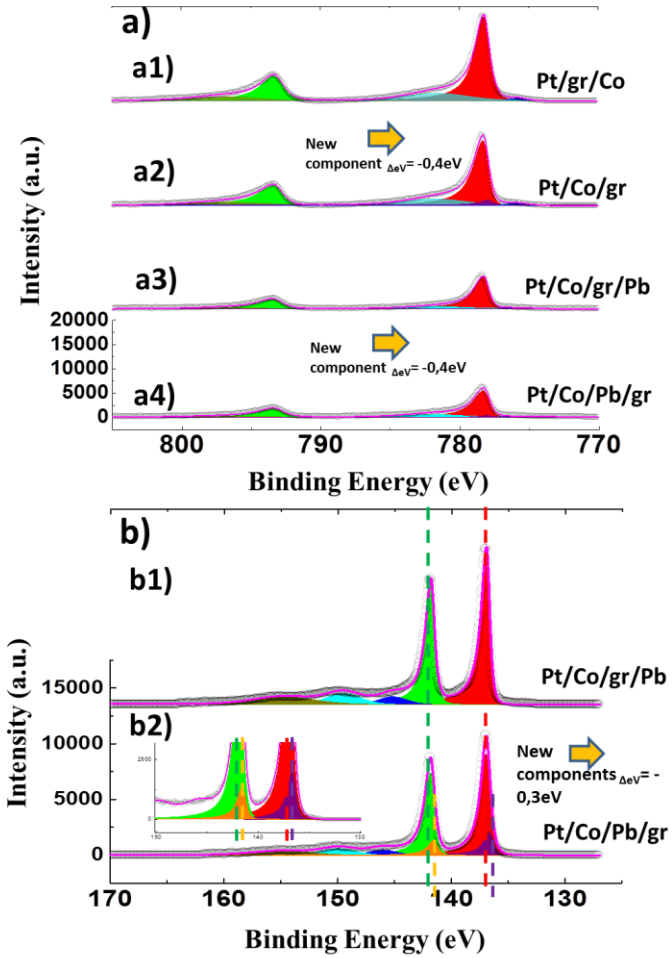

Figure (5.24) a) XPS spectra in the region of Co2p peaks at each stage of growth. a1) Co 2p core spectra present an asymmetric component at 778eV (red component). a2) After the Co intercalation a new component due to the atoms of the surface in contact with the graphene appears, which is shifted at -0.4eV from the first peak (i.e., same value with opposite sign than C). a3) After Pb evaporation the intensity of Co decreases and this new component disappears. a4) After Pb intercalation a small component at 777.6eV appears. b) XPS spectra of Pb 4f core level at each stage of the growth. b1) Spectrum of Pb 4f level. b2) A new component appears at -0.3eV due to the surface in contact with graphene

After lead evaporation the graphene "feels" the new layer on its surface and C1s core level shifts 0.1eV to higher BE following the same behavior than Co evaporation, a new component appears at BE=285eV and the intensity decreases due to the presence of Pb layer. The intensity of Co2p peak

decreases more than 50% and the component that had appeared during the intercalation is not necessary to get well fit. The second intercalation process was developed reaching as T_{max}=220°C. New charge transfer (0.3eV at higher BE) was measured in C1s peak due to the intercalation of Pb under the graphene. The new component appears at 284.8eV due to the stronger interaction of Pb and C atoms (Pb/gr brown in Figure (5.24)) with 46% of the total convolution area. It indicates a well intercalation of lead although a 20% of graphene surface is covered by lead not intercalated. The component at BE=284.5 represents the carbon atoms in contact with Co being less than 1/3 of the same component before the intercalation. It indicates that lead atoms have introduced by the same defects than Co and settled on its place. Due to the bonding Pb/C, a new component appears at lower BE 0.3eV in Pb4f core level (Figure (5.24)).

The behavior of Pt 4d peak has not been different compared to previous samples, it is shown in Figure (5.25)a with the rest of core levels measured. Once the growth of the sample was finished the magnetic properties was measured by using M(R)OKE set-up. The hysteresis loop Figure (5.25) panel b) present a semi square shape with several transitions and less than one order of magnitude of total reflectivity. It confirms the hypothesis of an island growth and makes us think in some problem with the evaporation or more absorption of the Pb atoms reducing the Kerr effect in these samples.

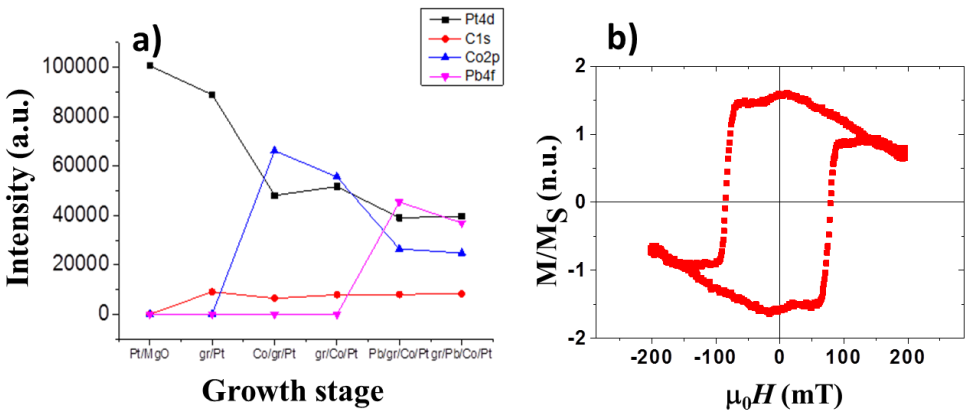

Figure (5.25)) a) XPS peak intensities of Pt 4d (black), C 1s (red), Co 2p (blue) and Pb 4f (purple) peaks at different stage of the growth. b) Vectorial resolved M-H loop normalized to the saturation magnetization Ms. of MgO(111)/Pt/Co/Pb/gr (Hc=100mT).

It has developed a systematic process of epitaxial growth and structural characterization of a set of samples based on graphene varying Co thickness. It has been established temperature limitations to avoid the interdiffusion and learn about the dynamics of the intercalation process. The following table summarize positions in BE, areas and components of all samples studied

5.3.3 Ir/Co/gr samples

From now on is presented an identical growth and characterization study of samples with Ir as buffer layer. Same epitaxial growth process is followed on MgO(111) substrate annealed at 400^{o}C, 30nm of Ir has been grown by sputtering deposition. Afterwards by CVD was grown epitaxial graphene Figure (5.26) show survey spectra of the four stages of the growth process, Ir Co and C are the materials presents in the survey scan. In panel a) spectra before and after graphene growth, where the only difference is the presence of carbon (C1s) at 284.1eV. Caption into panel a) shows a zoom of this area. As Pt based samples XPS study have been developed studying the Ir 4d, C1s and Co2p core levels, paying attention in the charge transfer between Co and C, and the shifts in C1s peak. Co was evaporated by MBE in UHV at RT on graphene surface and intercalated increasing the temperature, it is shown in panel b), and the presence of Co is demonstrated due to the change of background and the new peaks belongs to Co2s, Co2p and LMM Auger. After the intercalation the total intensity of Co decreases due to the top graphene layer. A set of samples have been grown varying the Co thickness in order to analyze the different behavior comparing Ir and Pt. The scheme of the samples is the following: MgO(111)/Ir(30)/Co(t)/gr being (t) the nominal thickness: 3, 2, 1 and 0.8nm.

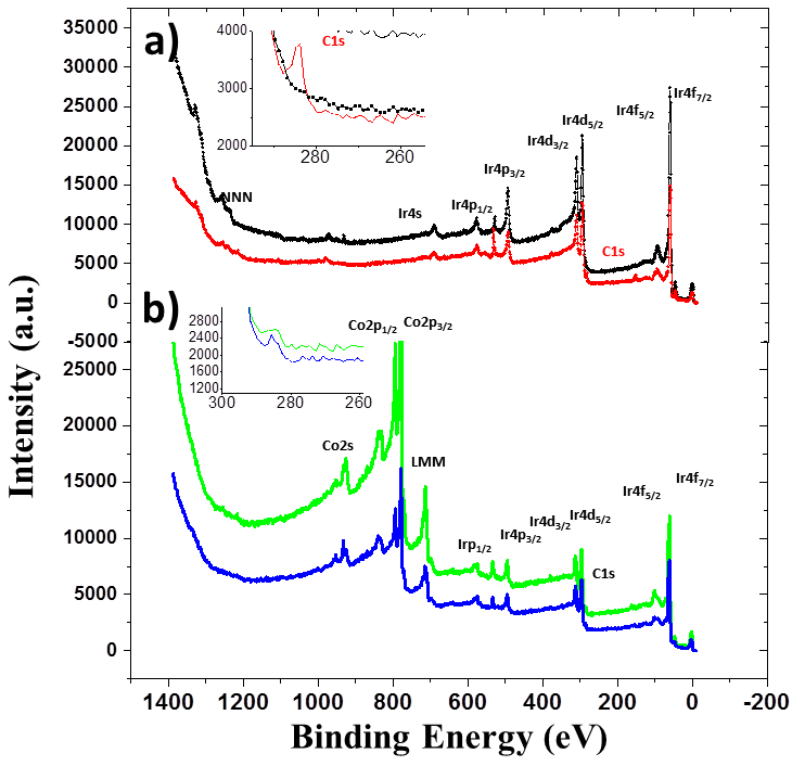

Figure (5.26) XPS survey spectra of the four stages of the growth process. a) Ir on MgO (black line) and gr on Pt (red line). Note the appearance of the C 1s peak after the graphene growth (inset panels). b) XPS survey spectra after the Co deposition (green) and after its intercalation (blue). The peaks centered at 793eV and 778eV correspond to metallic Co $2p_{1/2}$ and $2p_{3/2}$. After the intercalation, we notice a reduction of the Co peaks intensity due to the attenuation of the top graphene sheet. All spectra are vertically shifted for convenience.

The sample with 1nm Co nominal thickness has been considered as a reference sample and its spectra are shown in Figure (5.26), afterwards I will explain the particularities of the rest of growth processes. The interaction between Ir and gr is bigger than Pt [40], panel a) contents the C1s spectra core levels, in the upper part, is shown the peak of the carbon sp^2 on Ir at higher BE (+0.1eV) comparing to the same peak on Pt, the other component appears at 283.3eV due to rests of ethylene and defects of graphene. The evaporation like previous samples was not completely flat and homogenous, exiting parts of graphene surface not covering by Co. in the middle spectrum a new component appears (BE=285eV) next to the previous ones with the

same percentage than Ir/gr component (red) into the total convolution area. The other core levels show same behavior than previous samples, Co2p metallic peak without oxygen and decreasing of intensity of Pt4d under the new layer.

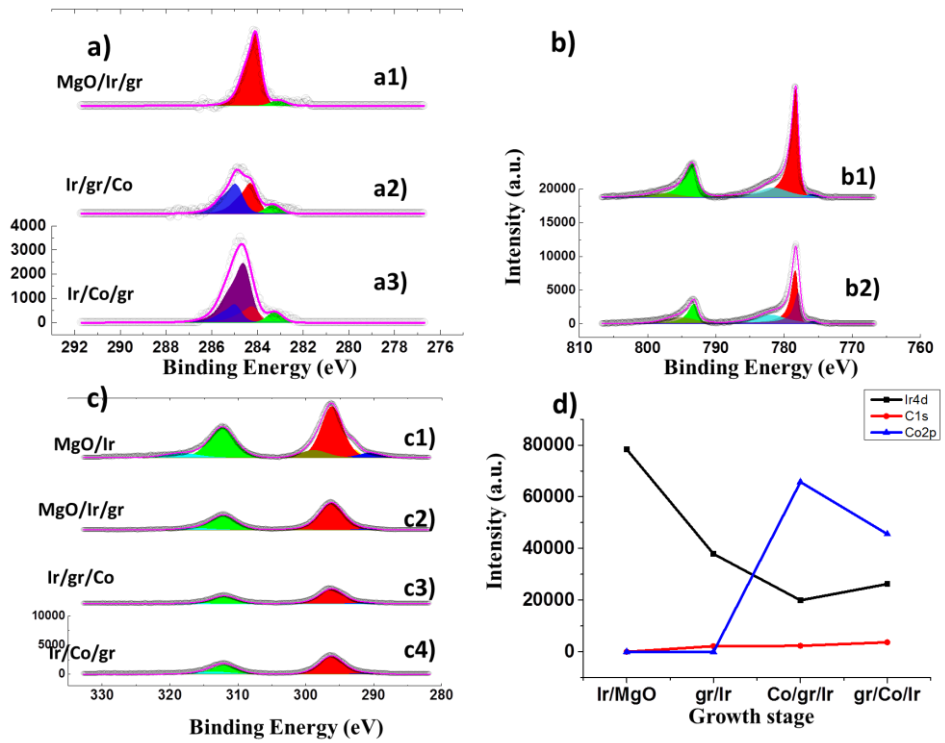

Figure (5.27) XPS spectra of a) C1s core level at each stage of growth process. a1) C1s peaks appears at B.E.=284.1eV (red component) before the evaporation of Co. a2) After the Co evaporation on graphene surface the spectrum presents a new component at 285eV (blue component). There is a chemical shift after the evaporation +0.1eV. a3) After the Co intercalation. The result of the intercalation is the appearance of a new component at 284.6eV (purple component), that is at +0.4eV from the original peak. b1) Co 2p core spectra present an asymmetric component at 778eV (red component). b2) After the Co intercalation a new component due to the atoms of the surface in contact with the graphene appears at -0.4eV from the first peak (i.e., opposite sign than C1s). c) XPS spectra of Ir $4d_{3/2}$ and $4d_{5/2}$ core levels in each stage of growth process. c1) Ir4d peaks appear at B.E.=296 and 312eV. c2) Pt4d core level shows a decreasing of the area due to the presence of the gr on the top. c3) After the Co evaporation, the Pt intensity decreases due to the presence of Co atoms on the top. c4) Increase of the total area of Pt 4d. It indicates the intermixing at the interface between Pt and Co. d) XPS peak intensities of Pt 4d (black), C 1s (red), Co 2p (blue) and Pb 4f (purple) peaks at different stage of the growth.

Due to the higher interaction Ir/gr, the intercalation of Co has been harder to achieve. It has been necessary higher temperatures to start the migration below the ML carbon. While the intercalation temperature was 180°C in the

Pt buffer case, with the Ir is necessary up to 220-250^{o}C to begin the process being necessary increase to almost 400^{o}C inducing in all the samples an intermixed surface Ir/Co. The ongoing work with this Ir/Co/gr samples will consist in improve temperature and intercalation control to avoid interdiffusion as much as possible. After intercalation a new majority component appears in C1s spectrum at 284.6eV due to the carbon atoms on Co. A shift of the convolution peak (0.4eV at higher EB) occurs once the Co spreads under graphene. This charge transfer appears in opposite BE direction in Co2p core level with a new component due to the surface interaction Co/gr at lower BE -0.4eV (panel c). The remaining component at 285eV (blue) indicates the non-intercalation of 100% of cobalt. The evidence of the intermixing is giving by Ir4d spectra in panel b, in the las stage the total area of Ir4d the core level is higher than the previous stage when it was covered by Co. Should be the same area if the Co intercalation would have been not intermixed.

The other samples with Co 3, 2 and 0.8nm have been grown following the reference. The bigger differences have been produced during the intercalation, only the sample with 0.8nm has the same behavior than the reference. In Figure (5.28) are shown the C1s core level after the intercalation and ball schemes for better understanding. The sample with 3nm of Co have been a 100% of intercalation (panel a). The component at 285eV gr/Co is almost cero, the component related to Ir/gr areas (red) indicates the areas where graphene is in contact with Ir buffer layer or due to the interdiffusion In the case of 2nm of Co sample, the intercalation was not complete, more than 60% of Co was intercalated before the thermal effect spread the 3d islands on the graphene. It is not possible to distinguish the atoms below graphene when other atoms are placed on the graphene. The component in C1s will appear always at 285eV, but analyzing the evolution in temperature during the intercalation (not shown), is possible to say that more than 60% of the total Co evaporated was intercalated. The last sample with 0.8nm shows the same behavior than the reference (panel c), successfully intercalation and homogeneity with small interdiffusion.

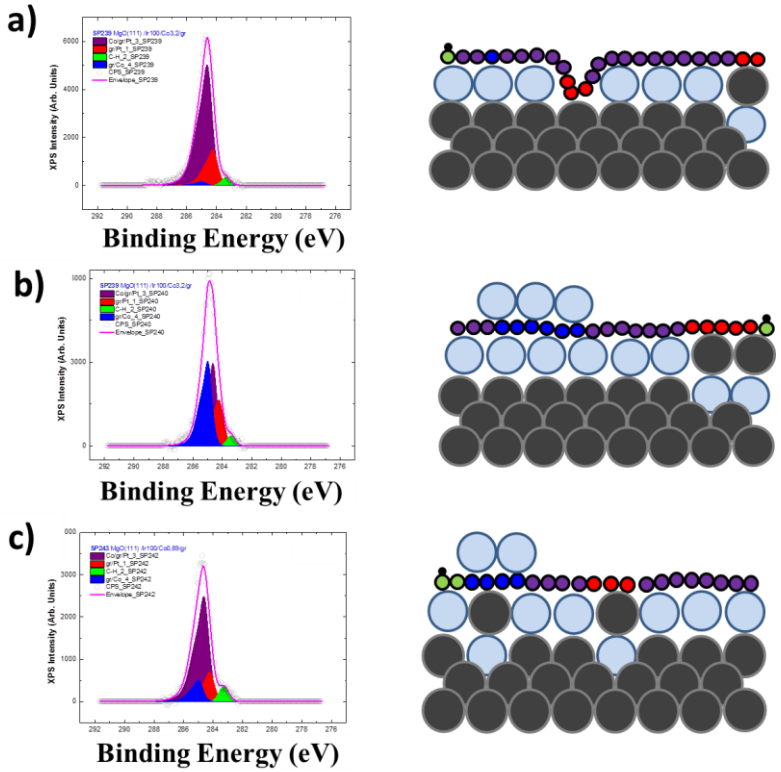

Figure (5.28) Schematic representation of the final situations after intercalation process in Ir buffers: a) 100% of Co intercalation, b) Not complete intercalation with intermixing between Co and Ir. c) Homogeneous intercalation with between Co and Ir.

5.4 Magnetic characterization and DMI determination

The magnetic characterizations have been performed at RT, the hysteresis loops by using a M(R)OKE set-up in IMDEA nanociencia, the MOKE microscopy images and SQUID measurements in Institut Néel (Grenoble).

5.4.1 Magnetic Characterization Pt/Co/gr and Ir/Co/gr

Thickness dependence has been observed after the realization of magnetic measurements. Figure (5.29) shows four different hysteresis loops, belongs to the samples analyzed. Sample with nominal thickness Co6nm, represented with the red curve, was finally defined with more than 60% intercalated, taking into account some interdiffusion, the estimation of the real thickness with PMA under graphene is around 3nm. The loop shows fully reversible transitions of the reversal processes of magnetization with less than 10% of remanence. PMA is not well defined but clear with thickness three times thicker than other metallic capping.

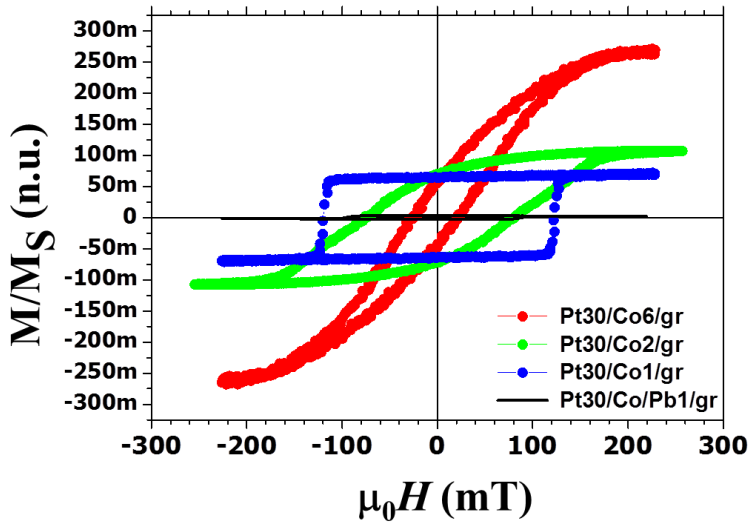

Figure (5.29) Vectorial resolved M-H loops normalized to the saturation magnetization Ms. of MgO(111)/Pt/Co (t) /gr with t=6nm (red dots), 2nm (green dots) and t=1nm (blue dots) and of MgO(111)/Pt/Co/Pb/gr (black dots). To note the reduced coercivity for thicker Co layers.

Decreasing the thickness till 1.5nm (2nm nominally) the enhancement of the PMA is evident (green curve), and the Hc also. It is necessary to remember that the sample has been intermixed and it affects increasing the coercivity field, even so, the change is evident and indicates that the thickness is the responsible. The reversal processes are reversible like the previous sample, with transitions due to the inhomogeneity of the film. The reference sample (blue curve) shows a square hysteresis loop with irreversible transitions and a well-defined PMA. This sample will be measured to try to determine the effective DMI. As have been said before, the sample with lead shows less reflectivity than the rest of the samples, in Figure (5.29) with black line, is almost imperceptible. Figure (5.30) panel a4 shows the same loop in higher scale, sharp and reversible mixed transitions govern the reversal processes of magnetization due to a non-homogeneous film.

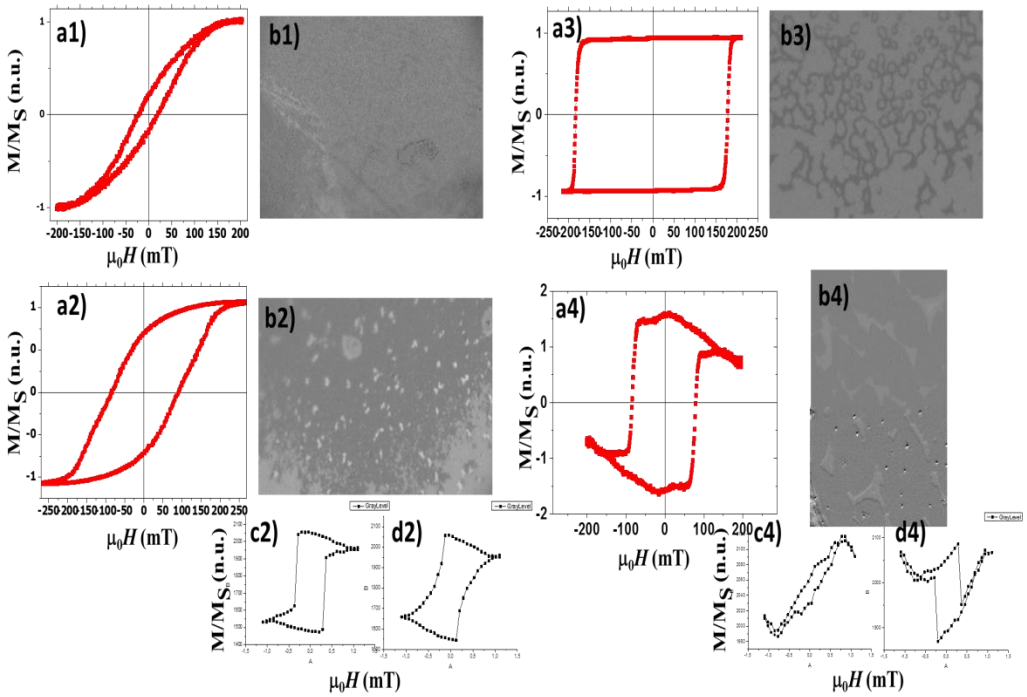

Figure (5.30) Images taken by means of KERR microscopy supported the predictions of all the samples. Panel a1) is presented the thicker nominal sample Pt/Co6/gr, shows a deficient magnetic contrast (b1) in the whole sample but enough to say that it has two levels of background and inhomogeneity film. The domains nucleate everywhere the system energy cost is lower nucleating than propagating the DW. Pt/Co2/gr (a2) shows a bright spots and grey magnetic background (b2). The magnetization reversal in the spots is always saturated up or down, hysteresis loop of the spots is shown in panel c2) with sharp and irreversible transitions meanwhile the resto of the sample has more reversible transitions (right hysteresis loop of panel d2). With the mix of both it has obtained the total loop. The image of the reference sample shows bigger domains and the possibility to nucleate and expand magnetic chiral bubbles. This sample presents 100% of remanence an the magnetic contrast is appropriate to good measurements(a3). The low reflectivity is explained supported by images in panel b3), scarce FM material was deposited on the surface 3d island-like (a4) with different behavior compared to the background. Left hysteresis loop c4) belongs to the bottom area and right loop d4) to the magnetic island with well define PMA.

The images taken by means of KERR microscopy supported the predictions of all the samples. Panel a1) is presented the thicker nominal sample Pt/Co6/gr, shows a deficient magnetic contrast (b1) in the whole sample but enough to say that it has two levels of background and inhomogeneity film. The domains nucleate everywhere the system energy cost is lower nucleating than propagating the DW. Pt/Co2/gr (a2) shows a bright spots and grey magnetic background (b2). The magnetization reversal in the spots is always saturated up or down, hysteresis loop of the spots is shown in panel c2) with

sharp and irreversible transitions meanwhile the resto of the sample has more reversible transitions (right hysteresis loop of panel d2). With the mix of both it has obtained the total loop. The image of the reference sample shows bigger domains and the possibility to nucleate and expand magnetic chiral bubbles. This sample presents 100% of remanence an the magnetic contrast is appropriate to good measurements (a3). The low reflectivity is explained supported by images in panel b3), scarce FM material was deposited on the surface 3d island-like (a4) with different behavior compared to the background. Left hysteresis loop c4) belongs to the bottom area and right loop d4) to the magnetic island with well define PMA.

The behavior of the Ir buffer samples is similar to the Pt based samples, and highly thickness-dependence has been found in these samples as well (Figure (5.33)). Ir/Co3/gr (red curve) with 100% of intercalation and 3nm thickness, shows like not saturated hard axis curve. 3nm of thickness is too thick to keep PMA and the easy axis is in plane. Is not possible to apply more field with this set-up to saturate the sample.

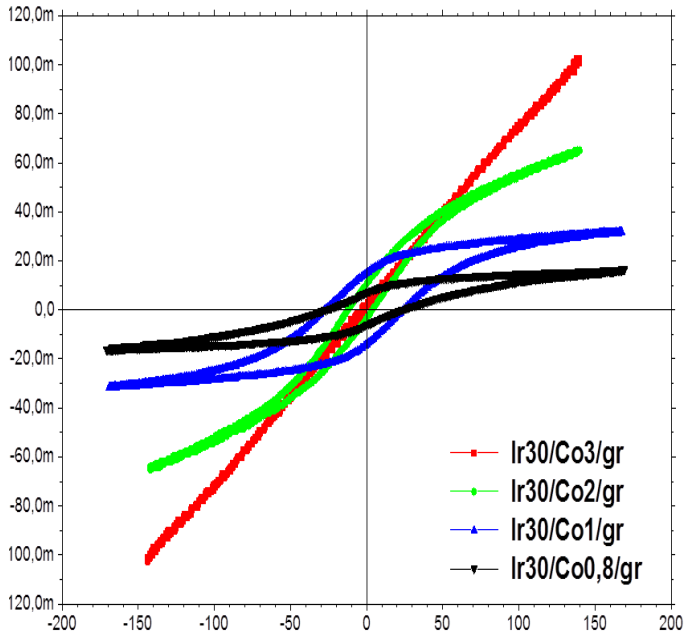

Figure (5.31) Vectorial resolved M-H loops normalized to the saturation magnetization M_S. of MgO(111)/Ir/Co (t)/gr with t=3nm (red dots), 2nm (green dots), 0.9nm (blue dots) and 0.8nm (black dots).

The sample with 2nm Co thickness presents a non-completely saturated hysteresis loop, with PMA, rotating DWs and 10% of remanence. Better PMA have been found in the samples with 1nm (blue) and 0.8nm (black), but the shape is not square like Pt based samples. This behavior may be caused by two factors. Due to the substrate or buffer layer, the mismatch and the crystallization was different, rotated 30 degrees each other Figure (5.8) and the buffer was not flat to induce a well define PMA. Or it is necessary more field to saturate this samples due to its high Hc and DMI roles bigger contribution make chiral and more reversible the DWs. There have been not possible made measurements by KERR microscopy due to the low magnetic contrast.

5.4.2 Direct observation of chiral DW

Following the same steps as in the previous chapter and tacking advantage of the skills acquired, have been carried out measurements to try to determinate the role of the graphene in the effective DMI. Two experiments have been developed to determine DMI by two different proceeds. To determinate $v_{W,}$ consecutive OOP pulses were applied measuring the velocity of displacement of DW. The curve is shown in panel a) of Figure (5.32) with a huge depinning field (300mT) with characteristic creepy displacement of DWs. Once the field has been passed H_{dep} the DW have been turned rounded and the velocity increase exponentially until saturation around 550mT with slow velocity v_W=65m/sec.

On the other hand the experiment performed to determine H_{DMI} applying at the same time a constant in plane field and OOP field pulses indicates (panel b) the presence of chiral DW. The minimum in the velocity at identical value of positive and negative fields determinate H_{DMI}=110mT. The asymmetric expansion of DW in presence of an IP field, present a clockwise write-handed chiral behavior. This is unexpected because graphene is a weak spin-orbit coupling material and is generally not expected to induce sufficient Dzyaloshinskii-Moriya interaction to affect magnetic chirality. Yan et al. consider this effect like a new DMI-like effect due to a Rashba effect [14].

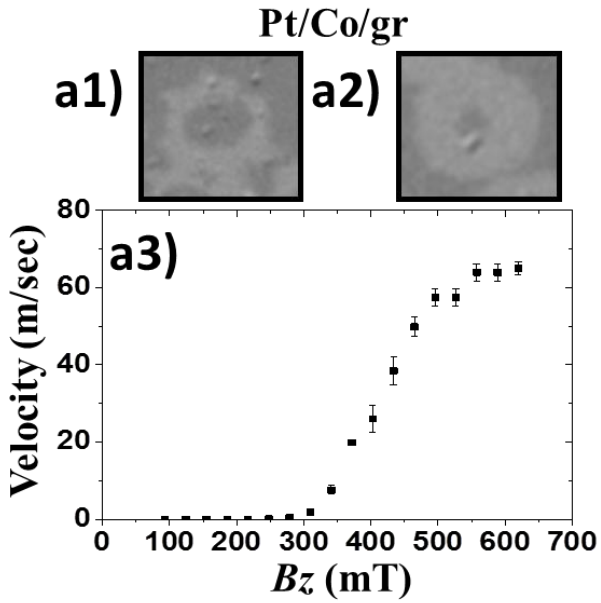

Figure (5.32) Magnetic bubble nucleated upon application of a perpendicular magnetic field pulse in the asymmetric Pt/Co/gr. Differential Kerr images showing the expansion of a domain during the application of an out-of-plane field Bz during a1) creep regime, and a2) flow regime. a3) DW velocity vs. Bz demonstrating a non-zero DMI.

After XPS study it has been confirmed the absence of intermixed interface and an estimation of 0.9nm of Co intercalated. Even so, there are more parameters to take into account. It is known that Co migrates under graphene trough the defects. The last atoms of Co placed near the "drains" have been oxidized and it is not possible to calculate the total amount of Co oxidized. On the other hand, it is also not possible determinate how flat the Co layer is. In consequence the quantification of the effective DMI or Ds like previous samples is only an approximation and it is presented in the following table (Table (5.1)).

Sample	Hc (mT)	Hs (mT)	Ms*t (A)	K_0 (J/m^3)	Δ (nm)	v_W (m/s)	H_{DMI} (mT)	D_S^V (pJ/m)	D_S^H (pJ/m)
Pt/Co/**gr**	180	2000	0,94x 10-3	$6.9x10^5$	4.13	65	120	0.37	0.28

Table (5.1) Coercive field Hc, in-plane saturation field Hs, spontaneous magnetization in function of thickness Ms*t, effective anisotropy energy K0, DW parameter Δ, Walker velocity v_W, DMI field $\mu_0 H_{DMI}$, DMI surface energy, Ds^V extracted from the Walker speed, and Ds^H extracted from the DMI field.

Graphene as top interface in a trilayer system with Pt/Co as bottom interface induce a effective DMI in the same range of Pt and have the same sign of chirality. (Figure (5.33)).

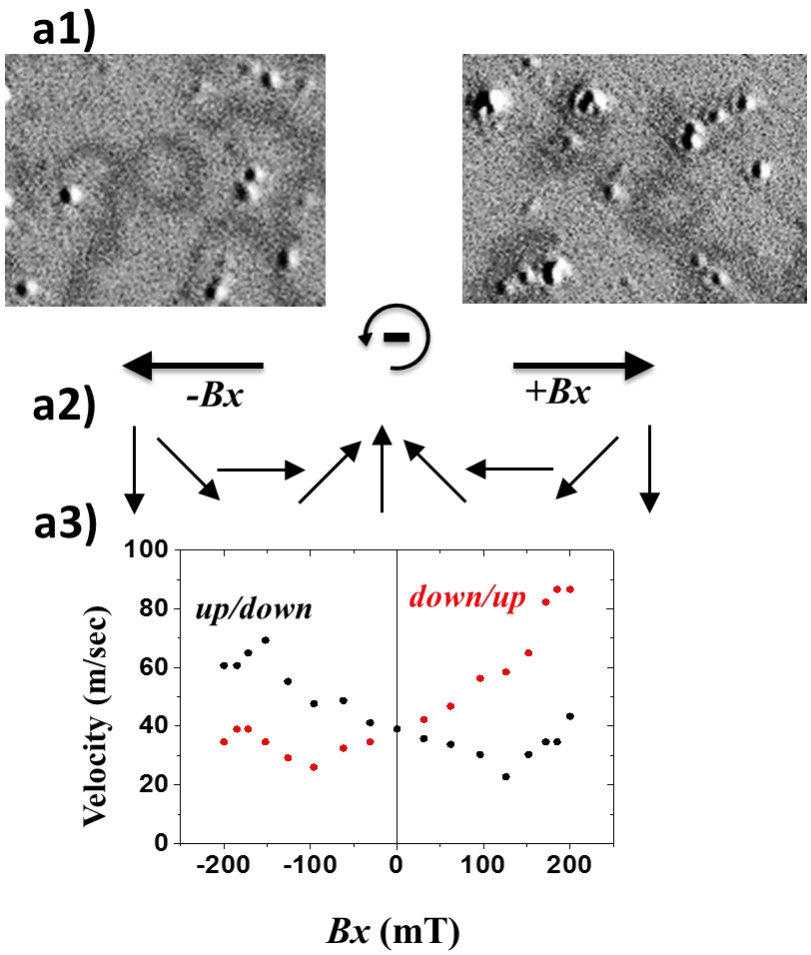

Figure (5.33) a1) Differential Kerr images showing the asymmetric expansion of DWs upon application of an out-of-plane field Bz pulses with the simultaneous application of an in-plane field positive (right) and negative (left), in Pt/Co/gr. a2) anticlockwise chirality direction. a3) DW velocity vs. in-plane field Bx for Pt/Co/gr (Bz = 465mT). Black squares: up/down DWs, red dots: down/up DWs demonstrating the presence of Néel type DW.

5.5 References

[1] C. Binns, S. H. Baker, C. Demangeat, and J. C. Parlebas, “Growth, electronic, magnetic and spectroscopic properties of transition metals on graphite,” *Surf. Sci. Rep.*, vol. 34, no. 4, pp. 107–170, 1999.

[2] A. T. N’Diaye, T. Gerber, C. Busse, J. Myslive??ek, J. Coraux, and T. Michely, “A versatile fabrication method for cluster superlattices,” *New J. Phys.*, vol. 11, 2009.

[3] N. Kheirabadi, A. Shafiekhani, and M. Fathipour, “Review on graphene spintronic, new land for discovery,” *Superlattices Microstruct.*, vol. 74, no. June, pp. 123–145, 2014.

[4] A. H. Castro Neto, F. Guinea, N. M. R. Peres, K. S. Novoselov, and A. K. Geim, “The electronic properties of graphene,” *Rev. Mod. Phys.*, vol. 81, no. 1, pp. 109–162, 2009.

[5] K. S. Novoselov *et al.*, “Two-dimensional gas of massless Dirac fermions in graphene,” *Nature*, vol. 438, no. 7065, pp. 197–200, 2005.

[6] SampaioJ., CrosV., RohartS., ThiavilleA., and FertA., “Nucleation, stability and current-induced motion of isolated magnetic skyrmions in nanostructures,” *Nat Nano*, vol. 8, no. 11, pp. 839–844, Nov. 2013.

[7] J. Balakrishnan *et al.*, “Giant spin Hall effect in graphene grown by chemical vapour deposition,” *Nat. Commun.*, vol. 5, p. 4748, 2014.

[8] A. Avsar *et al.*, “Spin–orbit proximity effect in graphene,” vol. 5, p. 4875, Sep. 2014.

[9] S. Mühlbauer *et al.*, “Skyrmion Lattice in a Chiral Magnet,” *Science (80-.).*, vol. 323, no. 5916, p. 915 LP-919, Feb. 2009.

[10] F. Calleja *et al.*, “Spatial variation of a giant spin–orbit effect induces electron confinement in graphene on Pb islands,” *Nat. Phys.*, vol. 11, no. January, pp. 43–47, 2015.

[11] N. Rougemaille, A. T. Ndiaye, J. Coraux, C. Vo-Van, O. Fruchart, and A. K. Schmid, “Perpendicular magnetic anisotropy of cobalt films intercalated under graphene,” *Appl. Phys. Lett.*, vol. 101, no. 14, pp. 1–9, 2012.

[12] V. M. Karpan *et al.*, “Graphite and Graphene as Perfect Spin Filters,” *Phys. Rev. Lett.*, vol. 99, no. 17, p. 176602, Oct. 2007.

[13] E. Cobas, A. L. Friedman, O. M. J. van’t Erve, J. T. Robinson, and B. T.

Jonker, “Graphene As a Tunnel Barrier: Graphene-Based Magnetic Tunnel Junctions,” *Nano Lett.*, vol. 12, no. 6, pp. 3000–3004, 2012.

[14] H. Yang *et al.*, “Significant Dzyaloshinskii-Moriya Interaction at Graphene-Ferromagnet Interfaces due to Rashba-effect,” pp. 1–21.

[15] B. Dlubak *et al.*, “Highly efficient spin transport in epitaxial graphene on SiC,” *Nat Phys*, vol. 8, no. 7, pp. 557–561, Jul. 2012.

[16] Y. S. Dedkov, M. Fonin, U. Rüdiger, and C. Laubschat, “Rashba Effect in the Graphene/Ni(111) System,” *Phys. Rev. Lett.*, vol. 100, no. 10, p. 107602, Mar. 2008.

[17] M. H. Liu, J. Bundesmann, and K. Richter, “Spin-dependent Klein tunneling in graphene: Role of Rashba spin-orbit coupling,” *Phys. Rev. B - Condens. Matter Mater. Phys.*, vol. 85, no. 8, pp. 1–10, 2012.

[18] C. L. Kane and E. J. Mele, “Quantum Spin Hall Effect in Graphene,” *Phys. Rev. Lett.*, vol. 95, no. 22, p. 226801, Nov. 2005.

[19] H. Yang *et al.*, “Anatomy and Giant Enhancement of the Perpendicular Magnetic Anisotropy of Cobalt–Graphene Heterostructures,” *Nano Lett.*, vol. 16, no. 1, pp. 145–151, 2016.

[20] Various authors, *Cambridge Dictionary “graphene definition.”* .

[21] J. C. Slonczewski and P. R. Weiss, “Band Structure of Graphite,” *Phys. Rev.*, vol. 109, no. 2, pp. 272–279, 1958.

[22] K. S. Novoselov *et al.*, “Electric Field Effect in Atomically Thin Carbon Films,” *Source Sci. New Ser. Gene Expr. Genes Action*, vol. 306, no. 5696, pp. 666–669, 2004.

[23] K. S. Novoselov *et al.*, “Two-dimensional atomic crystals,” *Proc. Natl. Acad. Sci. U. S. A.*, vol. 102, no. 30, pp. 10451–10453, 2005.

[24] C. Berger *et al.*, “Ultrathin Epitaxial Graphite: 2D Electron Gas Properties and a Route toward Graphene-based Nanoelectronics,” *J. Phys. Chem. B*, vol. 108, no. 52, pp. 19912–19916, 2004.

[25] P. Avouris, “Graphene: Electronic and Photonic Properties and Devices,” *Nano Lett.*, vol. 10, no. 11, pp. 4285–4294, 2010.

[26] A. C. Neto, F. Guinea, and N. M. Peres, “Drawing conclusions from graphene,” *Phys. World*, vol. 19, no. 11, pp. 33–37, 2006.

[27] J. Moser, A. Barreiro, and A. Bachtold, “Current-induced cleaning of

graphene," *Appl. Phys. Lett.*, vol. 91, no. 16, p. 163513, 2007.

[28] S. Chen *et al.*, "Raman Measurements of Thermal Transport in Suspended Monolayer Graphene of Variable Sizes in Vacuum and Gaseous Environments," *ACS Nano*, vol. 5, no. 1, pp. 321–328, 2011.

[29] S. V. Morozov *et al.*, "Giant intrinsic carrier mobilities in graphene and its bilayer," *Phys. Rev. Lett.*, vol. 100, no. 1, pp. 11–14, 2008.

[30] R. R. Nair *et al.*, "Fine Structure Constant Defines Visual Transparency of Graphene," *Science (80-.).*, vol. 320, no. 5881, p. 1308 LP-1308, Jun. 2008.

[31] N. Tombros, C. Jozsa, M. Popinciuc, H. T. Jonkman, and B. J. van Wees, "Electronic spin transport and spin precession in single graphene layers at room temperature," *Nature*, vol. 448, no. 7153, pp. 571–574, Aug. 2007.

[32] A. K. Geim and A. H. MacDonald, "Graphene: Exploring carbon flatland," *Phys. Today*, vol. 60, no. 8, pp. 35–41, 2007.

[33] J. Coraux *et al.*, "Growth of graphene on Ir(111)," *New J. Phys.*, vol. 11, 2009.

[34] B. Wang, X. Ma, M. Caffio, R. Schaub, and W.-X. Li, "Size-Selective Carbon Nanoclusters as Precursors to the Growth of Epitaxial Graphene," *Nano Lett.*, vol. 11, no. 2, pp. 424–430, 2011.

[35] P. Sutter, J. T. Sadowski, and E. Sutter, "Graphene on Pt(111): Growth and substrate interaction," *Phys. Rev. B - Condens. Matter Mater. Phys.*, vol. 80, no. 24, pp. 1–10, 2009.

[36] L. Gao, J. R. Guest, and N. P. Guisinger, "Epitaxial Graphene on Cu(111)," *Nano Lett.*, vol. 10, no. 9, pp. 3512–3516, 2010.

[37] K. Yamamoto, M. Fukushima, T. Osaka, and C. Oshima, "Charge-transfer mechanism for the (monolayer graphite) /Ni(111) system," *Phys. Rev. B*, vol. 45, no. 19, pp. 11358–11361, May 1992.

[38] E. Loginova, N. C. Bartelt, P. J. Feibelman, and K. F. McCarty, "Evidence for graphene growth by C cluster attachment," *New J. Phys.*, vol. 10, no. 1, 2008.

[39] C. Hwang, K. Yoo, S. J. Kim, E. K. Seo, H. Yu, and L. P. Biró, "Initial Stage of Graphene Growth on a Cu Substrate," *J. Phys. Chem. C*, vol. 115, no. 45, pp. 22369–22374, 2011.

[40] A. B. Preobrajenski, M. L. Ng, A. S. Vinogradov, and N. Mårtensson, "Controlling graphene corrugation on lattice-mismatched substrates," *Phys. Rev. B - Condens. Matter Mater. Phys.*, vol. 78, no. 7, pp. 2–5, 2008.

[41] L. Meng *et al.*, "Multi-oriented moiré superstructures of graphene on Ir(111): experimental observations and theoretical models," *J. Phys. Condens. Matter*, vol. 24, no. 31, p. 314214, 2012.

[42] N. Fairley, "CasaXPS." p. http://www.casaxps.com, ©Casa software Ltd., 2005., 2009.

[43] M. L. Ng *et al.*, "Controlling Hydrogenation of Graphene on Transition Metals.pdf," pp. 18559–18565, 2010.

[44] W. Moulder, J. Stickle, *Perkin-Elmer Handbook of X-ray photoelectron Spectroscopy*. 1992.

VI. Summary

This thesis addressed fundamental questions in the area of nanomagnetism, introducing relevant technological and scientific advances in the fields of spintronics and spin-orbitronics. In general, the work provides a general picture of the influence of the magnetic symmetry in model magnetic nanostructures, emphasizing that symmetry-breaking effects originating from an effective unidirectional contribution (e.g., interfacial exchange coupling in exchange-biased systems or interfacial Dzyaloshinskii-Moriya interaction in asymmetric perpendicular magnetic anisotropy systems) promotes chiral asymmetry effects of their physical properties. This knowledge will certainly open additional avenues to develop future advanced spintronic and spin-orbitronic devices. Future perspectives are also discussed.

This thesis provides a systematic study on magnetic nanostructures with well-defined (tailored) magnetic symmetry, including both spintronic and spin-orbitronic systems, and introduces both technological and scientific advances. In general, it is an experimental work where model sample preparation tasks (by sputtering, MBE, CVD) in ultra-high-vacuum (UHV) conditions were combined with in-situ characterization (LEED, XPS) and ex-situ (M(R)OKE, Kerr microscopy and XMCD) and it includes new technological developments.

Several model systems with the easy direction of magnetization contained in the plane of the surface (in-plane magnetic anisotropy, IP) or perpendicular to the surface (perpendicular magnetic anisotropy, PMA) have been prepared and characterized. In particular, the thesis discusses several (polycrystalline) IP spintronic systems (Block I), including:

- Ferromagnetic (FM) thin films with uniaxial (two-fold) anisotropy.
- Bilayers composed of an FM layer and an antiferromagnetic layer (AFM) exchange coupled at the interface (FM/AFM), where the

uniaxial anisotropy of the FM layer competes with the induced interfacial unidirectional anisotropy (one-fold).

- Spin-valve (two FM layers separated by a non-magnetic spacer NM) systems with one FM layer exchange coupled with an AFM layer, (exchange-biased spin valve, AFM/FM1/ spacer/FM2).

In Block II, (polycrystalline and epitaxial) spin-orbitronic PMA magnetic nanostructures are discussed, including:

- (Symmetric) systems composed of a FM layer between two NM layers of the same material (NM/ FM/NM) and multilayered systems ([NM / FM]n). The influence of the seed layers and the number of repetitions (n) are keys to control both PMA and magnetization reversal processes.
- (Asymmetric) NM1/FM/NM2 trilayers. The use of different NM layers promotes effective Dzyaloshinskii-Moriya (DMI) interaction of chiral nature which in turn influences the magnetization inversion mechanisms.

Respect the technological development it is necessary to emphasize:

- The development of a unique experimental technique named M(R)OKE, Magneto (Resistance)-Optic Kerr Effect magnetometry, that allows to study the magnetic and transport properties of nanostructures simultaneously at any field angle condition.
- The experimental methodology for preparing/controlling polycrystalline and epitaxial systems with PMA, including graphene-based systems.

From each of the two main Blocks in which the thesis is divided, three scientific contributions can be highlighted in each one:

I.1. Determination of the relationship between magnetic and transport properties of magnetic nanostructures (FM, FM/AFM, exchange-biased spin-valves).

I.2. Experimental demonstration of the universality of the anisotropic magneto-resistance, shown in systems with magneto-resistive processes of

different origin (AMR and GMR) and FM systems of different nature (metallic and oxides).

I.3. Determination of the symmetry-breaking effects. In general, magnetic nanostructures having a unidirectional anisotropic contribution exhibit a chiral symmetry transport properties.

II.1. Preparation and characterization of polycrystalline and monocrystalline systems with tailored PMA and effective DMI.

II.2. Identification of the key parameters controlling PMA and DMI and, therefore, magnetization reversal processes.

II.3. Observation and determination of chiral DMI effects in PMA trilayers with asymmetric interfaces.

Among these, and as a general highlight, the thesis provide a general picture of the influence of the magnetic symmetry in model magnetic nanostructures, emphasizing that symmetry-breaking effects promotes chiral asymmetry effects of their physical properties

Conclusions

This thesis addresses fundamental questions in the area of nanomagnetism, introducing relevant technological and scientific advances in the field of spintronics and spinorbitronics. The common nexus of the work stays in the SOC effects, whether the research focuses on the influence of magnetic symmetry on physical (magnetic and transport) properties or on the existence of chiral phenomena. In addition, this work explores the possibility to prepare novel full epitaxial graphene-based spin-orbitronic systems in order to can exploit the extraordinary electronic, mechanical and optical properties of graphene (gr), and in particular its long spin diffusion length and low resistivity. The thesis also illustrates how versatile can be the physical properties of magnetic nanostructures highlighting the importance of performing detailed angular-dependent measurements.

From the scientific point of view, it is worth to underline the experimental demonstration of the universality of anisotropic transport phenomena, the identification of chiral physical phenomena originated from symmetry-breaking effects in systems displaying a unidirectional contribution, as well as the preparation and characterization of PMA systems with tuneable physical properties (PMA and DMI). In analogy, from the technological point of view, remarkable are the development of the M(R)OKE instrument, that is unique at international level, as well as the methodology designed to prepare and control epitaxial graphene-based systems with chiral effects. The model magnetic nanostructures investigated permit to appreciate the great importance of both instrumentation and methodology used, which allow elucidating (and controlling) their physical properties. This knowledge will certainly open additional avenues to develop future advanced spintronic and spin-orbitronic devices.

Conclusiones

Esta tesis aborda cuestiones fundamentales en el campo del nanomagnetismo, introduciendo avances tecnológicos y científicos relevantes en el campo de la espintrónica y la espinorbitrónica. El trabajo se vertebra alrededor de los efectos del SOC, tanto en la influencia de la simetría magnética en las propiedades físicas (magnéticas y de transporte) como en la existencia de fenómenos quirales. Además, se explora la posibilidad de preparar nuevos sistemas epitaxiales de spin-orbitrónica basados en grafeno donde se podrían explotar sus extraordinarias propiedades: electrónicas, mecánicas, ópticas y en particular su larga longitud de difusión de spin y baja resistividad. La tesis también ilustra cuán versátiles pueden ser las propiedades físicas de las nanoestructuras magnéticas, resaltando la importancia de realizar mediciones angulares.

Desde el punto de vista científico, es muy remarcable la demostración experimental de la universalidad de los fenómenos de transporte anisotrópico, la identificación de fenómenos físicos quirales originados por efectos de ruptura de simetría en sistemas que tienen una contribución unidireccional, así como la preparación y caracterización de sistemas con anisotropía magnética perpendicular (PMA) y propiedades físicas diseñables (PMA y DMI). Desde el punto de vista tecnológico, destacan el desarrollo instrumental del sistema M (R) OKE, que es único internacionalmente, así como la metodología diseñada para preparar y controlar sistemas totalmente basados en grafeno epitaxial con efectos quirales. El modelo de nanoestructuras magnéticas investigadas ha permitido apreciar la gran importancia tanto de la instrumentación como de la metodología utilizadas para poder entender / controlar sus propiedades físicas. Este conocimiento ciertamente abrirá caminos adicionales para desarrollar futuros dispositivos espintronicos y spin-orbitrónicos avanzados.

Acknowledgements

First of all, I would like to thank *Prof. Julio Camarero* for his trust in me, for making me part of this motivating world of IMDEA nanoscience and, in particular, the group of nanomagnetism where I have learned and will learn so much about such an interesting science. Thanks for the motivation and the good atmosphere and for making me participate from the very beginning in conferences and international summer schools as well as marathoners beam times where I have met such wonderful people. I would also like to express my gratitude to *Dr. Paolo Perna* for his daily work, right from the construction of the first evaporators in the very early days of the lab to all his effort in helping me during the drafting of this paper, for his patience when repeating to me hundreds of times the same concepts and for all the confidence placed on me, my opinions and ideas. My thanks also go to *Dr Stefania Pizzini* for making me feel at home and like a true researcher during my short stay at Institut Néel. Thanks once again for her assistance and concern during the writing of part of this thesis. Likewise, I would like to thank the people with whom I have collaborated during my PhD and who have contributed to the development of this thesis:

My special thanks go to:

Dr Miguel Ángel Niño for being exceptionally patient and friendly with me, and for transmitting to me all his knowledge about the UHV system, photoemission spectroscopy and surface science, and for sharing with me his time and knowledge of physics while answering my many questions.

Dr. Cristina Navio, for her kindness and availability whenever necessary, helping to open, close and re-open the chambers. And for advising on UHV and photoemission spectroscopy.

Dr Laurence Méchin. for having received me at the GREYC and make me feel like one more in her group, and for introducing me into the oxide-world.

Dr Jan Vogel for his way of being, good humor and for sharing his time and knowledge during my measurements at Grenoble

Dr Stephan Flament and Dr Vincent Cros for their support letters for the application of my thesis for the International mention.

Dr Rubén Guerrero, Dr Eva Céspedes, Dr Davide Maccariello, Dr Juan Rojo and all IMDEA reserchers which in one way or another have contributed to my formation during these four years.

In addition, I would like to thank my IMDEA, UAM and stays colleagues *during my PhD: Karol, Gloria, Luiggi, Amjad, Adrian, Javi , Sergio, Gui-Lin, Noelia, Melek* and all the people for continuously contributing to providing a great and comfortable atmosphere. In particular to *Sandeep Kumar Chaluvadi, Dyane de Souza Chaves, Viola Křižáková, Patricia Pedraz and Almudena Inchausti* for performing XRD, XRR, MOKE microscopy and AFM measurements, which complement the work presented in this paper

I also wish to express my upmost gratitude to *my mother*, for without her efforts and support I would not have come this far, this thesis is yours. Also to m*y sisters, brothers in law, nephews and nieces, all my friends and the members of my band* for giving me all their support and understanding during this period in which I did not have much time to share with them.

Finally, I would like to express all my gratitude to and admiration for *Ceci,* for your understanding and helpfulness, for making things easy for me particularly during this last year, and for always being there to listen to me.

Publications

1. P. Perna, D. Maccariello, F. Ajejas, R. Guerrero, L. Méchin, S. Flament, J. Santamaria, R. Miranda, and J. Camarero,Engineering Large Anisotropic Magnetoresistance in La0.7Sr0.3MnO3Films at Room Temperature, Adv. Funct. Mater. (2017) 1700664.

2. P. Perna, **F. Ajejas**, D. Maccariello, R. Guerrero, J. Camarero, and R. Miranda, Chiral asymmetry driven by unidirectional magnetic anisotropy in Spin-Orbitronic systems, SPIE Nano. & Eng. **9931**, 99312I (2016)

3. P. Perna, **F. Ajejas**, D. Maccariello, J.L.F. Cuñado, R. Guerrero, M.A. Niño, M. Muñoz, J.L. Prieto, R. Miranda, and J. Camarero, 2D chiral asymmetry in unidirectional magnetic anisotropy structures, AIP Advances **6**, 055819 (2016)

4. P. Perna, **F. Ajejas**, D. Maccariello, J.L.F. Cuñado, R. Guerrero, M. A. Niño, A. Bollero, R. Miranda, and J. Camarero, "Interfacial exchange coupling induced chiral symmetry-breaking of spin-orbit effects, Phys. Rev. B Rapid Comm. **92**, 220422 (2015)

5. J.L..F. Cuñado, J. Pedrosa, **F. Ajejas**, A. Bollero, P. Perna, F. J. Teran, R. Miranda, and J. Camarero, Vectorial-magneto optical Kerr effect technique combined with variable temperature and full angular range all in a single setup, Rev. Sci. Instrum.**86**, 046109 (2015).

Publicaciones en progreso

6. **F. Ajejas**, A. Gudín, R. Guerrero, M. A. Niño, S.Pizzini, J. Vogel, M. Valvidares, P. Gargiani, J. Camarero, R. Miranda, and P. Perna. Large perpendicular magnetic anisotropy and Dzyaloshinskii–Moriya chiral interaction at room temperature in epitaxial graphene-based nanostructures. Submitted to Nanoletters (2017).

7. **F. Ajejas**, D. Chaves, J. Vogel, P. Perna, J. Camarero, J. Sampaio, A. Thiaville and S. Pizzini. Domain wall and skyrmion dynamics in multilayer films with perpendicular magnetic anisotropy. In preparation (2017).

8. **F. Ajejas**, A. Gudín, R. Guerrero, J. Camarero, R. Miranda, and P. Perna. Universality of anisotropic magnetoresistance in magnetic systems. In preparation (2017).

9. **F. Ajejas**, A. Gudín, D. Maccariello, V. Cros, R. Guerrero, J. Camarero, P. Perna. Evidence of unidirectional anisotropy induced by Dzyaloshinskii-Moriya interaction in perpendicular magnetic anisotropy structures. In preparation (2017).

Otras

10. J. L. F. Cuñado, J. Pedrosa, **F. Ajejas**, P. Perna, A. Bollero, R. Miranda, J. Camarero. Direct observation of temperature-driven magnetic symmetry transitions by vectorial-MOKE magnetometry. Submitted (2017).

11. J.L.F. Cuñado, A. Bollero, T. Pérez-Castañeda, P. Perna, **F. Ajejas**, J. Pedrosa, A. Gudín, A. Maldonado, M. A. Niño, Rubén Guerrero, D. Cabrera, F. J. Teran, R. Miranda, and J. Camarero, Emergence of the Stoner-Wohlfarth astroid in thin films at dynamic regime. Submitted Nature Scientific Report (2017).